

Material characterization for stamping simulation of automotive body components

A fundamental study on the identification of the macromechanical post-
necking behaviour of metallic materials

A thesis in partial fulfilment of the requirements
for the degree of
Master of Science in Automotive Engineering

Supervisors: Prof Graziano Ubertalli
Mr Daniele De Caro
Mr Matteo Ferrea

Author: Saeid Ghaffari

Politecnico di Torino
Turin, Italy
March 2021



**POLITECNICO
DI TORINO**

Collegio di Ingegneria Meccanica,
Aerospaziale, dell'Autoveicolo e della
Produzione



Table of Contents

Chapter One: Material matters	20
1.1 Macromechanical material characterization for stamping simulation.....	21
1.1.1 Yield criteria.....	21
1.1.2 Flow stress curve and strain hardening laws	22
1.1.3 Forming limits	23
1.2 How to characterize materials	23
1.3 Metal forming simulation	25
1.3.1 The Fidelity of a Simulation Model	26
1.4 Material matters	27
1.4.1 Materials.....	27
1.4.2 Material testing and challenges	35
1.5 Challenges in material model selection for forming simulation.....	36
1.6 Goals and Approaches	37
1.6.1 Scopes.....	37
1.6.2 Methodology	38
Chapter Two: Post-necking flow curve identification through tensile testing.....	39
2.1 Introduction: four classes of methods to identify post-necking hardening behaviour.....	40
2.2 First level of approximation	41
2.3 Second level of approximation with respect to the problem of diffuse necking ...	41
2.4 Third level of approximation with respect to the problem of diffuse necking	42
2.5 Virtual fields method	44
2.6 Extending tensile test data using Siebel and Schwaigerer's model.....	45
2.6.1 Methodology	45
2.6.2 Measurement setup.....	46

2.6.3	Stress-strain curve evaluation.....	47
2.7	Optimization algorithms for material modelling	49
Chapter Three: Hardening laws investigation on Novelis AA5000, Constelium AA5000, Constelium AA6000		50
3.1	Introduction	51
3.2	An introduction into common strain hardening laws	52
3.2.1	Hollomon hardening law	53
3.2.2	Swift hardening law	54
3.2.3	Voce hardening law (classical Voce saturation law)	56
3.2.4	Swift-Voce hardening law.....	58
3.2.5	Hollomon-Voce hardening law	59
3.2.6	Hockett-Sherby hardening law	62
3.2.7	Swift/Hockett-Sherby hardening law	64
3.2.8	k -exponent function.....	66
3.3	Hardening laws investigation on Novelis and Constelium data sheets	66
3.3.1	Novelis AA5000 tensile test results	66
3.3.2	Constelium AA5000 tensile test results	80
3.3.3	Constelium AA6000 tensile test results	93
Chapter Four: Hydraulic bulge test		107
4.1	Introduction	108
4.2	Hydraulic bulge test and tensile test	109
4.3	Bulge test equipment	111
4.4	Data collection and analysis of hydraulic bulge test	112
4.4.1	Indirect method	113
4.4.2	Direct methods	124
4.5	ISO 16808 recommended procedure for hydraulic bulge test.....	127

4.5.1	Determination of the curvature and strains at the pole.....	128
4.5.2	Calculation of biaxial stress-strain curves.....	129
4.6	From yield point to fracture by combining tensile test data with bulge test data	130
4.6.1	Introduction	130
4.6.2	Tensile test data extrapolation using scaled bulge test data	131
4.6.3	Plotting flow curve using anisotropy of the material	133
4.7	Post-necking identification using ISO 16808 procedure	135
4.7.1	Aluminium 6000 Novelis	135
4.7.2	DP600 1.2mm Arcelor	143
Chapter Five: Post-necking tensile stress–strain behaviour identification of AHSSs using Digital Image Correlation technique.....		150
5.1	Introduction	151
5.2	Bridgman method: Yes, but not for a Flat Specimen	151
5.3	Behind the scene: Theory	154
5.3.1	Hill’s 1948 Yield Criterion: A short review	155
5.4	Necking: criteria and mechanism	161
5.4.1	Criteria and prediction.....	161
5.5	Tensile test results of CP 1400HD subsize specimen using DIC technique and GOM Correlate SW	162
5.5.1	Position of the neck	163
5.5.2	Equivalent stress and equivalent plastic strain evaluation	167
5.5.3	Necking mechanism in CP 1400HD subsize specimen using DIC technique	
	177	
5.6	Tensile test results of QP 1180-subsize specimen using DIC technique and GOM correlate SW.....	182
5.7	A review on the proposed method	189
Chapter Six: Validation of the equivalent flow stress curve using FEA.....		190

6.1	Introduction	191
6.2	Finite element modelling and analysis	191
6.2.1	Pre-processing	191
6.2.2	Post-processing: analysis of the numerical results	196
6.2.3	Further investigation on FE results	205
6.3	A review on the FEA of the tensile test	213
Chapter Seven: Conclusion and possible future works		214
Bibliography		218
Appendix A		226
Appendix B		230

List of figures

Figure 1 Example of a forming limit curve for an aluminium alloy-CRF data	23
Figure 2 aluminium alloys generally employed for body structures (9)	29
Figure 3 Steel Strength Ductility Diagram for Today's AHSS Grades (includes a comparison of traditional low-strength and high-strength steels) (14)	34
Figure 4 Normal anisotropy variation during deformation, 0° to RD, cold-rolled DC04 steel (35)	46
Figure 5 material modelling process evolution	49
Figure 6 Hollomon hardening law fitting to an aluminium alloy and the position of corresponding diffuse necking	54
<i>Figure 7 The experimentally measured stress-strain curve and the fit by swift law (44) ...</i>	<i>54</i>
Figure 8 Swift hardening law fitting to a flow curve and the position of diffuse necking ..	56
Figure 9 Voce hardening law fitting to a flow curve and the position of diffuse necking ..	57
Figure 10 Swift-Voce hardening law for small values of strain	58
Figure 11 Swift-Voce hardening law for large values of strain	59
Figure 12 Hollomon-Voce hardening law for small values of strain	60
Figure 13 Hollomon-Voce hardening law for large values of strain	60
Figure 14 Hollomon-Voce hardening vs Swift-Voce hardening law for small strains	61
Figure 15 Hollomon-Voce hardening vs Swift-Voce hardening law for large strains	61
Figure 16 Hockett-Sherby hardening law for small strains	63
Figure 17 Hockett-Sherby hardening law for large strains	63
Figure 18 Swift/Hockett-Sherby hardening law for small strains	64
Figure 19 Swift/Hockett-Sherby hardening law for large strains	65
Figure 20 Swift/Hockett-Sherby hardening law, $\alpha = 0.75$ for aluminium	65
Figure 21 Tensile specimen cut at the angle θ (measured from the rolling direction) (48) ..	68
Figure 22 Hockett-Sherby hardening law, Novelis AA5000, zero degree roll angle, small strains	69

Figure 23 Hockett-Sherby hardening law applied to Novelis AA5000 for large strains	69
Figure 24 50 data points imported into FEA from Hockett-Sherby law for Novelis AA5000.....	70
Figure 25 Swift/Hockett-Sherby hardening law applied to Novelis AA5000 for small strains	71
Figure 26 Swift/Hockett-Sherby hardening law applied to Novelis AA5000 for large strains	71
Figure 27 diffuse necking point for Swift/Hockett-Sherby hardening law	72
Figure 28 50 data points imported into FEA from Swift/Hockett-Sherby law for Novelis AA5000.....	72
Figure 29 Swift-Voce hardening law applied to Novelis AA5000 for small strains	74
Figure 30 Swift-Voce hardening law applied to Novelis AA5000 for large strains	74
Figure 31 Swift-Voce vs Swift/Hockett-Sherby for large strains-Novelis AA5000.....	75
Figure 32 Swift-Voce vs Swift/Hockett-Sherby for small strains-Novelis AA5000.....	75
Figure 33 Swift/Hockett-Sherby hardening law, Novelis AA5000, 45 degree roll angle ..	77
Figure 34 Swift-Voce (0.25) hardening law, Novelis AA5000, 45 degree roll angle	77
Figure 35 SV (0.25) vs SHS (0.75) hardening law, Novelis AA5000, 45 degree roll angle	78
Figure 36 Swift/Hockett-Sherby hardening law, Novelis AA5000, 90 degree roll angle ..	78
Figure 37 Swift-Voce (0.25) hardening law, Novelis AA5000, 90 degree roll angle	79
Figure 38 SV (0.25) vs SHS (0.75) hardening law, Novelis AA5000, 90 degree roll angle	79
Figure 39 Hockett-Sherby hardening law, Constelium AA5000, zero degree roll angle, small strains	81
Figure 40 Hockett-Sherby hardening law, Constelium AA5000, zero degree roll angle, large strains	82
Figure 41 Swift/Hockett-Sherby hardening law, Constelium AA5000, zero degree roll angle, small strains.....	83

Figure 42 Swift/Hockett-Sherby hardening law, Constelium AA5000, zero degree roll angle, small strains.....	83
Figure 43 goodness of fits: Swift/Hockett-Sherby law for Constelium AA5000	84
Figure 44 50 data points imported into FEA from Swift/Hockett-Sherby law for Constelium AA5000	84
Figure 45 Swift-Voce hardening law, Constelium AA5000, zero degree roll angle, small strains	85
Figure 46 Swift-Voce hardening law, Constelium AA5000, zero degree roll angle, large strains	86
Figure 47 Swift-Voce vs Swift/Hockett-Sherby for small strains-Constelium AA5000, zero degree roll angle.....	87
Figure 48 Swift-Voce vs Swift/Hockett-Sherby for large strains-Constelium AA5000.....	87
Figure 49 Swift/Hockett-Sherby hardening law, Constelium AA5000, 45° roll angle	88
Figure 50 Swift-Voce hardening law, Constelium AA5000, 45° roll angle	89
Figure 51 Swift-Voce vs Swift/Hockett-Sherby-Constelium AA5000, 45 degree roll angle	90
Figure 52 Swift/Hockett-Sherby hardening law, Constelium AA5000, 90° roll angle	90
Figure 53 Swift-Voce hardening law, Constelium AA5000, 90° roll angle	91
Figure 54 Swift-Voce vs Swift/Hockett-Sherby-Constelium AA5000, 90° roll angle.....	92
Figure 55 Hockett-Sherby hardening law, Constelium AA6000, zero degree roll angle, small strains	94
Figure 56 Hockett-Sherby hardening law, Constelium AA6000, zero degree roll angle, large strains	94
Figure 57 Swift/Hockett-Sherby hardening law, Constelium AA6000, zero degree roll angle, small strains.....	95
Figure 58 Swift/Hockett-Sherby hardening law, Constelium AA6000, zero degree roll angle, large strains	95
Figure 59 50 data points imported into FEA from Swift/Hockett-Sherby law for Constelium AA6000	96

Figure 60 Swift-Voce hardening law, Constelium AA6000, zero degree roll angle, small strains	97
Figure 61 Swift-Voce hardening law, Constelium AA6000, zero degree roll angle, large strains	98
Figure 62 Swift-Voce vs Swift/Hockett-Sherby for small strains-Constelium AA6000, zero degree roll angle.....	98
Figure 63 comparison between k-exponent function and HS hardening law for pre-necking flow stress curve fitting of AA6000, zero degree roll angle.....	99
Figure 64 Swift/Hockett-Sherby hardening law, Constelium AA6000, 45° roll angle	100
Figure 65 Swift-Voce hardening law, Constelium AA6000, 45° roll angle, small strain.	100
Figure 66 Swift-Voce hardening law, Constelium AA6000, 45° roll angle, large strain .	101
Figure 67 Swift-Voce vs Swift/Hockett-Sherby for small strains-Constelium AA6000, 45° roll angle	101
Figure 68 Swift-Voce vs Swift/Hockett-Sherby for large strains-Constelium AA6000, 45° roll angle	102
Figure 69 Swift/Hockett-Sherby hardening law, Constelium AA6000, 90° roll angle, small strains	103
Figure 70 Swift/Hockett-Sherby hardening law, Constelium AA6000, 90° roll angle, large strains	103
Figure 71 Swift-Voce hardening law, Constelium AA6000, 90° roll angle, small strains	104
Figure 72 Swift-Voce hardening law, Constelium AA6000, 90° roll angle, large strains	104
Figure 73 Swift-Voce vs Swift/Hockett-Sherby for small strains-Constelium AA6000, 90° roll angle	105
Figure 74 Swift-Voce vs Swift/Hockett-Sherby for large strains-Constelium AA6000, 90° roll angle	105
Figure 75 a scheme of hydraulic bulge test (50)	108
Figure 76 hydraulic bulge test equipment (50)	112

Figure 77 thickness variation at the dome apex proposed by Chakrabarty and Alexander (64).....	114
Figure 78 Shang's adjusted radius of curvature for analytical model of hydraulic bulging (67).....	115
Figure 79 Atkinson's analytical model for hydraulic bulge test (68)	116
Figure 80 Atkinson's analytical model for hydraulic bulge test-mean thickness of the polar cap (68)	116
Figure 81 Kruglov's approach for analytical study of the bulging test (69).....	117
Figure 82 Schematic representation of the specimen subjected to hydraulic bulging-Kruglov's approach (60).....	118
Figure 83 Stresses on double curved element in cross section at the pole (70)	119
Figure 84 methodology for the determination of bulge test stress-strain curve.....	124
Figure 85 Sheet specimens before and after bulge testing (52)	125
Figure 86 Cross-section of the bulge die (52).....	126
Figure 87 Example for possible positions of oil shielding plates and lamps (50)	127
Figure 88 Choice of r_1 and r_2 for calculation of true stress and true strain for each forming stage (50).....	129
Figure 89 ISO 16808 approach for extrapolating tensile test data with bulge test (50)....	133
Figure 90 converting uniaxial test result to biaxial considering anisotropy (55).....	134
Figure 91 Engineering stress – strain curve aluminium 6000 Novelis	136
Figure 92 True stress – strain curve aluminium 6000 Novelis	136
Figure 93 true stress – strain curves for tensile and bulge tests aluminium 6000 Novelis	137
Figure 94 flow stress curve from tensile test data extrapolation with bulge test-aluminium 6000 Novelis	139
Figure 95 tensile test extrapolation using SHS hardening law-aluminium 6000.....	139
Figure 96 tensile test data extrapolation using bulge test data fitted by SHS hardening law-without data refinement	140

Figure 97 tensile test data extrapolation using bulge test data fitted by SHS hardening law-with data refinement	140
Figure 98 50 data points required to import into FEA SW-aluminium 6000	141
Figure 99 tensile test extrapolations comparison using bulge test data and SHS hardening law-aluminium 6000	141
Figure 100 Al6000 flow stress curve fitting, k-exponent function and HS hardening law using ISO16808	142
Figure 101 True stress – strain curve DP600	144
Figure 102 flow stress curve from tensile test data extrapolation with bulge test-DP600	145
Figure 103 tensile test extrapolation using SHS hardening law-DP600	146
Figure 104 tensile test data extrapolation using bulge test data fitted by SHS hardening law-without data refinement	146
Figure 105 tensile test data extrapolation using bulge test data fitted by SHS hardening law-with data refinement	147
Figure 106 50 data points required to import into FEA SW-DP600.....	147
Figure 107 tensile test extrapolations comparison using bulge test data and SHS hardening law-DP600	148
Figure 108 comparison between the flow stress curve fitting of DP600 using ISO 16808	148
Figure 109 the difference between localized and diffused neck during necking of a thin strip (74).....	153
Figure 110 equivalent stress and equivalent plastic strain flowchart.....	160
Figure 111 the position of the transversal section at neck-GOM SW.....	162
Figure 112 local long. strain distribution along the GL at 7.23% engineering strain level	163
Figure 113 local long. strain distribution along the GL at 7.73% engineering strain level	164
Figure 114 local long. strain distribution along the GL at 8.31% engineering strain level	165

Figure 115 local long. strain distribution along the GL at various engineering strain level-CP 1400HD.....	165
Figure 116 local width strain distribution along the GL at various engineering strain level-CP 1400HD.....	166
Figure 117 local thickness strain distribution along the GL at various engineering strain level-CP 1400HD.....	167
Figure 118 virtual extensometer in GOM software along the GL	168
Figure 119 Standard geometrical specification of the subsize specimen ASTM E8/E8M	169
Figure 120 engineering stress-strain curve of CP 1400HD subsize specimen and the corresponding diffuse necking point.....	169
Figure 121 Contours of local strain component (ϵ_x) at various overall engineering strain levels along GL	172
Figure 122 Evolution of local strain component (ϵ_x) at neck in various overall strain levels in width direction	173
Figure 123 Evolution of local strain component (ϵ_y) at neck in various overall strain levels in width direction	173
Figure 124 evolution of the local average strain components for various overall engineering strain levels	174
Figure 125 variation of normal anisotropy-CP 1400HD.....	176
Figure 126 variation of strain rate ratio-CP 1400HD.....	176
Figure 127 equivalent stress-equivalent plastic strain for CP 1400HD including post-necking behaviour.....	177
Figure 128 two crossing localisation bands immediately after the onset of inhomogeneous deformation.....	178
Figure 129 'X' shape bands during plastic deformation.....	179
Figure 130 evolution of the strain field during post-necking deformation	180
Figure 131 transition between the symmetric hourglass and asymmetric 'X' CP1400HD	181

Figure 132 Engineering stress-strain curve for QP 1180-subsize specimen.....	182
Figure 133 true stress-strain curve for QP 1180-subsize specimen	182
Figure 134 distribution of local longitudinal strain (ϵ_x) in various overall engineering strain levels-QP 1180 subsize specimen.....	183
Figure 135 longitudinal local strain distribution in QP 1180 subsize specimen.....	184
Figure 136 longitudinal local strain (ϵ_x) distribution along the width at neck-QP 1180 ..	185
Figure 137 transversal local strain (ϵ_y) distribution along the width at neck-QP 1180 ...	185
Figure 138 variation of normal anisotropy-QP 1180	186
Figure 139 variation of strain ratio-QP 1180	186
Figure 140 equivalent stress-equivalent plastic strain for QP 1180 including post-necking behaviour.....	187
Figure 141 evolution of the longitudinal strain distribution along the GL of a QP 1180 subsize specimen.....	188
Figure 142 subsize specimen meshing in Abaqus.....	195
Figure 143 equivalent flow stress curve for CP 1400HD	197
Figure 144 equivalent flow stress curve for QP 1180.....	197
Figure 145 fitting and extrapolation of the equivalent flow curve with RO hardening law-CP 1400HD.....	198
Figure 146 fitting and extrapolation of the equivalent flow curve with RO hardening law-QP 1180	198
Figure 147 reaction force in FEA obtained at the centre of the model	199
Figure 148 relative displacement between two sections to obtain the elongation in FEA200	
Figure 149 load vs elongation curve of the tensile test and that of the numerical simulation-CP 1400HD.....	200
Figure 150 load vs elongation curve of the tensile test and that of the numerical simulation-QP 1180	201
Figure 151 elements used to obtain the longitudinal strain distribution along the gage length.....	202

Figure 152 longitudinal strain (ϵ_{xx}) distribution along the gage length from FEA-CP 1400HD.....	202
Figure 153 longitudinal strain (ϵ_{xx}) distribution along the gage length from tensile test-CP 1400HD.....	203
Figure 154 longitudinal strain (ϵ_{xx}) distribution along the gage length from FEA-QP 1180	204
Figure 155 longitudinal strain (ϵ_{xx}) distribution along the gage length from tensile test-QP 1180.....	204
Figure 156 Strain field in longitudinal, width and thickness directions	205
Figure 157 Strain in longitudinal direction (ϵ_{xx}) at neck from FEA-CP 1400HD	206
Figure 158 Strain in longitudinal direction (ϵ_{xx}) at neck from tensile test-CP 1400HD...	206
Figure 159 Strain in longitudinal direction (ϵ_{xx}) at neck from FEA-QP 1180.....	207
Figure 160 Strain in longitudinal direction (ϵ_{xx}) at neck from tensile test-QP 1180	207
Figure 161 Strain in longitudinal direction (ϵ_{yy}) at neck from FEA-CP 1400HD	208
Figure 162 Strain in longitudinal direction (ϵ_{yy}) at neck from tensile test-CP 1400HD...	208
Figure 163 Strain in longitudinal direction (ϵ_{yy}) at neck from FEA-QP 1180.....	209
Figure 164 Strain in longitudinal direction (ϵ_{yy}) at neck from tensile test-QP 1180	209
Figure 165 Strain in longitudinal direction (ϵ_{zz}) at neck from FEA-CP 1400HD.....	210
Figure 166 Strain in longitudinal direction (ϵ_{zz}) at neck from tensile test-CP 1400HD ...	211
Figure 167 Strain in longitudinal direction (ϵ_{zz}) at neck from FEA-QP 1180	211
Figure 168 Strain in longitudinal direction (ϵ_{zz}) at neck from tensile test-QP 1180.....	212
Figure 169 flowchart for the iterative procedure of FLC evaluation using MMFC	233

List of tables

Table 1 parameters required for a selection of common yield models	21
Table 2 information about common aluminium alloys in automotive industry (9)	32
Table 3 chemical composition of DP600 used in the present work	34
Table 4 Current production grades of CP steels and example automotive applications (12)	35
Table 5 goodness of fits: Swift-Voce and Hollomon-Voce laws.....	62
Table 6 mechanical properties of Novelis AA5000	67
Table 7 50 data points imported into FEA from Hockett-Sherby law for Novelis AA5000	70
Table 8 goodness of fits: Swift/Hockett-Sherby law for Novelis AA5000	71
Table 9 50 data points imported into FEA from Swift/Hockett-Sherby law for Novelis AA5000.....	73
Table 10 goodness of fits: Swift-Voce law for Novelis AA5000	73
Table 11 goodness of fits: Swift-Voce vs SHS-Novelis AA5000, zero degree roll angle..	75
Table 12 goodness of fit: SV (0.25) vs SHS (0.75) hardening law, Novelis AA5000, 45 degree roll angle.....	78
Table 13 summary: material constants and RMS errors of Novelis AA5000.....	80
Table 14 mechanical properties of Constelium AA5000	80
Table 15 50 data points imported into FEA from Swift/Hockett-Sherby law for Constelium AA5000	85
Table 16 goodness of fits: Swift-Voce law for Constelium AA5000, zero degree roll angle	86
Table 17 goodness of fits: Swift-Voce vs SHS-Constelium AA5000, zero degree roll angle	87
Table 18 goodness of fits: Swift-Voce law for Constelium AA5000, 45 degree roll angle	89
Table 19 goodness of fits: Swift-Voce vs SHS-Constelium AA5000, 45 degree roll angle	90

Table 20 goodness of fits: Swift-Voce law for Constelium AA5000, 90° roll angle	91
Table 21 goodness of fits: Swift-Voce vs SHS-Constelium AA5000, 90° roll angle.....	92
Table 22 mechanical properties of Constelium AA6000	93
Table 23 goodness of fits: Swift/Hockett-Sherby law for Constelium AA6000, zero degree roll angle	95
Table 24 50 data points imported into FEA from Swift/Hockett-Sherby law for Constelium AA6000	96
Table 25 goodness of fits: Swift-Voce law for Constelium AA6000, zero degree roll angle	97
Table 26 Swift-Voce vs SHS-Constelium AA6000, zero degree roll angle	99
Table 27 goodness of fits: Swift-Voce law for Constelium AA6000, 45° roll angle	101
Table 28 Swift-Voce vs SHS-Constelium AA6000, 45° roll angle	102
Table 29 goodness of fits: Swift-Voce law for Constelium AA6000, 90° roll angle	104
Table 30 Swift-Voce vs SHS-Constelium AA6000, 90° roll angle	106
Table 31 geometrical specifications of subsize specimen ASTM E8/E8M	192

Abstract

Continuous advances in simulation systems for analysing metal forming processes are expanding the capabilities available for the modelling of materials. There is a wide variety of attempts to attain a method that is not only reliable, but can also be used for a vast range of materials and forming conditions. Post-necking identification of a material subjected to uniaxial loading has been both the subject of debate and a serious challenge for manufactures dealing with sheet metal forming processes, especially in automotive industries whenever a new material is intended to be used. Up to now, depending on the fidelity level of the simulation model in the developing process of a component, the identification can be conducted through four main classes of methods. Recent methods are more complicated both to be studied and implemented, wherein even complex, non-standardized test methods and experiments are needed to be designed so as to derive the necessary parameters of the material model. However, even after evaluating the model parameters, a whole new challenge may arise: reliable implementation of these parameters for various forming conditions. In this research, the focus will be on the post-necking behaviour of 5xxx and 6xxx series of aluminium, as well as AHSSs, wherein a first approximation of flow stress curve at large values of strain beyond diffuse necking will be studied first and then validated in FEA.

Keywords: *sheet metal forming simulation, material characterization, post-necking identification, tensile test, hydraulic bulge test, digital image correlation technique, FEA, aluminium, AHSS*

Acknowledgement

Honestly, the knowledge I acquired throughout this thesis work is not comparable with ‘what I thought I knew’ in the beginning; a step towards growth. For this, I really appreciate my supervisors, first of all because of their trust, and then because of their time, patience and support along this path.

To my dear brother, Mehdi
(1986-2020)

CHAPTER ONE: MATERIAL MATTERS

Before embarking upon discussions on ‘*goals*’ and ‘*methodology*’ the two important parts of this thesis work, ‘*material characterization*’ and ‘*metal forming simulation*’ will be looked closely first.

1.1 MACROMECHANICAL MATERIAL CHARACTERIZATION FOR STAMPING SIMULATION

The main purpose of conducting the stamping simulation is to anticipate the level of strain, thinning (regarding a forming limit curve), wrinkling and springback during the forming process of a metallic sheet. Generally, the material properties of sheet metals alter with respect to its rolling direction (*anisotropic* behaviour), and cold forming is done at room temperature with quasi-static strain rates. Hence, yield models and flow curves are employed in order to model Deformation, failure is studied by observing material’s forming limit curves, while elastic modulus is enough to investigate the springback behaviour (1).

1.1.1 Yield criteria

Anisotropic yield models divide into two main categories: *quadratic* and *non-quadratic* (2). It is generally considered that although defining quadratic models needs fewer number of parameters, they are not accurate enough, especially when it comes to lightweight materials, like aluminium. On the other hand, Barlat 2000 or Banabic 2005 are the more complex yield models; having more parameters, they provide far more accurate matching with experimental data, and thus lead to better predictions in forming simulation (3).

In the following table, the necessary test data required for a selection/calibration of yield models are presented,

Model	Type	σ_{y0}	σ_{y45}	σ_{y90}	σ_{yb}	r_0	r_{45}	r_{90}	r_b
von Mises	Quadratic	x							
Hill 48	Quadratic	x				x	x	x	
Barlat 89	Non-quadratic	x	x	x		x	x	x	
Barlat 2000	Non-quadratic	x	x	x	x	x	x	x	x
Banabic 2005	Non-quadratic	x	x	x	x	x	x	x	x

Table 1 parameters required for a selection of common yield models

Where,

- σ_{y0} , σ_{y45} , σ_{y90} : yield stresses in the 0°, 45° and 90° to the grain direction¹,
- r_0 , r_{45} , r_{90} : anisotropic parameters in the 0°, 45° and 90° to the grain direction,
- σ_{yb} , r_b : biaxial yield stress and biaxial anisotropic parameter respectively.

Standard sheet tensile tests must be conducted to acquire yield stresses, anisotropic parameters and work-hardening indices (n-values), where the required approaches are introduced in the following standards,

- Yield stresses: ISO 6892-1:2019 (tensile testing of metallic materials and defining the mechanical properties, both at room temperature and elevated temperature),
- Anisotropic *r-values*: ISO 10113:2020 (plastic strain ratio of flat products (sheet and strip) made of metallic materials),
- Work-hardening index, *n-values*: ISO 10275:2007, (tensile strain hardening exponent *n* of flat products (sheet and strip) made of metallic materials),
- *Biaxial yield and anisotropic parameters* are evaluated through bulge tests while the measurement process is standardized by ISO 16808:2014, (biaxial true stress-true strain curve of metallic sheets having a thickness below 3 mm in pure stretch forming without significant friction influence).

The specimen must be cut at different angles to the rolling direction of the received sheet in order to determine yield and anisotropic parameters in different directions.

1.1.2 Flow stress curve and strain hardening laws

As it will be observed in chapter two, flow stress curves are drawn by *fitting the post-yield tensile test data* using hardening laws, such as the *Swift equation* for steels and the *Voce phenomenological hardening law* for aluminium alloys and few grades of high strength steels (1) (2).

$$\sigma_{\text{swift}} = C(\epsilon_0 + \epsilon_p)^n$$

$$\sigma_{\text{voce}} = K_0 + Q(1 - \exp(-\beta\epsilon_p))$$

¹ Grain direction is a term used to describe the rolling direction of metal after being manufactured into sheet, plate or coil.

Flow curves are normally considered as isotropic; thus, the n -value evaluated in the rolling direction is employed to demonstrate the plastic behaviour in all directions (4).

1.1.3 Forming limits

In contrast with the flow stress curve, forming limits are treated as *anisotropic* and standardised tests (ISO 12004 2:2008) are needed to be conducted to evaluate them.

In the test, specimens of different geometries are bulged using a punch, where considerable amount of attention must be paid to the lubrication of the surfaces between the sample and the dome-shaped punch in order to minimise the effect of friction. Furthermore, significant amount of post-processing work is required before obtaining forming limits (1). Generally, by increasing the sheet thickness, forming limits also increases, implying the fact that, for each available thickness, the bulge test must be repeated as well (1). The below forming limit curve of an aluminium alloy is derived from Nakazima test,

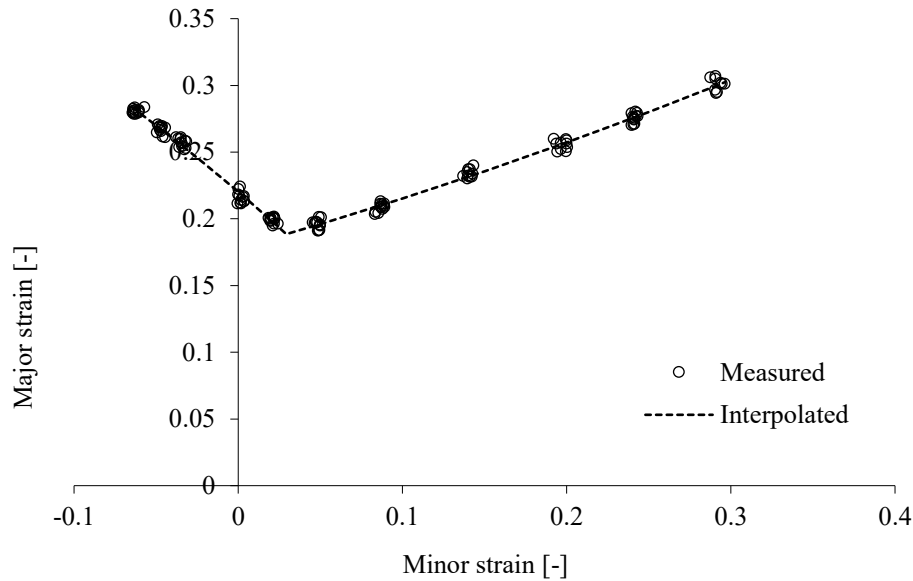


Figure 1 Example of a forming limit curve for an aluminium alloy-CRF data

1.2 HOW TO CHARACTERIZE MATERIALS

Generally, to characterize a constitutive material model, two factors are required to be known (1),




- a **model** that describes a certain behaviour of the material, and
- the **actual data** to find the model's unknown parameters.

For instance, in order to describe yielding behaviour of a material, one can implement the von Mises yield criterion (as a *Model*), yet the *size of the yield ellipse* can be fully determined by conducting the uniaxial tensile test (finding the yield stress of the material) (*Actual Data*).

Multiple models are normally employed to introduce different aspects of material deformation during a forming process; models to describe elasticity, yielding, hardening, failure, deformation at different and/or elevated temperatures, variable strain rates, more complex models for certain material behaviours such as solidification (casting) (1).

The *fidelity level of the simulation model* and the *required work to collect the data for obtaining model's parameters* will influence the choice of the desired material model. Consequently, the required tests to be done will depend on the chosen model (1).

Automotive manufacturers collect test data from various resources,

	<i>Open Repositories</i>	range from free online databases to data published in literature and journals' articles.
	<i>Material Suppliers</i>	provide only basic material properties that can solely be employed in the 'standard' material models, such as von Mises yield function for modelling the yielding.
	<i>Commissioning Tests</i>	In order to exploit an advanced material model or to validate predictions, bespoke tests (tailored and specially-made tests) may be requested by the analyst to be conducted. Then, the company may enquire another department/firm to retrieve a specific test's results. It is also advisable that, these tests should be conducted according to the standards (1).

However, the analyst is responsible to do '*due diligence*' on the final data and to ensure that the data is permissible to be used in the simulation model (1). This process is done in this study in the final chapter, whereby the theoretical post-necking result is used in a FEA to ensure the validity of the model. Bespoke tests can be conducted at test houses or universities with appropriate equipment. Even *standardized tests* may include specific details that need to be considered a priori (1).

An analyst should pay a considerable amount of attention to the following points,

- the *requirements* of the chosen material model,
- the *capabilities* of test facilities,

- the chosen test *method*,
- the chosen method for *data collection* during the test,
- *data post-processing* procedure.

Further and even more importantly though, significant amount of time and attention should be allocated to convert the format of the test data to the format which is executable in the simulation model (a solver-readable format) (1).

1.3 METAL FORMING SIMULATION

Continuous development in the field of metal forming processes simulation has significantly affected the available capabilities for material modelling (1). Many elements must be taken into account in the material characterization for stamping process, among which, stamping simulation mainly depends on anisotropic material data for cold stamping. The numerical simulation of metal forming processes have been progressively employed by automotive industries not only to improve the quality and performance of products and processes, but also to reduce the length of product development; as a result, these products can be introduced to market in a shorter time span (4). Consequently, ‘how the manufacturing process is modelled’ strongly depends on the quality of the input data.

In order to define a simulation model for a metal forming process, a number of inputs should be considered (1),

- Material deformation and failure descriptions (material model),
- The geometry of the workpiece (CAD model),
- The boundary conditions of the model,
- The adequate number of elements used to describe the geometry of the tooling and the component to be manufactured,
- The simulation time-step, used to define how often the results are needed to be stored in the output for post-processing analysis,

The reliability and accuracy of numerical simulations are significantly affected by the validity of the implemented material model (5). It should also be underlined that, material models need a lot of hard work to be defined, as they require data collected through physical tests (1).

1.3.1 The Fidelity of a Simulation Model

The assessment of '*How much the simulation model is representative of the actual manufacturing process*' is described by the fidelity of a simulation model; the *amount of detail* included in a material model, and the purpose of the simulation itself will influence the fidelity of the simulation model (4).

The acquired knowledge about the forming process, material and tooling extend gradually during a product development program. This '*improved knowledge*' should be exploited by analysts to empower the quality of material model and simulation, in order to heighten the fidelity of the simulation model (1).



Low fidelity simulation models

They are used to,

- estimate deformation modes and the financial feasibility of the process within the initial steps of development,
- demonstrate the overall performance of the process,
- demonstrate the process sensitivity to BCs and material properties,



Medium fidelity simulation models

They include accurately defined material models to obtain more precise results. Medium fidelity models are employed to foster the process performance, where the predictions can then be regarded as the basis for tooling geometries.



High fidelity simulation models

They normally contain information about the variations in BCs and material parameters so as to define a '*process window*'.



Higher fidelity simulation models

They are employed as a ‘*digital twin*’ of the real process.

Using information from general datasheets are not acceptable in high fidelity modelling, while feeding low fidelity modelling with detailed characterization data seems to be unnecessary (4).

1.4 MATERIAL MATTERS

As it is already mentioned, material testing is an important element in providing inputs for the simulation of a forming process. Obtaining an accurate material properties from tests leads to generating a reliable material model which in turns establishes a link between the material’s microstructure and the observed macroscopic behaviour (6).

However, due to the following factors this approach may not be implemented readily (6),

- For a certain applications, the relation between the microscale and macroscopic behaviour is often physically unknown,
- Material model may perform well only for a certain nominal state, while it cannot work efficiently in many other conditions or larger scales,
- The complexity of the material, structure and process makes it quite difficult to consider all the parameters included.

In order to overcome the above challenges, tests, either standardized or bespoke, should be carried out to generate the required input data. Although conducting tests has always been with its own predicaments, such top-down approaches are very helpful to tackle the problems within the microscale modelling (6).

1.4.1 Materials

Although the micromechanical behaviour of materials does not lie within the scope of the present thesis work, a short study on their general properties, development trends, as well as applications is almost essential.

1.4.1.1 Aluminium: Almost infinite

Aluminium is the third most plentiful element on earth (next to oxygen and silicon) but its production cost was quite high until the late 1800s (7).

While its lightweighting properties seems to be the main reason for its popularity, automotive industries are also fond of aluminium's good durability, high corrosion resistance, and improved maintenance as well (8).



Lightweight

Lighter vehicles, lower energy consumption and reduced emissions by possessing solely 1/3 of the density of steel. Besides, although it has lower tensile strength than steel, its specific strengths (i.e. strength-to-weight ratios) is quite satisfying (7).



Recyclability

It is nontoxic and can be recycled with around 5% of the required energy to produce it from alumina. Besides, 75% of all aluminium produced is still in use. From the total aluminium produced in 2016, about 25% was entered the transportation industry, another 25% was used in the packaging (like, aluminium cans), about 15% in construction and 15% in electrical applications (7).



Formability

Makes it possible to integrate different technologies into one solution, e.g. in buildings.



Corrosion resistance

Natural oxide layer preserve the metal underneath against corrosion and makes it nearly maintenance free (7).



Alloying technology

Depending on the its application, tailor-made alloys can be developed. For instance, benefiting from strengthening mechanisms, aluminium alloys can be made 30 times stronger than pure aluminium (7).



Impermeability

It is a perfect barrier against light, odour and contamination.



Conductivity

An excellent conductor for heat and electricity (twice as good as copper) (8).

Depending on their chemical composition and properties, automotive aluminium alloys are designated by series; aluminium sheet of 2xxx series, 5xxx series, 6xxx series, and 7xxx series are often used in automotive body components, where except for 5000 series aluminium alloy, the other three series are heat-treated and their strength can be improved by coating and baking (9).

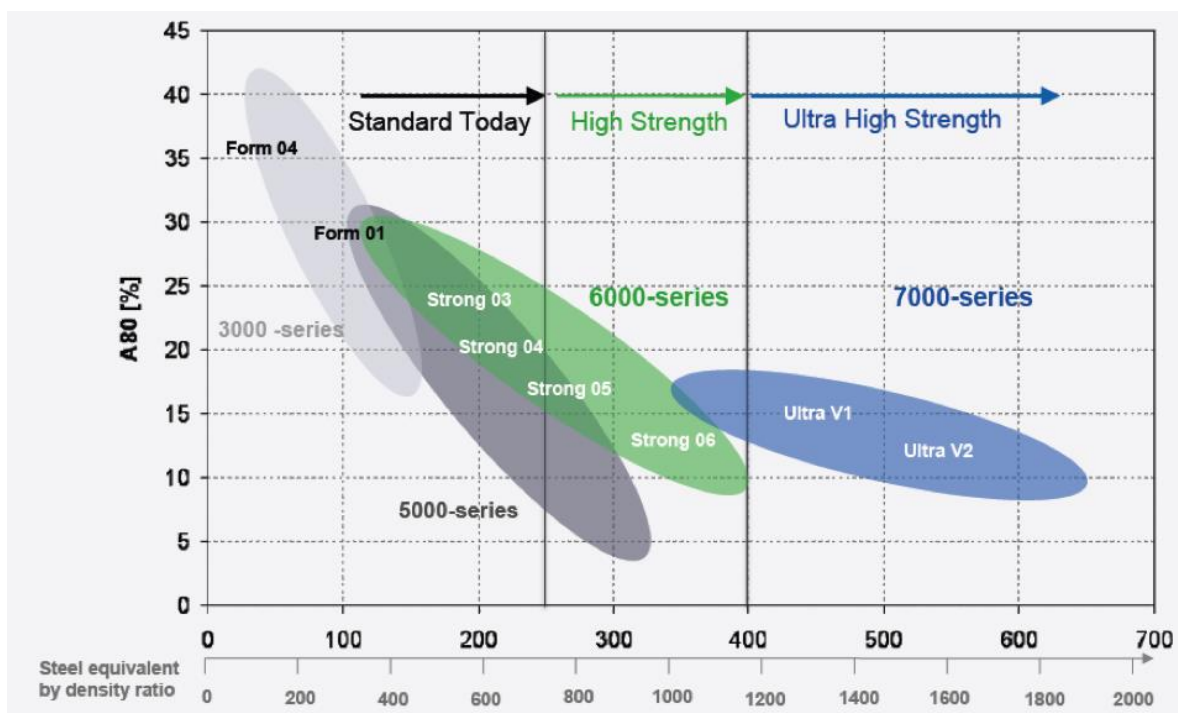


Figure 2 aluminium alloys generally employed for body structures (9)

Since OEMs demand higher strengths, the supply balance is more towards AA6xxx than AA5xxx, according to *Innoval Technology*², where it constitutes at least 80% of the supplied aluminium to carmakers (9).

5000 series aluminium is an aluminium-magnesium alloy, in which the magnesium content is between 3% and 6%. With regard to the desired application, changing magnesium content results in different alloy grade of 5xxx series (10).

Amongst the advantages of the 5000 series aluminium sheet, the following features stand out (10),

- It is the most resistant to acid and alkali corrosion amongst different series,
- Its high plasticity and good processing performance makes it suitable for a wide range of forming processes,
- Excellent strength-to-weight ratio,
- Full recycling compatibility,
- It has excellent thermal conductivity,
- Its hardness is the highest amongst different series of aluminium.

6000 series aluminium is a high quality aluminium-magnesium-silicon alloy product. Its manufacturing cost is slightly higher than other series of aluminium sheets because generally more advanced equipment and complex production processes are required. 6000 aluminium sheet is a heat-treated aluminium forged product, making it a good choice for applications requiring high corrosion resistance and oxidation (11). In addition, it has the following advantages (11):

- Strong corrosion resistance, as it contains magnesium and silicon,
- High toughness,
- Dense structure and few defects, due to the characteristics of the main alloying elements, 6000 series aluminium has a very compact structure, so that during forming no defects appear.
- Good welding performance,
- Quite suitable for surface treatment,

² *Innoval Technology* was formed in 2003, in Oxfordshire, UK, by people from Alcan's Banbury Technical Centre. For seven decades 'Banbury Laboratories', as it was known, was responsible for some of the most significant technological developments in aluminium, including the leading automotive sheet technology used by today's car manufacturers.

- Good performance in the oxidation processing.

Some examples of common aluminium alloys in automotive industry are as follows (8),

AA6016A	<ul style="list-style-type: none"> - with excess silicon content originally launched by Alusuisse³ - mainly used in Europe for external panels in vehicles. - produced by most of the major aluminium sheet suppliers such as Novelis⁴, Aleris⁵, Constellium⁶, Hydro⁷
AA6111	<ul style="list-style-type: none"> - used in aluminium intensive models developed by Jaguar and Land Rover - with copper as an alloying metal (0.5-0.9 wt%) - stronger than AA6016A, - less corrosion resistant than AA6016A - more common in USA
Comparison between AA6016A and AA6111	
<ul style="list-style-type: none"> - AA6016A is less stronger but more formable alloy than AA6111 - AA6016A has a lower bake hardening response than AA6111 - to obtain the same level of dent resistance, OEMs use AA6016A at rather thicker gauges than AA6111 - AA6111 enabled Jaguar (Jaguar Land Rover) to employ thinner closure panels than most German OEMs 	
AA6451	<ul style="list-style-type: none"> - possesses the features of both AA6111 and AA6016A - Novelis introduces it for external panels as Advanz e600 - Novelis can produce it readily from recycled scrap - Advanz e600 is a heat treatable alloy - Is designed and optimized for high-strength requirements, both for bodywork and structural applications - By achieving strengths of around 350 MPa, it is ideal for structural applications in chassis and cross member components
AA6181A	<ul style="list-style-type: none"> - Was produced more recently due to recycling features - Mostly employed for outer panels in gauges of 0.9-1.0 mm for parts that require high strength with good formability
AA6022	<ul style="list-style-type: none"> - Was Alcoa's choice for outer panels - As it is a low copper and iron alloy, it is difficult to produce it from recycled stock

³ Alusuisse was a Swiss industrial group founded as Aluminium Industrie Aktien in 1898 in Zurich, Switzerland.

⁴ Novelis is a subsidiary of Hindalco Industries Limited, an industry leader in aluminium, copper and metals.

⁵ Novelis has acquired Aleris, extending its position as the leading producer of flat-rolled aluminium products and the world's largest recycler of aluminium.

⁶ Constellium is a global leader in the development and manufacturing of high value-added aluminium products and solutions.

⁷ Hydro is in a broad range of market segments for aluminium, energy, metal recycling, renewables and batteries.

AA6061	<ul style="list-style-type: none"> - Used in car steering knuckles - was optimised by adding small quantities of zirconium, zinc and copper.
AA5182 AA5754	<p>AlMg5Mn (AA5182)</p> <ul style="list-style-type: none"> - has high magnesium content - used for high strength and complex stampings - good corrosion resistance and high formability <p>AA5754</p> <ul style="list-style-type: none"> - offers very good surface quality - used in structural sheet applications
RC5754	<ul style="list-style-type: none"> - Novelis has supplied Jaguar Land Rover with RC5754 - Novelis produces it from 50% production scrap - Is mostly used in truck trailer sheet
Newly-developed alloys	
ACMZ	<ul style="list-style-type: none"> - Created by FCA and the Oak Ridge National Laboratory - is resistant at significantly higher temperatures compared to existing materials (up to 300°C) making it suitable for some engine components - enabling the production of smaller engines with the same power, so lower fuel consumption
AA6056	<ul style="list-style-type: none"> - Made by Arconic's Enduralum - With tensile strength of up to 460 MPa - Is a lightweight alloy
C6A1	<ul style="list-style-type: none"> - Made by Arconic⁸ and used by FCA - Enables automakers to build highly deformable and lightweight components

Table 2 information about common aluminium alloys in automotive industry (9)

Regardless of their natural chemical properties, final alloys can obtain more desirable properties like higher strength, formability or hemming quality through various techniques, such as bake hardening, work and precipitation hardening, heating and annealing (9).

⁸ a market leader industry in providing aluminium sheet to the North American automotive market.

1.4.1.2 DP600 Arcelor

Arcelor has reported the specifications and applications of its Dual Phase steels in 2020. The following paragraphs are extracted from the company's reports⁹.

Characteristics of dual phase steel

Developed particularly for automotive industries, dual phase steels are one of the advanced high strength steels (AHSS). Their microstructure typically consists of a soft ferrite phase with dispersed islands of martensite, where the martensite phase is considerably stronger than the ferrite phase. Almost using any kind of welding processes, DP steels can be welded; processes such as, resistance spot welding, resistance seam welding, arc and laser welding. According to the recommendation of Arcelor on DP steels, the specific work hardening and bake hardening characteristics of DP steels are required to be carefully employed in FEA of crash models.

Applications of dual phase steel

Dual phase steels permits designers to exploit high yield strength steels for automotive safety cage; components that are too complex to be produced by higher strength steels. Two of the low to intermediate grades of Dual phase steels are introduced in the following,

DP500	<ul style="list-style-type: none">- 500 MPa tensile strength- Designed for exposed body panels: hood, doors and fender.- Its excellent formability, high work hardening and bake hardening behaviours lead to reduce outer panel gauge and weight, while maintaining/improving <i>dent resistance</i>- Substantial reduction of closure weight, instead of using more costly and lower density materials
DP 600 Arcelor used in chapter four	<ul style="list-style-type: none">- Used in components requiring high energy absorption: the crumple zones, front and rear longitudinal rails and supporting structure- Its low yield strength keeps the initial deceleration pulse low- Its high work hardening rate and excellent ductility absorb larger deformation energy than conventional steels- Its good formability allows forming complicated shapes- Its good weldability allows using in tailored blank and hydroformed tube applications

Components such as, rockers, pillars, pillar reinforcements, roof rails and cross members require high yield strength to avoid any intrusion into the passenger safety compartment during a collision; the intermediate to highest strength grades of dual phase steels are typically exploited in such components in which both extremely high yield strength and adequate

⁹ This report can be found in the following link, <https://usa.arcelormittal.com/~media/Files/A/Arcelormittal-USA-V2/what-we-do/markets/automotive/2020-02-DataSheet-DualPhase-v3.pdf>

formability are a must. Chemical compositions of a number of low to intermediate DP steels are presented in table below,

	<i>C</i>	<i>Mn</i>	<i>Si</i>	<i>Other</i>
<i>Hot roll</i>				
<i>DP590/600</i>	0.05	1.2	0.6	Cr
<i>Cold roll</i>				
<i>DP590/600</i>	0.10	1.0	0.3	
<i>DP690</i>	0.15	1.4	0.3	
<i>Galvanize</i>				
<i>DP590/600</i>	0.09	1.6-1.9	0.2-0.3	Cr, Mo
<i>DP780</i>	0.09	2.1	0.3	Cr, Mo, Nb

Table 3 chemical composition of DP600 used in the present work

1.4.1.3 Complex phase steels

Similar to DP steel family, Complex Phase (CP) steels are also considered as the transition to steel with very high ultimate tensile strengths (12), and were specially developed for roll-profiling, bending and edging processes (13).

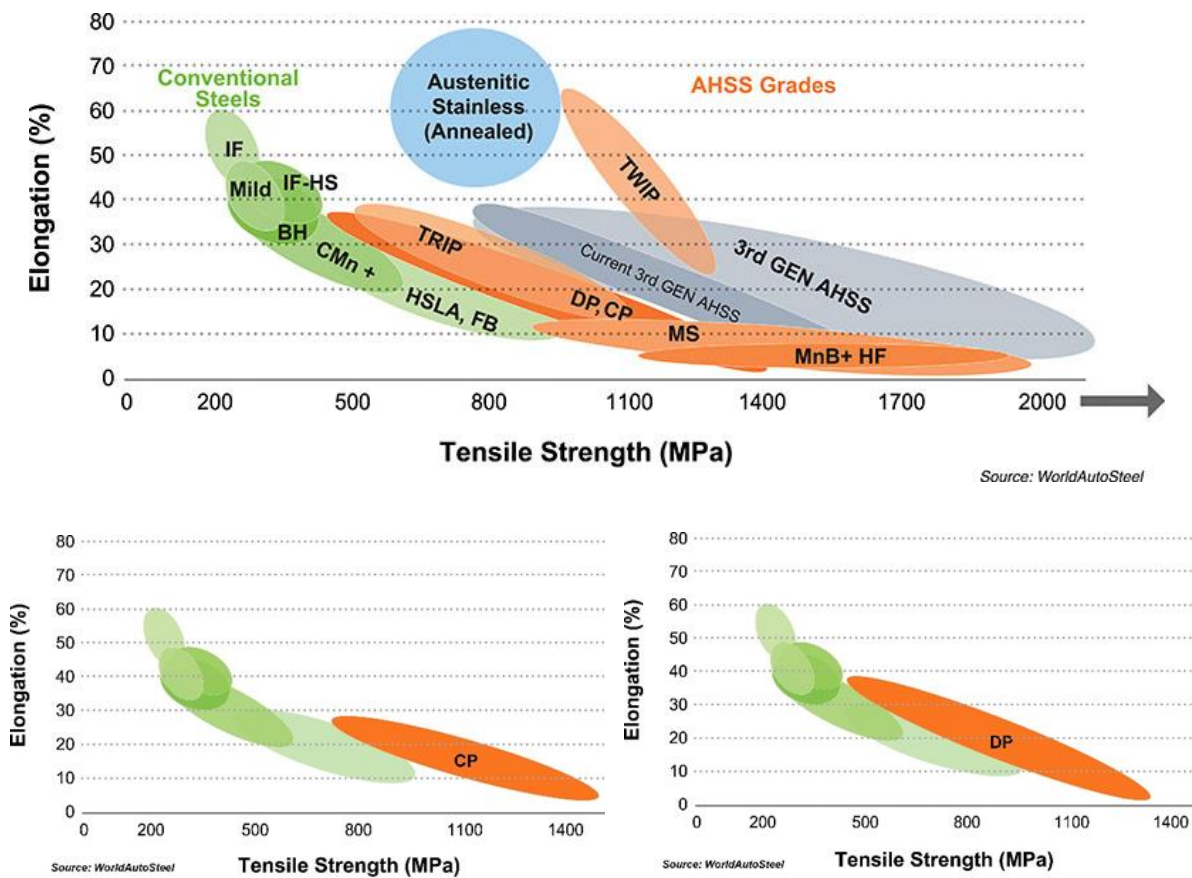


Figure 3 Steel Strength Ductility Diagram for Today's AHSS Grades (includes a comparison of traditional low-strength and high-strength steels) (14)

Small amounts of martensite, retained austenite and pearlite within the ferrite/bainite matrix typically constitutes the microstructure of CP steels. Retarded recrystallization or precipitation of microalloying elements like Ti or Nb result in an extreme grain refinement (12).

Due to its balanced property profile, complex-phase steels are excellent choices for crash components when light-weight design also is needed to be considered; high energy absorption, high residual deformation capacity, good hole expansion and high resistance to edge cracking while maintaining excellent bending properties are among the prominent characteristics of CP steel (12). Furthermore, they are also considered in *innovative light-weight automotive applications* such as stiffeners, sills, door impact bars, seat mounting rails and auto chassis components (13).

Some examples of current applications of CP steels can be highlighted based on the published documents on CP steels,

Grade	Application
CP 680/780	Frame rails, chassis components, transverse beams
CP 750/900	B-pillar reinforcements, tunnel stiffener
CP 800/1000	Rear suspension brackets, fender beam
CP1000/1200	Rear frame rail reinforcements, rocker outer
CP1050/1470	Rocker panels, bumper beams

Table 4 Current production grades of CP steels and example automotive applications (12)

1.4.1.4 QP 1180

Although conventional low-carbon TRIP (*transformation-induced plasticity*) steels with microstructures containing ferrite, carbide-free bainite, retained austenite and small amounts of martensite present excellent ductility, they hardly achieve tensile strengths above 1100 MPa. In order to overcome this shortcoming, while *maintaining high ductility*, several novel steels have been developed recently, such as nanocrystalline bainitic steel (or super bainite), maraging-TRIP steel and quenching and partitioning (Q&P) steel (15).

Quench & Partitioning (QP) steels are characterized by an excellent balance of high tensile strength and acceptable elongation, and produced in a quenching and a partitioning step. The resultant microstructure mainly entails tempered martensite and retained austenite, so that a higher strength can be achieved in comparison with conventional TRIP steels (15).

1.4.2 Material testing and challenges

Testing of material makes it possible to capture all the relevant effects around the test. Thus, the results are both more comprehensive and more reliable than that of a completely analytical

approach. While the numerical or multi-scale procedure for collecting material data leaves us with a decision on which effects to include, provided that it is possible to model. Furthermore, the analyses of defects and anomalies can be conducted during an experiment. Hence, a more reliable material model can be constructed. Exploiting an extended test program, the process window (variability of a certain parameter) can be fully studied, especially when a parameter's extreme values should be known to obtain a safety critical behaviour (6).

A challenge that comes with material testing is that a vast number of experiments are required to be done in order to attain a *full material response surface* regarding all the independent variables (6).

As another predicament, standardization of a test method must be considered when data from a variety of test programs are required to be utilized. *Standardization* can guarantee that the same approaches are employed in different test laboratories across the world, and so the test results can be aggregated, for example, into a specific material response model. However, a key obstacle in this context needed to be dealt with is that there are still some advanced material properties used in forming process simulations that are not yet standardised (6).

Other challenges of testing are the amount of required data and the possibility to reuse data across different projects. This field of work is still developing where publishing standards for testing and introducing methods to share data will improve the availability of forming process simulation (6).

All in all, undoubtedly, testing materials is the most important means to achieve material data needed to simulate forming processes. It is also considered as a complementary approach to construct the data from basic physics models, like in multi-scale simulation. The most comprehensive approach to obtain material data can be outlined by a combination made of: acquiring knowledge regarding the physics of the problem, and data derived from material testing so as to find the unknown variables and effects within the process (6).

1.5 CHALLENGES IN MATERIAL MODEL SELECTION FOR FORMING SIMULATION

The basic approximation to calibrate *material parameters in order to implement in forming simulation* might be to choose a constant yield curve extrapolation method (e.g. Swift) in **combination** with a yield locus that can be obtained particularly through uniaxial tensile testing in parallel, diagonal and transverse to the rolling direction (e.g. Hill '48). The advantages

attained via this approach will be multifold if it is able to describe the material behaviour sufficiently well (3) (16),

- The procedure can be readily applied to new materials with few data,
- Simple variation of parameters in the assessment of process robustness is allowed by clear correlations of yield locus shape or hardening,
- Only a couple of special tests are required in order to obtain certain modelling outlines for material groups.

However, supplementary experiments must be conducted in case the material require specific extrapolation methods or yield models (3). Even by executing biaxial bulge test, it is still quite problematic to obtain the specific shape of the whole yield locus by running further experiments. Test results have demonstrated that, not only the orientation of the additional experiment to the rolling direction, but also the number of additional experiments can affect the identification of the yield locus. However, with regard to this experimental approach, it should be observed that if it is possible to find optimally the yield model parameters for all the possible practical forming conditions (3). The studies have shown that, since standard experiments are not capable of optimally calibrating complex yield loci, an complementary process, such as, optimization approach seems to be quite essential, which also brings the possibility of limiting the number of additional experiments (3) (17) (16).

1.6 GOALS AND APPROACHES

1.6.1 Scopes

Having the big picture of ‘*the importance of material characterization*’ in mind, some aspects of this subject will be introduced and dealt with accordingly in this thesis work. Focusing on the plastic part of deformation, post-necking behaviour identification is one of the most important problems that costs automotive part manufacturers a considerable amount of time and money. Although there are some classes of methods to obtain the material’s deformation behaviour in a macroscopic scale and in large values of strain, up to now no one can safely say that a certain method is the most suitable approach to achieve this goal for any kind of forming process simulation. Generally, this is the point where a single method and merely a forward approach are not able to produce a remedy for this complicated condition. In the other words, for high fidelity simulation models, the material model parameters should

come out of a '*cycle of continuous validation and adjustment*' using both experimental tests and FEA until the difference between the last obtained results reaches a negligible amount.

1.6.2 Methodology

In order to attain the goals that are primarily set for this thesis work, a preliminary study on the post-necking behaviour prediction of some aluminium alloys and AHSSs will be done in the following chapters. The optimum identification of the behaviour, even for a certain material requires a considerable endeavour, the present work, nevertheless, can be regarded as a brief but still fundamental approach before going into the details of the problem; which is not only necessary for the sake of the comparison, but it also helps to acquire a general understanding of the nature of the subject. Different classes of identification are discussed in the beginning of chapter two, providing an outline of the main approaches to tackle this problem. This chapter is then followed by an example of the second class of approximation, namely Siebel and Schwaigerer's Model. Chapter three looks at the first class of post-necking identification, extrapolation method (EM). On the basis of this method, several hardening laws are firstly introduced and then applied to real test data of three aluminium alloys. It will be shown in chapter four that with the aid of biaxial test results of one aluminium alloy and a dual phase steel, the corresponding uniaxial tests can be extended beyond their limits; wherein, hydraulic bulge test is introduced in detail, and different methods are introduced as well to both collect and analyse the data. Going through chapter five, Digital Image Correlation technique is used to observe the strain field on the surface of two types of AHSS's test specimen. Although the basics of DIC technique does not lie in the outline of this work, a rather deep study will be conducted on the results of image processing. As it was discussed, FEA can be exploited both to calibrate the material model parameters and validate the outcome of the post-necking identification prior to its implementation in the next metal forming simulation.

CHAPTER TWO: POST-NECKING FLOW CURVE IDENTIFICATION THROUGH TENSILE TESTING

2.1 INTRODUCTION: FOUR CLASSES OF METHODS TO IDENTIFY POST-NECKING HARDENING BEHAVIOUR

As long as standard equipment and common analytical formulas are employed to evaluate load-elongation data, the hardening behaviour can only be identified up to the point of *maximum uniform elongation* (i.e. the point of *diffuse necking*).

With regard to the problem of *extended flow curve identification of sheet metal through a tensile test* numerous approaches have been proposed in the past. However, with the advent of *Digital Image Correlation* (DIC) the *strain field inside the diffuse neck* can be assessed in a considerable detail. Furthermore, the material behaviour hidden in the post-necking regime of a tensile specimen can be identified by means of the previously obtained strain fields. Based on this, four classes of methods to identify post-necking hardening behaviour of sheet metal through tensile testing can be considered (18); the methods are based on,

- Average values across the neck,
- Bridgeman correction and modified Siebel/Schwaigerer correction,
- Complete solution of the general problem,
- Special case of the Virtual Fields Method (VFM).

Percy Williams Bridgman
(1882-1961)



Received the 1946 Nobel Prize in Physics for his work on the physics of high pressures

Based on the pioneering work of Bridgman (19) three levels of approximation with respect to the problem of diffuse necking in a tensile specimen can be highlighted.

The *first class* of methods takes necking into account by *using average values across the diffuse neck and assuming a uniaxial stress state*.

The *second* and more sophisticated class of methods, *concerned with the distribution of stress and strain across the diffuse neck*.

The *third class* of methods employs *the complete solution of the general problem and considers the material state and the shape of the whole tensile specimen during diffuse necking* (18).

An overview of these methods and a classification with regard to their level of approximation are presented in the following.

2.2 FIRST LEVEL OF APPROXIMATION

With respect to the problem of diffuse necking, the first level of approximation takes diffuse necking into account by averaging strain and stress over the minimum cross section. This means that the stress state is assumed to remain *uniaxial* in the post-necking regime. Moreover, the true stress is usually approximated by dividing the total tensile load on the specimen by the current minimum cross section. The true strain corresponding with a certain true stress level is estimated by,

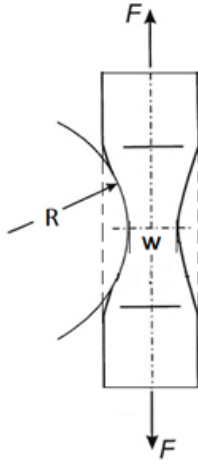
$$\varepsilon_{true} = \ln \left(\frac{A_{min}}{A_0} \right)$$

A_{min} minimum cross section
 A_0 initial cross section

Another common method in this class is to extrapolate the pre-necking hardening behaviour to high plastic strains using a phenomenological hardening law. The extrapolation method (EM) is considered here as a first approximation which may or may not be valid depending on the a priori chosen hardening law. This method will be applied to tensile test data in the next chapter and discussed extensively (18).

2.3 SECOND LEVEL OF APPROXIMATION WITH RESPECT TO THE PROBLEM OF DIFFUSE NECKING

The second level of approximation tries to take the *stress and strain distribution across the diffuse neck* into account. The mathematical analysis is based on describing equilibrium state across the diffuse neck and provides a correction to the average stress σ_{avg} , in order to deal with the introduction of transverse stresses (19). Bridgman derived an analytical solution for flat specimen as follows,



$$\sigma_{eq} = \frac{\sigma_{avg}}{(1 + \frac{4R}{w})^{1/2} \log \left[1 + \frac{w}{2R} + \left(\left(\frac{w}{R} \right) \left(1 + \frac{w}{4R} \right) \right)^{1/2} \right] - 1}$$

Geometrical parameters in the diffuse neck (w and R) can be obtained by pausing the experiment or by measuring these parameters continuously during the test. Similar to Bridgman, Siebel and Schwaigerer also proposed a correction factor for flat specimen (20),

$$k_f = \sigma_l \frac{4R}{4R + w}$$

The disadvantage of the second class, however, is that solely the conditions at the cross section of the diffuse neck would be observed; while the shape of the neck and the conditions in the remaining plastically deforming areas are ignored. Therefore, in order to take the strain heterogeneity into account, a more detailed numerical analysis was performed by Ghosh (21) and Ayres et al. (22). Later on, numerical simulations to provide an analytical calculation of the true cross section of a flat specimen was also introduced by Zhang et al. (23) (24). Siebel and Schwaigerer approach on the extending tensile test data will be discussed in detail in section 2.6.

2.4 THIRD LEVEL OF APPROXIMATION WITH RESPECT TO THE PROBLEM OF DIFFUSE NECKING

The complete solution of the general problem constitutes the third class of methods in which both the material state and the shape of the whole tensile specimen during diffuse necking are considered (18). Researchers have found that, in order to study the post-necking hardening behaviour, a Finite Element-based (FE-based) inverse strategy (25) can also be employed.

Koc et al. (26) suggested a FE-based inverse procedure based on the measured tensile forces during the experiment, so that, a special combined experimental/numerical technique has been developed. The technique relied on a comparison between the real material response, and the

response obtained from a numerical simulation of the same test. By the proper tuning of material constants within the material strain hardening law, the numerical response can be drawn close to the measured one. For this purpose a special numerical approach, based on mathematical optimization methods was employed.

Kajberg and his co-workers (27) exploited experimental full-field data to feed the inverse procedure. Due to the use of full-field data analysis which also assessed the necking shape, the identified behaviour was expected to be more accurate.

Another possibility to extend the range of application for a material model was proposed by Ghouati and Gelin (28) (29), where the FEM was accompanied by an optimisation algorithm. The general idea in the papers was to use the forming operation of the material to the parameter estimation process. In order to match (using the least-square method) the evaluated response from the FEA to the measured response from the forming process, the adjustments of the material parameters in the simulation were then made. However, this approach is not practical when no physical large-scale or production forming process present for drawing a comparison (18).

2.5 VIRTUAL FIELDS METHOD

Another *complete solution* for identifying constitutive behaviour of materials is the Virtual Fields Method (VFM) (30). VFM has also been aimed at *avoiding the shortcomings of the FE-based inverse method*; for instance, from a practical point of view, the coupling between the experimentally measured quantities and the numerically computed response can be a significant challenge. Moreover, the iterative FE simulations to predict the plastic instability are always a very time-consuming task (31). VFM is based on the *principle of virtual work* which is written in terms of a number of particular virtual fields. The basic equation for quasi-static non-linear VFM can be written as (18),

$-\int_V \bar{\sigma} : \bar{\varepsilon}^* dV + \int_S \bar{T} \cdot \bar{u}^* dS = 0$	$\bar{\sigma}$: actual stress tensor \bar{T} : actual traction vector \bar{u}^* : virtual displacement field ¹⁰ $\bar{\varepsilon}^*$: virtual strain field, derived from \bar{u}^*
---	---

Further and even more importantly though, $\bar{\sigma}$ and $\bar{\varepsilon}^*$ are not linked via constitutive equations. The virtual displacement field, however, can be any function but a kinematically admissible one (KA)¹¹; hence, based on the main rules of the VFM, it is permissible to exploit the actual displacement fields in the previous equation as they are defined as KA.

Based on the *principle of virtual work*, the work performed by the external forces equals the internal work, the following equation holds (18)

$W_{int} = \int_V \bar{\sigma} : \bar{\varepsilon} dV = \int_S \bar{T} \cdot \bar{u} dS = W_{ext}$	$\bar{\sigma}$ actual stress tensor \bar{T} actual traction vector \bar{u} actual displacement field $\bar{\varepsilon}$ actual strain field
--	---

Choosing this particular virtual field (the actual field) results in obtaining an energy balance between internal and external work like the above equation. Furthermore, in this particular case $\bar{\sigma}$ and $\bar{\varepsilon}$ are associated by the constitutive material behaviour (18). Thus, through the

¹⁰ A virtual displacement field is defined as the difference between two neighbouring kinematically admissible displacement fields. In other words, it is a vector field u which is such that, if u is a kinematically admissible displacement field, then so is $u + \delta u$. It is furthermore assumed that the virtual displacement field is infinitesimal, that is, $|\delta u_{i,j}| \ll 1$. Corresponding to a virtual displacement field δu we may define the virtual strain field $\delta \varepsilon$ by $\delta \varepsilon_{ij} = \frac{1}{2}(\delta u_{j,i} + \delta u_{i,j})$.

¹¹ A displacement field is called kinematically admissible if it is mathematically well-behaved (for example, continuous and piecewise continuously differentiable) and obeys the external and internal constraints, if any.

constitutive equations we can write the stress field in terms of the strain field $\bar{\epsilon}$ as, $\bar{\sigma} = f(\bar{\epsilon}, \mathbf{q})$. The finite set of unknown parameters \mathbf{q} (elasto-plastic material constants) can then be identified by the minimization of a cost function as follows,

$$C(\mathbf{q}) = \sum_{j=1}^l \left[- \int_V f(\bar{\epsilon}_j, \mathbf{q}) : \bar{\epsilon}_j dV + \int_S \bar{T}_j \cdot \bar{u}_j dS \right]^2 = \sum_{j=1}^l [-(W_{int})_j + (W_{ext})_j]^2$$

In which, $\bar{\epsilon}$ is the actual deformation field, $f(\bar{\epsilon}, \mathbf{q})$ is the stress associated through the yield surface of the material and l is the number of trials.

Pannier and his co-workers introduced the first application of VFM in metal plasticity by employing actual experimental data (32), in order to find the reference parameters of a Voce law. This discussion is introduced in Appendix A of this thesis work.

Exploiting 3D displacement fields, Rossi et al extracted the constitutive parameters of a plasticity model at large plastic strains by VFM-based procedure (33). Coppieters and his colleagues investigated the possibility of employing actual fields instead of virtual fields to study the post-necking hardening behaviour of metallic sheets (34).

2.6 EXTENDING TENSILE TEST DATA USING SIEBEL AND SCHWAIGERER'S MODEL

Employing Siebel and Schwaigerer's model, a method to evaluate the strain in the necking zone of a tensile specimen was proposed by Hoffmann and Vogl (35), in which benefiting from optical systems the possibility to extend the flow stress beyond necking can be facilitated.

2.6.1 Methodology

As it will be seen in chapter six, a *median stress-strain curve plus anisotropy values* of three rolling directions (0°, 45°, and 90° obtained by tensile tests) are normally implemented in the numerical simulations. However, the amount of information that one can collect from a uniaxial tensile test through measurement systems is always of paramount importance.

Owing to the necking of the specimen, at the conventional tensile test, only the data up to a small amount of equivalent strain can be obtained from the conventional measurement equipment. In this way, as it was mentioned, numerical extrapolation based on pre-necking data points always comes with inevitably erroneous results in the computer simulation of the forming process (35). Likewise, as far as normal anisotropy is concerned, the evaluation must

be stopped at the onset of diffuse necking (when the stress reaches the material's UTS). Despite the fact that, normal anisotropy is dependent on the strain level (36), an average value is often used to define the anisotropy of material. Therefore, the material properties commonly employed in the FEA of forming processes are not accurate enough, especially during large deformations.

Hoffmann and Vogl (35) then verified their results by conducting the stretch forming process experiment (Nakazima test) both experimentally and numerically. The simulation using improved material properties not only showed a better strain distribution than the results using conventional material properties in high strain areas, but also had a good agreement with experimental results. Furthermore, forming simulation could be extended, particularly up to the large values of strain before failure. It is worth noting that, the implementation of variable anisotropy in numerical simulation tools can improve the accuracy of the material failure prediction in the forming process (35).

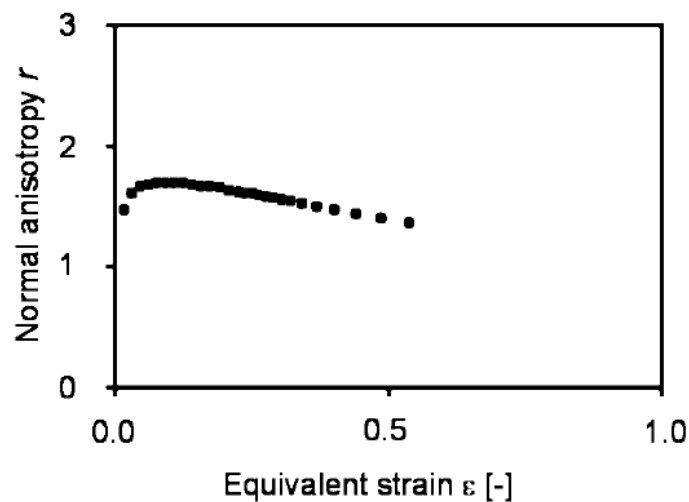


Figure 4 Normal anisotropy variation during deformation, 0° to RD, cold-rolled DC04 steel (35)

Although in the past the measurement of anisotropy for large values of strain was a problematic task (and that is why the normal anisotropy has always been considered as a constant), with the advent of optical measurement systems the anisotropy variations with current strain level can be captured with less difficulties.

2.6.2 Measurement setup

An optical system, entailing two CCD cameras, take pictures of the tensile specimen simultaneously in each time interval that previously introduced to the system. Benefiting from two back-to-back cameras has demonstrated to be quite important in order to eliminate out-of-

plane effects (32). The tensile specimen is randomly gridded by a colour spray, so that the shape and the position of the spackles can be readily recognized by the computer. Each picture is then divided into many small facets¹², so that the local strain tensor of each facet can be evaluated by the system with a very high accuracy. Employing the volume constancy criterion for plastic deformation, the component of strain in the thickness direction can be calculated in the next phase. In the meantime, the optical measurement system, then, compares the pictures of the two cameras in each corresponding time. Besides, in order to have synchronous data collection, the force signal of the tensile test machine is provided to the optical measurement system (35).

2.6.3 Stress-strain curve evaluation

The longitudinal stress σ_l of each facet is calculated by the following equation, where the axial force is read from the tensile test equipment and the local strain is derived from image processing software,

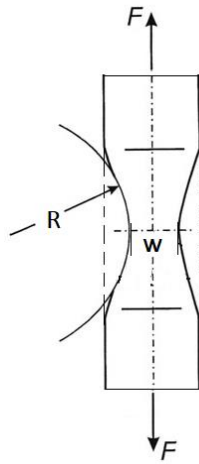
$$\sigma_l = \frac{F}{A} = \frac{F}{w s} = \frac{F}{w_0 e^{\varepsilon_w} s_0 e^{\varepsilon_s}}$$

F: tensile force
A: area of the specimen cross section
w, w₀ : current/initial width of the specimen
s, s₀ : current/initial thickness of the specimen
ε_w, ε_s: transvers/thickness strain of a facet

Considering the fact that the facets located in the necked zone always possesses maximum strain in each time step, in order to reduce the computation time, only the central part of the test specimen (where necking occurs later on) can be considered in drawing the stress-strain-curve (35). The stress value derived from the last equation can be considered as the flow stress only before the onset of necking; *when necking takes place in the specimen, however, the deformation is no longer uniform along the gage length and the state of stress does not remain uniaxial.*

The study of the true stress of a ‘constricted cylindrical specimen’ was conducted by Siebel and Schwaigerer in 1948, where they closely observed the geometry of the necking area (20). It was shown in the work of Banabic and his colleagues that for a flat specimen the flow stress can then be modified like the following equation (37).

¹² Very small surface marked by the coloured spray



$$k_f = \sigma_l \frac{4 R}{4R + w}$$

k_f : modified flow stress

σ_l : longitudinal stress

R : radius of necking

w : smallest width in the area of necking

The flow stress for materials with significant neck (such as, cold-rolled steel) can be calculated via this relation during the necking of the tensile specimen by monitoring the radius and the width of the specimen at neck for each image at given time. However, as it will be shown in chapter five, this method is not applicable to a wide range of materials, especially those in which necking geometry variation is not quite significant and symmetric during the deformation, so that the measurement of the radius of curvature at neck is neither practical nor acceptable.

2.7 OPTIMIZATION ALGORITHMS FOR MATERIAL MODELLING

The process of material modelling has evolved gradually; step by step more parameters have entered the modelling, and hence the complexity has increased at the same rate.

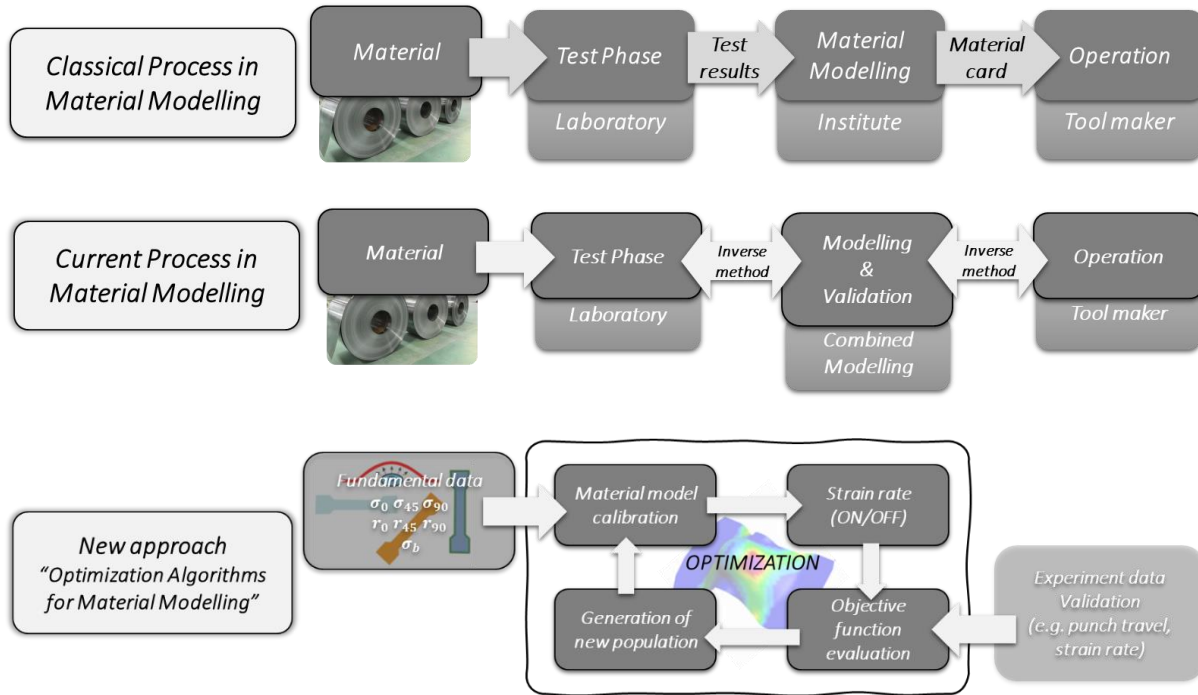


Figure 5 material modelling process evolution

‘New Approach’ in material calibration is mostly concerned with the fact that the descriptions of strain hardening and yield criterion are completely interrelated, although they were often investigated separately in the past. In order to obtain the material model parameters of more complex yield criteria, researchers admit that *non-standardized test methods* are necessary to be set. Thus, after conducting the classic tensile test and hydraulic bulge test, final identification of yield locus shape and parameters would be attained by specially designed validation experiments (inhomogeneous field problems) which are then simulated by FEM (3). The process principle entails both experiment and simulation, making it possible to assess models relatively quickly and effectively with regard to modelling real material behaviour under forming conditions (3).

In the *new approach*, an inverse method in combination with the consideration of strain rate sensitivity is exploited to obtain the yield locus in an optimization process. Considering the available resources in the lab, the amount of additional experiments can be reduced significantly by using this optimization approach.

CHAPTER THREE: HARDENING LAWS
INVESTIGATION ON NOVELIS AA5000, CONSTELIUM
AA5000 AND CONSTELIUM AA6000

3.1 INTRODUCTION

The tensile test data of three aluminium alloys produced by two different manufacturers are investigated in this chapter, so as to study the post-necking material behaviour using various strain hardening laws. As a first level of approximation, the following procedures is normally adopted to find the material constants in different hardening laws,

According to the adopted hardening law and theoretical constraints, a number of theoretical relations among different material constants can be derived. Moreover, using the least squares method, a hardening law will be fitted to pre-necking tensile test data points, by minimising the sum of squares of the residuals at every single points.

Two constraints are considered,

- First condition, *Considère criterion*: is one simple mathematical definition for diffuse necking point, in which, the first derivative of stress by strain equals to the value of stress at that point: $d\sigma_1/d\varepsilon_1 = \sigma_1$.
- Second condition, is obtained from the yield point information, where the plastic strain is zero.

For a certain hardening law, upper and lower bounds are imposed to each material constant in order to reduce the number of attempts during regression analysis. Then, by minimising the sum of squares of the errors, it is possible to find the value of each material constant with which the amount of error (RMSE) is the lowest with respect to the pre-necking experimental data.

In order to obtain flow stress curve out of the raw tensile test data, the following steps should be taken,

1. **Raw data from tensile test**: “Elongation [%]” and “Engineering Stress [MPa]”, where Elongation is defined as, $e = \Delta l / l_0 \times 100$.
2. **Calculating true strain (ε %) from elongation (e %)**, $\varepsilon = \ln(1 + \frac{e}{100}) \times 100$.
3. **True stress derivation**, $\sigma_{true} = \sigma_{eng}(1 + \frac{e}{100})$. Furthermore, the values above the maximum stress (the onset of necking) will be ignored, due to non-uniform distribution of strain along the gage length.

4. **Flow curve**, after obtaining engineering plastic strain by subtracting elastic part of the strain from the total strain value, the first point of the flow curve will be chosen by 0.2% plastic strain offset method; corresponding to engineering plastic strain of 0.002.

In this way, true stress vs true plastic strain curve, i.e. the plastic behaviour of the material along a certain roll angle in tensile test, will be drawn.

3.2 AN INTRODUCTION INTO COMMON STRAIN HARDENING LAWS

As the plastic deformation develops in the material, the initial yield surface evolves and can be described by a certain hardening law. So that, by parametrizing the material's post-necking hardening behaviour, the next step will then be to optimize a finite set of unknown parameters using pre-necking available data points (31). In other words, introducing strain hardening laws is aimed at mathematically presenting the true stress-true plastic strain relationship for a certain material. Furthermore, the resulted equation can then be exploited to draw the post-necking behaviour where no information from tensile test is available. A strain hardening law is sometimes a *phenomenological law* whose parameters possess no physical meaning, and clearly there is no guarantee that the extrapolation will be valid beyond the point of uniform elongation (38).

A hardening law, comes in the following general form,

$$\sigma_{eq} = f(\epsilon_{eq}^{pl}, \mathbf{p})$$

\mathbf{p} is a finite set of unknown hardening parameters,
 ϵ_{eq}^{pl} is the plastic equivalent strain.

The function f can be either *phenomenological* (i.e. its parameters have nothing to do with the micromechanical aspects of the material itself) or can be described by a *physics-based model* tightly connected to micromechanical behaviour of the material (dislocation interaction processes which leads to strain hardening in metallic materials) (38).

Strain hardening representations are often can be grouped as follows,

- *Saturated Law*

The description of the flow curves of FCC metals, such as aluminium and copper, can be improved by imposing saturated stress at large strain values through saturated laws such as, Voce (39) and Hockett and Sherby (40).

- *Power Law*

An unbounded stress at high strain levels is produced by this law; in this group, hardening laws such as, Ghosh (41) and Swift (42) normally lead to acceptable results for the BCC structure.

Generally, within the large values of strain, the saturated law underestimates the flow stress, while the power law may overestimate the flow stress. A number of alternative approaches have been suggested, which entails the use of a *linear* or *nonlinear combination* of both laws.

The rest of this chapter is dedicated to conduct the *nonlinear regression analysis* by employing either *Excel solver* or different *algorithms in MATLAB* (e.g. lsqnonlin, nlinfit). The goodness of the fits will then be compared via RMSE calculation for a number of commonly-used strain hardening laws.

3.2.1 Hollomon hardening law

Shedding light on Hollomon's hardening law constants,

$$\sigma_{hollomon} = K(\varepsilon_p)^m$$

An acceptable fitting will be derived only by applying one constraint to the solver as there are only two material constants for this hardening law. This constraint results from the Considère criterion (diffuse necking), so that

$$m = \varepsilon_{p,diffuse}.$$

Thus, only one material constant (K) should be solved to obtain the least amount of error.

The following diagram shows that Hollomon's hardening law comes with a very good fitting when we are working on aluminium, which agrees with the literature mentioned before (43).

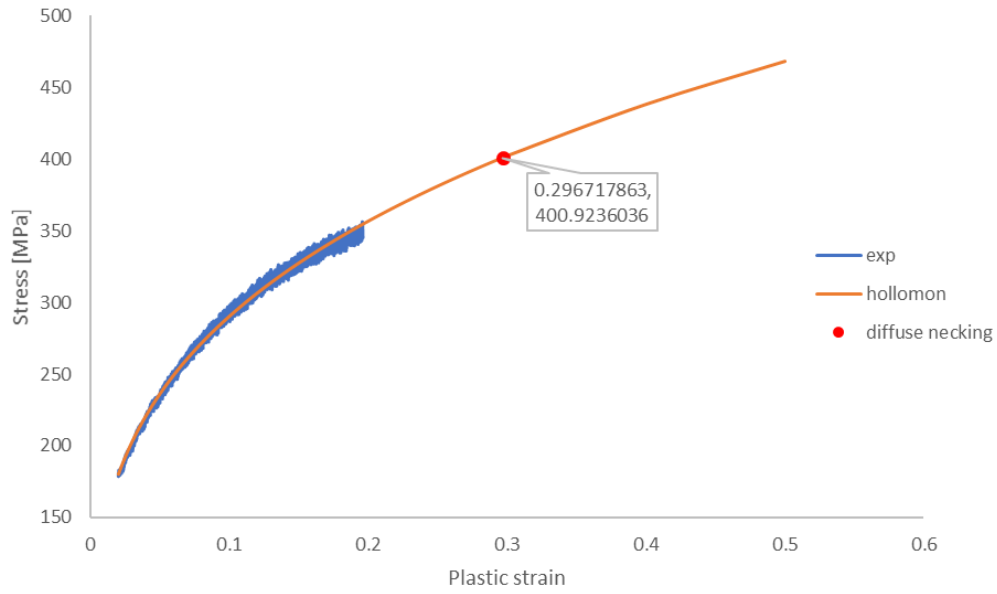


Figure 6 Hollomon hardening law fitting to an aluminium alloy and the position of corresponding diffuse necking

3.2.2 Swift hardening law

The phenomenological Swift power law can describe a *monotonic increasing strain hardening behaviour*, in which there are three material constants,

$$\sigma_{\text{swift}} = C(\epsilon_0 + \epsilon_p)^n.$$

Where, C is the stress amplitude, n is the hardening exponent and ϵ_0 is the strain shift parameter. In many practical problems the magnitude of plastic strain is much larger than the parameter ϵ_0 , leading to a simpler *power hardening law* (44). Again, as these parameters have no physical basis, there is no guarantee that the extrapolation is valid for strain values larger than maximum uniform strain.

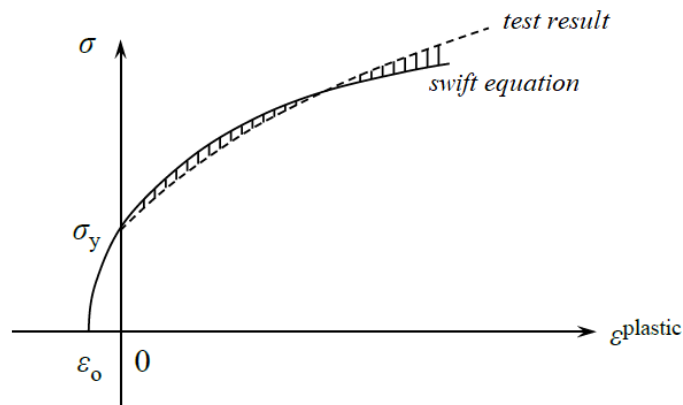


Figure 7 The experimentally measured stress-strain curve and the fit by swift law (44)

For a wide range of metals the exponent n has the range of $n = 0.1 - 0.3$, while the amplitude can vary a lot, regarding the grade of steel, for instance (44).

First condition, diffuse necking (Considère criterion),

$$d\sigma_1/d\varepsilon_1 = \sigma_1.$$

After applying this criterion to our test data points, we are able to find the true plastic strain value in which diffuse necking is going to start, named $\varepsilon_{p,diffuse}$.

Applying the Considère criterion to swift law, one can obtain the following relationship between two of the unknown material constants, n and ε_0 ,

$$n = \varepsilon_0 + \varepsilon_{p,diffuse}$$

Second condition, yielding, $\varepsilon_p = 0$ and $\sigma = \sigma_y$; at plastic strain equal to zero ($\varepsilon_p = 0$), stress is equal to yield stress σ_y ; thus, we will have,

$$C = \frac{\sigma_y}{\varepsilon_0^n}.$$

While n is already obtained by the first condition, another material constants, C will be derived as,

$$C = \frac{\sigma_y}{\varepsilon_0^{(\varepsilon_0 + \varepsilon_{p,diffuse})}}$$

This constraint is quite important as it affects the behaviour of the material at the boundary point between elastic and plastic region. In the other words, if this is not considered in our study, the last data point of elastic region will not coincide on the first data point of plastic region, leading to an unacceptable result in FEA.

With regard to the Excel solver parameters, two constraints are affecting the solver. The first one is related to the material constant, C , evaluated at yield point; while, the second constraint is describing the hardening exponent, n , benefiting from Considère criterion. Then, using least square method, the solver is able to find the proper value for pre-strain ε_0 .

As an example, applying Swift hardening law to one of the alloys, the following result is obtained,

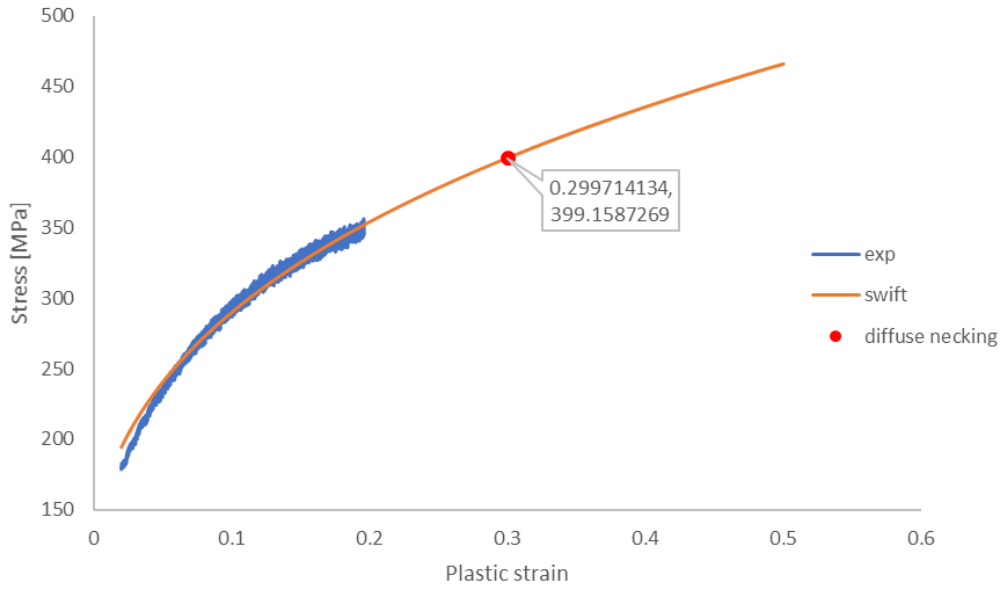


Figure 8 Swift hardening law fitting to a flow curve and the position of diffuse necking

As can be seen from the above diagram, for this type of material behaviour, due to pre-strain term, swift hardening law does not show a good fitting to the experimental data for small strains.

By studying the behaviour of various hardening laws, studies have found that the Swift hardening law can be fitted best to the experimental data for austenitic stainless steels for IN 718 and for SS 304, while for aluminium alloys, the Hollomon hardening law ($\sigma_{hollomon} = K(\varepsilon_p)^m$) was demonstrated to result in the best fit (43).

3.2.3 Voce hardening law (classical Voce saturation law)

Unlike Swift's hardening law, Voce's hardening law was derived from micro-mechanical considerations. Voce's law allows to describe strain hardening saturation behaviour which is naturally present in some material structures (45).

The law is defined by the following equation, with three material constants,

$$\sigma_{voce} = K_0 + Q (1 - \exp(-\beta \varepsilon_p))$$

First condition, diffuse necking (Considère criterion),

$$d\sigma_1/d\varepsilon_1 = \sigma_1.$$

Where, this condition leads to obtain a relation between Q and β at diffuse necking strain,

$$Q = \frac{\sigma_y}{(\beta + 1) \exp(-\beta \varepsilon_{p,diffuse}) - 1}$$

Second condition, yielding, $\varepsilon_p = 0$ and $\sigma = \sigma_y$,

$$K_0 = \sigma_y$$

Considering the solver parameters adopted for Voce material constants, the objective of the solver is set to minimise the sum of square of errors up to diffuse necking point on the Voce hardening law. However, as it can be seen from the next diagram, since diffuse necking occurred beyond the available experimental data point, it was not possible to calculate the sum up to diffuse necking as no experimental data was available for the respective Voce fitting curve. Thus, it can be said that Voce hardening law will not result in a good approximation of diffuse necking for this type of material. In order to find the correct location of diffuse necking on the fitted curve, it is vitally important to extrapolate the curve with the same strain increment as before, otherwise a wrong evaluation of diffuse necking may result.

As far as material constants are concerned, K_0 is set to be equal to yield stress, while as it was mentioned, Considère criterion will provide us a relation between Q and β . The least amount of error was evaluated by changing the values of Q and β .

Voce comes with a good approximation of the diffuse necking point, quite close to the experimental diffuse necking.

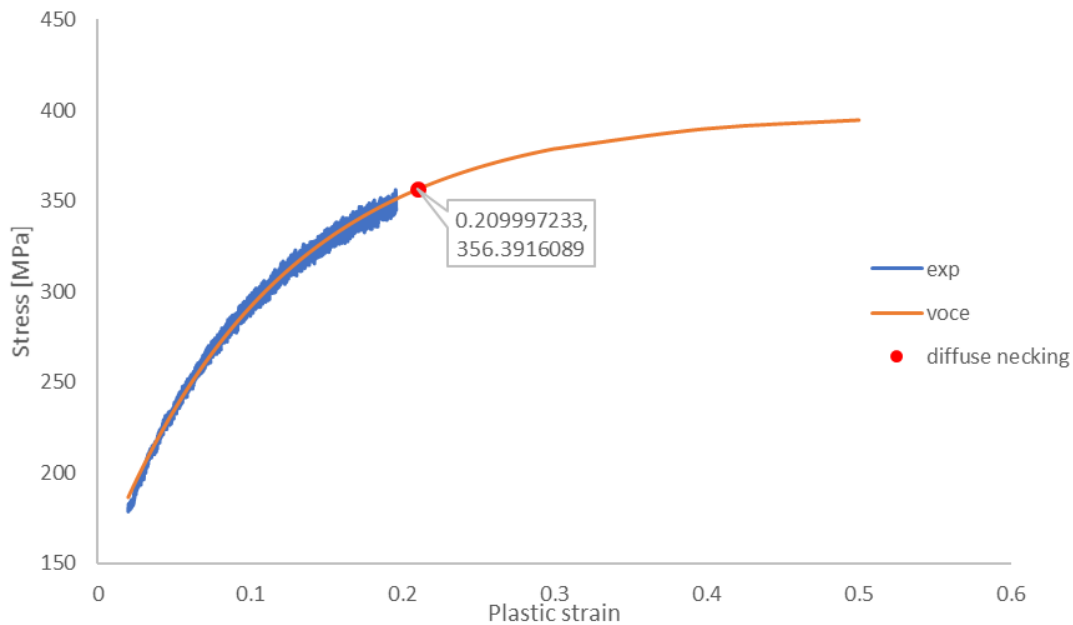


Figure 9 Voce hardening law fitting to a flow curve and the position of diffuse necking

It can be seen that both Voce and Swift law provide acceptable fits for small strains, but behave quite differently in the extrapolated area. Assuming that the true strain hardening curve lies somewhere in between these lower (Voce) and upper (Swift) bounds, a hardening model

can be introduced so that it is able to capture both extreme cases as well as intermediate behaviour of strain hardening (46).

3.2.4 Swift-Voce hardening law

With the assumption that the real post-hardening behaviour is somewhere between saturated Voce and Swift hardening law, the linear combination of them can be employed with a proper coefficient to describe the behaviour of material beyond diffuse necking using following equation,

$$\sigma_{Swift-Voce} = (1 - \alpha) \sigma_{Voce} + \alpha \sigma_{Swift}$$

The method followed by the manufacturing team was to work on material constants of Swift and Voce laws separately and use the above relation to superimpose the influence of each hardening law. Moreover, the number of data points is prescribed to reduce to 50 so as to import the flow curve into the FE software.

For small values of strain, below diffuse necking, different values of α will affect the flow curve only slightly (figure 7). While for larger strains, with $\alpha=0$, swift-Voce hardening law shows a saturation stress as Voce plays a dominant role; increasing the weight, hardening will be more evident and varies quite differently (figure 8).

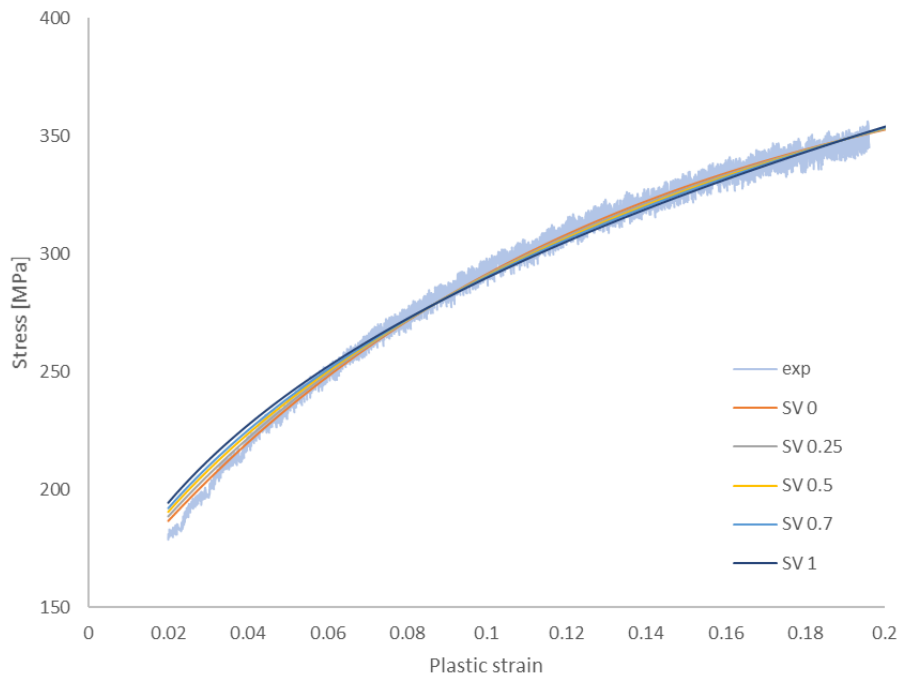


Figure 10 Swift-Voce hardening law for small values of strain

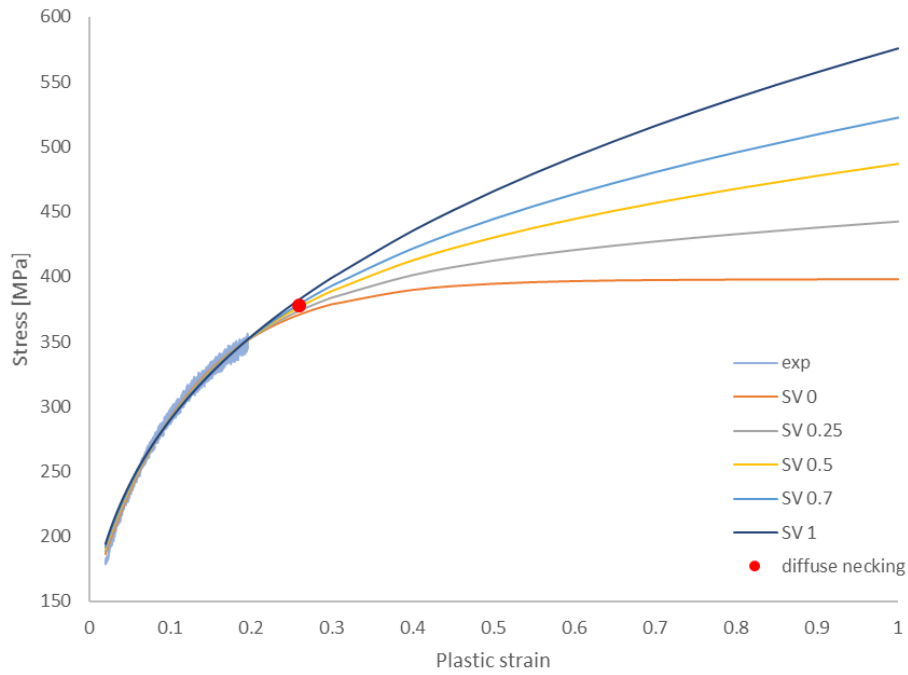


Figure 11 Swift-Voce hardening law for large values of strain

In order to decide about the proper value of α for Swift-Voce hardening law, we need more investigation and evidence, such as complementary bulge test result; herein, based on the previous test results, $\alpha = 0.7$ is prescribed by the research group for aluminium.

3.2.5 Hollomon-Voce hardening law

With the assumption that the real post-hardening behaviour is somewhere between saturated Voce and Hollomon hardening law, the combination of their effects can be used with a proper coefficient to describe the behaviour of material beyond diffuse necking by the following equation,

$$\sigma_{Hollomon-Voce} = \alpha \sigma_{Hollomon} + (1 - \alpha) \sigma_{Voce}$$

Considering small values of strain (smaller than diffuse necking), only small deviations are observed when adjusting the value of α , and a good fitting is resulted. Figures below illustrate the fitting for both small and large value of strain,

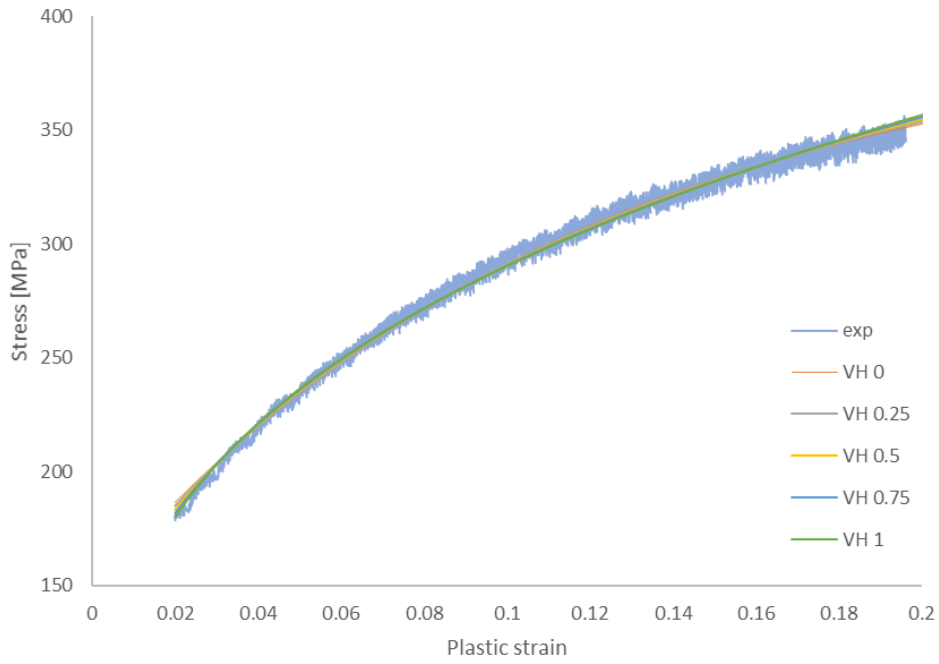


Figure 12 Hollomon-Voce hardening law for small values of strain

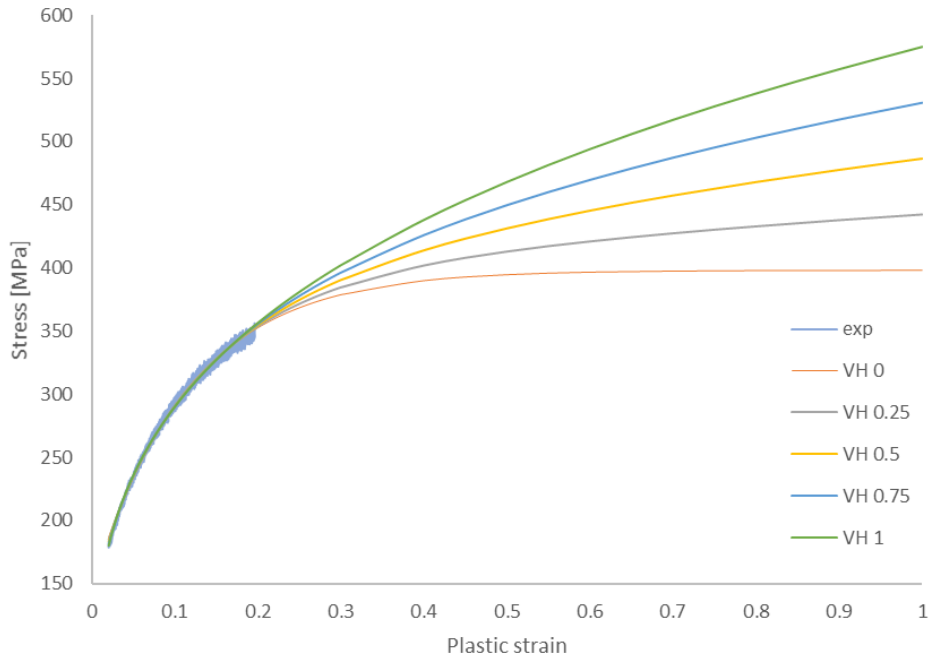


Figure 13 Hollomon-Voce hardening law for large values of strain

In order to study the goodness of fits, a comparison between Hollomon-Voce and Swift-Voce hardening laws are made in the following.

For small strains, and $\alpha = 0.75$,

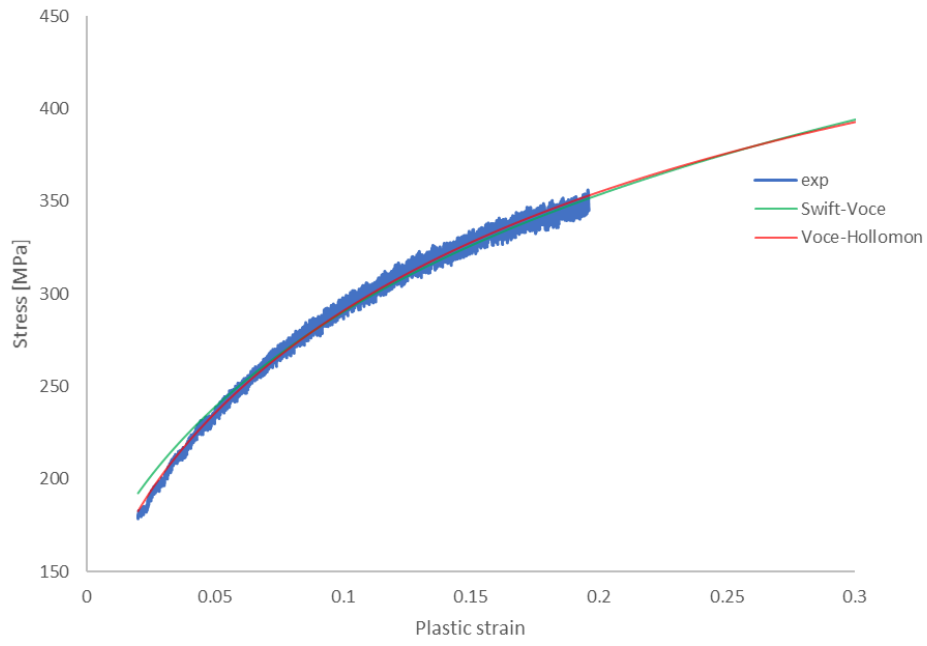


Figure 14 Hollomon-Voce hardening vs Swift-Voce hardening law for small strains

For large strains, and $\alpha = 0.75$,

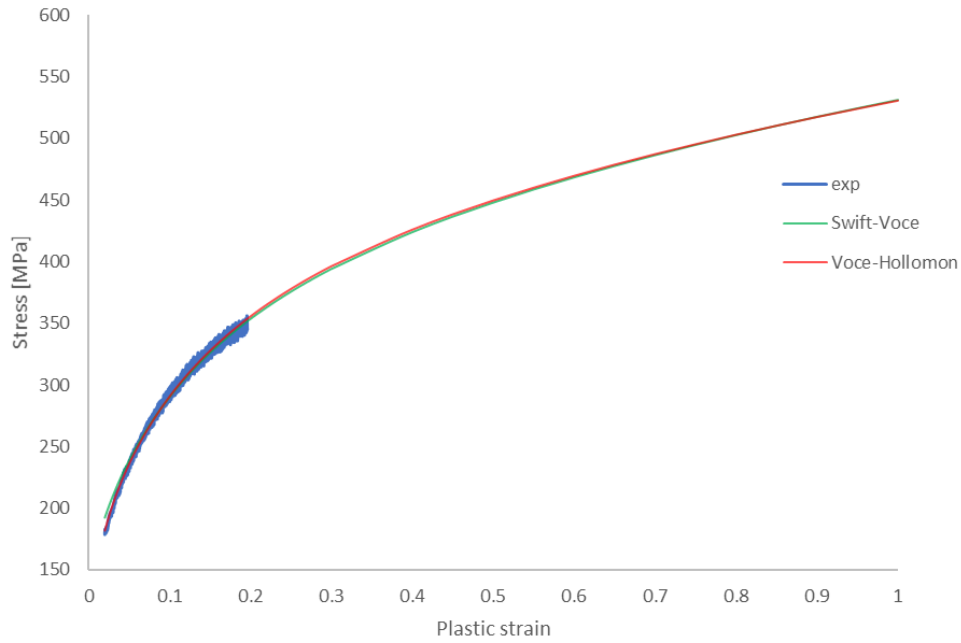


Figure 15 Hollomon-Voce hardening vs Swift-Voce hardening law for large strains

The goodness of fits can be studied by comparing the Root Mean Square Error of Hollomon-Voce law with that of Swift-Voce for $\alpha = 0.75$. Looking at the results reported in the following table, Hollomon-Voce hardening law shows a much better performance,

	<i>Swift-Voce</i>	<i>Hollomon-Voce</i>
RMSE	4.993	0.242

3.2.6 Hockett-Sherby hardening law

This law, defined by the following equation, normally leads to a good fit for aluminium alloys flow curve,

$$K_f(\varphi) = \sigma_{sat} - (\sigma_{sat} - \sigma_{0.2})e^{-m\varphi^c}$$

Where it can also be written like the following relation,

$$K_f(\varphi) = A - B e^{-m\varphi^c},$$

There are four material-related constants; σ_{sat} is the saturation stress, $\sigma_{0.2}$ is the initial yield stress, m is the hardening coefficient and c is the material's hardening exponent.

First condition, diffuse necking (Considère criterion),

$$dK_f/d\varphi = K_f.$$

Where, this condition leads to obtain a relation among the material constants at diffuse necking strain,

$$A = B \exp(-m\varphi_{diffuse}^c) [1 + mc\varphi_{diffuse}^{c-1}]$$

Having this equation, rather than four constants, the solver only needs to work on three constants to find the least amount of error. However, firstly, plastic strain at diffuse necking must be found through initial settings of constants. Although reducing the number of constants normally leads to hindering the fitting problem, first and second condition must be applied to obtain a realistic fit.

Since the stress-strain curves of some aluminium alloys seem to approach an asymptote indicating a saturation of strain hardening, Hockett-Sherby is able to track this behaviour benefiting from the $e^{-m\varphi^c}$ term in its definition.

Second condition, condition at yield point, does not lead to an acceptable relation for the Hockett-Sherby law.

In conclusion, for small strains the following result is obtained for an aluminium alloy,

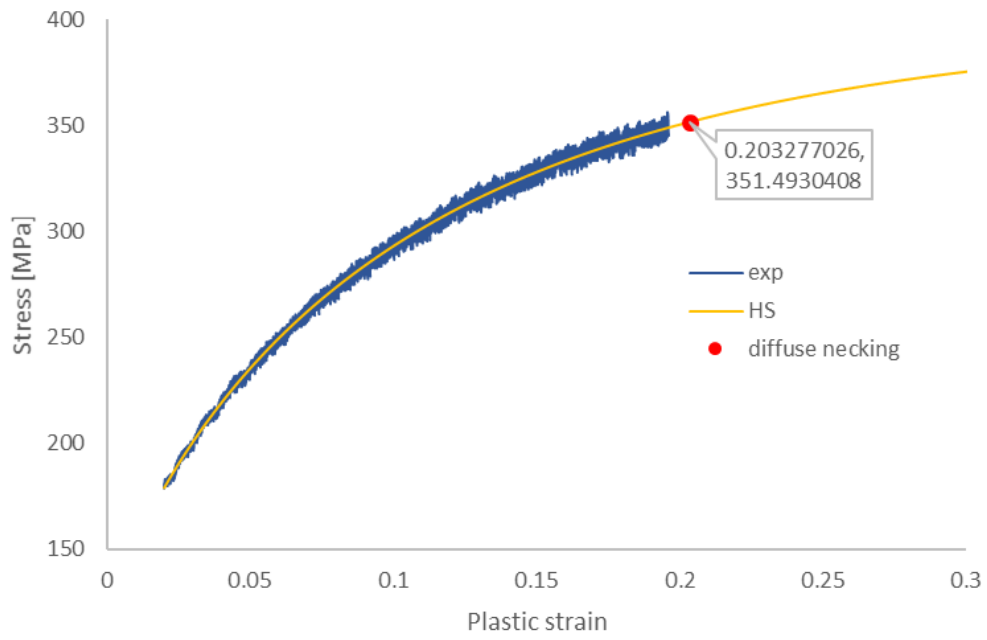


Figure 16 Hockett-Sherby hardening law for small strains

And for large values of strain,

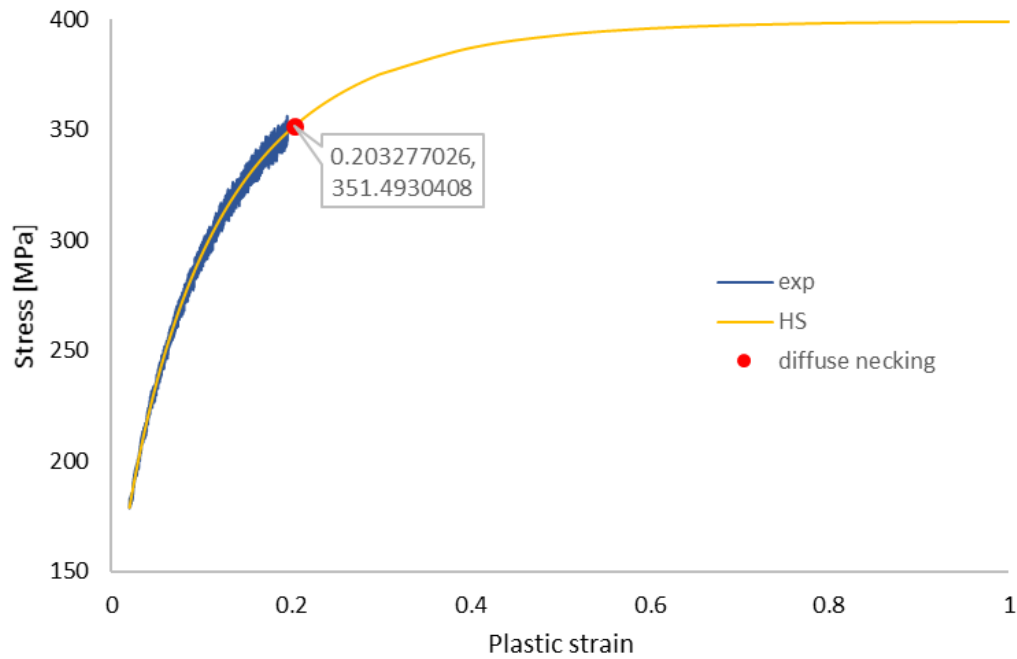


Figure 17 Hockett-Sherby hardening law for large strains

Moreover, it is clear that Hockett-Sherby gives a very good approximation of diffuse necking initiation for aluminium.

3.2.7 Swift/Hockett-Sherby hardening law

Imposing Swift hardening law to Hockett-Sherby will result in a reduction in Hockett-Sherby's stress saturation with large values of strain. The law is defined as the following equation,

$$\sigma_{\text{Swift/Hockett-Sherby}} = (1 - \alpha) \sigma_{\text{Swift}} + \alpha \sigma_{\text{Hockett-Sherby}}$$

The following diagram shows the behaviour of this law with respect to different weights (α) for Swift and Hockett-Sherby terms.

It can be seen for small plastic strains, (between 2% and 22%, i.e. in the range of valid experimental data below diffuse necking), increasing the share of Hockett-Sherby will result in a better fitting to the experimental data. This is another evidence that swift law cannot be a reliable choice for aluminium alloys.

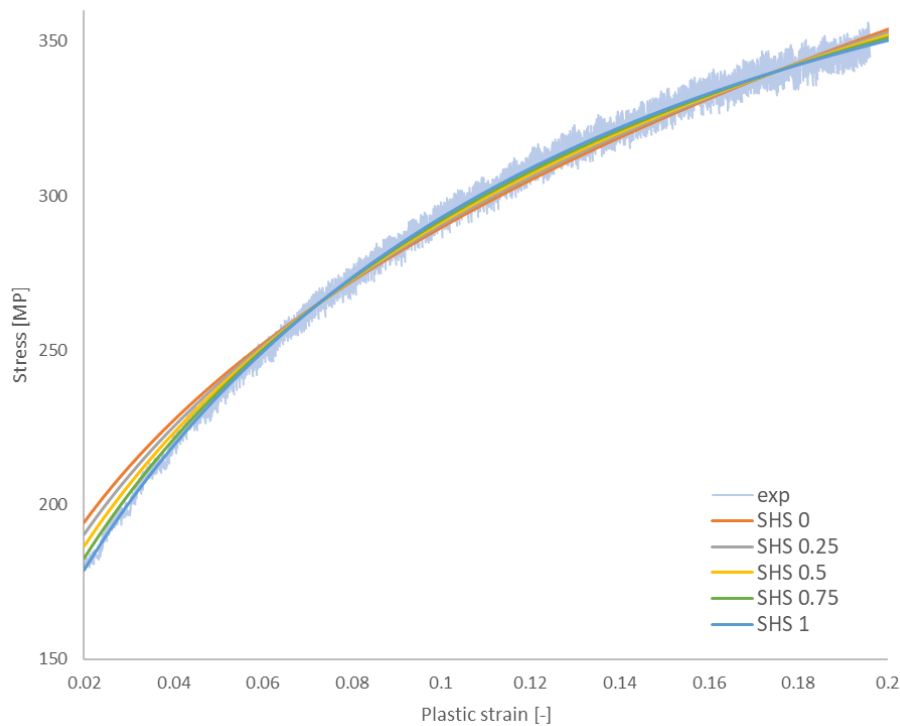


Figure 18 Swift/Hockett-Sherby hardening law for small strains

Looking at large values of strain in (figure 16), changing the weight will affect the fitting considerably. Thus, the decision about the best value for weight (α), that satisfies both small and large values of strain, depends on complementary tests such as bulge test which provides us with data for larger values of strain.

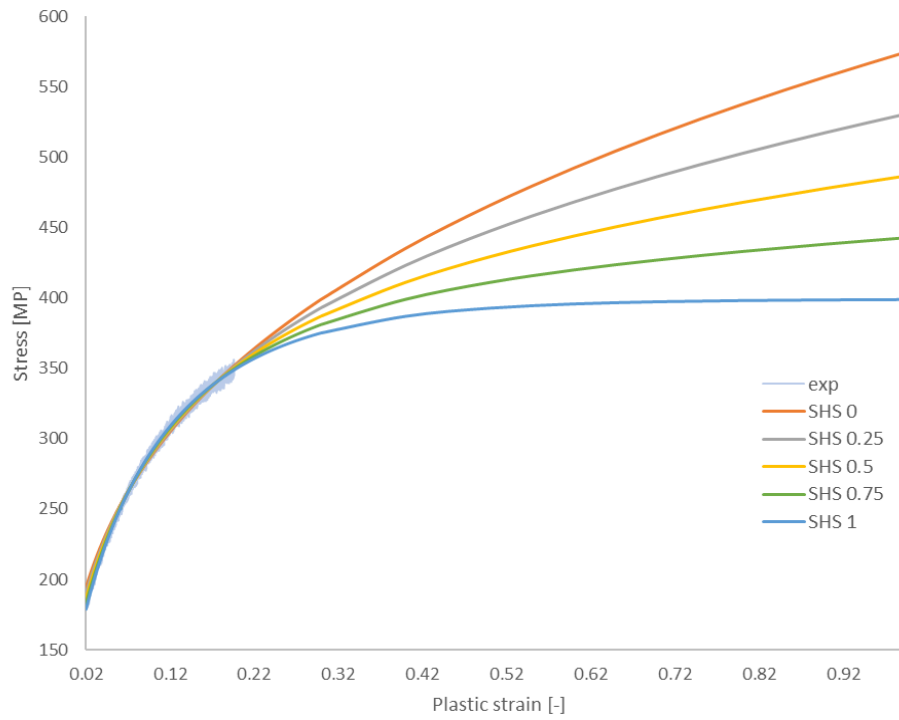


Figure 19 Swift/Hockett-Sherby hardening law for large strains

However, considering Swift/Hockett-Sherby law, the observation of the research group advises to factor in $\alpha = 0.75$ for aluminium and $\alpha = 0.25$ for steel. Applying this instruction, the Swift/Hockett-Sherby flow curve will be derived as the following figure,

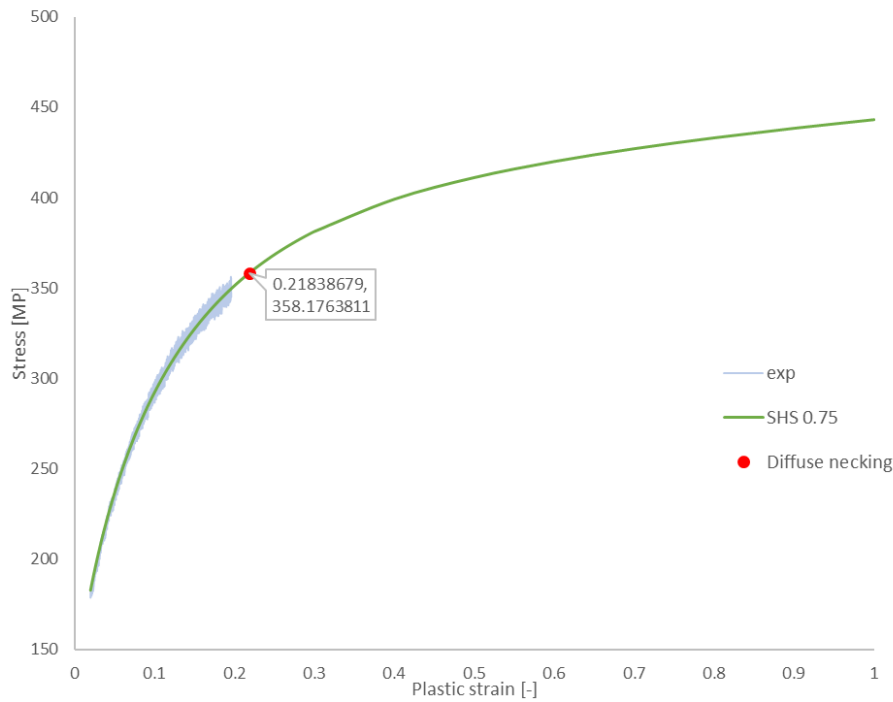


Figure 20 Swift/Hockett-Sherby hardening law, $\alpha = 0.75$ for aluminium

3.2.8 k -exponent function

The new exponential function (47) can be considered in this study as a phenomenological strain hardening law, in order to find a fitting function by means of a nonlinear regression analysis of pre-necking data points according to the following relation; where at low t or when the deformation parameter κ approaches the value zero the new exponential function behaves like the ordinary exponential function holding (47),

$$\begin{aligned} \exp_{\kappa}(t) &= (\sqrt{1 + \kappa^2 t^2} + \kappa t)^{1/\kappa} & \exp_{\kappa}(t) &\approx \exp(t), t \rightarrow 0 \\ & & \exp_{\kappa}(t) &\approx \exp(t), \kappa \rightarrow 0 \end{aligned}$$

By inserting the expression of the new exponential function defined in the above equation into Voce's hardening law, it obtains the following explicit formula defining the new model (47),

$$y = k_0 + Q \left[1 - \left(\sqrt{1 + \kappa^2 \beta^2 x^2} - \kappa \beta x \right)^{\frac{1}{\kappa}} \right] .$$

This formula depends on four fitting parameters (k_0 , Q , β , κ). Due to its four parameters which makes the process of finding them quite difficult, the applicability of this function as a strain hardening law in combination with a yield criterion is still unknown to the writer. However, its ability as a fitting function to the pre-necking data will be carefully examined in the following section.

3.3 HARDENING LAWS INVESTIGATION ON NOVELIS AND CONSTELIUM DATA SHEETS

3.3.1 Novelis AA5000 tensile test results

Looking at Novelis AA5000 data sheet, firstly, Hockett-Sherby hardening law is used to construct the flow curve up to 100% plastic strain, then a comparison will be made considering Swift-Voce hardening law. Furthermore, in order to import the results into the AutoForm software, 50 data points will be extracted from Swift/Hockett-Sherby approximated flow curve only for zero degree roll angle.

<i>Material</i>	<i>Novelis AA5000</i>
<i>E</i> <i>[MPa]</i>	69573
<i>Average Thickness</i> <i>[mm]</i>	0.895

	<i>True Rupture Stress</i> <i>[MPa]</i>	<i>A_g</i> <i>[%]</i>	<i>A₈₀</i> <i>[%]</i>	<i>n-Krupkowski</i>	<i>r -average</i> <i>(4%-A_g)</i>	<i>Yield stress</i> <i>[MPa]</i>	<i>R_m</i> <i>[MPa]</i>
<i>0°</i>	346.2	22.26	22.73	0.34025	0.743	146.8	291.9
<i>45°</i>	349.8	25.96	29.51	0.33884	0.925	143.6	282.1
<i>90°</i>	344.2	24.05	25.91	0.34091	0.811	147.5	283.1

Table 6 mechanical properties of Novelis AA5000

In the first column of the table, true rupture stress is given, above which not real test data is available (i.e. it is the last data point in the given data set provided by the supplier). Furthermore, true rupture stress is reported at A_g where it can be said that necking will start above this point. A_g is the percentage of *total uniform elongation at rupture*; together with true rupture stress the stress-strain values at necking are determined. Above this value of elongation, necking will take place, where strain distribution is no longer uniform along the gage length. A_{80} is the *total engineering elongation at fracture*. The following flow curves are obtained, based on the 0.2% offset method (i.e. 0.2% engineering plastic strain criterion).

Due to their crystallographic structure and the characteristics of the rolling process, sheet metals generally exhibit a significant anisotropy of mechanical properties. In fact, the rolling process induces a particular anisotropy characterized by the symmetry of the mechanical properties with respect to three orthogonal planes. Such a mechanical behaviour is called orthotropy (48). With respect to the rolling direction, three specimens are normally cut from the sheet in order to conduct the tests; zero degree direction, 45° direction, 90° direction.

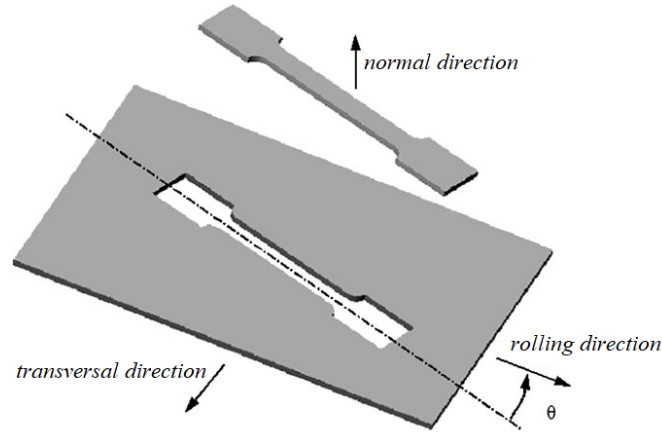


Figure 21 Tensile specimen cut at the angle θ (measured from the rolling direction) (48)

3.3.1.1 Zero degree roll angle

At zero degree angle with respect to rolling direction of the sheet, three hardening laws are observed in the following paragraphs; Hockett-Sherby, Swift/Hockett-Sherby and Swift-Voce laws. Besides, a comparison is made in the end to study the goodness of the fits.

- ***Hockett-Sherby hardening law***

Considering the theoretical constraints method described in section 4.1, and by applying the first condition, diffuse necking (Considère criterion), it is just needed to solve the problem with respect to three material constants, out of total four constants present in the law.

$$K_f(\varphi) = A - B e^{-m\varphi^c}$$

Within the range of small of strains, a good approximation of plastic strain at diffuse necking (20.298%) is observed, which is quite close to the true plastic uniform (mentioned in data sheet, 19.604%). Furthermore, Hockett-Sherby RMSE within the range of experimental data is approximated to be, 2.627.

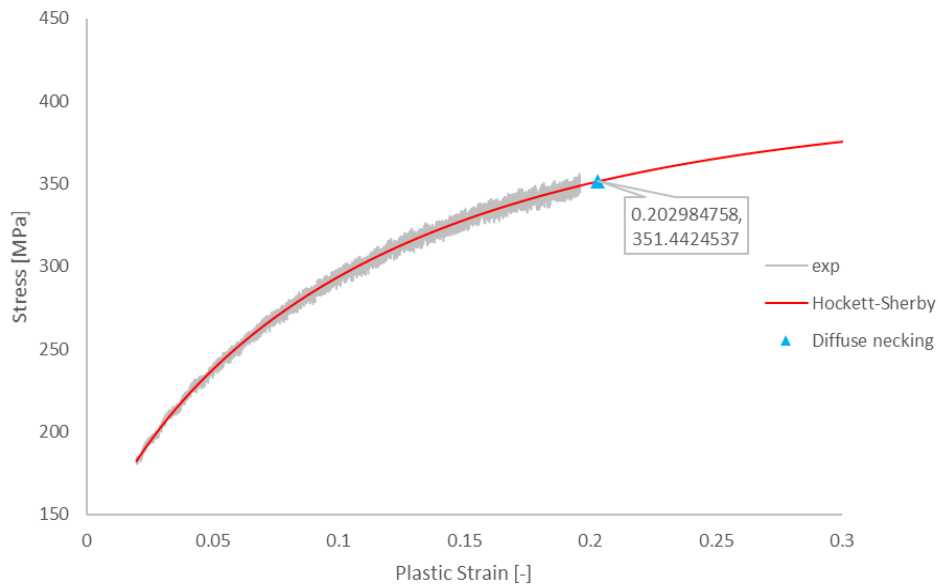


Figure 22 Hockett-Sherby hardening law, Novelis AA5000, zero degree roll angle, small strains

And for larger values of strain, Hockett-Sherby hardening law results in the following diagram,

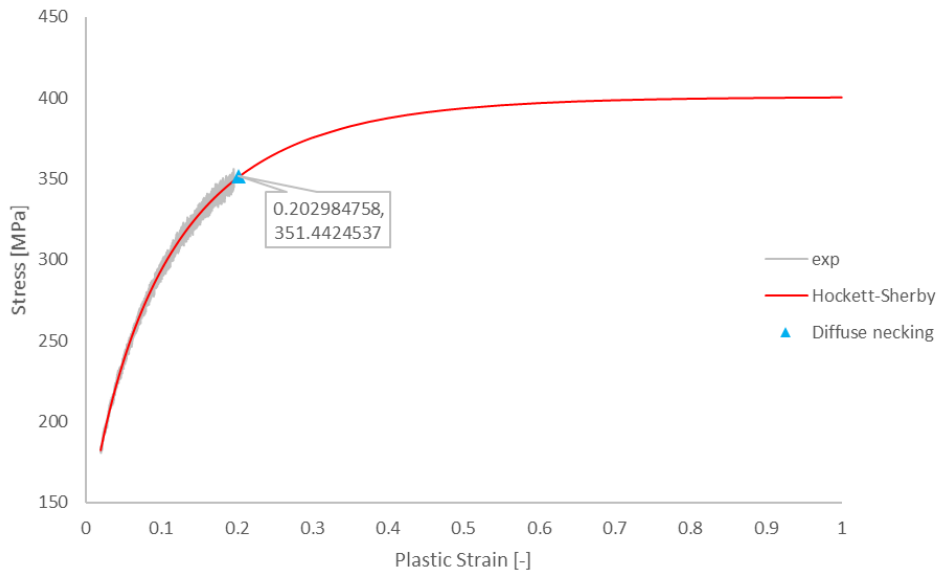


Figure 23 Hockett-Sherby hardening law applied to Novelis AA5000 for large strains

As no more than 50 data points must be imported into FEA software, based on the derived material constants, we redraw the flow curve, this time with 50 data points,

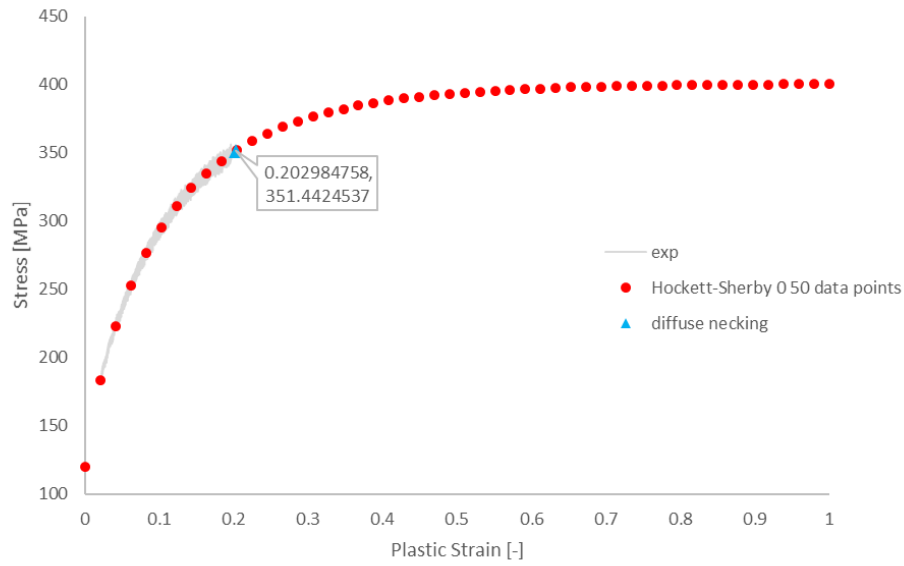


Figure 24 50 data points imported into FEA from Hockett-Sherby law for Novelis AA5000

No.	True Plastic Strain	HS stress	No.	True Plastic Strain	HS stress
1	0.000	120.3219	26	0.510	394.0887
2	0.020	183.8139	27	0.531	394.8627
3	0.041	223.2251	28	0.551	395.5421
4	0.061	253.0036	29	0.571	396.139
5	0.082	276.5299	30	0.592	396.6639
6	0.102	295.5558	31	0.612	397.1261
7	0.122	311.1746	32	0.633	397.5332
8	0.143	324.1339	33	0.653	397.8923
9	0.163	334.9742	34	0.673	398.2091
10	0.184	344.1009	35	0.694	398.489
11	0.204	351.8257	36	0.714	398.7364
12	0.224	358.3933	37	0.735	398.9551
13	0.245	363.9985	38	0.755	399.1488
14	0.265	368.7984	39	0.776	399.3203
15	0.286	372.9209	40	0.796	399.4723
16	0.306	376.4709	41	0.816	399.6071
17	0.327	379.5353	42	0.837	399.7267
18	0.347	382.1862	43	0.857	399.8329
19	0.367	384.4839	44	0.878	399.9272
20	0.388	386.4792	45	0.898	400.011
21	0.408	388.2146	46	0.918	400.0856
22	0.429	389.7265	47	0.939	400.152
23	0.449	391.0456	48	0.959	400.211
24	0.469	392.1979	49	0.980	400.2636
25	0.490	393.2059	50	1.000	400.3105

Table 7 50 data points imported into FEA from Hockett-Sherby law for Novelis AA5000

- **Swift/Hockett-Sherby hardening law**

The combined SHS hardening law is evaluated in this section, where α will be considered as the weight factor of Hockett-Sherby.

$$\sigma_{\text{Swift/Hockett-Sherby}} = (1 - \alpha) \sigma_{\text{Swift}} + \alpha \sigma_{\text{Hockett-Sherby}}$$

Figures below show the influence of α on the behaviour of the SHS fitting upon experimental data, both for small and large strains respectively,

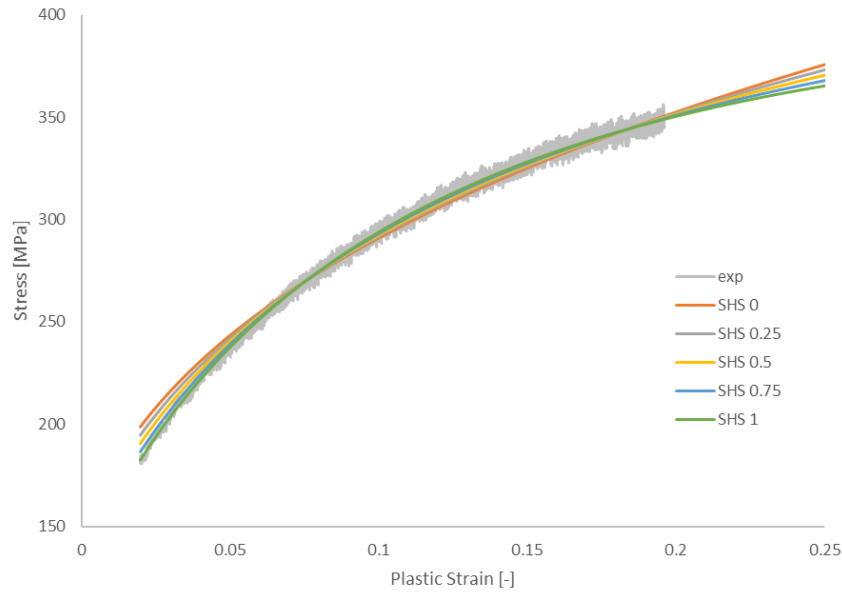


Figure 25 Swift/Hockett-Sherby hardening law applied to Novelis AA5000 for small strains

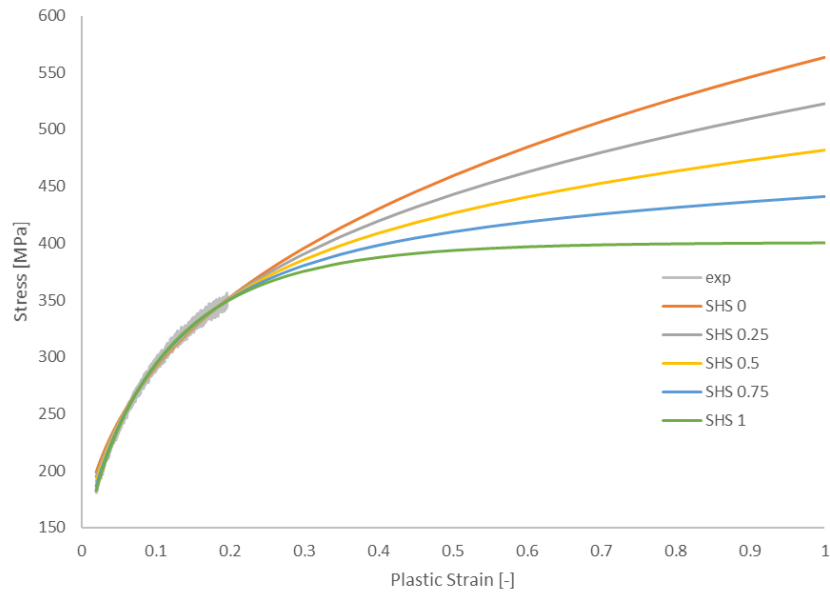


Figure 26 Swift/Hockett-Sherby hardening law applied to Novelis AA5000 for large strains

Following table reports RMSE for different values of α , where for $\alpha = 0.75$ the best fitting to the experimental flow curve in the range of small strains can be obtained,

	<i>SHS 0.25</i>	<i>SHS 0.5</i>	<i>SHS 0.75</i>
<i>RMSE</i>	4.882	3.800	2.965

Table 8 goodness of fits: Swift/Hockett-Sherby law for Novelis AA5000

Moreover, as can be observed in the following figure, for $\alpha = 0.75$, diffuse necking point (at true plastic strain of 21.59%) approximated by SHS is beyond the experimental uniform elongation point (at true plastic strain of 19.60%),

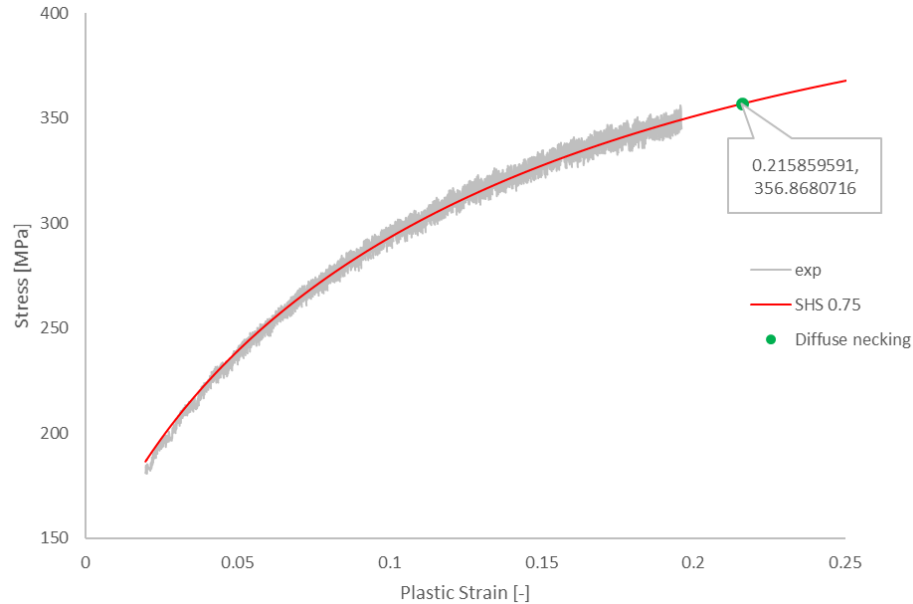


Figure 27 diffuse necking point for Swift/Hockett-Sherby hardening law

50 data points exported to AutoForm software are also shown in the figure below, where the points are presented in the next table,

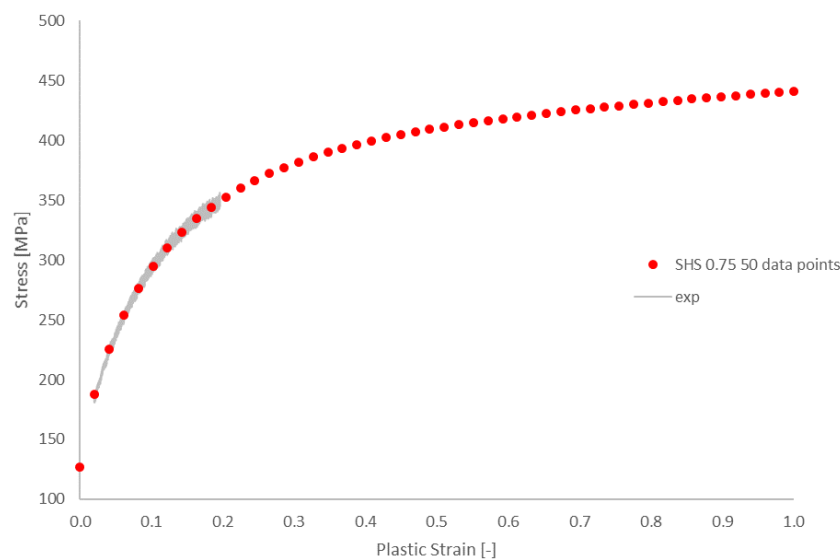


Figure 28 50 data points imported into FEA from Swift/Hockett-Sherby law for Novelis AA5000

No.	True Plastic Strain	SHS 0.75 stress	No.	True Plastic Strain	SHS 0.75 stress
1	0.000	126.96	26	0.510	411.0828
2	0.020	187.8157	27	0.531	412.9993
3	0.041	225.3773	28	0.551	414.8101

4	0.061	253.7353	29	0.571	416.5264
5	0.082	276.3095	30	0.592	418.158
6	0.102	294.799	31	0.612	419.7134
7	0.122	310.2299	32	0.633	421.2003
8	0.143	323.2878	33	0.653	422.6251
9	0.163	334.4599	34	0.673	423.9936
10	0.184	344.107	35	0.694	425.3111
11	0.204	352.5042	36	0.714	426.5819
12	0.224	359.8661	37	0.735	427.8102
13	0.245	366.3626	38	0.755	428.9994
14	0.265	372.1307	39	0.776	430.1527
15	0.286	377.2814	40	0.796	431.2729
16	0.306	381.906	41	0.816	432.3625
17	0.327	386.0798	42	0.837	433.4239
18	0.347	389.8658	43	0.857	434.4589
19	0.367	393.3166	44	0.878	435.4695
20	0.388	396.4765	45	0.898	436.4572
21	0.408	399.383	46	0.918	437.4235
22	0.429	402.068	47	0.939	438.3697
23	0.449	404.5588	48	0.959	439.2971
24	0.469	406.8786	49	0.980	440.2067
25	0.490	409.0475	50	1.000	441.0996

Table 9 50 data points imported into FEA from Swift/Hockett-Sherby law for Novelis AA5000

- **Swift-Voce hardening law**

A linear relationship with $\alpha = 0.25$ is considered in this hardening law, as it is advised for aluminium alloy,

$$\sigma_{\text{Swift-Voce}} = \alpha \sigma_{\text{Swift}} + (1 - \alpha) \sigma_{\text{Voce}}$$

Evaluated error using the Root mean square approach shows a value of 3.678, for $\alpha = 0.25$,

	SV 0.25	SV 0.5	SV 0.75
RMSE	3.597	4.265	4.993

Table 10 goodness of fits: Swift-Voce law for Novelis AA5000

The following figures show the Swift-Voce approximated flow curves for small and large values of strain, respectively,

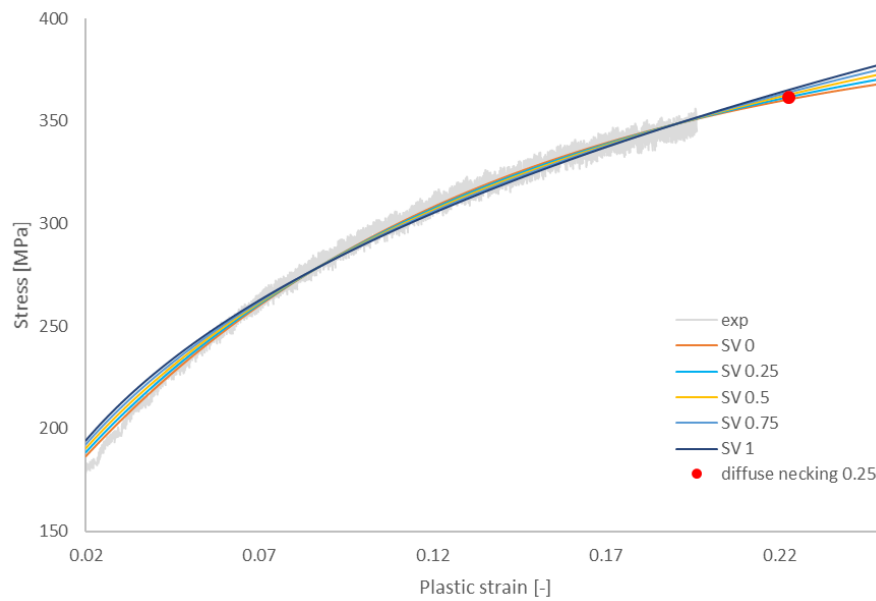


Figure 29 Swift-Voce hardening law applied to Novelis AA5000 for small strains

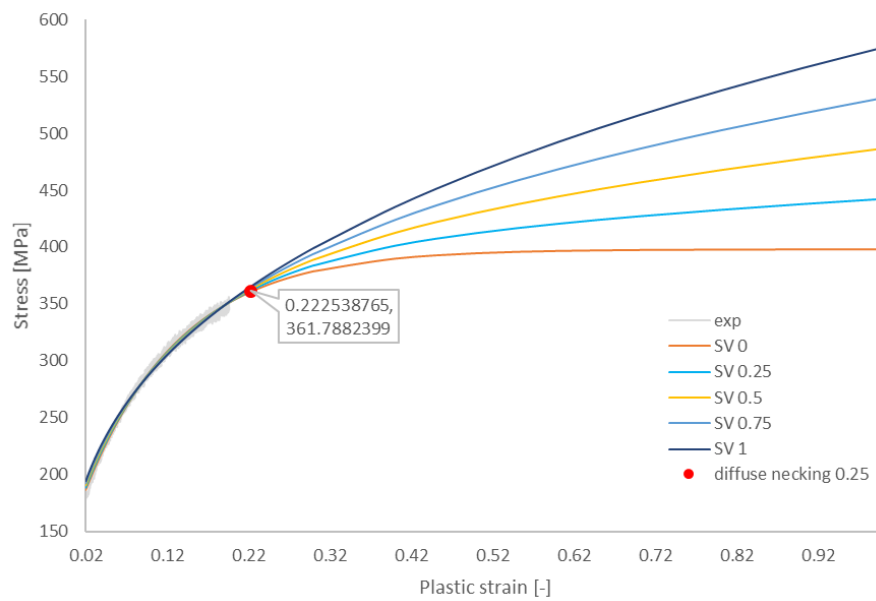


Figure 30 Swift-Voce hardening law applied to Novelis AA5000 for large strains

- **Comparing Swift/Hockett-Sherby with Swift-Voce hardening laws for Novelis AA5000 zero degree roll angle**

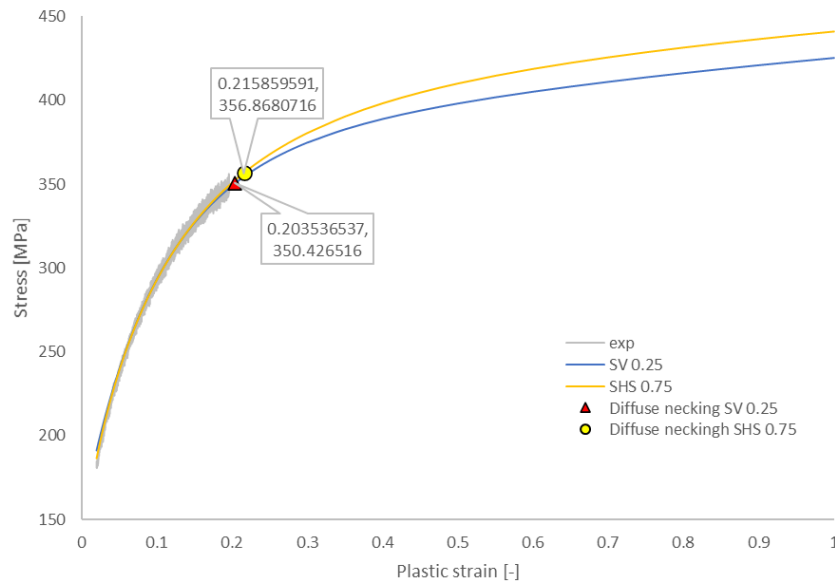


Figure 31 Swift-Voce vs Swift/Hockett-Sherby for large strains-Novelis AA5000

For small values of strain, both Swift/Hockett-Sherby and Swift-Voce show almost the same trend, although SHS fits better to experimental data according to the RMSE values reported in the following table,

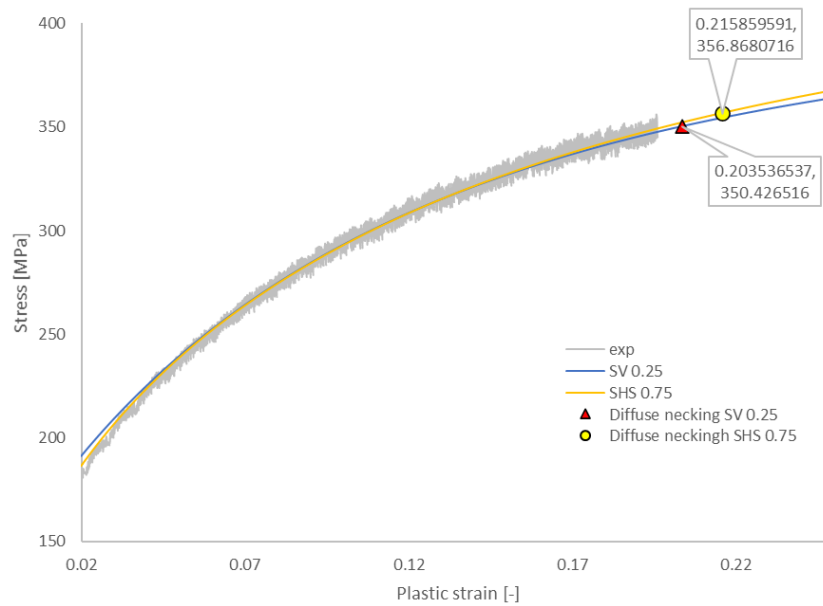


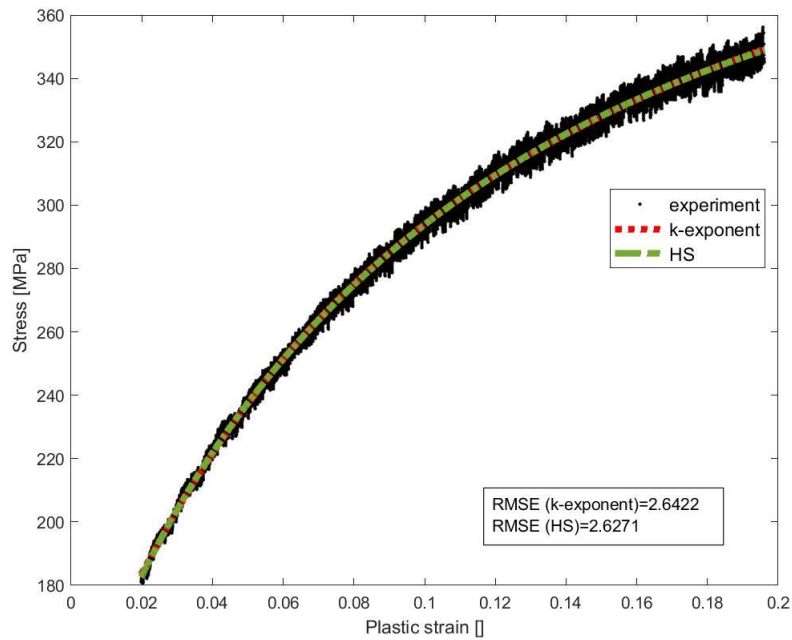
Figure 32 Swift-Voce vs Swift/Hockett-Sherby for small strains-Novelis AA5000

	SV 0.25	SHS 0.75
RMSE	3.597	2.965

Table 11 goodness of fits: Swift-Voce vs SHS-Novelis AA5000, zero degree roll angle

- *k-exponent function*

As it is described before, κ -exponent function is used to fit a function into the pre-necking data points. The nonlinear regression command of MATLAB (lsqnonlin) is used, where the results are compared with Hockett-Sherby. It is clear from the figure that both provide a very good fitting to the experimental data points.



3.3.1.2 45° roll angle

- *Swift/Hockett-Sherby ($\alpha=0.75$)*

Figure below illustrates the approximated flow stress curve for experimental data of a specimen cut in 45 degree direction with respect to rolling direction,

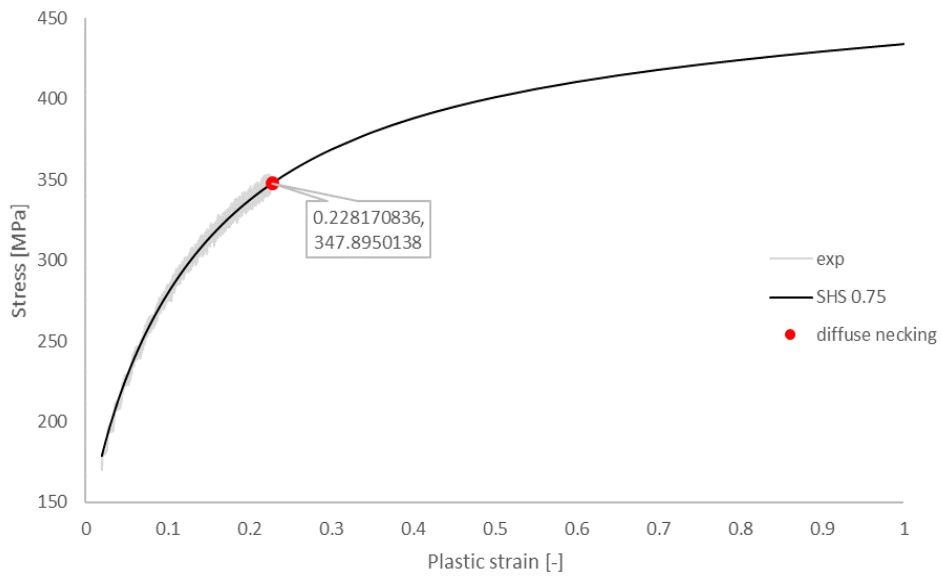


Figure 33 Swift/Hockett-Sherby hardening law, Novelis AA5000, 45 degree roll angle

- **Swift-Voce ($\alpha = 0.25$)**

After evaluating Swift/Voce ($\alpha = 0.25$) hardening law's flow curve for the given tensile test data, we can also see a comparison between Swift/Hockett-Sherby ($\alpha = 0.75$) and Swift-Voce ($\alpha = 0.25$) in the figure below,

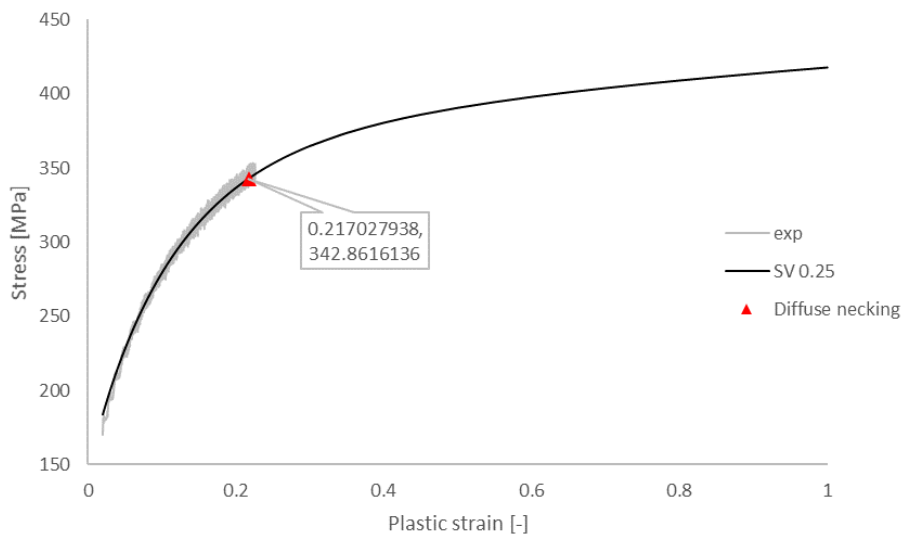


Figure 34 Swift-Voce (0.25) hardening law, Novelis AA5000, 45 degree roll angle

- **Comparing Swift/Hockett-Sherby ($\alpha = 0.75$) with Swift-Voce ($\alpha = 0.25$)**

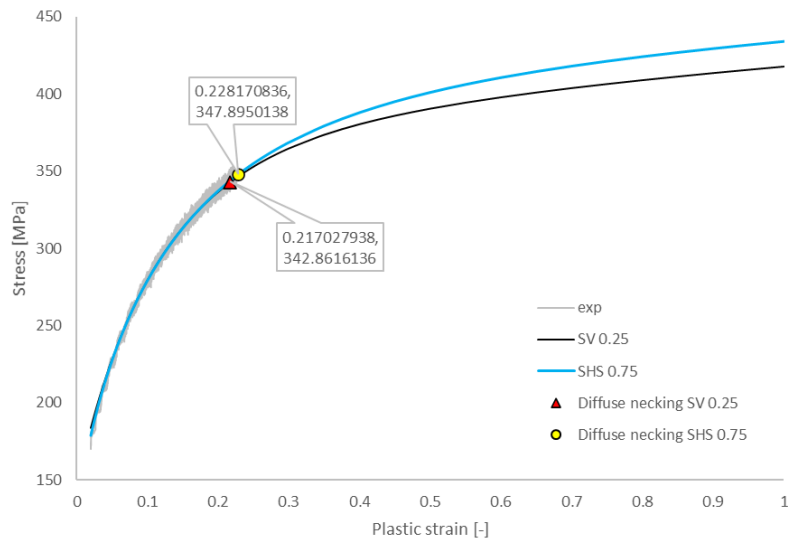


Figure 35 SV (0.25) vs SHS (0.75) hardening law, Novelis AA5000, 45 degree roll angle

As it can be observed from the figure, SHS hardening law with ($\alpha=0.75$) yields a better fitting in comparison with SV ($\alpha=0.25$) hardening law.

	SV 0.25	SHS 0.75
RMSE	3.804	3.186

Table 12 goodness of fit: SV (0.25) vs SHS (0.75) hardening law, Novelis AA5000, 45 degree roll angle

3.3.1.3 90° roll angle

- Swift/Hockett-Sherby**

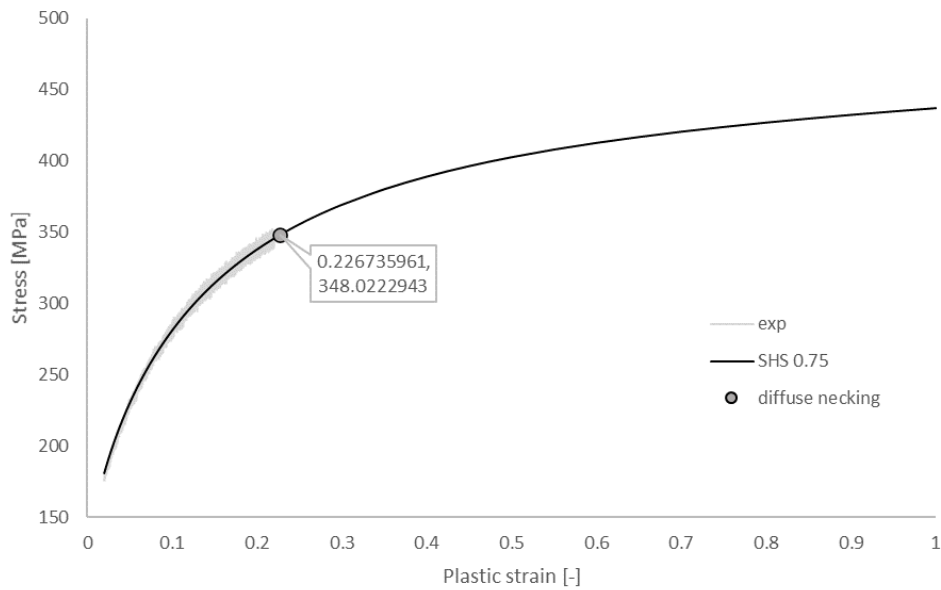


Figure 36 Swift/Hockett-Sherby hardening law, Novelis AA5000, 90 degree roll angle

- **Swift-Voce ($\alpha=0.25$)**

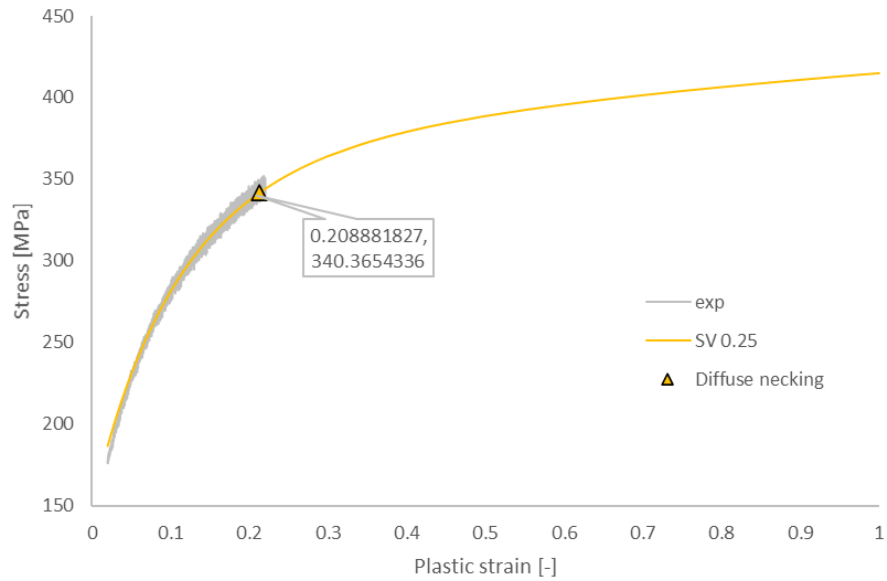


Figure 37 Swift-Voce (0.25) hardening law, Novelis AA5000, 90 degree roll angle

- **Comparing Swift/Hockett-Sherby ($\alpha=0.75$) with Swift-Voce ($\alpha=0.25$)**

Making a comparison between Swift-Voce and Swift/Hockett-Sherby can help us to observe the trends of approximated flow curves, where the former has a higher tendency to reach a saturated stress at larger strains,

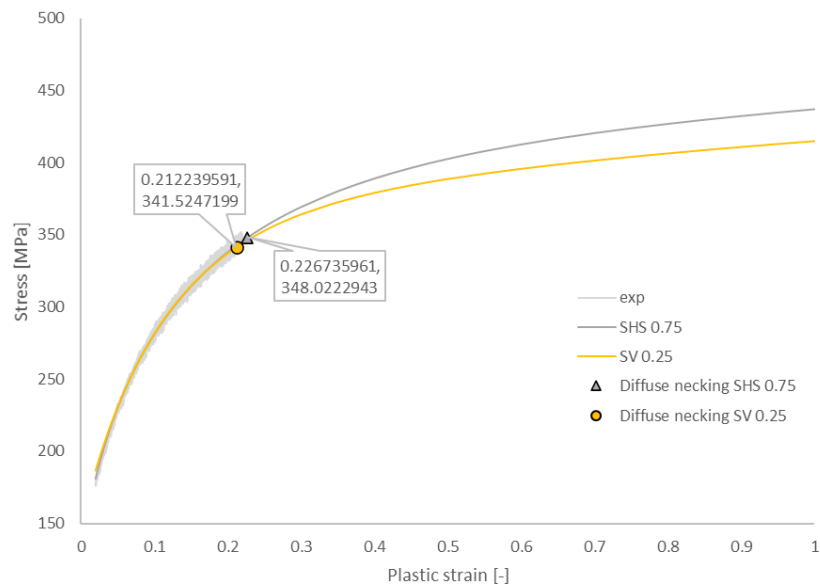


Figure 38 SV (0.25) vs SHS (0.75) hardening law, Novelis AA5000, 90 degree roll angle

3.3.1.4 Summary table of Novelis AA5000

Material constants and RMS errors of Novelis AA5000 are reported in the next table,

	<i>Law</i>	<i>A</i>	<i>B</i>	<i>m</i>	<i>c</i>	<i>C</i>	ϵ_0	<i>n</i>	<i>K₀</i>	<i>Q</i>	β	<i>RMSE</i>
0°	<i>HS</i>	400.707	280.385	6.561	0.833	-	-	-	-	-	-	2.627
	<i>SHS</i>					561.562	0.011	0.300	-	-	-	2.965
	<i>SV</i>								146.874	232.412	10.036	3.597
45°	<i>HS</i>	400.059	282.679	5.636	0.819	-	-	-	-	-	-	2.872
	<i>SHS</i>					537.123	0.0129	0.302	-	-	-	3.186
	<i>SV</i>	-	-	-	-				144.269	233.112	8.727	3.804
90°	<i>HS</i>	406.332	294.171	5.027	0.767	-	-	-	-	-	-	2.697
	<i>SHS</i>					533.052	0.0128	0.295	-	-	-	3.008
	<i>SV</i>	-	-	-	-				147.180	227.823	8.960	3.636

Table 13 summary: material constants and RMS errors of Novelis AA5000

3.3.2 Constelium AA5000 tensile test results

Looking at the data provided by Constelium, firstly we throw light on the flow curve up to 100% of plastic strain using Hockett-Sherby approach, then a comparison will be made with Swift-Voce hardening law.

<i>Material</i>	<i>Constelium AA5000</i>
<i>E</i> [MPa]	68087
<i>Average Thickness</i> [mm]	0.902

	<i>True Rupture Stress</i> [MPa]	<i>A_g</i> [%]	<i>A₈₀</i> [%]	<i>n-Krupkowski</i>	<i>r -average</i> (4%- <i>A_g</i>)	<i>Yield stress</i> [MPa]	<i>R_m</i> [MPa]
0°	354.2	25.32	26.63	0.32799	0.685	131.2	283.9
45°	333.2	23.58	26.82	0.34237	0.754	127.7	277.4
90°	338.1	25.07	27.46	0.33393	0.559	128.8	277.8

Table 14 mechanical properties of Constelium AA5000

3.3.2.1 Zero degree roll angle

- *Hockett-Sherby hardening law*

Also here benefiting from diffuse necking criterion, and applying the following result to the solver,

$$A = B \exp(-m\varphi_{diffuse}^c) [1 + mc\varphi_{diffuse}^{c-1}]$$

Approximated RMS error is lower here (2.384) in comparison with that of Novelis AA5000 (2.627); moreover, diffuse necking point is estimated quite close to the uniform elongation point reported in the data sheet. In more details, diffuse necking is evaluated to be at 22.32% of true plastic strain, where based on Constelium data sheet, it yields to be at 22.08% of true plastic strain.

Within the range of small of strains, the following figure shows the HS fitting for Constelium AA5000 test results,

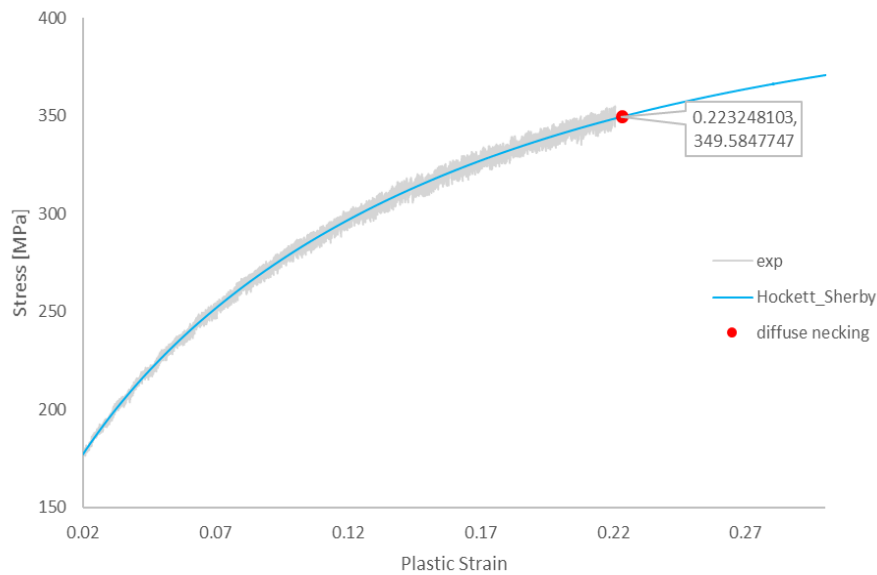


Figure 39 Hockett-Sherby hardening law, Constelium AA5000, zero degree roll angle, small strains

While for larger values of strain,

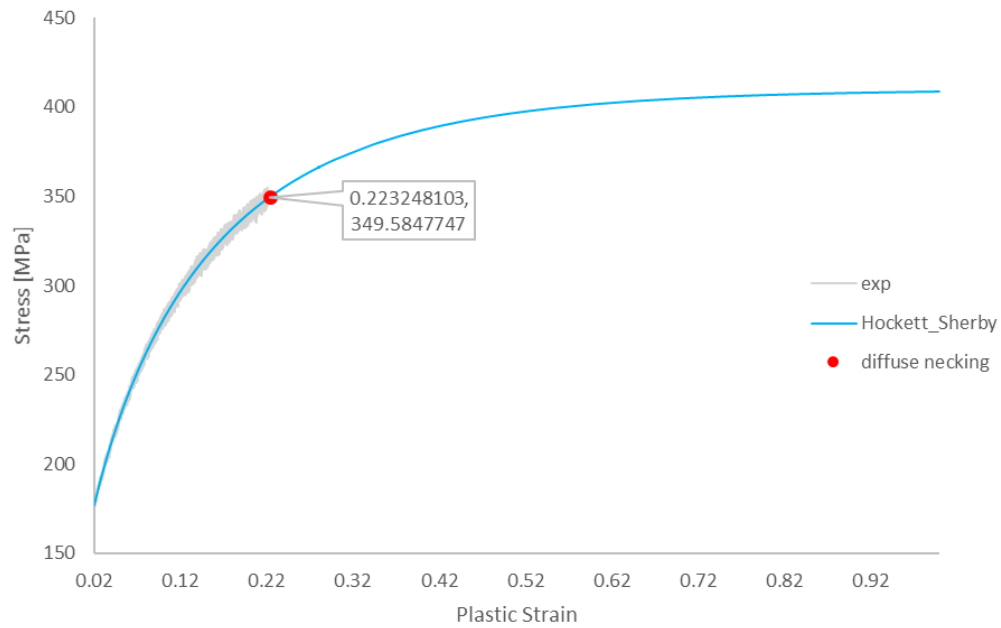


Figure 40 Hockett-Sherby hardening law, Constelium AA5000, zero degree roll angle, large strains

Within the experimental range, Hockett-Sherby estimates the material behaviour quite good, although complementary tests are needed to see its efficiency for larger values of plastic strain (above 20%).

- **Swift/Hockett-Sherby hardening law**

With regard to the Swift/Hockett-Sherby hardening law,

$$\sigma_{\text{Swift/Hockett-Sherby}} = (1 - \alpha) \sigma_{\text{Swift}} + \alpha \sigma_{\text{Hockett-Sherby}}$$

Figure below shows the influence of α on the behaviour of the SHS fitting upon experimental data, both for small and large strains respectively,

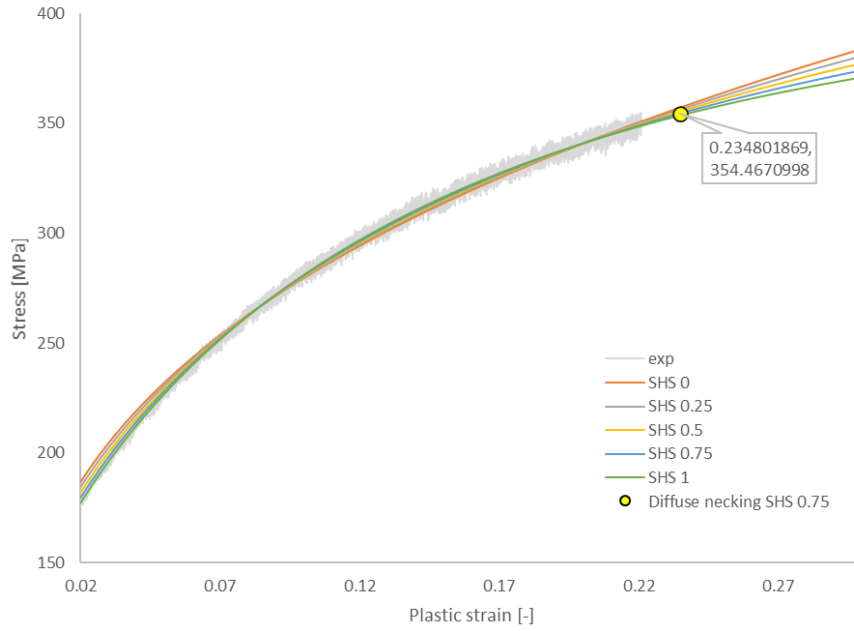


Figure 41 Swift/Hockett-Sherby hardening law, Constelium AA5000, zero degree roll angle, small strains

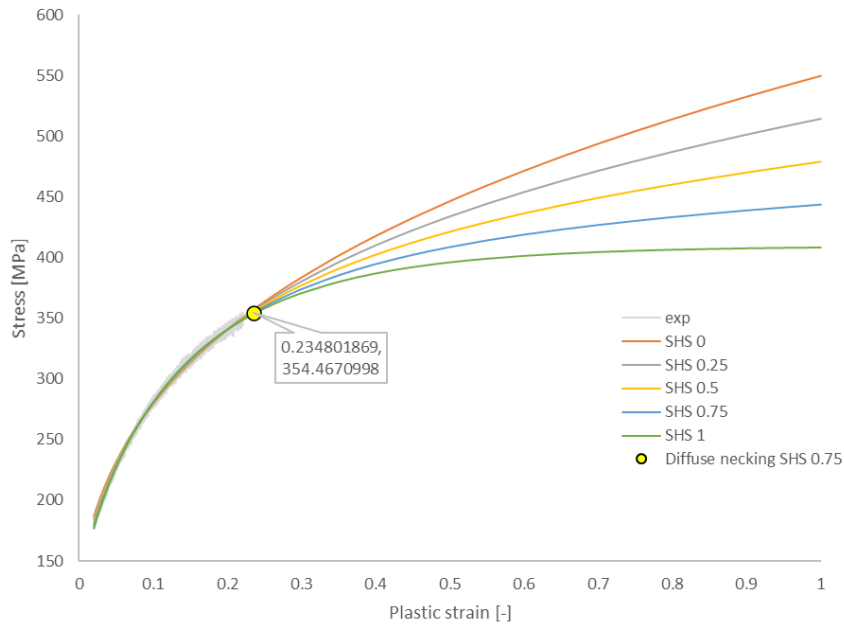


Figure 42 Swift/Hockett-Sherby hardening law, Constelium AA5000, zero degree roll angle, small strains

Following table reports RMSE for different values of α , where for $\alpha = 0.75$ the best fitting to the experimental flow curve in the range of small strains can be obtained,

	SHS 0.25	SHS 0.5	SHS 0.75
RMSE	3.685	2.987	2.478

Figure 43 goodness of fits: Swift/Hockett-Sherby law for Constelium AA5000

Reducing the number of data points is also applied here; in this way, one can import the data into AutoForm software for further FEA of a body part made of Constelium AA5000,

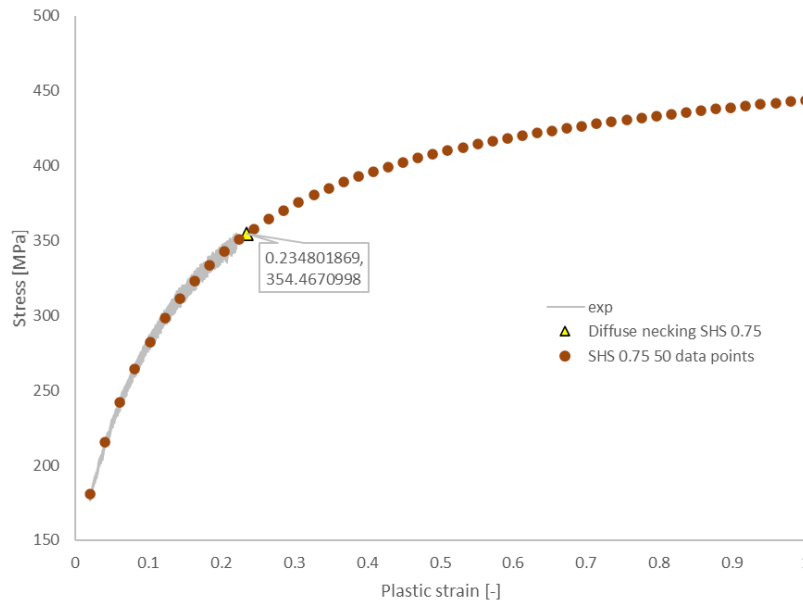


Figure 4450 data points imported into FEA from Swift/Hockett-Sherby law for Constelium AA5000

No.	True Plastic Strain	SHS 0.75 stress	No.	True Plastic Strain	SHS 0.75 stress
1	0.000	125.1458	26	0.510	410.0292
2	0.020	180.6641	27	0.531	412.2929
3	0.041	215.4578	28	0.551	414.4248
4	0.061	242.3047	29	0.571	416.4379
5	0.082	264.1593	30	0.592	418.3435
6	0.102	282.4521	31	0.612	420.1516
7	0.122	298.038	32	0.633	421.8714
8	0.143	311.4875	33	0.653	423.5106
9	0.163	323.2078	34	0.673	425.0764
10	0.184	333.5032	35	0.694	426.5753
11	0.204	342.608	36	0.714	428.0128
12	0.224	350.7076	37	0.735	429.3942
13	0.245	357.9509	38	0.755	430.7239
14	0.265	364.4596	39	0.776	432.006
15	0.286	370.334	40	0.796	433.2444
16	0.306	375.6581	41	0.816	434.4424
17	0.327	380.5022	42	0.837	435.6029
18	0.347	384.926	43	0.857	436.7287
19	0.367	388.9806	44	0.878	437.8222
20	0.388	392.7094	45	0.898	438.8859
21	0.408	396.15	46	0.918	439.9216
22	0.429	399.3349	47	0.939	440.9312

23	0.449	402.2922	48	0.959	441.9164
24	0.469	405.0465	49	0.980	442.8788
25	0.490	407.6192	50	1.000	443.8198

Table 15 50 data points imported into FEA from Swift/Hockett-Sherby law for Constelium AA5000

- **Swift-Voce hardening law**

A linear relationship with factor α is considered in this hardening law. Although it is advised to use $\alpha = 0.25$ for aluminium alloys, RMSE values for different values of α ($\alpha = 0.25, 0.5$ and 0.75) are compared to observe whether the prescribed value of α is valid here or not.

$$\sigma_{\text{Swift-Voce}} = \alpha \sigma_{\text{Swift}} + (1 - \alpha) \sigma_{\text{Voce}}$$

The following figures show the flow curves for small and large values of strain, respectively,

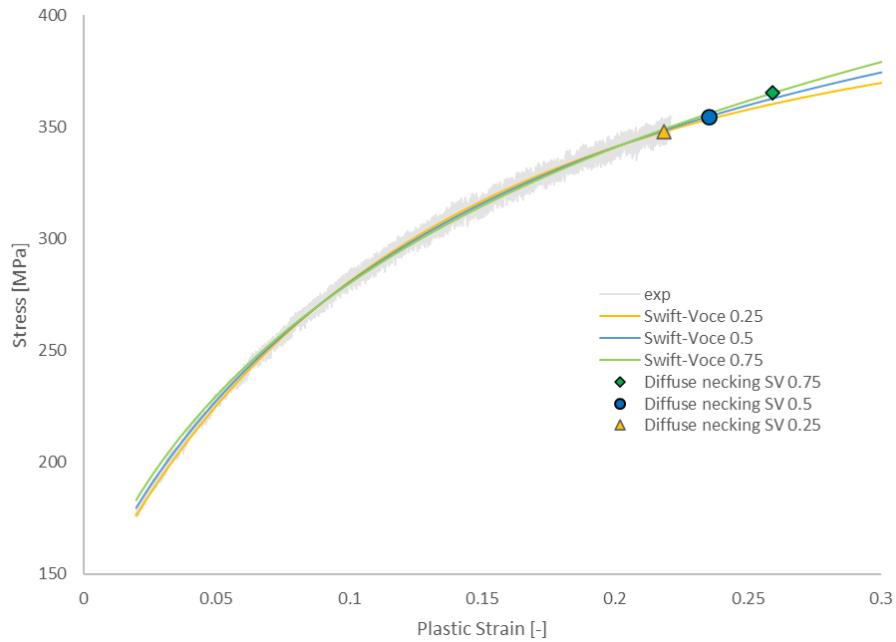


Figure 45 Swift-Voce hardening law, Constelium AA5000, zero degree roll angle, small strains

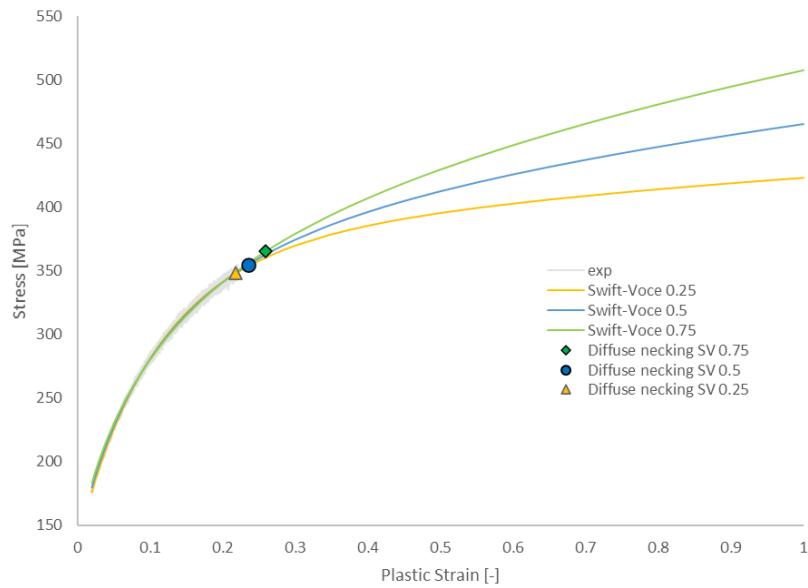


Figure 46 Swift-Voce hardening law, Constelium AA5000, zero degree roll angle, large strains

The goodness of the fit is reported in the following table with respect to the corresponding RMSEs,

	<i>SV 0.25</i>	<i>SV 0.5</i>	<i>SV 0.75</i>
RMSE	2.542	2.492	3.201

Table 16 goodness of fits: Swift-Voce law for Constelium AA5000, zero degree roll angle

As it can be found from the table, within the experimental range, lowest RMSE belongs to $\alpha = 0.5$. In the following sections, both $\alpha = 0.25$ and $\alpha = 0.5$ will be considered for Swift-Voce hardening law.

- ***Comparing Swift/Hockett-Sherby and Swift-Voce hardening laws for Constelium AA5000, zero degree roll angle***

The following figures demonstrate the behaviour of SHS and SV hardening laws when they are applied to Constelium AA5000. Within the range of small strains,

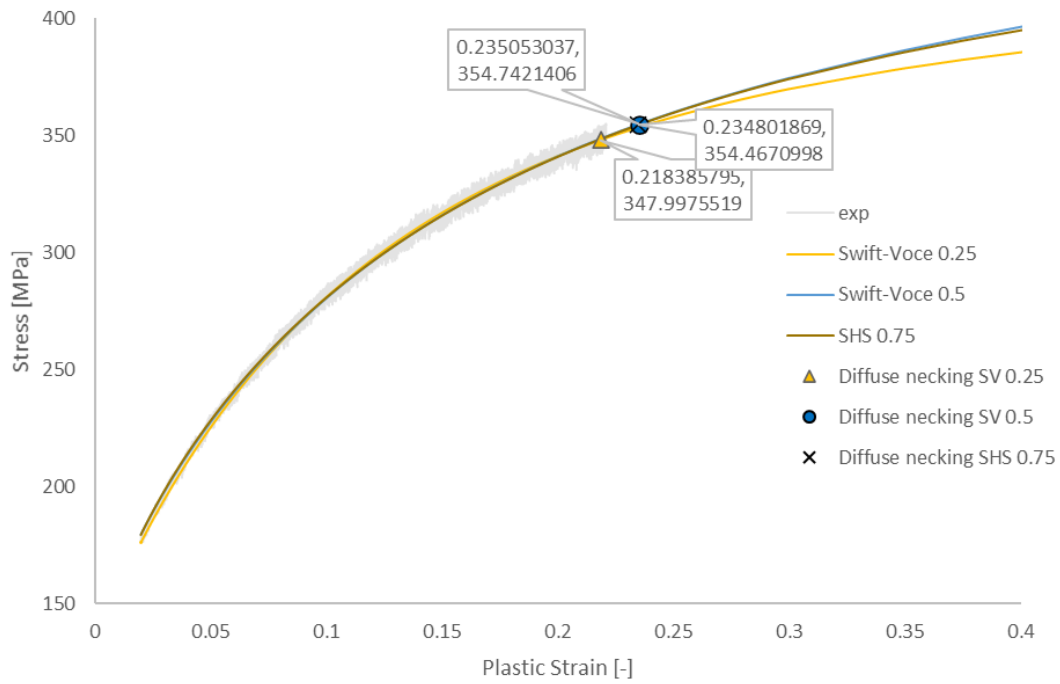


Figure 47 Swift-Voce vs Swift/Hockett-Sherby for small strains-Constelium AA5000, zero degree roll angle

And for the larger values of plastic strain,

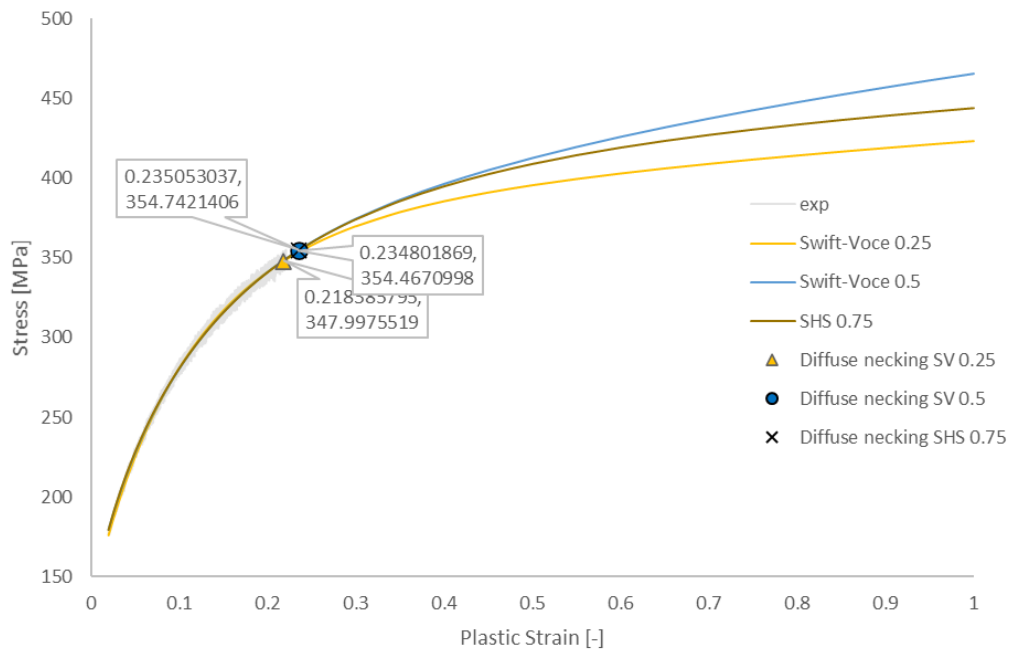


Figure 48 Swift-Voce vs Swift/Hockett-Sherby for large strains-Constelium AA5000

	<i>SV 0.25</i>	<i>SV 0.5</i>	<i>SHS 0.75</i>
<i>RMSE</i>	2.542	2.492	2.478

Table 17 goodness of fits: Swift-Voce vs SHS-Constelium AA5000, zero degree roll angle

3.3.2.2 45° roll angle

- **Swift/Hockett-Sherby hardening law**

Applying combined Swift/Hockett-Sherby hardening law, the following flow curve will be approximated for the given test data of Constelium AA5000 at 45° roll angle,

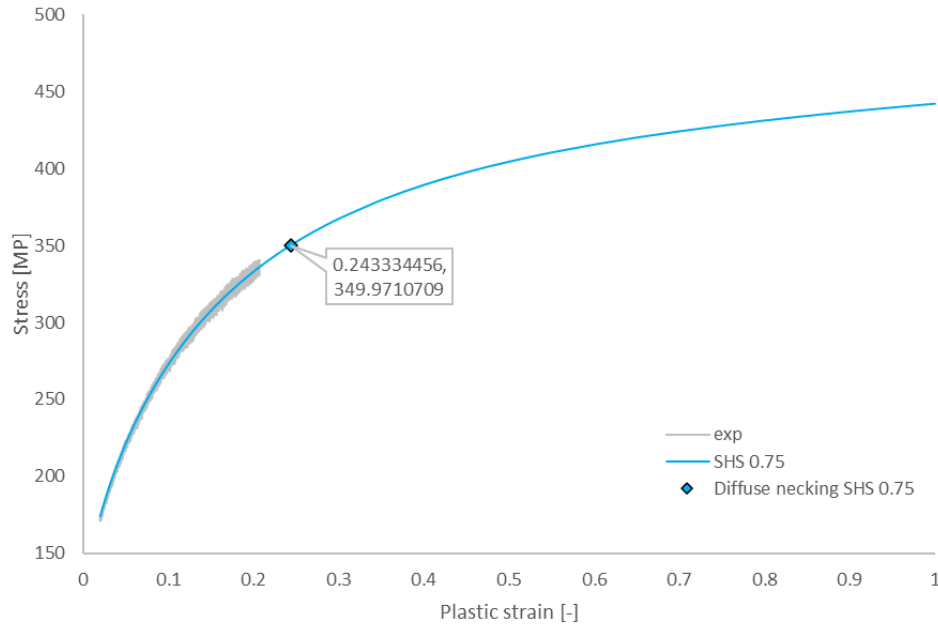


Figure 49 Swift/Hockett-Sherby hardening law, Constelium AA5000, 45° roll angle

- **Swift-Voce hardening law**

Considering Swift-Voce hardening law, increasing α will reduce the tendency towards the stress saturation, while it deteriorates diffuse necking approximation, which could be anticipated a priori. Looking at the following table, RMSE is evaluated to be at its minimum when α is equal to 0.5; meaning that with this value of α , Swift-Voce is a better option for small values of strain, i.e. in the range of tensile test data.

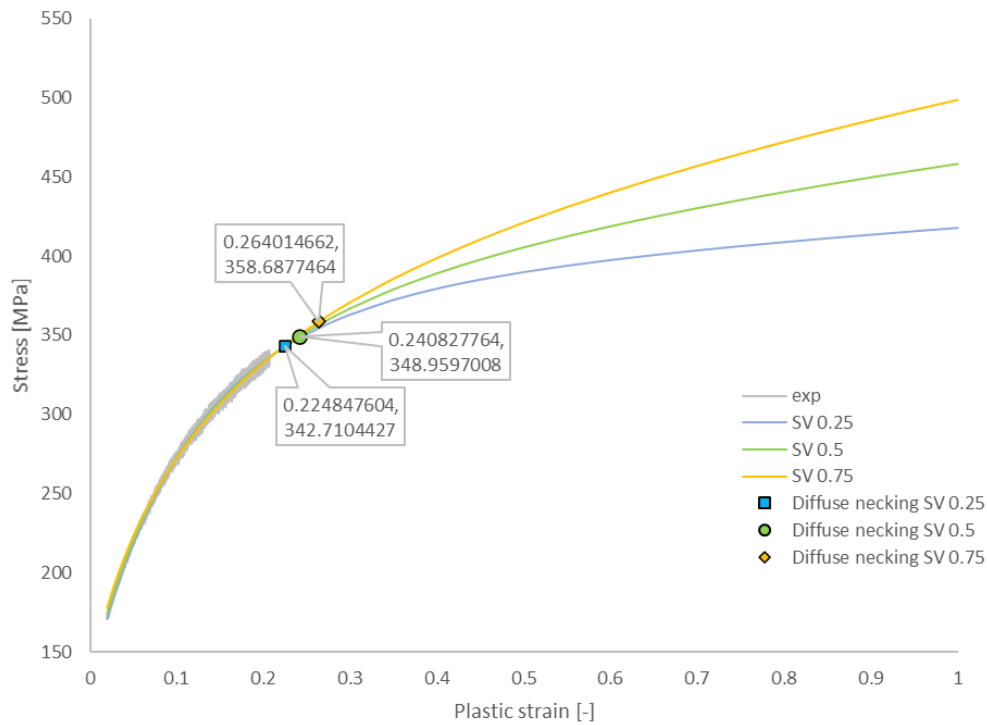


Figure 50 Swift-Voce hardening law, Constelium AA5000, 45° roll angle

	<i>SV 0.25</i>	<i>SV 0.5</i>	<i>SV 0.75</i>
RMSE	2.431	2.376	3.209

Table 18 goodness of fits: Swift-Voce law for Constelium AA5000, 45 degree roll angle

- **Comparing Swift/Hockett-Sherby and Swift-Voce hardening laws for Constelium AA5000, 45 degree roll angle**

The following figures illustrate the behaviour of SHS and SV hardening laws when they are applied to a Constelium AA5000 specimen cut at 45 degree roll angle,

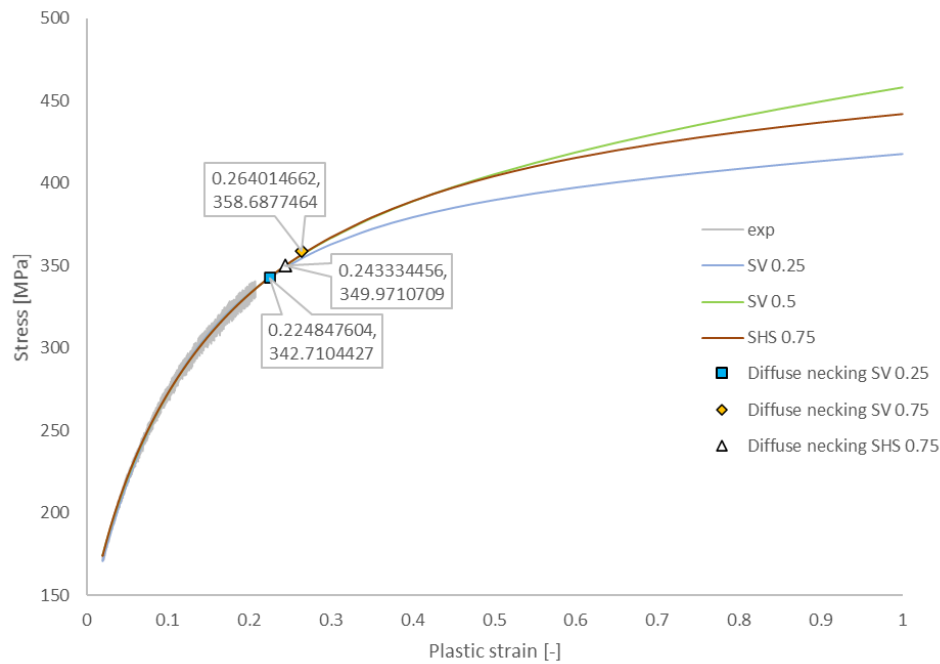


Figure 51 Swift-Voce vs Swift/Hockett-Sherby-Constelium AA5000, 45 degree roll angle

	SHS 0.75	SV 0.25	SV 0.5
RMSE	2.445	2.431	2.376

Table 19 goodness of fits: Swift-Voce vs SHS-Constelium AA5000, 45 degree roll angle

In order to find a hardening law that suits the most, it is needed to rely on complementary tests such as Bulge test, as it provides us with test data in a wider range of strain in comparison with tensile test.

3.3.2.3 90° roll angle

- **Swift/Hockett-Sherby hardening law**

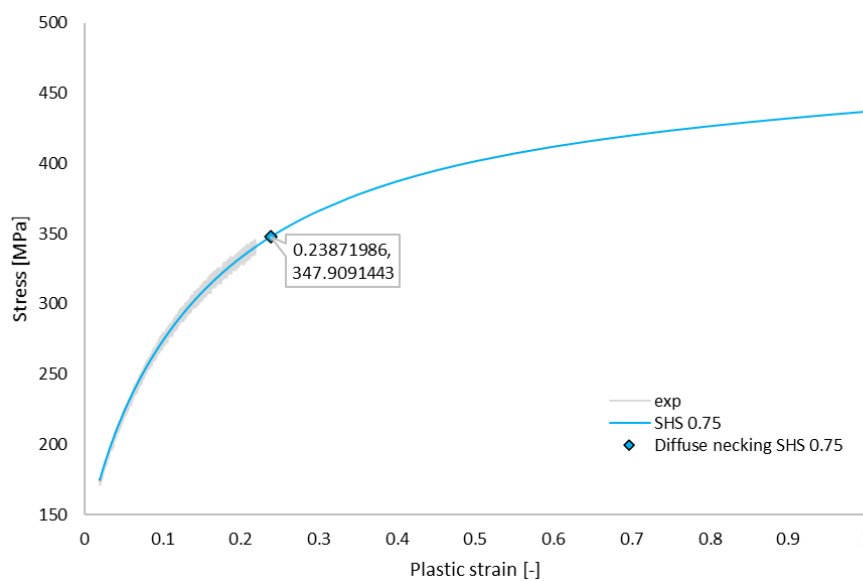


Figure 52 Swift/Hockett-Sherby hardening law, Constelium AA5000, 90° roll angle

- **Swift-Voce hardening law**

Throwing light on the Swift-Voce flow curve shows that for $\alpha = 0.25$, RMSE value is the lowest, coming with better approximation for diffuse necking,

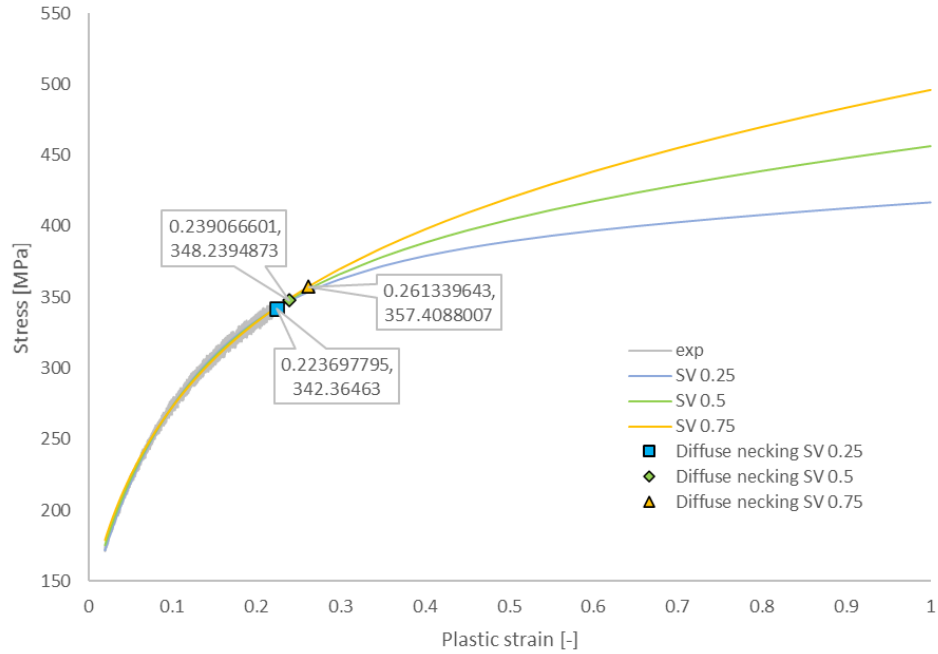


Figure 53 Swift-Voce hardening law, Constelium AA5000, 90° roll angle

	SV 0.25	SV 0.5	SV 0.75
RMSE	2.428	2.448	3.303

Table 20 goodness of fits: Swift-Voce law for Constelium AA5000, 90° roll angle

- **Comparing Swift/Hockett-Sherby with Swift-Voce for Constelium AA5000, 90° roll angle**

The following figure illustrates the behaviour of SHS and SV hardening laws when they are applied to a Constelium AA5000 specimen cut at 90 degree roll angle,

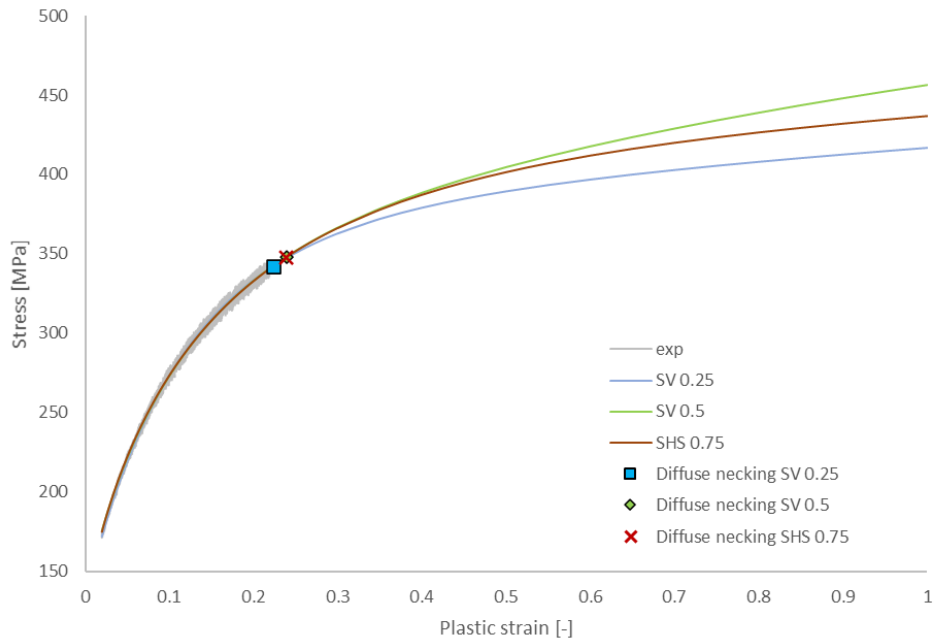


Figure 54 Swift-Voce vs Swift/Hockett-Sherby-Constelium AA5000, 90° roll angle

	<i>SHS 0.75</i>	<i>SV 0.25</i>	<i>SV 0.5</i>
RMS	2.482	2.428	2.448

Table 21 goodness of fits: Swift-Voce vs SHS-Constelium AA5000, 90° roll angle

3.3.2.4 Summary table of Constelium AA5000

Material constants and RMSE values for Constelium AA5000 are reported in the next table,

	Law	<i>A</i>	<i>B</i>	<i>m</i>	<i>c</i>	<i>C</i>	ϵ_0	<i>n</i>	<i>K</i> ₀	<i>Q</i>	β	RMSE
0°	HS	409.695	286.473	5.443	0.832	-	-	-	-	-	-	2.627
	SHS					548.427	0.009	0.304	-	-	-	4.309
	SV								130.919	249.987	9.207	2.492*
45°	HS	411.937	293.377	4.879	0.814	-	-	-	-	-	-	2.248
	SHS					537.435	0.009	0.307	-	-	-	2.445
	SV	-	-	-	-				127.945	249.499	8.713	2.376*
90°	HS	405.488	285.007	5.209	0.829	-	-	-	-	-	-	2.279
	SHS					534.066	0.009	0.303	-	-	-	2.482
	SV	-	-	-	-				129.07	248.216	8.728	2.428*

*lowest is written amongst different values of α .

3.3.3 Constelium AA6000 tensile test results

Considering the data sheet provided by the Constelium on AA6000, flow curve from Hockett-Sherby hardening law will be evaluated. Then, Swift-Voce law will be presented to make a comparison with the curve of Hockett-Sherby.

<i>Material</i>	<i>Constelium AA6000</i>
<i>E</i> <i>[MPa]</i>	66554
<i>Average</i> <i>Thickness[mm]</i>	0.916

	<i>True Rupture Stress</i> <i>[MPa]</i>	<i>A_g</i> <i>[%]</i>	<i>A₈₀</i> <i>[%]</i>	<i>n-Krupkowski</i>	<i>r -average</i> <i>(4%-A_g)</i>	<i>Yield stress</i> <i>[MPa]</i>	<i>R_m</i> <i>[MPa]</i>
<i>0°</i>	293.9	21.52	26.07	0.27122	0.723	126.6	242.1
<i>45°</i>	288.2	22.67	28.52	0.27124	0.61	122.5	235.1
<i>90°</i>	288.3	22.40	28.53	0.27365	0.665	122.6	235.7

Table 22 mechanical properties of Constelium AA6000

3.3.3.1 Zero degree roll angle

- *Hockett-Sherby hardening law*

Having in mind the diffuse necking criterion, the following relation describes material constant A as a function of the other constants in Hockett-Sherby hardening law,

$$A = B \exp(-m\varphi_{diffuse}^c) [1 + m\varphi_{diffuse}^{c-1}]$$

This data set (Constelium AA6000) has a much smoother behaviour than the previous ones; as a result, the Hockett-Sherby approximation shows a very low amount of RMSE of 0.16826, which means the fitting is quite close to the experimental values in the range of given data.

Figure below shows the result in the range of small values of strain,

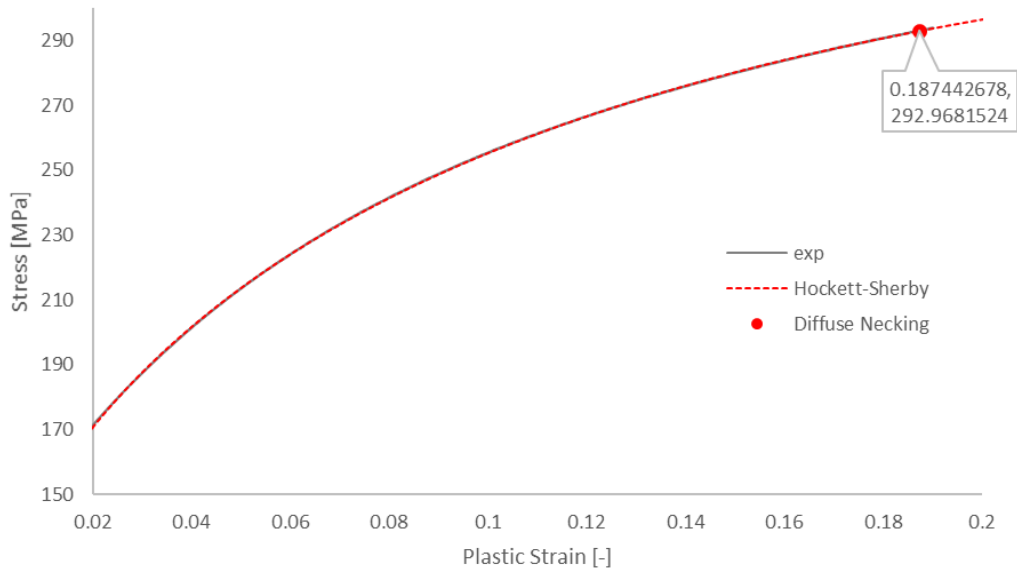


Figure 55 Hockett-Sherby hardening law, Constelium AA6000, zero degree roll angle, small strains

Diffuse necking is anticipated at 18.74% of true plastic strain, while according to the data sheet, it is predicted to take place at 19.03% true plastic strain.

For larger values of strain,

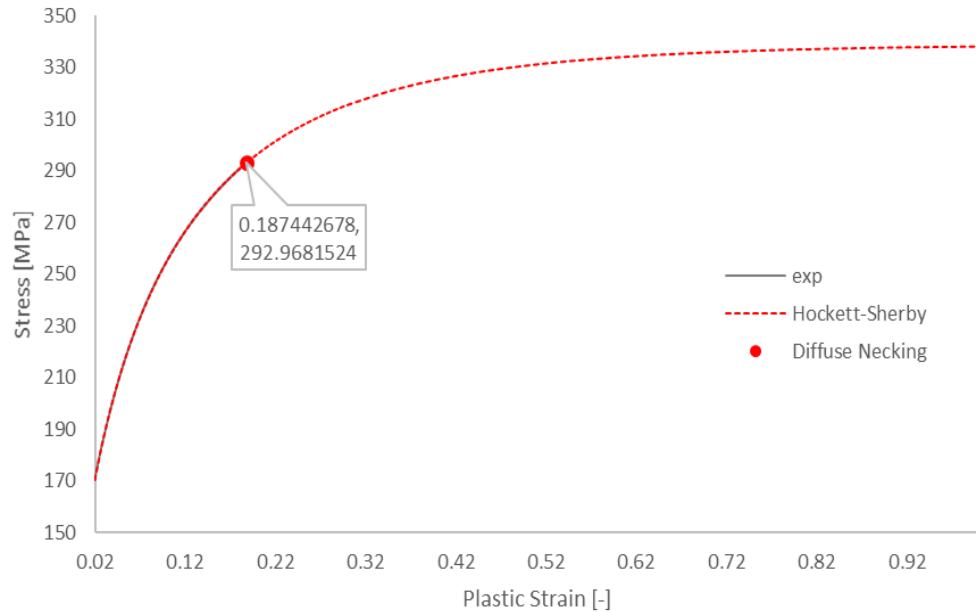


Figure 56 Hockett-Sherby hardening law, Constelium AA6000, zero degree roll angle, large strains

- **Swift/Hockett-Sherby hardening law**

Remembering SHS hardening law relation,

$$\sigma_{\text{Swift/Hockett-Sherby}} = (1 - \alpha) \sigma_{\text{Swift}} + \alpha \sigma_{\text{Hockett-Sherby}}$$

The influence of α on the behaviour of the SHS flow curve fitting is shown in the following figure, both for small and large strains respectively,

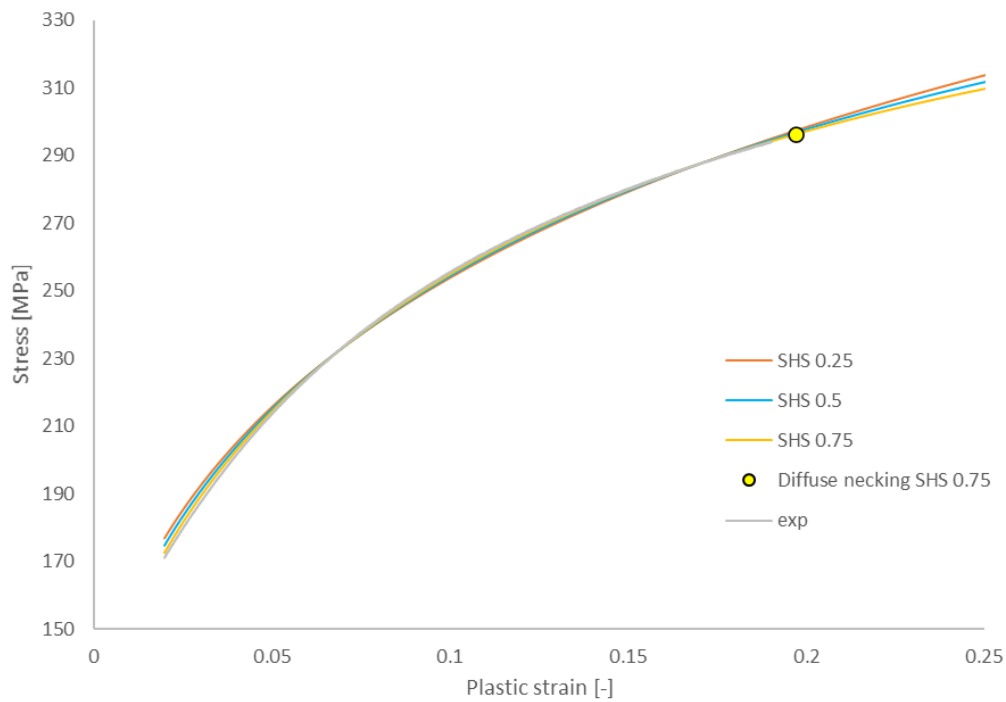


Figure 57 Swift/Hockett-Sherby hardening law, Constelium AA6000, zero degree roll angle, small strains

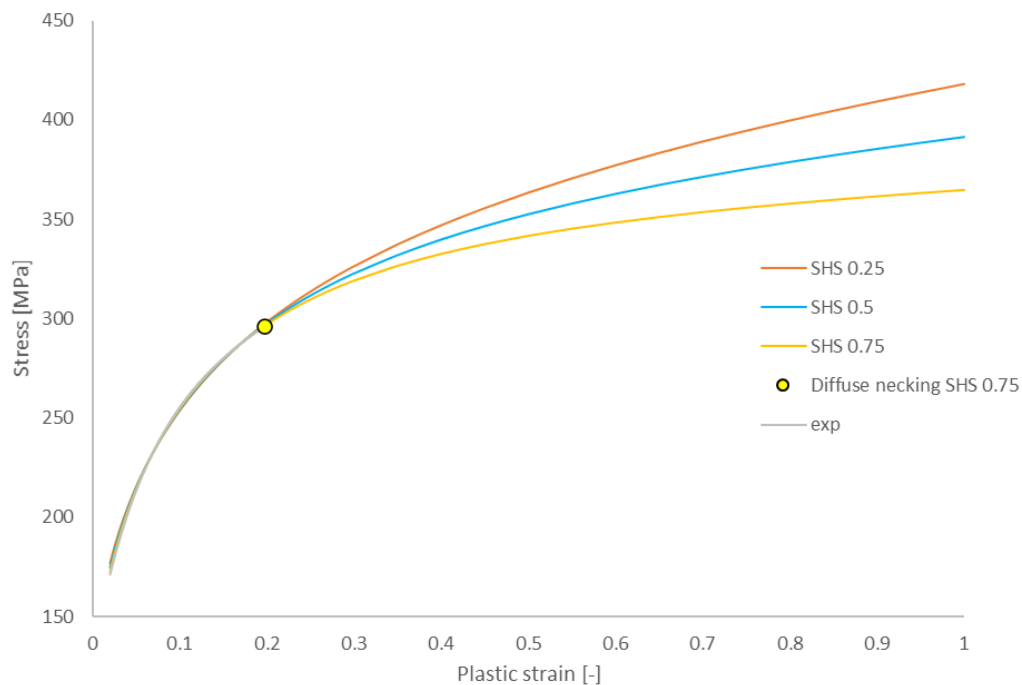


Figure 58 Swift/Hockett-Sherby hardening law, Constelium AA6000, zero degree roll angle, large strains

	<i>SHS 0.25</i>	<i>SHS 0.5</i>	<i>SHS 0.75</i>
<i>RMSE</i>	2.152	1.446	0.747

Table 23 goodness of fits: Swift/Hockett-Sherby law for Constelium AA6000, zero degree roll angle

As it is obvious, SHS 0.75 shows the best fit withing tensile test data range, so by extracting 50 data points to be used in FEA SW,

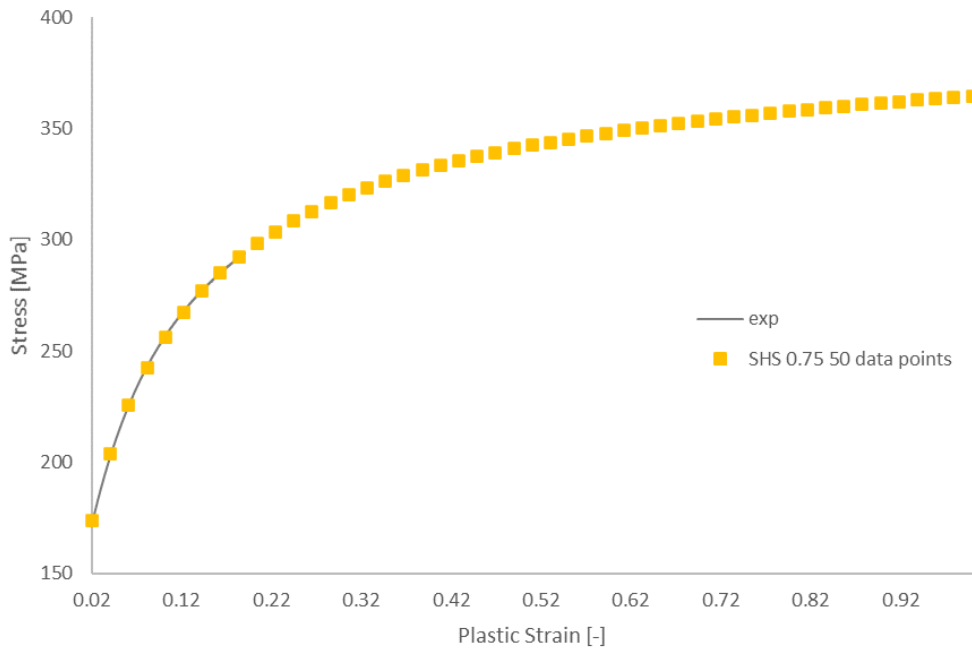


Figure 59 50 data points imported into FEA from Swift/Hockett-Sherby law for Constelium AA6000

No.	True Plastic Strain	HS stress	No.	True Plastic Strain	HS stress
1	0.000	115.9808	26	0.510	342.4465
2	0.020	173.6113	27	0.531	343.9209
3	0.041	203.7836	28	0.551	345.3117
4	0.061	225.5108	29	0.571	346.6272
5	0.082	242.3893	30	0.592	347.8745
6	0.102	256.0289	31	0.612	349.0602
7	0.122	267.3326	32	0.633	350.1897
8	0.143	276.8709	33	0.653	351.2682
9	0.163	285.0317	34	0.673	352.3
10	0.184	292.0926	35	0.694	353.2891
11	0.204	298.2592	36	0.714	354.2391
12	0.224	303.6884	37	0.735	355.1532
13	0.245	308.5027	38	0.755	356.0341
14	0.265	312.7988	39	0.776	356.8845
15	0.286	316.6548	40	0.796	357.7066
16	0.306	320.1344	41	0.816	358.5026
17	0.327	323.2899	42	0.837	359.2742
18	0.347	326.1646	43	0.857	360.0232
19	0.367	328.795	44	0.878	360.7512
20	0.388	331.2117	45	0.898	361.4594
21	0.408	333.4407	46	0.918	362.1493
22	0.429	335.5042	47	0.939	362.8219
23	0.449	337.4212	48	0.959	363.4783
24	0.469	339.2082	49	0.980	364.1196
25	0.490	340.8791	50	1.000	364.7465

Table 24 50 data points imported into FEA from Swift/Hockett-Sherby law for Constelium AA6000

- **Swift-Voce hardening law**

Swift-Voce hardening law defining by the following relation, with $\alpha = 0.75$, will be applied to Constelium AA6000 data set,

$$\sigma_{\text{Swift-Voce}} = \alpha \sigma_{\text{Swift}} + (1 - \alpha) \sigma_{\text{Voce}}$$

The following figures show the flow curves for small and large values of strain, respectively. Focusing on the true plastic strain range below 27%,

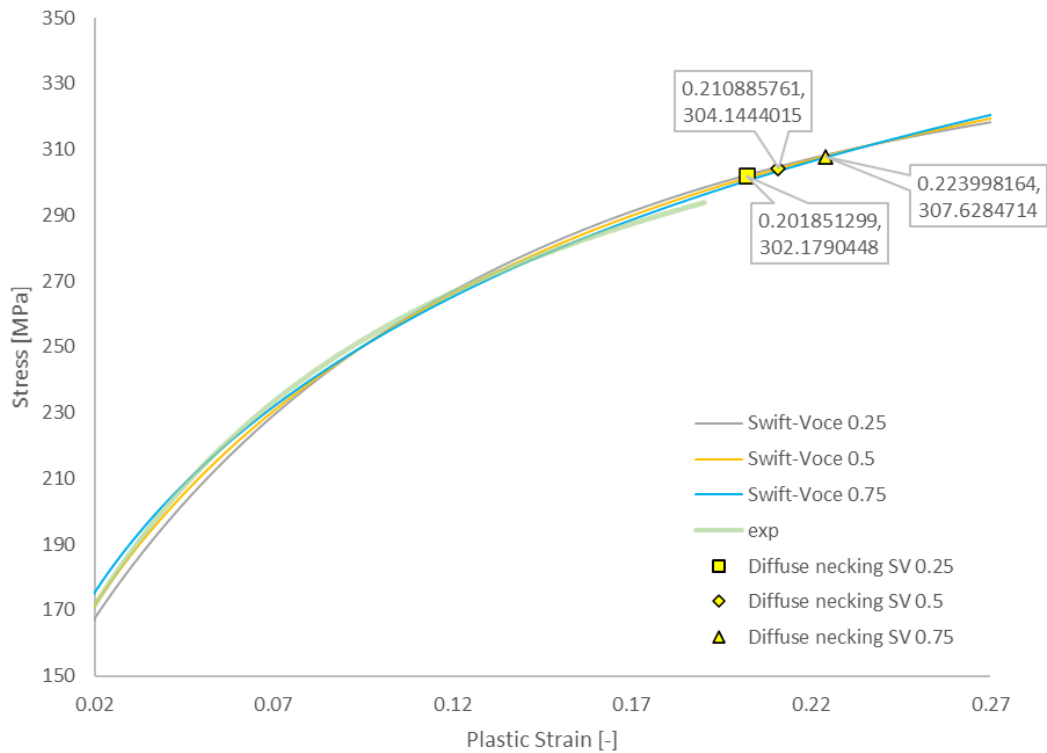


Figure 60 Swift-Voce hardening law, Constelium AA6000, zero degree roll angle, small strains

	SV 0.25	SV 0.5	SV 0.75
RMSE	3.508	2.022	1.646

Table 25 goodness of fits: Swift-Voce law for Constelium AA6000, zero degree roll angle

SV 0.75 shows the lowest error within tensile test data; in this section we also consider SV 0.25 to see the comparison between Swift/Hockett-Sherby,

Extending the strain range till 100% plastic strain,

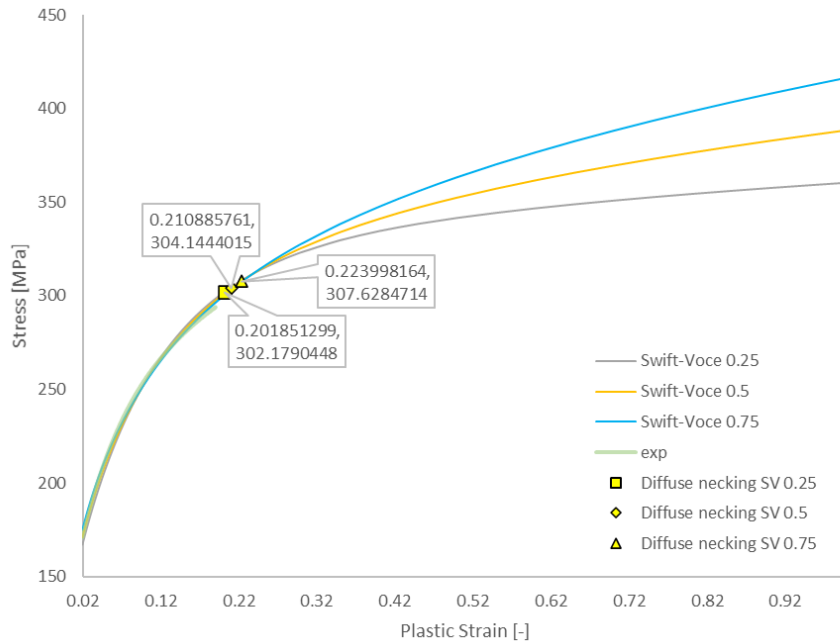


Figure 61 Swift-Voce hardening law, Constelium AA6000, zero degree roll angle, large strains

- **Comparing Swift/Hockett-Sherby with Swift-Voce hardening laws for Constelium AA6000 zero degree roll angle**

Comparing the two hardening laws, it is quite obvious that Swift/Hockett-Sherby is following the experimental flow curve of Constelium AA6000 with a very low amount of RMSE, while Swift-Voce has some deviations with respect to the experimental data,

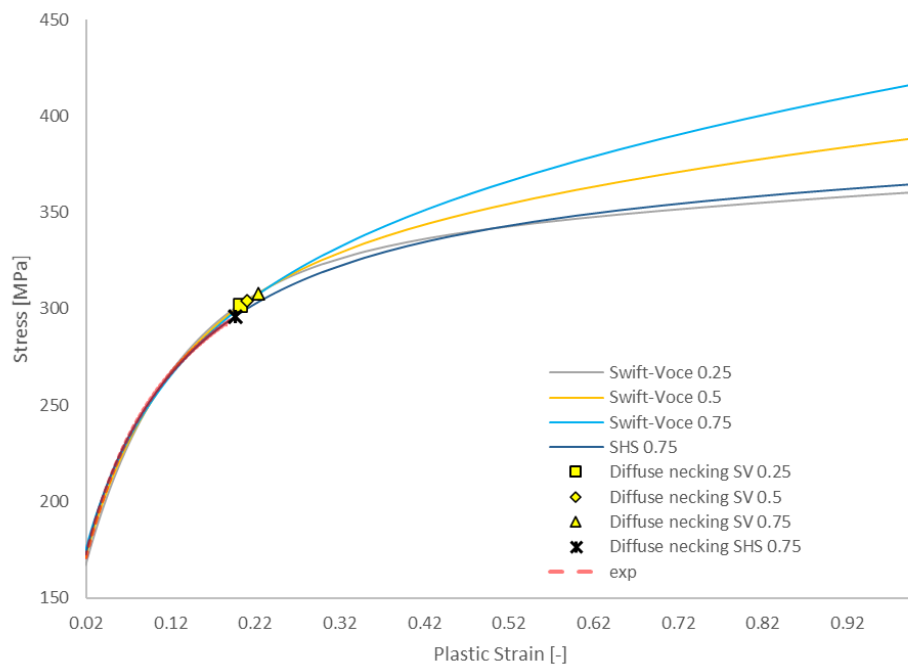


Figure 62 Swift-Voce vs Swift/Hockett-Sherby for small strains-Constelium AA6000, zero degree roll angle

	<i>SV 0.25</i>	<i>SV 0.75</i>	<i>SHS 0.75</i>
RMSE	3.508	1.646	0.747

Table 26 Swift-Voce vs SHS-Constelium AA6000, zero degree roll angle

- ***k*-exponent function**

κ -exponent function (which is employed as a phenomenological hardening law) is employed here in order to fit to the pre-necking data points. Here the nonlinear regression command of MATLAB (*lsqnonlin*) is used to have more control on the fitting parameters of this function. Then, the result will be compared with Hockett-Sherby law (as it will be seen that it has the lowest RMSE value of all).

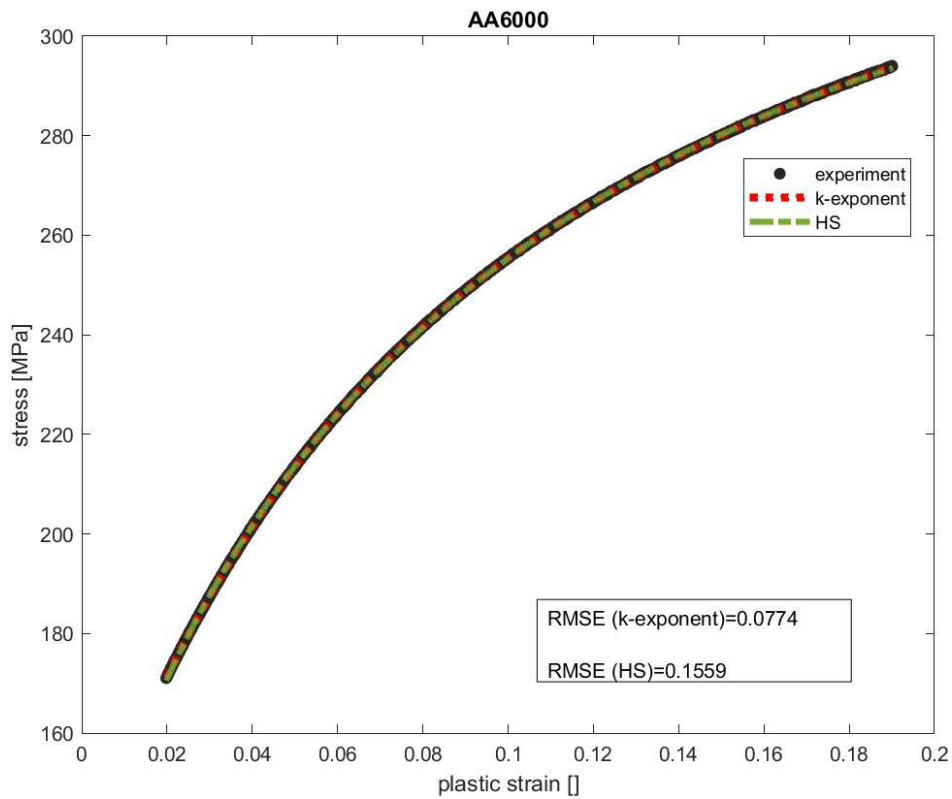


Figure 63 comparison between *k*-exponent function and HS hardening law for pre-necking flow stress curve fitting of AA6000, zero degree roll angle

3.3.3.2 45° roll angle

- **Swift/Hockett-Sherby hardening law**

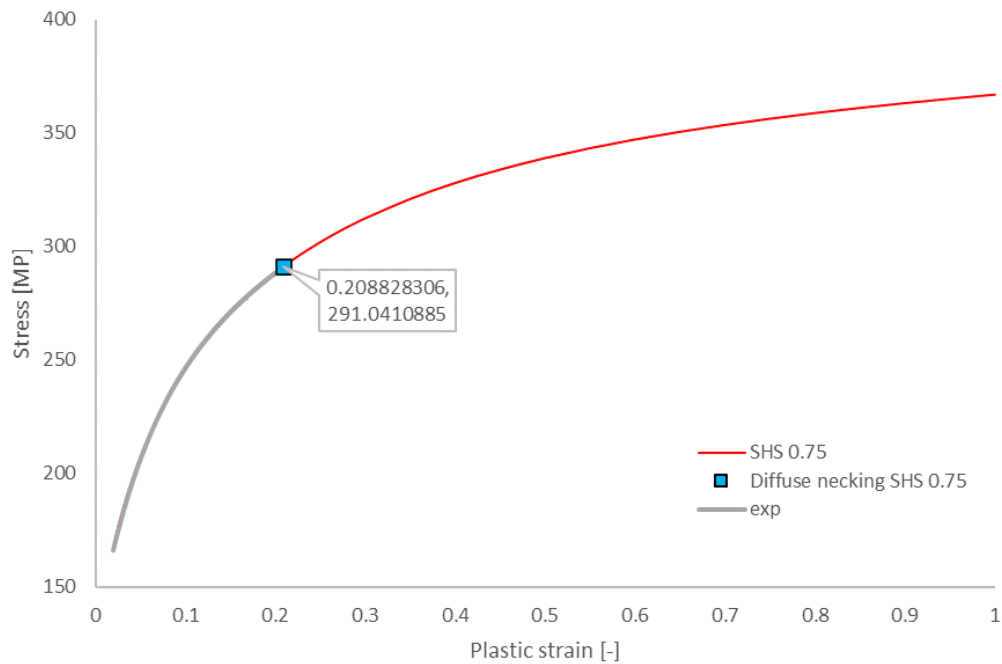


Figure 64 Swift/Hockett-Sherby hardening law, Constelium AA6000, 45° roll angle

- **Swift-Voce hardening law**

Within the range of small strain,

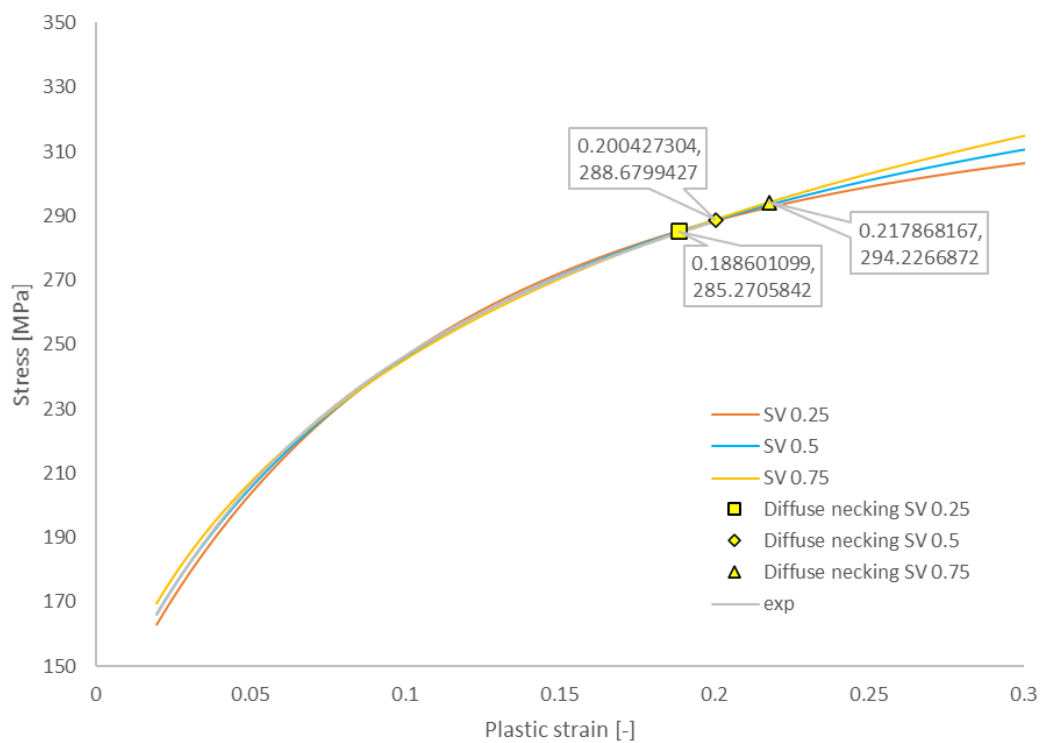


Figure 65 Swift-Voce hardening law, Constelium AA6000, 45° roll angle, small strain

Having a wider vision for the Swift-Voce law up to 100% plastic strain,

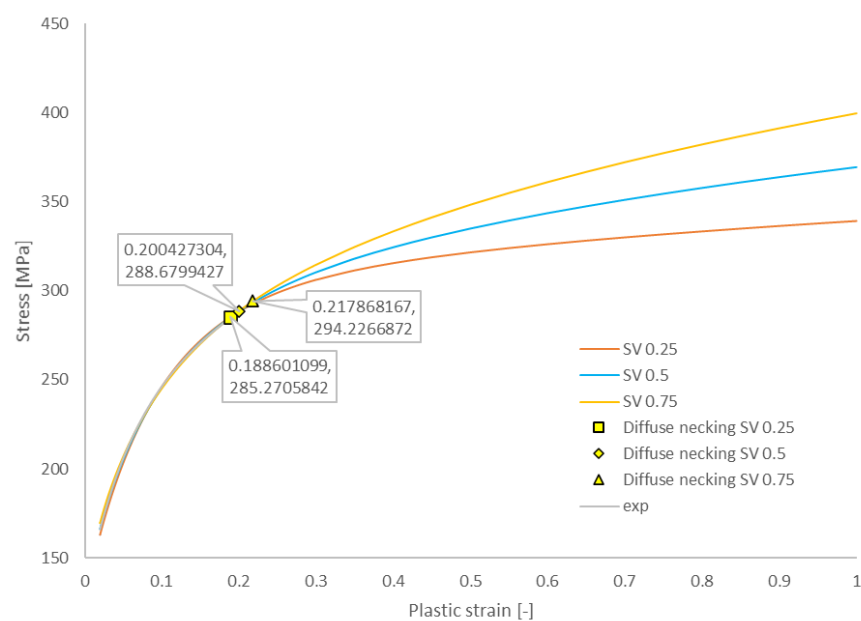


Figure 66 Swift-Voce hardening law, Constelium AA6000, 45° roll angle, large strain

	SV 0.25	SV 0.5	SV 0.75
RMS	1.638	0.561	1.253

Table 27 goodness of fits: Swift-Voce law for Constelium AA6000, 45° roll angle

- Comparing Swift/Hockett-Sherby with Swift-Voce hardening laws for Constelium AA6000 45° roll angle

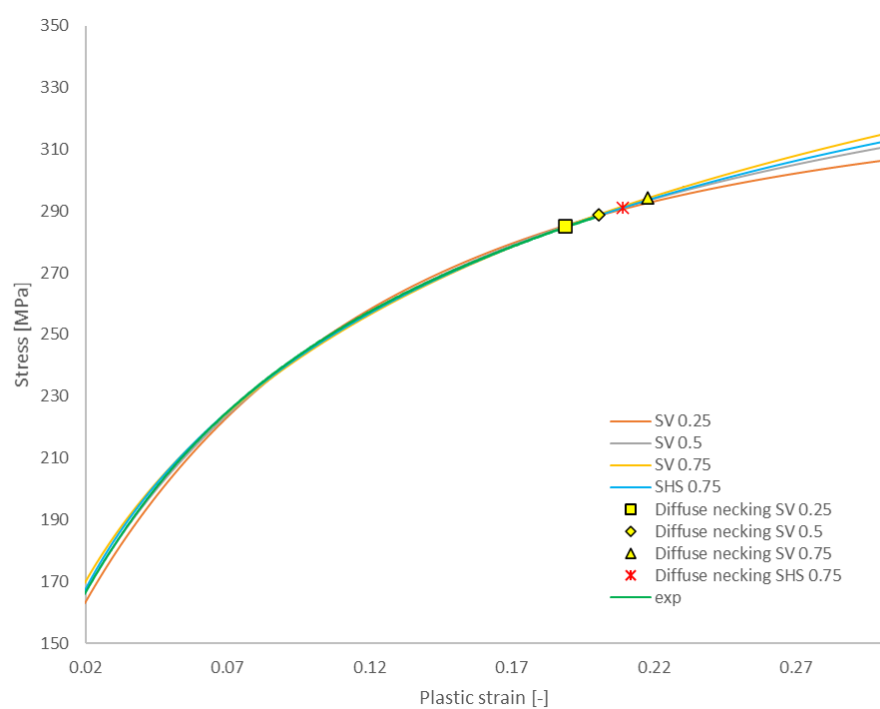


Figure 67 Swift-Voce vs Swift/Hockett-Sherby for small strains-Constelium AA6000, 45° roll angle

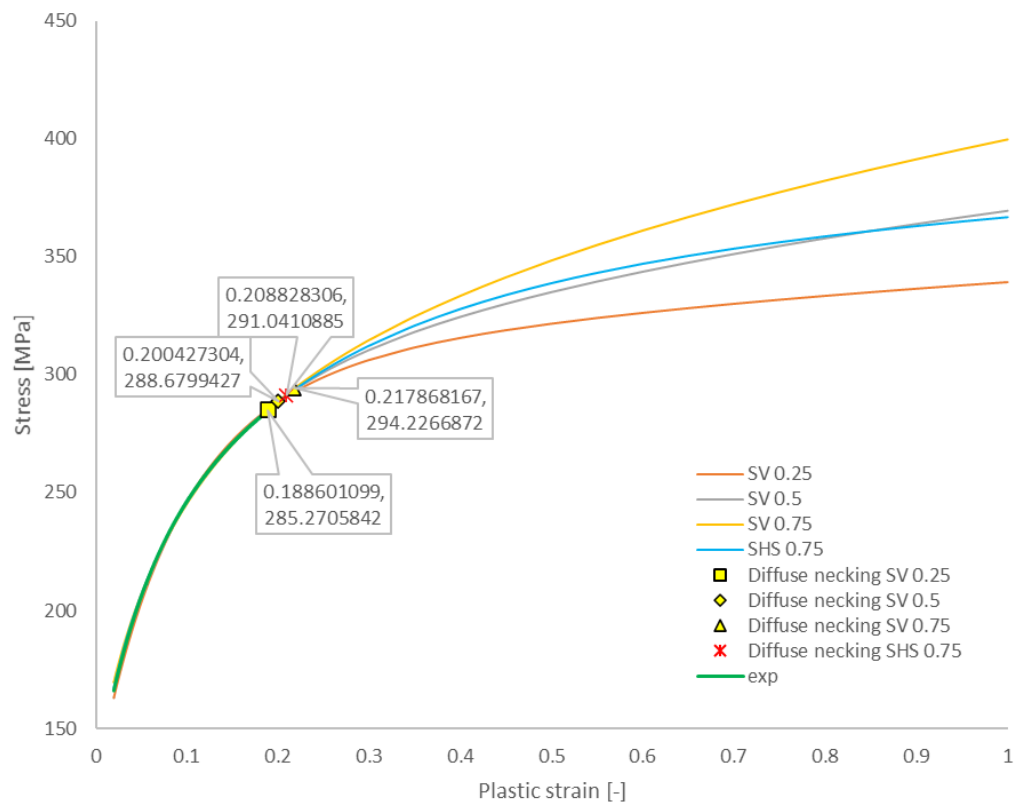


Figure 68 Swift-Voce vs Swift/Hockett-Sherby for large strains-Constelium AA6000, 45° roll angle

	SHS 0.75	SV 0.25	SV 0.5	SV 0.5
RMSE	0.689	1.638	0.561	1.253

Table 28 Swift-Voce vs SHS-Constelium AA6000, 45° roll angle

3.3.3.3 90° roll angle

- *Swift/Hockett-Sherby hardening law*

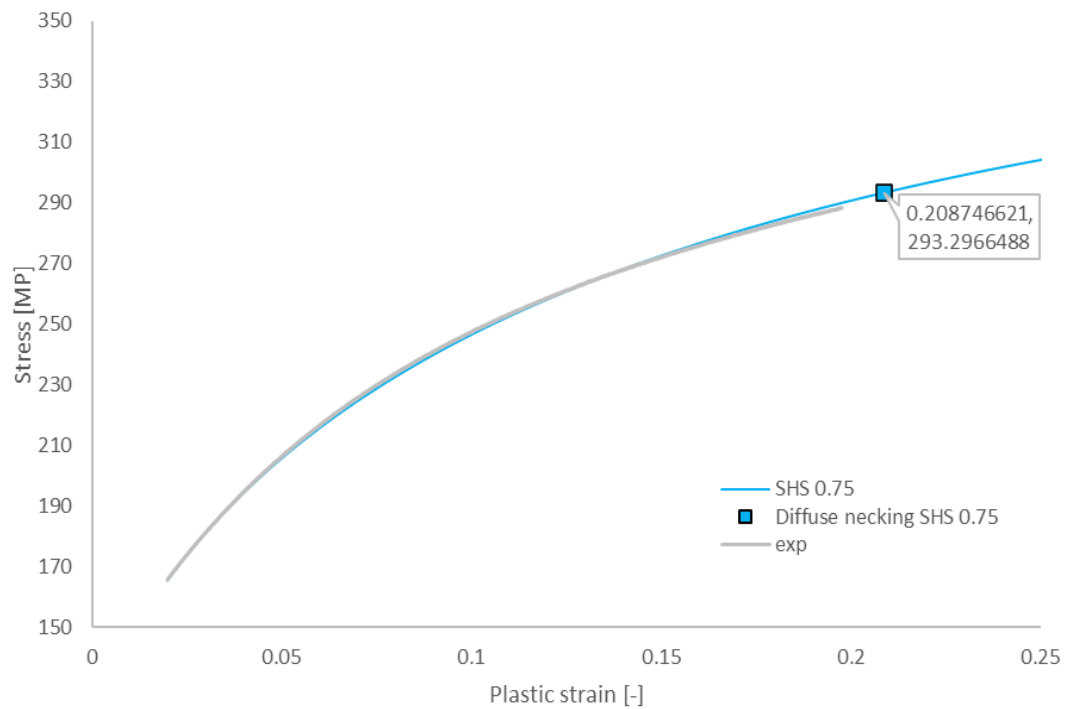


Figure 69 Swift/Hockett-Sherby hardening law, Constelium AA6000, 90° roll angle, small strains

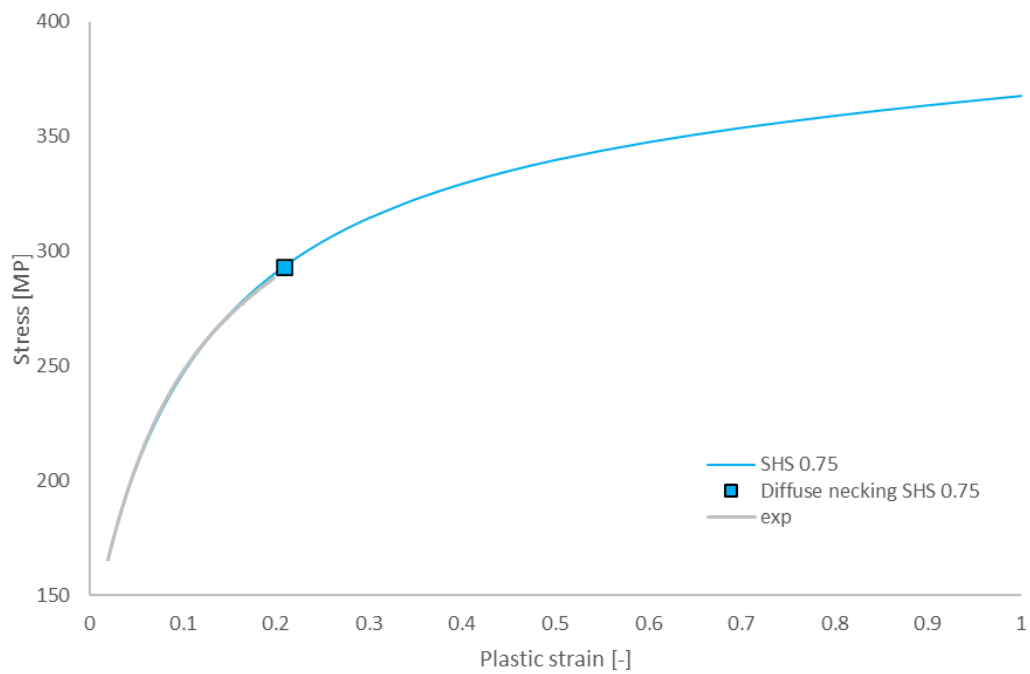


Figure 70 Swift/Hockett-Sherby hardening law, Constelium AA6000, 90° roll angle, large strains

- **Swift-Voce hardening law**

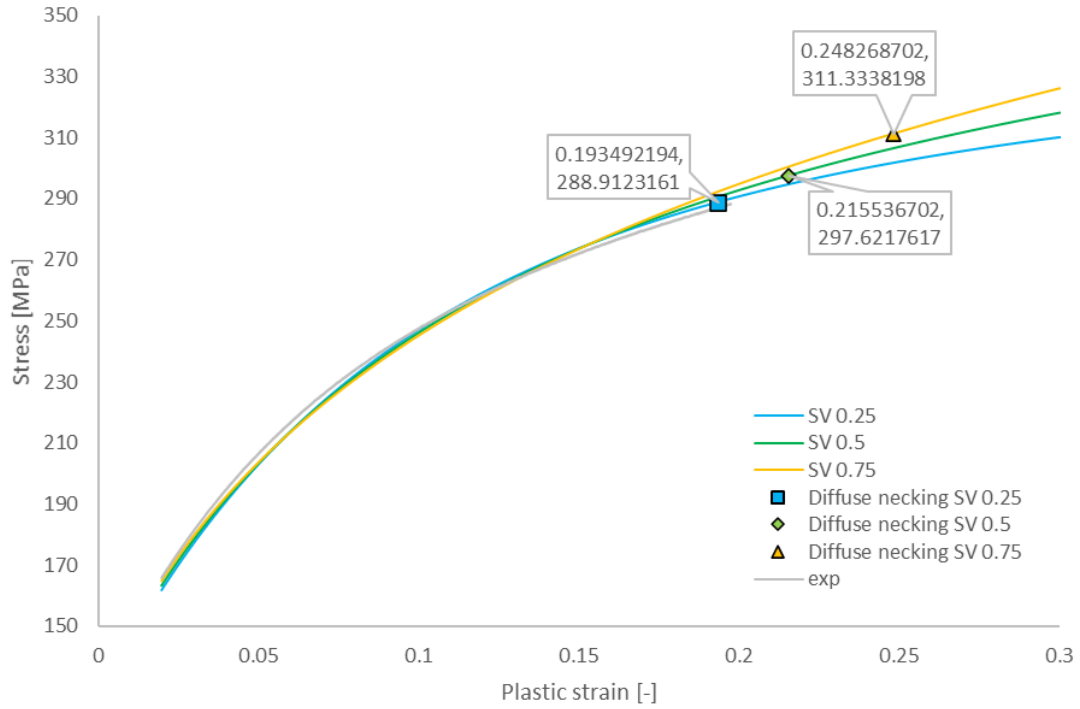


Figure 71 Swift-Voce hardening law, Constelium AA6000, 90° roll angle, small strains

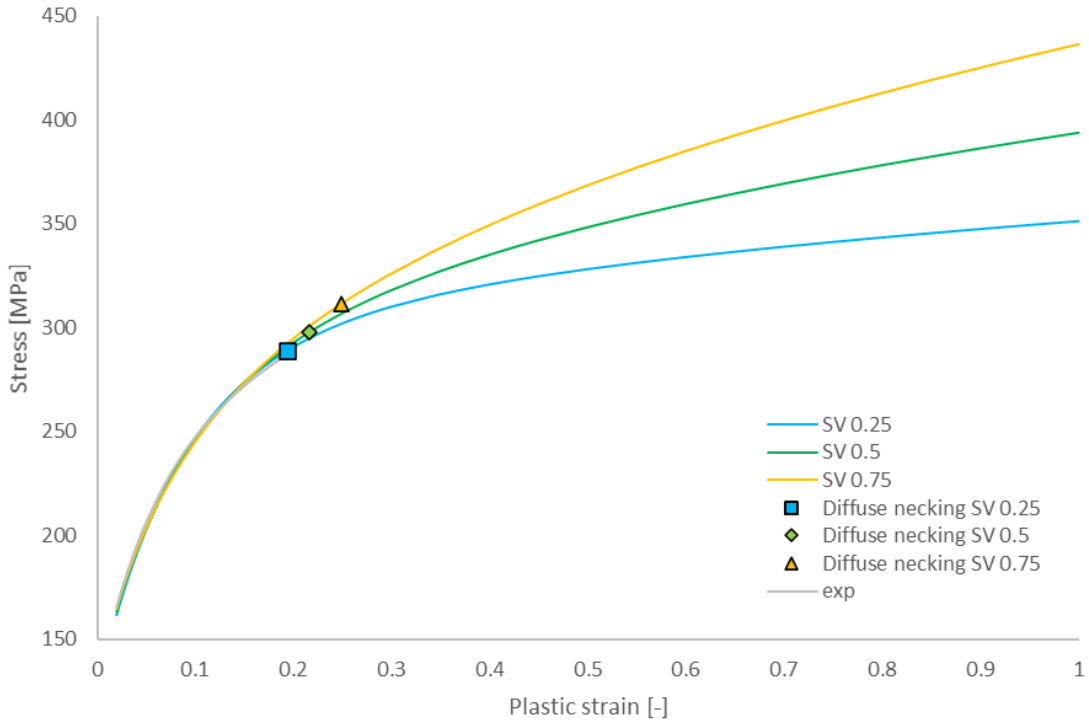


Figure 72 Swift-Voce hardening law, Constelium AA6000, 90° roll angle, large strains

	<i>SV 0.25</i>	<i>SV 0.5</i>	<i>SV 0.75</i>
RMSE	2.301	2.367	2.702

Table 29 goodness of fits: Swift-Voce law for Constelium AA6000, 90° roll angle

- **Comparing Swift/Hockett-Sherby with Swift-Voce hardening laws for Constelium AA6000 90° roll angle**

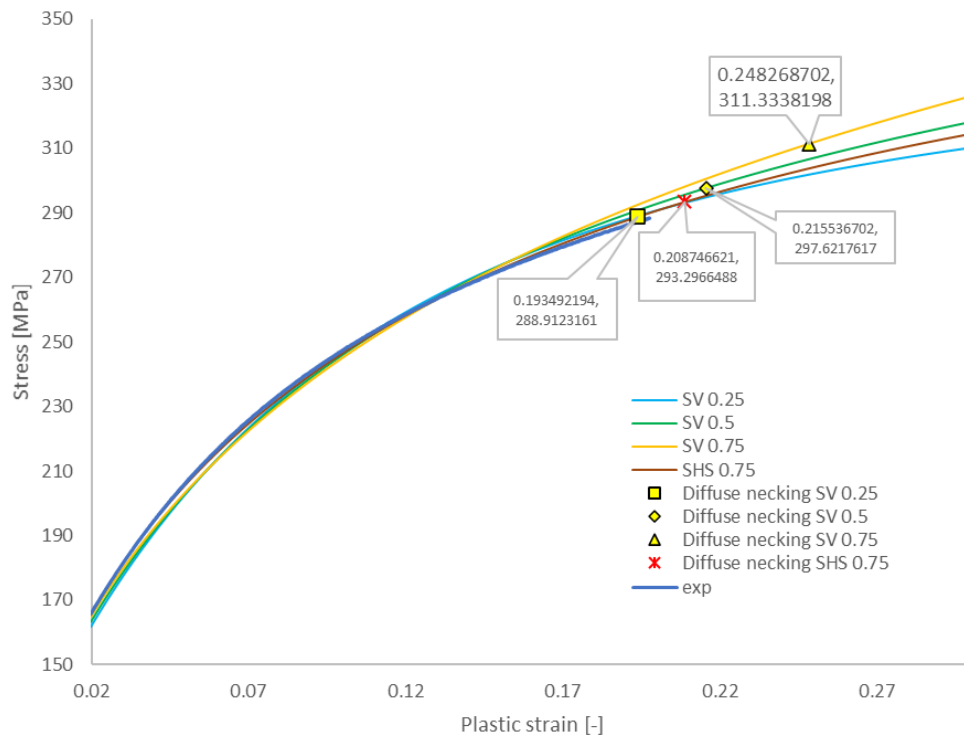


Figure 73 Swift-Voce vs Swift/Hockett-Sherby for small strains-Constelium AA6000, 90° roll angle

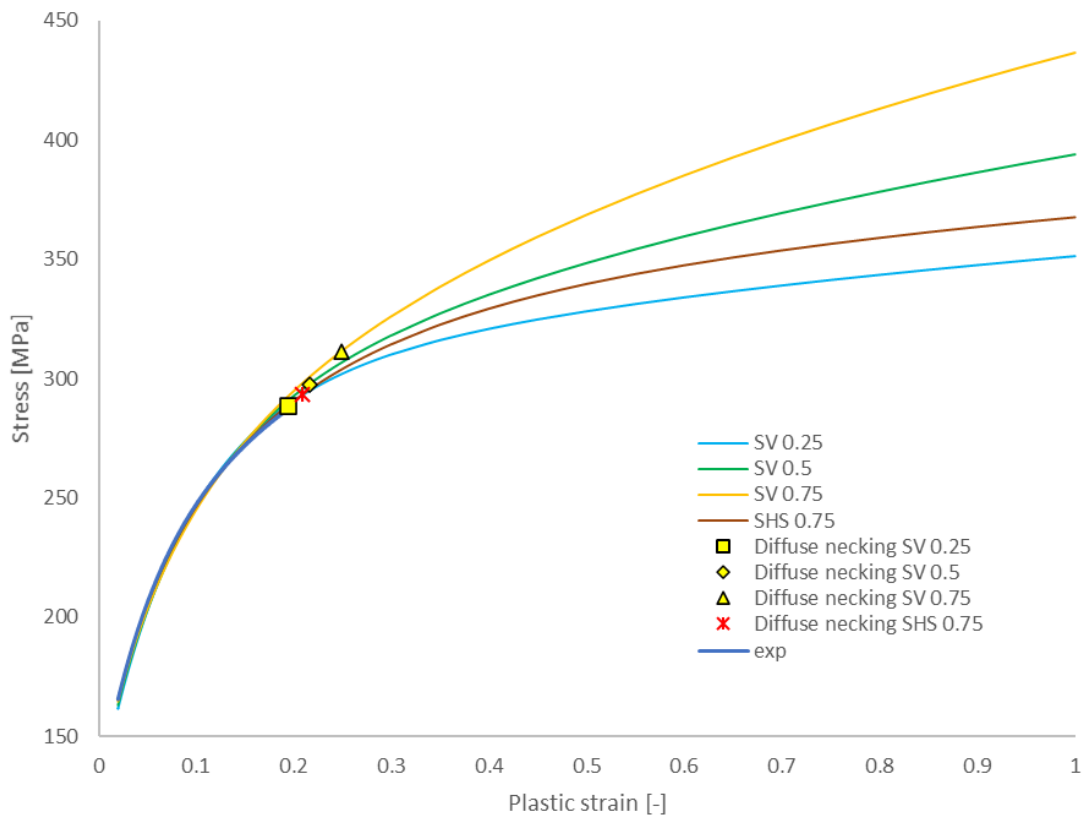


Figure 74 Swift-Voce vs Swift/Hockett-Sherby for large strains-Constelium AA6000, 90° roll angle

	SHS 0.75	SV 0.25	SV 0.5	SV 0.5
RMSE	0.817	2.301	2.367	2.702

Table 30 Swift-Voce vs SHS-Constelium AA6000, 90° roll angle

3.3.3.4 Summary table of Constelium AA6000

Material constants and RMS errors of Constelium AA6000 are reported in the next table,

	<i>Law</i>	<i>A</i>	<i>B</i>	<i>m</i>	<i>c</i>	<i>C</i>	ε_0	<i>n</i>	<i>K₀</i>	<i>Q</i>	β	<i>RMSE</i>
0°	<i>HS</i>	338.953	226.881	5.586	0.748	-	-	-	-	-	-	0.168
	<i>SHS</i>					443.904	0.007	0.251	-	-	-	0.747
	<i>SV</i>								127.708	204.768	9.609	1.646*
45°	<i>HS</i>	349.630	245.521	4.156	0.682	-	-	-	-	-	-	0.205
	<i>SHS</i>					429.266	0.0070	0.251	-	-	-	0.689
	<i>SV</i>	-	-	-	-				123.602	185.476	10.916	0.561*
90°	<i>HS</i>	331.170	217.980	5.673	0.774	-	-	-	-	-	-	0.154
	<i>SHS</i>					477.302	0.012	0.306	-	-	-	0.817
	<i>SV</i>	-	-	-	-				123.669	185.036	11.123	2.301*

Considering the above results it can be inferred that, extrapolation of the pre-necking data deep into the diffuse necking regime depends strongly on the phenomenological hardening law, while the material behaviour above diffuse necking is completely ignored. Thus, relying solely on the EM at large plastic strains cannot be a reliable approach in post-necking flow curve identification studies.

CHAPTER FOUR: HYDRAULIC BULGE TEST

4.1 INTRODUCTION

The successful implementation of the finite element simulation in the design phase of sheet metal forming process depends on the accuracy of the employed material characteristics. Among various different material properties that can affect the simulation results, *flow stress curve* (true stress/true plastic strain curve) of the material has a great importance. As it was observed in previous chapter, the *hardening law* defining the relationship between the flow stress and the plastic strain has a significant effect on the quality of the numerical results. In order to estimate the flow stress curve of a metal sheet at room temperature, tensile and hydraulic bulge tests are the most commonly used experiments; however, plane strain compression, shear test, and in-plane compression test are also exploited to achieve this purpose (49).

Bulge test is a destructive test method conducted to obtain the material properties of a sheet metal. Due to the state of stress, significantly higher (more than double) maximum effective strain can be attained in comparison with the tensile test without any evidence of localized necking.

Hydraulic bulge test¹³ is employed in the evaluation of the strain hardening properties of sheet materials under biaxial tension. During the test, the specimen is fixed at its edges as shown in the following figure, and is stretched biaxially and equally against circular die when oil/viscous fluid is used as a pressurizing medium. The sheet metal bulges into a hemispherical dome until it bursts (49).

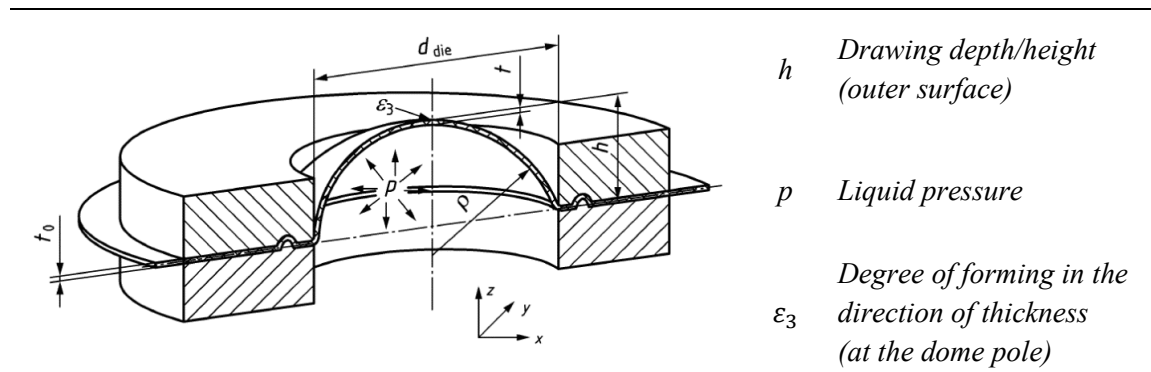


Figure 75 a scheme of hydraulic bulge test (50)

¹³ also known as the viscous pressure bulge test

The *maximum height of the dome at burst* can be used as an index of the Stretchability¹⁴ of the material; the higher the value of dome height prior to burst, the better will be the stretchability. In contrast with Nakazima test, there is no effect of friction on the deformation of the sheet material in the hydraulic bulge test, leading to an accurate evaluation of the stretchability of the material. The stress and strain values in hydraulic bulge test are calculated through the measurements of pressure, the curvature and surface extension in the center of the disc (49).

The writer started to study the bulge test with an aim to compare the two main approaches for the evaluation of the bulge test flow stress curve: ISO 16808 procedure and Modified Kruglov's method. However, based on the initial goals of this thesis work, post-necking behaviour identification through ISO 16808 prescribed method was seemed to be more related to this discussion.

4.2 HYDRAULIC BULGE TEST AND TENSILE TEST

Uniaxial tensile test can be employed to determine material properties such as flow stress data, Young's modulus, yield stress, ultimate tensile stress, uniform elongation, total elongation, and Lankford coefficients (r-value) (51). Tensile test is simple and inexpensive to conduct, but, in comparison with hydraulic bulge test, there are some considerations which are needed to be taken into account,

1. *Flow stress over very large plastic strain can be studied through hydraulic bulge test,*

A major advantage of the bulge test over the uniaxial tensile test is that the stress-strain curve can be extended to a wider range of effective strain (more than double) which is normally found in forming processes (52). Equibiaxial bulging is a very useful method for obtaining the strain hardening behaviour of the material beyond diffuse necking.

In the hydraulic bulge test (HBT), stress and strain can be obtained up to failure of the specimen, while in the conventional uniaxial test, only the uniform strain range can be utilized. Since the strains in stamping are normally larger than the uniform strain, the bulge test would be a better choice to describe the plastic properties of sheet metal at large strains.

¹⁴ *Stretchability is the ability of the material to be stretched biaxially without failure. The Erichsen cup test, limiting dome height (LDH) test, and hydraulic bulge test are commonly used tests to assess the stretchability (49).*

True strain calculation is only valid when the deformation is uniform along the gage length. Uniform elongation has a limited span, and presents between the initial yield point and the start of diffuse necking. On the contrary, due to the nature of the deformation process in HBT, not only Ludering is less evident, but also in case of having diffuse necking, it does not result in non-uniform deformation within the gage zone. Therefore, true stress-strain can also be evaluated beyond diffuse necking, up to the advent of localized necking or fracture (52).

2. *Extrapolation of test data comes with error,*

Since the range of strain obtained from tensile test is limited, extrapolation of tensile data would be quite necessary to conduct if one needs further information on material behaviour, causing noticeable errors in the forming simulation using FEM. Bulge test is an alternative to obtain a range of deformation wider than tensile test without an urge to use extrapolation techniques to achieve material behaviour. As a result, the material data obtained from the bulge test is more accurate than the conventional uniaxial tensile test data. Consequently, the simulation of the process would be more accurate when flow stress data from the bulge test is exploited (53).

3. *Tensile test only provides the stress–strain behaviour of the sheet material under uniaxial deformation conditions, so it provides the material behaviour in uniaxial strain path.*

In contrast though, in many forming processes such as stamping operation, the material deforms under biaxial condition of deformation. Likewise, in other sheet metal forming processes such as bending and deep drawing, materials deform in a wide variety of different strain paths, ranging from pure shear to biaxial tension.

4. *Improving the material anisotropy measurements, based on a comparison of tensile and bulge test stress-strain curves.*

Tensile tests of a metallic sheet show anisotropy in different directions in the plane of the sheet. *Normal Anisotropy* is an important parameter in forming operations. In general, a higher through thickness strength is beneficial as the material shows resistance to thinning during deformation. However, in order to avoid anomalies, an improved measure can be employed on the basis of a comparison between tensile and bulge test stress-strain curves (54).

5. *The bulge test cannot provide flow stress data for low strain values close to the yield point.*

Following the importing of data from bulge test assessment into forming simulation, the yield point of the material cannot be defined accurately. This can particularly affect the elastic behaviour of the material in the simulation and yields inaccurate simulation results, especially when springback must be predicted (55).

6. *Combining tests for greater accuracy.*

Despite the fact that HBT is commonly employed to assess the material characteristics of metallic sheets, plastic flow curves under bulge test and uniaxial tensile test are different; hence, both of these two tests should be performed, not only to obtain material parameters needed for satisfactory modelling of forming processes, but also, for determining more accurately the flow stress data from the initial yield point up to the largest strain values which is achievable by the bulge test, through combining the results from the bulge and tensile tests.

Comparatively more accurate flow stress data at high strain values can be obtained from bulge test, while tensile test is only able to provide material properties up to the yield point. This fact leads to a useful conclusion that by combining the two tests' results one can access to a better approximation of the flow stress data from yield to the strain at fracture in the biaxial stress condition (55).

Section 4.5 is dedicated to ISO 16808 method and how to combine the results of the two tests.

4.3 BULGE TEST EQUIPMENT

The bulge test equipment mainly consists of,

- hydraulic die,
- test stand,
- hydraulic power supply,
- electronic console,
- measuring unit and data acquisition equipment interfaced to a remotely located minicomputer.

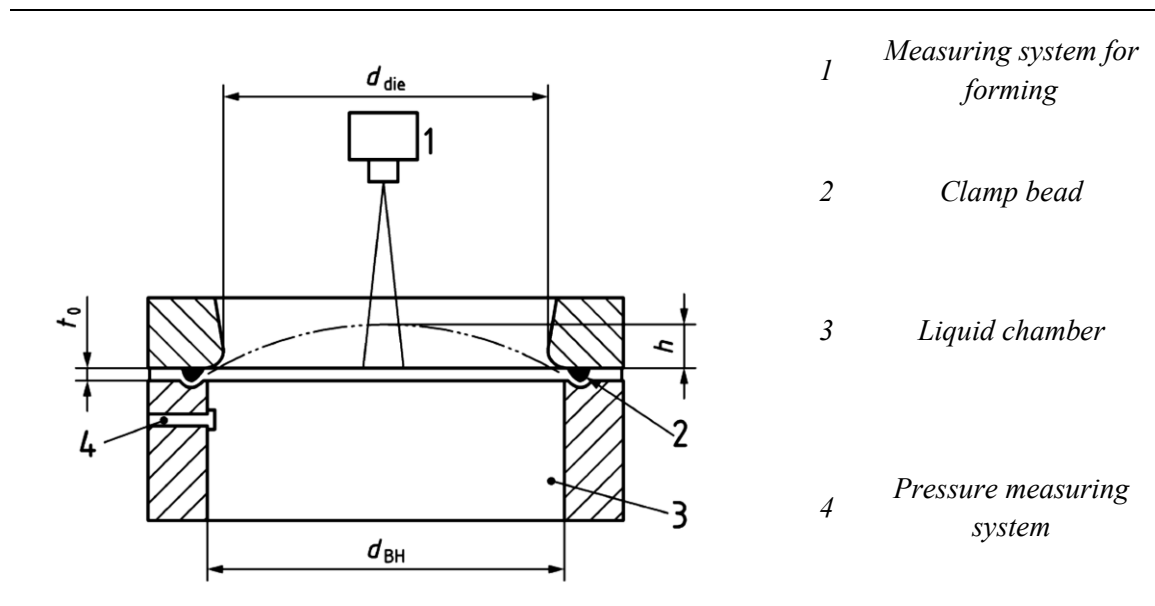


Figure 76 hydraulic bulge test equipment (50)

The dies assembly is designed in such a way that it is able to clamp the specimen for test, and facilitate bulging the specimen with hydraulic fluid and unclamping the specimen after the test. Servovalve provides the flow of oil coming from the hydraulic power supply to the die. The flow itself is controlled by the electronic console (52).

4.4 DATA COLLECTION AND ANALYSIS OF HYDRAULIC BULGE TEST

Automated data acquisition systems were not available in the first bulge test setups. Therefore, tests must have been conducted through an incremental method, so that, the deformation had to be stopped every time for collection of required data, such as, pressure, dome height, bulge radius. Incremental data acquisition method came with the risk of creep unless the pressure was dropped to almost 90% before taking the measurements. Automated bulge test equipped with sensors and data acquisition systems was designed in the 1970's (56). Continuous measurements (whether optical or mechanical) of bulge pressure, curvature of bulge specimen, its thickness at the pole in parallel with the application of membrane theory are used to evaluate the flow stress curve of the material under the test (53).

Among bulge parameters, bulge pressure is normally obtained directly from bulge machine itself, while curvature and thickness data may obtain through different approaches.

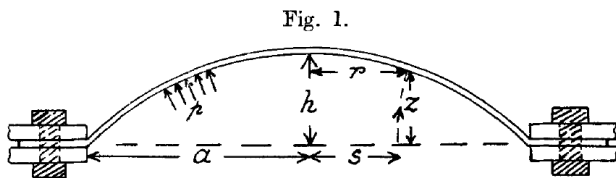
Two procedures are common as far as data collection from bulge test is concerned; indirect method and direct method (57).

4.4.1 Indirect method

In this section biaxial stress-strain curves by hydraulic bulging tests with circular die will be determined indirectly, through the *estimation of curvature and/or thickness based on analytical equations*, while the pressure, polar height and curvature radius are measured either in different stages of the deformation process or continuously during the test. Almost all of the methodologies in this group are based on analytical formulas describing the polar thickness and the curvature radius of the specimen in relation with one or more process parameters (58) (59) (60).

The problem of the hydrostatic bulging of circular diaphragms was first studied in 1948 by Gleyzal on the basis of the total-strain theory of plasticity (61).

Two years later, R. Hill developed an analytical model of the hydraulic bulging process based on the Mises theory (62). The shape of the dome was considered to be spherical and he neglected the effect of the fillet radius on the geometry of the specimen,



From a simple kinematical assumption regarding the evolution of the specimen surface, Hill also obtained a relation for the evaluation of the radius of the curvature and polar thickness (62),

$$\rho = \frac{a^2 + h^2}{2h} \quad , \quad t = t_0 \left[\frac{1}{1 + \frac{h^2}{a^2}} \right]^2$$

In 1959, Panknin performed experimental studies on the hydraulic bulging in his PhD thesis at the university of Stuttgart. The accurate determination of the process parameters was his main goal. He suggested a formula for the calculation of the curvature radius, while

RODNEY HILL

(1921-2011)



taking into account the effect of the *fillet radius* (R) on the dimensional characteristics of the dome (63),

$$\rho = \frac{1}{2h} \left(\frac{d}{2} + R \right)^2 + \frac{h}{2} - R$$

He found that for large polar heights, a deviation around 10% may be seen in the analytical results with respect to experimental data.

In 1970, by considering the hardening effect, Chakrabarty and Alexander improved the accuracy of the formulas previously proposed by Hill. In their paper, the plastic bulging of circular diaphragms by lateral fluid pressure was developed by assuming the bulge to be spherical and employing Tresca's yield criterion and the associated flow rule. They introduced an unknown parameter (λ) into Hill's formula, which was a function of the strain hardening exponent of the material (64),

$$\lambda = 1 - n$$

For all real cases, (λ) must be between 0 and 1 to ensure that the rate of plastic work is positive. Furthermore, they proposed that the polar (compressive) thickness strain rate can be evaluated via (64),

$$\frac{d\varepsilon_b}{dh} = (1 + \lambda) \frac{2h}{a^2 + h^2}.$$

This equation was integrated to attain the polar thickness strain ε_b as,

$$\varepsilon_b = (2 - n) \ln \left(1 + \frac{h^2}{a^2} \right).$$

Since $\varepsilon_b = -\varepsilon_3$, then the thickness at the dome apex was derived as,

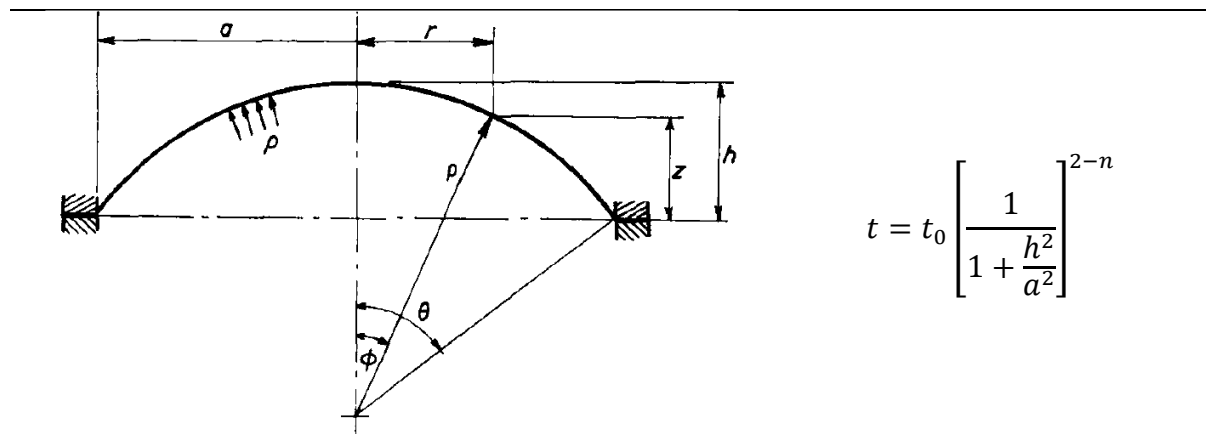


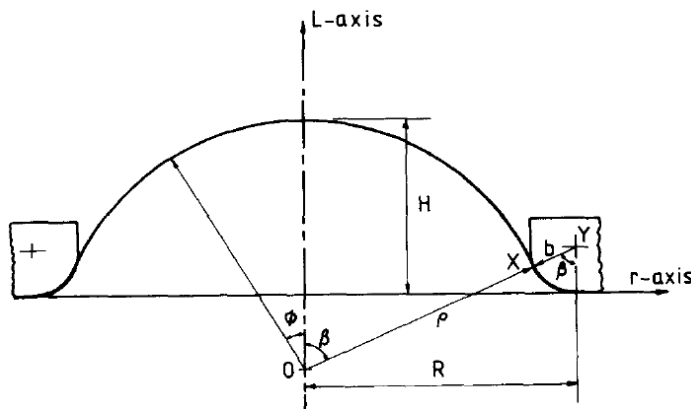
Figure 77 thickness variation at the dome apex proposed by Chakrabarty and Alexander (64)

While Hill's theory was already in line with experimental results of sufficiently work-hardened materials, Chakrabarty compared his theory with experiments for soft materials (64).

Alharthi and his colleagues improved the accuracy of the Chakrabarty and Alexander idea, by considering the effect of the plastic strain ratios instead of the hardening effect. Having the constant volume assumption in mind, the principal strains generated during a biaxial test can be related to compressive thickness strain. They also found that the biaxial strain deformation is sensitive to the plastic anisotropy; thus, instead of the strain hardening exponent of the material, they defined λ as a function of the normal plastic anisotropy (65).

Min and his co-workers developed a new method to accurately calculate stresses and strains for both isotropic and orthotropic sheet materials in circular bulge testing with the application of DIC. The method was based on a more accurate calculation of the local thickness, by taking into account the spherical or ellipsoidal shape of the metal, and the elastic volume change. Although they observed that the *stress condition in the bulge test is extremely close to balanced biaxial stress, this may not be the case for all anisotropic metals* (66).

Shang developed Hill's analytical model in order to take into account the fillet radius of the die insert (67). Thus, the adjusted radius of curvature (ρ) with respect to Hill's special solution (sharp-edged die) for the profile between the pole and point X (blank-die interface) can be achieved from the geometry of the model as follows,



$$\rho = \frac{H^2 + R^2}{2H} - b$$

Figure 78 Shang's adjusted radius of curvature for analytical model of hydraulic bulging (67)

He also found that the local shell thickness is influenced by the size of the die shoulder only at locations farther from the pole; consequently, the pressure-growth curve will not be

affected by the die shoulder radius. Besides, based on his experimental observations, the value of the fillet radius has a small influence on the polar strains (67).

Atkinson also tried to improve the accuracy of the analytical predictions with regard to the polar thickness and dome radius (68).

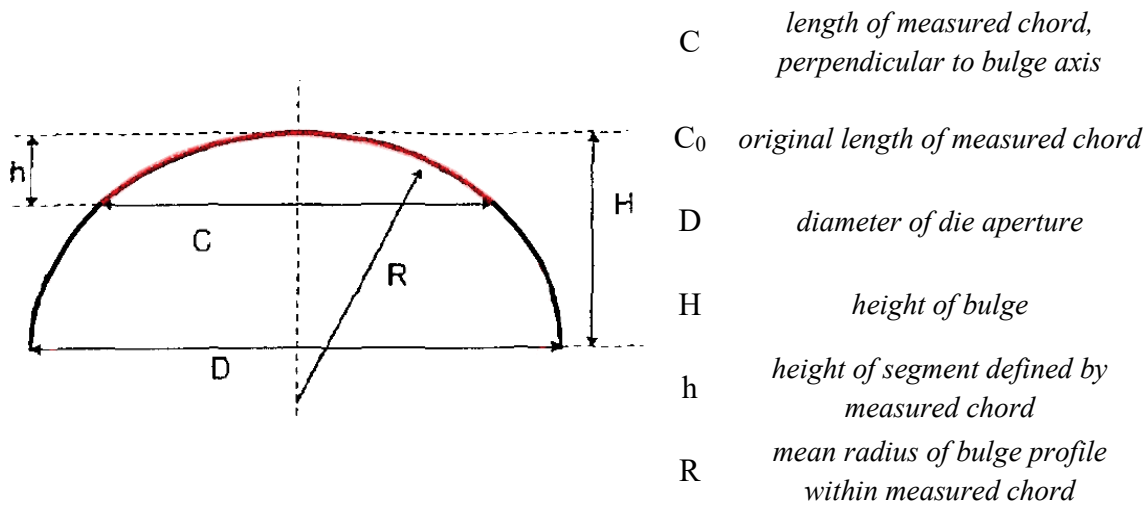
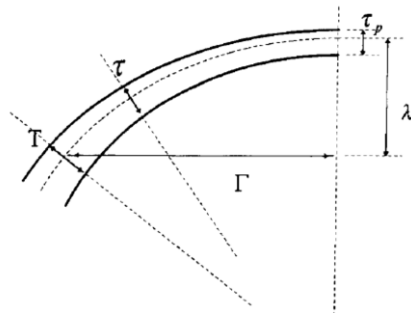


Figure 79 Atkinson's analytical model for hydraulic bulge test (68)

According to Atkinson's assessment, mean thickness of the polar cap defined by the gage length (C), highlighted by red, can be described as,



$$\tau \approx \frac{R - \sqrt{R^2 - t_0^2 C_0^2 / 2h}}{2}$$

t₀ : original sheet thickness

Geometry of polar cap

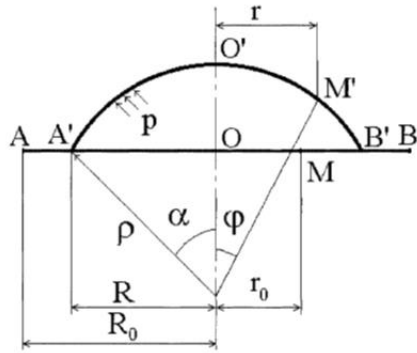
Figure 80 Atkinson's analytical model for hydraulic bulge test-mean thickness of the polar cap (68)

Kruglov developed a simple formula for the calculation of the polar strains. This formula was based on the assumption that the meridian strain is uniformly distributed on the dome surface (69); moreover, there were other hypothesis in his work (69),

- (a) The sheet material is isotropic and incompressible,
- (b) Forming process is isothermal,
- (c) The initial sheet thickness, s₀, is considered to be small compared with the envelope's radius R₀ (s₀/R₀ << 0).

In this case, the sheet metal under bulge test can be treated as a membrane and so one can employ the principal equations of the thin shell theory (membrane theory) in order to analyse the *superplastic free forming*.

- (d) The flow stress is a single-valued function of the strain rate,
- (e) The shape of the deforming shell is considered as a part of a sphere with the radius of curvature denoted as ρ ,
- (f) Since the envelope is made of two sheets by welding, the thickness of the shell in the vicinity of the weld is assumed to be constant in its value during the whole process of forming (in other words, it is assumed that the weld does not influence the sheet deformation).



Thickness at the pole

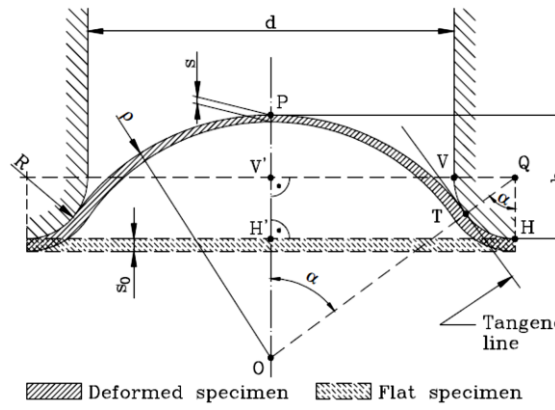
$$s = s_0 \left(\frac{\alpha}{\sin \alpha} \right)^{-2}$$

Figure 81 Kruglov's approach for analytical study of the bulging test (69)

4.4.1.1 Kruglov's approach: Stress and strain evaluation in hydraulic bulge test

Both *Kruglov* and *Modified Kruglov* approaches are described in the following paragraphs in order to derive *biaxial stress and strain* through hydraulic bulge test. The modification takes into account the *non-uniform distribution of the strains on the specimen surface* by means of a *correction factor*. An improved accuracy was observed from the *Modified Kruglov's formula* by comparing the results with experiments equipped with optical measurement systems (60).

Table below shows the principle of the *Kruglov's approach* for the hydraulic bulging test with the following specifications,



O, *current centre and pole of the dome surface*
P *(approximated by a spherical cap)*

Q, *centre and ends of the fillet joining the orifice*
V, *and the bottom surface of the bulging die*
H

point where the free profile of the specimen

T *becomes tangent to the fillet arc of the bulging die*

V', *projections of the points V (Q) and H,*
H' *respectively, on the vertical axis OP*

d *diameter of the bulging orifice*

R *fillet radius of the bulging orifice*

s₀ *initial (nominal) thickness of the specimen*

s *current thickness of the specimen in the polar region (point P)*

ρ *current radius of the dome surface*

h *height defining the current position of the pole P*

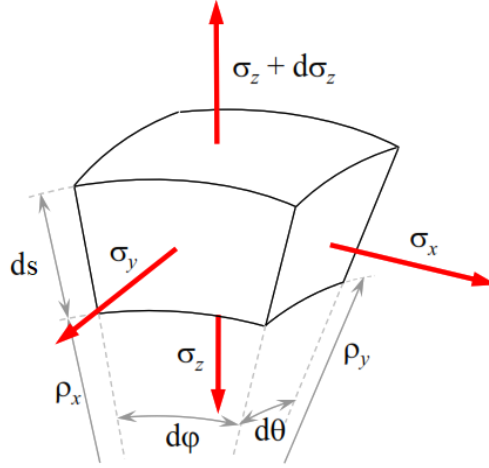
α *angle spanned by the arc TP or TH (α is expressed in radians)*

Figure 82 Schematic representation of the specimen subjected to hydraulic bulging-Kruglov's approach (60)

Both the diameter (d) and the fillet radius (R) are *constants*, describing dimensional characteristics of the experimental device. In a certain experiment, the initial thickness of the specimen (s_0) is also constant. All the other quantities mentioned above (s , ρ , h , and α) are variables depending on the current level of the pressure (p) acting on the bottom surface of the sheet metal (60).

Stress state

In order to determine the biaxial flow curves, *membrane theory* is commonly exploited. As it was demonstrated in the previous figure, when the sheet is clamped between the die and blank holder, the flow curves can be evaluated based on the analysis of measurable variables from bulge test; however, *membrane theory is only valid when the ratio of the sheet thickness to the bulge diameter is small*. It assumes that the through thickness stress is zero and a relationship can be established using Laplace's formula (70),



$$\frac{\sigma_x}{\rho_x} + \frac{\sigma_y}{\rho_y} = \frac{p}{s}$$

(s) is the sheet thickness at the dome apex

Figure 83 Stresses on double curved element in cross section at the pole (70)

Based on the *membrane theory*, the stress state is characterized by two stresses on the material surface: *meridian stress* and *tangential stress*, where it is assumed that these stresses are uniformly distributed along the shell thickness (70).

It is also important to note that for a bulge test evaluation method with *high accuracy* the influence of bending stresses and through thickness stress at the pole on the force equilibrium must be known. Furthermore, although the assumption of an equibiaxial stress state will also lead to deviations in accuracy, *normally* (and also here in this section) the bulge test is considered as axisymmetric case for the region *quite close to the pole*; hence, the principle stress can be considered equivalent and equal the membrane stress, i.e. ($\sigma_1 = \sigma_2 = \sigma_b$). The same holds for the curvature radii, i.e. $\rho_1 = \rho_2 = \rho$ (70).

Under these simplifications the current biaxial stress or membrane stress σ_b is defined as (70),

$$\sigma_b = \frac{p\rho}{2s}$$

Strain state

For strain calculation, the volume consistency assumption is employed, which is based on the fact that the plastic deformation in metals and alloys takes place without any significant change in volume (60),

$$\varepsilon_1 + \varepsilon_2 = -\varepsilon_3$$

Therefore, the corresponding thickness (radial) strain (the so-called biaxial strain ε_b) can be evaluated using the relationship,

$$\varepsilon_b = -\varepsilon_3 = \ln \frac{s_0}{s}$$

Analytical expressions for biaxial stress and biaxial strain can be exploited to *find a biaxial stress-strain diagram* only if the quantities p , ρ and s are either *measured* or *derived* from other experimental data (60).

The current level of the *pressure* (p) can be readily measured via a sensor connected to the hydraulic chamber; on the contrary, the *curvature radius* ρ and the *polar thickness* s cannot be obtained directly. Thus, they would be available indirectly by employing approximate formulas consisting of the current value of the *polar height* h . This parameter can be monitored continuously either through a displacement sensor (e.g. linear voltage displacement transducer (LVDT)) or by digital image correlation (DIC) system (60).

Experimental results show that areas close to the centre of the bulge has nearly a spherical shape, and the area expands as the bulge height increases. Considering the fact that membrane solution cannot be accurate enough near the clamped edge, it is reasonable estimation that the bulge is quite spherical for large values of strain (64).

The curvature radius ρ can be evaluated with *Panknin's formula* (60) (63),

$$\rho = \frac{1}{2h} \left(\frac{d}{2} + R \right)^2 + \frac{h}{2} - R .$$

The experimental studies performed by other researchers (71) proved that amongst the numerous relationships that can be employed to assess the current value of the polar thickness (s), Kruglov's formula (69) leads to the best results. At the level of the polar region, volume consistency assumption can be written as follows, where ε_m is the meridian (circumferential) strain (60),

$$\varepsilon_b = 2\varepsilon_m .$$

According to Kruglov's approach, one assumes that ε_m can be calculated using the approximation (according to figure 78) (60),

$$\varepsilon_m = \ln \frac{\widehat{TP} + \widehat{TH}}{HH'} ,$$

Provided that the meridian strain were uniformly distributed on the dome surface. However, this relation is not valid thoroughly, based on the fact that the local thickness of the specimen gradually decreases from the clamping region towards the pole (60). Hence, adjustments to this approach was introduced by '*modified version of Kruglov's formula*', by

taking into account the variation of the thickness. In order to improve its accuracy, the modification will be applied by defining the meridian strain as a function of α (60).

The following relations can be written based on the last equation and the previous figure (60):

$$\widehat{TP} = \rho\alpha, \widehat{TH} = R\alpha, HH' = \frac{d}{2} + R,$$

Where according to Panknin's (ρ) definition,

$$\sin\alpha = \frac{V'Q}{OQ} = \frac{\frac{d}{2} + R}{\rho + R} = \frac{\frac{d}{2} + R}{\frac{1}{2h}\left(\frac{d}{2} + R\right)^2 + \frac{h}{2}},$$

i.e.

$$\alpha = \arcsin\left(\frac{\frac{d}{2} + R}{\frac{1}{2h}\left(\frac{d}{2} + R\right)^2 + \frac{h}{2}}\right).$$

Thus, meridian strain can be rewritten as,

$$\varepsilon_m = \ln \frac{\alpha}{\sin\alpha}.$$

By replacing ε_m into biaxial strain relation, one obtains the following expression for the polar biaxial strain,

$$\varepsilon_b = 2\ln \frac{\alpha}{\sin\alpha}$$

Which is the formula introduced by Kruglov. In combination with the definition of biaxial strain, this relation leads to the evaluation of the current polar thickness (60),

$$s = s_0 \exp(-\varepsilon_b) = s_0 \left(\frac{\alpha}{\sin\alpha}\right)^{-2}.$$

Interestingly, the last two equations only require the measurement of the dome height h , as α is only a function of dome height. As mentioned previously, although Kruglov's approach led to acceptable results in comparison with the experiments, its accuracy can be improved further by the modification of the geometrical definition of median strain,

$$\varepsilon_m = (1 + c\alpha) \ln \frac{\widehat{TP} + \widehat{TH}}{HH'}.$$

After updating the definition of median strain into biaxial strain definition, the polar biaxial strain can be derived as (60),

$$\varepsilon_b = 2 (1 + c\alpha) \ln \frac{\hat{TP} + \hat{TH}}{HH'} .$$

The presence of a *correction factor containing the constant parameter c* makes this formula more attractive with respect to the original Kruglov's formula. This relation allows the evaluation of the *updated current polar thickness* (60),

$$s = s_0 \exp(-\varepsilon_b) = s_0 \left(\frac{\alpha}{\sin \alpha} \right)^{-2(1+c\alpha)} .$$

It is obvious that in order to implement the last two equations, coefficient c needs to be obtained first by assessing the final value of the polar thickness s_{min} , which can be observed after the specimen is freed from the dies (60).

The thickness can be observed using a measuring device attached to the upper and lower surfaces of the specimen. Considering h_{max} and α_{max} as the polar height and the angle spanned by the dome surface, respectively, corresponding to the final stage of the process, thickness s can be formulated as follows (60),

$$s_{min} = s_0 \left(\frac{\alpha_{max}}{\sin \alpha_{max}} \right)^{-(1+c\alpha_{max})} ,$$

So that,

$$\alpha_{max} = \arcsin \left(\frac{\frac{d}{2} + R}{\frac{1}{2h_{max}} \left(\frac{d}{2} + R \right)^2 + \frac{h_{max}}{2}} \right) ,$$

Coefficient c can be derived from the thickness at apex at the final stage of the bulging process (60),

$$c = \frac{\ln \sqrt{\frac{s_0}{s_{min}}} - \ln \frac{\alpha_{max}}{\sin \alpha_{max}}}{\alpha_{max} \ln \frac{\alpha_{max}}{\sin \alpha_{max}}} .$$

All in all, the two approaches to evaluate biaxial stress and biaxial strain analytically are briefly highlighted here (according to the method used to calculate the polar thickness, there would be a number of approaches, however, it is shown in the literature that Kruglov's approach is more reliable than the rest),

KRUGLOV'S APPROACH

Distribution of median strain is assumed to be UNIFORM along the dome

- Import test-related constants: (d), (R) and (s_0),
- Monitor pressure (p) and dome height (h) continuously,
- Evaluate dome radius (ρ) from Panknin's equation continuously,

$$\rho = \frac{1}{2h} \left(\frac{d}{2} + R \right)^2 + \frac{h}{2} - R$$

- Evaluate (α) derived from test geometric constants and dome height continuously,

$$\alpha = \arcsin \left(\frac{\frac{d}{2} + R}{\frac{1}{2h} \left(\frac{d}{2} + R \right)^2 + \frac{h}{2}} \right)$$

- Evaluate constantly the polar thickness (s) using Kruglov's formula

$$s = s_0 \left(\frac{\alpha}{\sin \alpha} \right)^{-2}$$

- Biaxial strain and stress can be assessed continuously using the following equations,

$$\varepsilon_b = 2 \ln \frac{\alpha}{\sin \alpha} \quad \sigma_b = \frac{p\rho}{2s}$$

MODIFIED KRUGLOV'S APPROACH

Distribution of median strain is not UNIFORM practically

$$\varepsilon_m = (1 + c\alpha) \ln \frac{\alpha}{\sin \alpha}, \quad \varepsilon_b = 2 \varepsilon_m$$

- Evaluate constantly the polar thickness (s) using Modified Kruglov's formula,

$$s = s_0 \left(\frac{\alpha}{\sin \alpha} \right)^{-2(1+c\alpha)}$$

- Coefficient (c) will be defined at the pole, and at the final stage of the test, where, $s = s_{min}$, $h = h_{max}$ and $\alpha = \alpha_{max}$.

$$c = \frac{\ln \sqrt{\frac{s_0}{s_{min}}} - \ln \frac{\alpha_{max}}{\sin \alpha_{max}}}{\alpha_{max} \ln \frac{\alpha_{max}}{\sin \alpha_{max}}}, \quad \alpha_{max} = \arcsin \left(\frac{\frac{d}{2} + R}{\frac{1}{2h_{max}} \left(\frac{d}{2} + R \right)^2 + \frac{h_{max}}{2}} \right)$$

Coefficient (c) can be easily established if the final value of the polar thickness s_{min} is measured after removing the specimen from the hydraulic bulging device.

An overview of the methodology for the determination of bulge test stress-strain curve is described by the flow chart shown in figure below,

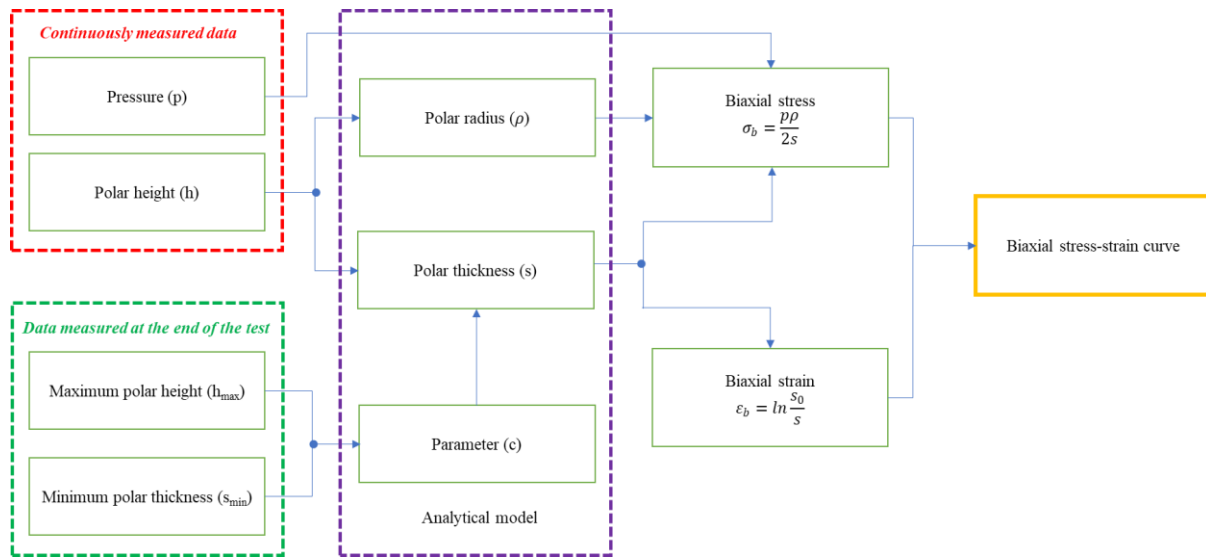


Figure 84 methodology for the determination of bulge test stress-strain curve

4.4.2 Direct methods

Breakthroughs in the field of sheet metal testing are still possible by the development of the computers and data acquisition systems. Direct methods benefit from continuous data acquisition of bulge geometry to evaluate curvature and thickness (57).

Two groups may be seen with regard to direct methods:

(a) Mechanical measurements

Mechanical measuring systems entail *spherometer* and *extensometer* that employs physical tactile devices, to evaluate curvature and thickness, respectively. This approach provides a possibility for both the applicability and exchangeability of bulge test results (52).

(b) Optical measurements

In the field of the hydraulic bulging, recent development has been mainly in the area of *optical strain measuring* systems. Such systems consist of CCD cameras whose functions are monitored by a *videogrammetric* software. Besides, 3D optical measurement system can be used for the continuous observing of the polar height, curvature radius and polar thickness of the specimens (72).

The *potentiometer* is a very sensitive device and cannot tolerate the impact loading during bursting of the specimen. Therefore, tests used to be done at two steps: (1) all the way up to burst point without the potentiometer to get the burst pressure (P_{burst}) and (2) after installing

the potentiometer, testing up to $\sim 90-95\% P_{burst}$. However, with the new laser sensor, it is possible to determine the data up to P_{burst} (73).

4.4.2.1 Mechanical measurements

Strain rate sensitivity is the dependence of the stress-strain curve on the rate at which the test specimen is deformed. This behaviour can be taken into account by a *feed-back control* on the hydraulic bulging system. The data processing system transforms test signals (transducer signals for the three variables, pressure (p), spherometer height (h) and extension) into data output. The signals are converted into digital form and then stored in a minicomputer. After the test, these are computed to obtain stress-strain data pairs, and the information is transferred to a central computer for subsequent analysis or plotting (52).

The specimen is a circular blank as shown in figure below. in order to facilitate the strain measurements at the end of the test for validation, gridded blanks are normally employed (52).

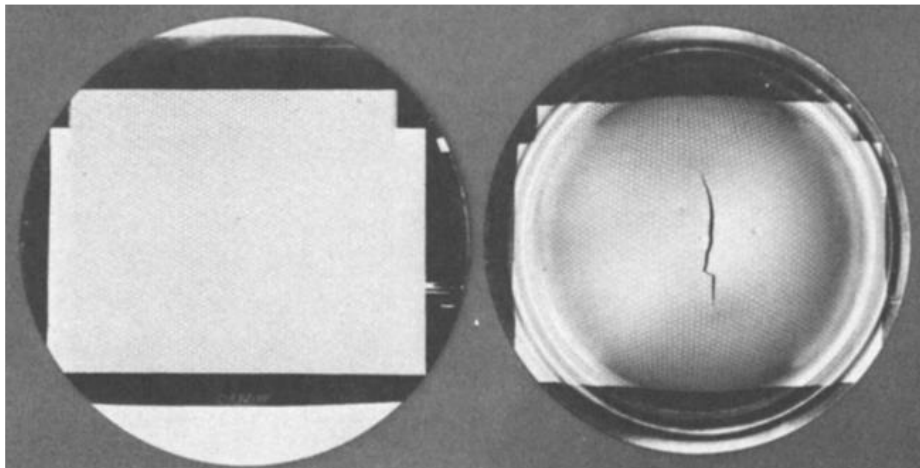
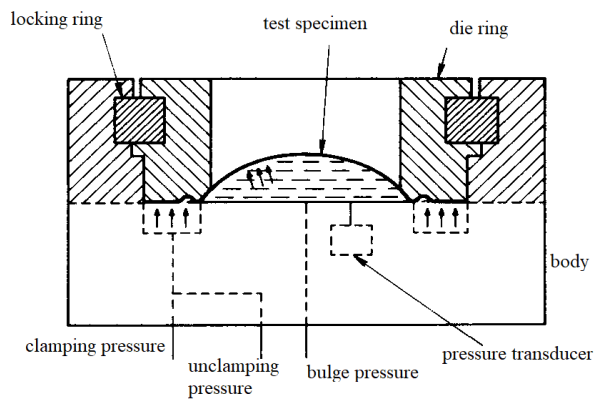


Figure 85 Sheet specimens before and after bulge testing (52)

Different diameters used for determination of curvature and strain have a strong influence on obtained flow curve, especially for strains higher than 0.3 of the evaluated curve (57).

In order to become familiar with mechanical measurements, the test procedure is described here. Firstly, the test specimen is placed in the die, as shown in the next figure,



Internal pressure (p)

- measured continuously using a pressure sensor,
- located on one end of the rod holding the hydraulic cylinder.

Bulge height of the sheet (h)

- measured continuously by a Linear Potentiometer Transducer,
- fixed on the upper die (58).

Figure 86 Cross-section of the bulge die (52)

The die ring is inserted and locked, and the test-piece is clamped. The *extensometer* and *spherometer* must be carefully calibrated while sitting on a ground surface plate, as the stress-strain data are highly sensitive to errors in curvature measurement. The unit is then placed on the specimen, and the control console is set to initiate a test in a similar fashion to any normal servo-controlled system. The thickness and the reading rate of the data sets are entered by the operator.

The test is run and goes on until the rupture, when the control system senses an abrupt fall in pressure level and deactivates the hydraulic system. The, the specimen can be removed and the data is transmitted to the central computer for further processing as discussed before (52).

In conclusion, the main procedure of bulge test can be divided into the following steps (58),

1. Expand the metallic sheet by hydraulic pressure while the edge of the specimen is held firmly to avoid axial movement,
2. Meanwhile, the internal pressure (internal pressure is recorded 30 times per second to measure the pressure precisely, which is used in the analytical equations) and bulge height are measured continually during expansion,
3. The measured parameters are then converted into true stress-strain data using analytical equations (in case of indirect method),
4. Exploiting the least-squares method, stress-plastic strain data can be fitted into a strain hardening law to obtain a flow stress curve.

4.4.2.2 Optical measurements

In comparison with classical mechanical measuring systems, optical measuring systems provide in-depth information about the deformation of the specimen during the test; for example, due to the practical shortcomings of mechanical measuring, the shape of the bulged sheet is approximated by a sphere. Furthermore, the additional information coming from optical measuring devices provide not only detailed assessments on the bulged surface, but also more accurate *determination of the stress and strain state at the pole* (70). Mulder and his colleagues showed that if the surface coordinates are fitted into an *ellipsoid shape function*, more accurate results can be obtained. In the next step, the accurate flow curve can be retrieved both from the fit and the local strain data to estimate the curvature of the midplane (70).

4.5 ISO 16808 RECOMMENDED PROCEDURE FOR HYDRAULIC BULGE TEST

The following section highlights the main features of ISO 16808 standard on the determination of biaxial stress-strain curve by means of bulge test with optical measuring systems (50).

Generally, the proposed approach exploiting optical measuring systems is an evolution of the method using a spherometer and an extensometer. A configuration for optical measuring system for bulge test is shown below,

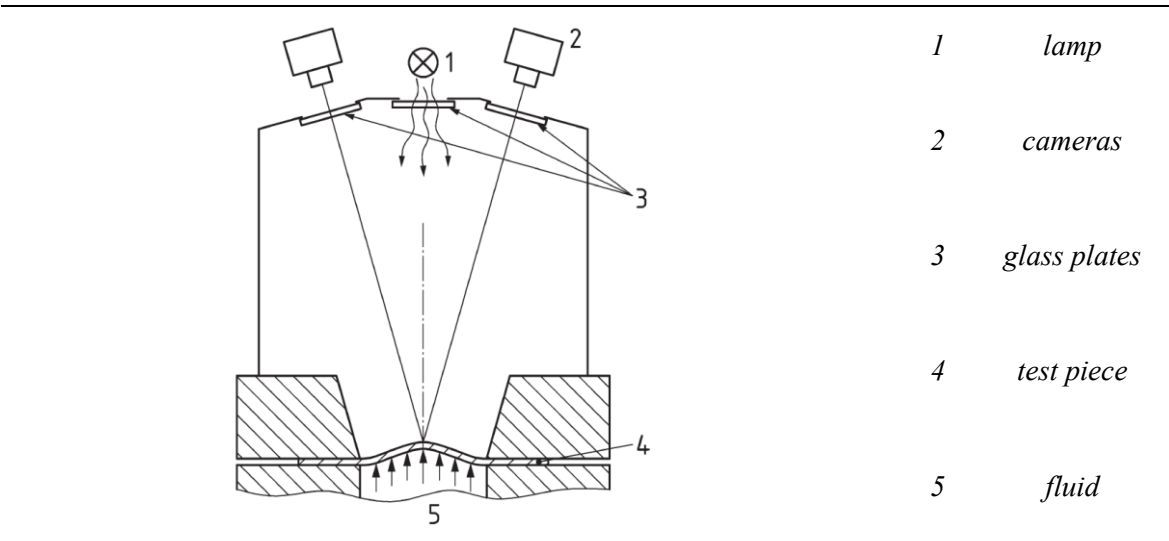


Figure 87 Example for possible positions of oil shielding plates and lamps (50)

4.5.1 Determination of the curvature and strains at the pole

A *spherically shaped surface near the pole (best-fit sphere)* is assumed for the following calculation of the curvature and strains. The area of the dome with the highest deformation is selected in the last image before bursting takes place and defined as the location in which the true stress and the true thickness strain (ϵ_3) should be assessed. The *best fit sphere* can be evaluated based on a selected area of points in order to obtain a stable radius of curvature of the dome (50).

Herein, points inside the radius (r_1) around the pole in the last image (time step) before failure are chosen in a ***best sphere fit*** to *obtain the radius of curvature, rather than employing a spherometer*. The same selection of points are used for all forming stages. The disadvantage of this method is that depending on the deformation in the final stage more or less points are included. The consistency is improved by applying it to all points within an initial radius or within a current radius (r_1) (50).

Similarly, *instead of using an extensometer the thickness strain* of points within a radius (r_2) is averaged. The points within that radius are also selected in the last image before bursting and that selection applies again to all forming stages (50).

As it is illustrated in the next figure, a radius (r_1) is defined around the apex of the dome in the last image before bursting and the fit is performed for all forming stages with the same selection of points. A certain number of the first forming stages (images) are rejected, since the specimen is still too flat for a reliable determination of the best-fit sphere, since the bending radius is very large and the fit is not stable. For robust values of the true strain and thinning in the apex, the average value of a number of selected points is taken. Therefore, a second area is defined by a radius r_2 in a similar manner (50).

Based on this procedure, after measuring the *radius of curvature* and the *average thickness strains* for every forming stage (image), the corresponding *thickness and stress values at the dome apex* are then **calculated** accordingly. This evaluation can be carried out for different (r_1) and (r_2) values. However, for a good convergence and robust values, the recommended range of (r_1) and (r_2) is defined as in the following figure,

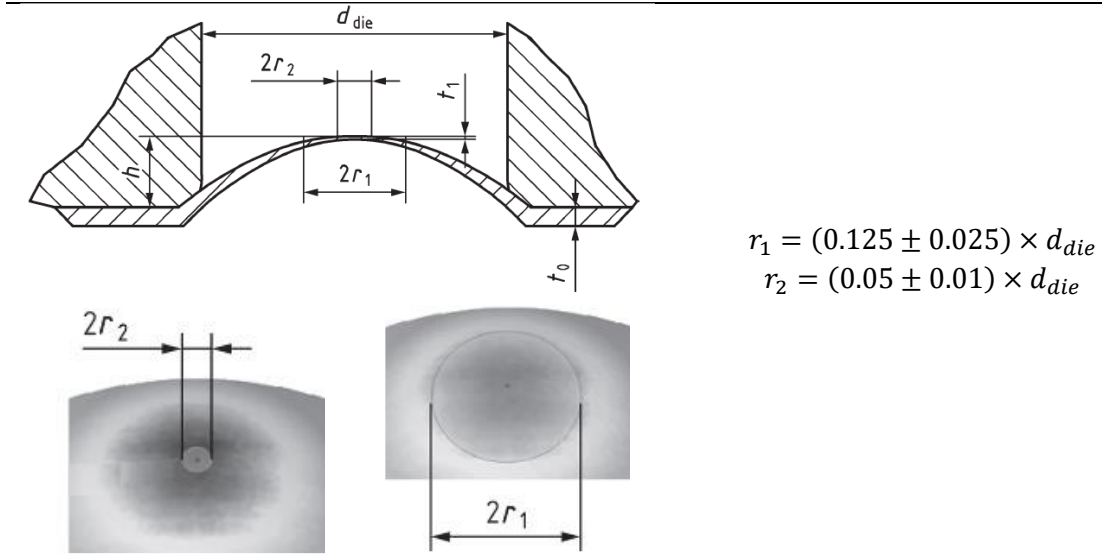


Figure 88 Choice of r_1 and r_2 for calculation of true stress and true strain for each forming stage (50)

4.5.2 Calculation of biaxial stress-strain curves

For the derivation of the biaxial stress-strain curve, both radius of curvature and thickness strain at dome are already known through optical measurements; thus, in the next step to achieve this goal, a simple membrane stress state of a thin-walled spherical pressure vessel is considered at the centre of the blank (50). This leads to the following simplifications:

- (a) As before, an equibiaxial stress state is assumed,

$$\sigma_x = \sigma_y = \sigma_b$$

- (b) Defining the curvature by the mean curvature radius (ρ_a) at the pole.

Then the biaxial true stress can be evaluated using the following equation,

$$\sigma_b = \frac{p \rho_a}{2t} ,$$

Where the radius of curvature is the average radius of curvature using equation (ρ_a), established on the outer surface, and (p) is the measured fluid pressure.

According to the definition of the thickness strain (ε_3), actual thickness will be,

$$t = t_0 \exp(\varepsilon_3) .$$

Assuming *plastic incompressible deformation* of the material and *neglecting elastic strains*, the total thickness strain for the calculation of the actual thickness can be estimated by the *total major and minor true strain* on the outer surface,

$$\varepsilon_3 \approx -\varepsilon_1 - \varepsilon_2 .$$

Employing the plastic work principle, the *biaxial stress-strain curve is a function of the plastic strain in thickness direction: $\sigma_b(\varepsilon_3^{pl})$* . Provide that the material has an isotropic linear elastic behaviour and taking into account the volume consistency (plastic incompressibility rule), the *plastic thickness strain* can be obtained by,

$$\varepsilon_3^{pl} = -\varepsilon_1 - \varepsilon_2 + 2 \frac{1 - \nu}{E} \sigma_b \quad .$$

It is important to note that the *die diameter to thickness ratio should be large enough to ensure a near membrane stress state in the specimen, and an inconsiderable effect of bending* (50). Therefore, there is no prescription for bending correction, except for die diameter to thickness ratios lower than 100, where it is recommended to *observe if the bending strains are comparatively small with respect to the actual thickness strain result* (ε_3) using the following estimate for the bending strains (50),

$$\varepsilon_{bending} \approx -\ln\left(1 - \frac{t_0}{2\rho} \exp(\varepsilon_3)\right) \quad .$$

4.6 FROM YIELD POINT TO FRACTURE BY COMBINING TENSILE TEST DATA WITH BULGE TEST DATA

4.6.1 Introduction

Since neither the tests are able to describe accurately the whole material's plastic behaviour, a complete description can be achieved merely through combining the data coming from the two tests; so that, the deformation around the yield point is evaluated from tensile test, while the rest of the flow curve is derived from bulge test results.

It is observed that the flow curve obtained from the bulge test is normally placed higher compared to tensile test for the same level of strain, however there are exceptions like DP600, and an aluminium alloy studied here (54).

Furthermore, the anisotropy values resulted from bulge test are smaller in comparison with that of the tensile test. This may come from the fact that in the bulge test the anisotropy values are obtained for strain range of 0.05 to 0.4, while in tensile test it is measured at strain of ~ 0.2 (54).

4.6.2 Tensile test data extrapolation using scaled bulge test data

Briefly, the aim of this section is to extrapolate tensile test data beyond UTS, by exploiting bulge test results. The following procedure is prescribed by ISO 16808-2014. Herein, the approach is introduced first and then will be implemented in some materials tested in CRF's labs.

Usually, the true stress-strain curve, determined from uniaxial tensile test data in rolling direction, is employed as a reference for hardening evaluation and the calculation of the stress points of the yield locus. On the other hand, bulge test provides equibiaxial stress-strain curves, where the average of the major and minor stress from the bulge tests can be drawn against the absolute value of the plastic true thickness strain (50).

The approach used for the evaluations of the *equibiaxial stress ratio* and *scaling bulge test results to extend the uniaxial stress-strain curve beyond uniform deformation* is described in the following according to ISO 16808-2014 prescription. By comparing the curves of the 'stress-strain data of the equibiaxial stress state' with the 'uniaxial reference curve', the *equibiaxial stress point* can be derived and the *equibiaxial stress-plastic strain curve* can be converted to an *equivalent stress-plastic strain curve* presenting work hardening data at strains higher than the uniform elongation (50).

The method described in this section is merely one of the approaches for studying the stress-strain data from a bulge test. However, it is mentioned in the standard that: "it is the responsibility of the operator to observe whether the underlying assumptions are fulfilled adequately in a way that *it is in line with the actual material behaviour*" (50). The following assumptions are made based on ISO 16808:

- isotropic hardening,
- the yield locus shape does not change with the strain,
- the work hardening is independent from the strain path (loading path),
- the loading path and strain path of the test are constant,
- the strain rate and temperature of the bulge test are close to the strain rate and temperature of the tensile test.

In order to enable extrapolation in the post-uniform strain range of the tensile test, as a reference value for the equivalent strain (ε_{E-ref}), the true plastic strain at Uniform Elongation of the tensile tests (ε_{1-UE}) in the rolling direction is chosen,

$$\varepsilon_{1-UE} = \varepsilon_{E-ref} \quad .$$

It is the last valid point of the true stress true strain curve of the tensile test, from which the hardening curve will be extrapolated using bulge test data.

As far as a reference value for stress is concerned, the *stress at the uniform strain of the tensile tests* is used as the *reference flow stress* (σ_{f-ref}) i.e. the ultimate tensile strength transformed to a true stress.

The *corresponding reference stress value of the bulge test* (σ_{B-ref}) are looked up by comparing the two sides of the following equation,

$$\sigma_{B-ref} \cdot |\varepsilon_{3-ref}| = \sigma_{f-ref} \cdot \varepsilon_{E-ref} \quad .$$

ε_{3-ref} is defined as the corresponding reference thickness strain for the bulge test.

Since the bulge test curve consists of *discrete values*, there might not be a pair which completely satisfies the condition shown in the above formula. Therefore, the point (m) in the bulge test data matches the following condition,

$$\left\{ \begin{array}{l} \sigma_{B,m} \cdot |\varepsilon_{3,m}| \leq \sigma_{f-ref} \cdot \varepsilon_{E-ref} \\ \text{and} \\ \sigma_{B,m+1} \cdot |\varepsilon_{3,m+1}| \geq \sigma_{f-ref} \cdot \varepsilon_{E-ref} \end{array} \right. \quad .$$

The requested reference stress of the bulge test can now be computed by *simple linear interpolation*,

$$\sigma_{B-ref} = \sigma_{B,m} + \frac{\sigma_{B,m+1} - \sigma_{B,m}}{\sigma_{B,m+1} \cdot |\varepsilon_{3,m+1}| - \sigma_{B,m} \cdot |\varepsilon_{3,m}|} \cdot (\sigma_{f-ref} \cdot \varepsilon_{E-ref} - \sigma_{B,m} \cdot |\varepsilon_{3,m}|) \quad .$$

The value of the *biaxial stress ratio* (f_{bi}) is obtained by,

$$f_{bi} = \frac{\sigma_{B-ref}}{\sigma_{f-ref}} \quad .$$

With the biaxial stress factor (f_{bi}), the bulge test curve can be transformed into an equivalent strain-stress curve,

$$\left\{ \begin{array}{l} \sigma_{fk} = \frac{\sigma_{Bk}}{f_{bi}} \\ \varepsilon_{Ek} = |\varepsilon_{3k}| f_{bi} \end{array} \right. \quad .$$

In combination with uniaxial stress-strain curves from tensile tests, this transformed curve can be used to generate a hardening curve with data extrapolated beyond strain at uniform elongation.

The method is shown graphically in the following figure,

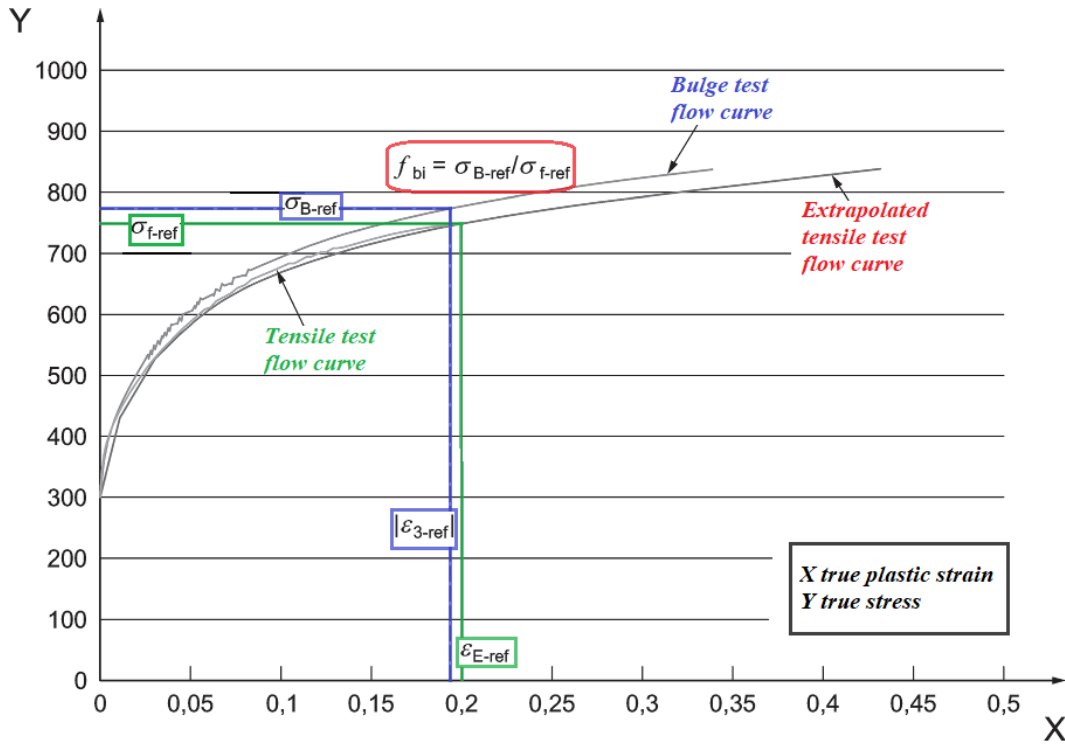


Figure 89 ISO 16808 approach for extrapolating tensile test data with bulge test (50)

4.6.3 Plotting flow curve using anisotropy of the material

In a study at CPF¹⁵, researchers have proposed a new method by considering anisotropy of the material in order to achieve a more accurate determination of the flow stress data from the actual yield point up to the largest strain values obtained from the bulge test. As it was highlighted before, combining the tests can provide more accurate flow stress curve ranging from yield point to the strain at failure in the biaxial stress condition (55).

Benefiting from the following formula, the result of the tensile test (engineering stress-strain data), can be converted into true strain-stress values, that is essential before combining them with the bulge test results.

$$\begin{cases} \varepsilon_{true} = \ln(1 + \varepsilon_{eng}) \\ \sigma_{true} = \sigma_{eng}(1 + \varepsilon_{eng}) \end{cases} .$$

Since the tensile test provides the *uniaxial yield stress*, this value is converted to the biaxial stress using the following equation,

¹⁵ Center for Precision Forming, The Ohio State University

$$\sigma_{biaxial} = \sigma_{uniaxial} \sqrt{\frac{(1 + r_0)r_{90}}{r_0 + r_{90}}}.$$

Where r_0 and r_{90} are the Lankford coefficients defining the anisotropy of the material in rolling and transverse directions, respectively. The *biaxial yield stress* (derived from the above relation) would become as the first point of the flow stress curve. This point is included in the data point obtained from the bulge test, and the curve is fitted into these data points (55).

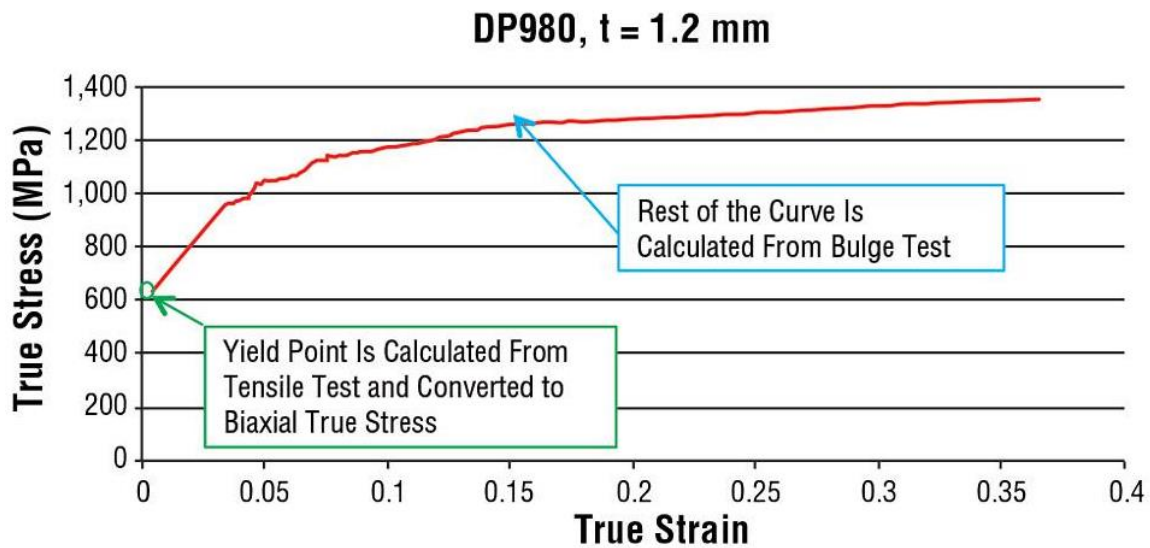


Figure 90 converting uniaxial test result to biaxial considering anisotropy (55)

With this method, the flow stress curve entails both the large strain levels from the bulge test and the accurate yield point obtained from the tensile test. This method was exploited extensively at CPF to determine the flow stress of a variety of advanced, high-strength materials, including CP800, DP590, DP980, TRIP1180, TWIP900, and TWIP980 (55).

4.7 POST-NECKING IDENTIFICATION USING ISO 16808

PROCEDURE

In this section the proposed approach in ISO 16808 is employed to identify the flow stress curves of Aluminium 6000 and DP600 steel.

4.7.1 Aluminium 6000 Novelis

The specimen's geometrical and mechanical characteristics, derived from uniaxial tensile test, are given in the table below,

R_m (N/mm²)	273.84	Tensile strength Stress corresponding to the maximum force (F_m)
$R_{p0.2}$ (N/mm²)	146.81	Proof strength, non-proportional extension, Stress at which a non-proportional extension is equal to a specified percentage of the extensometer gauge length (L_e), normally 0.2% .
A (%)	24.47	Percentage of elongation after fracture, permanent elongation of the gauge length after fracture ($L_u - L_o$), where: final gauge length (L_u): gauge length after rupture of the test piece, original gauge length (L_o): gauge length before application of force.
A_{gt} (%)	22.87	Percentage of total elongation at maximum force (F_m)
E (N/mm²)	58610.80	
r @8.00-12.00%	0.55	
r @10.00%	0.57	
n @4.00-6.00% (%)	0.28	
n @10.00-20.00% (%)	0.26	
Thickness (a) (mm)	2.10	
Width (b) (mm)	20.13	
Parallel length	110.00	Parallel portion of the reduced section of the test piece (L_c)
Original length	80.00	Gage length before application of force (L_o)
Original extensometer length	80.00	Original extensometer gage length

Engineering stress – strain curve as well as flow stress curve obtained from tensile test are shown below, where the last valid data coming from tensile test (regarding to the end of uniform elongation) is also highlighted,

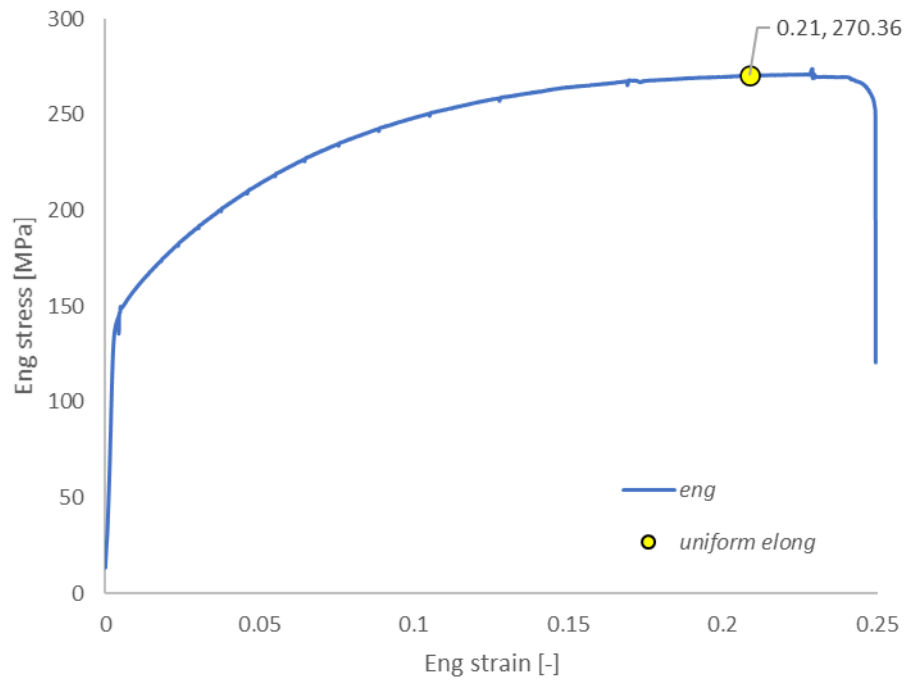


Figure 91 Engineering stress – strain curve aluminium 6000 Novelis

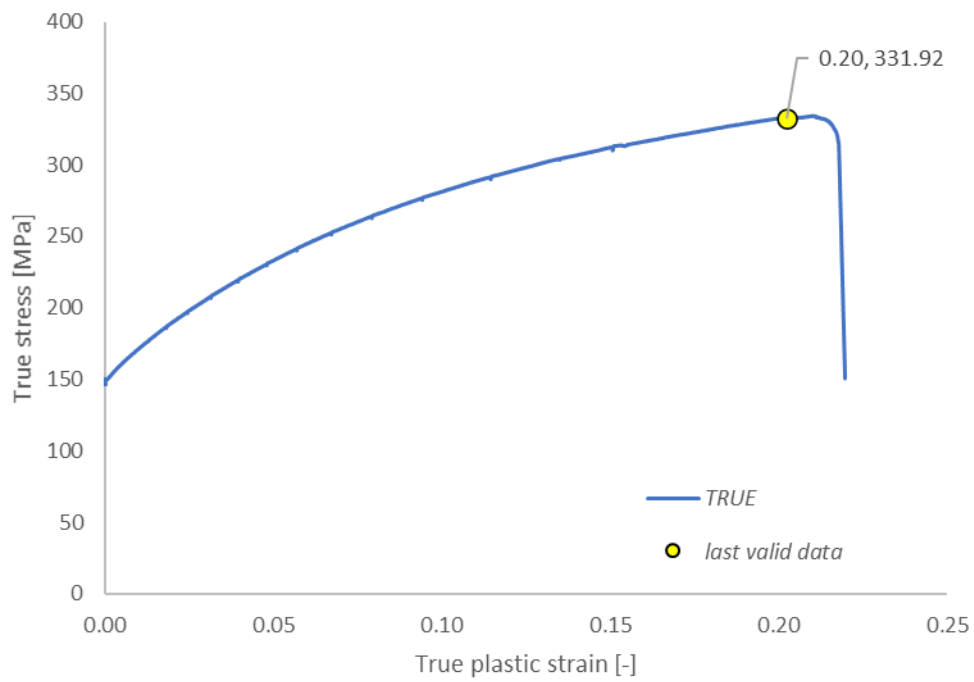


Figure 92 True stress – strain curve aluminium 6000 Novelis

The following figure, shows the flow curves derived from both tensile and bulge test for this material,

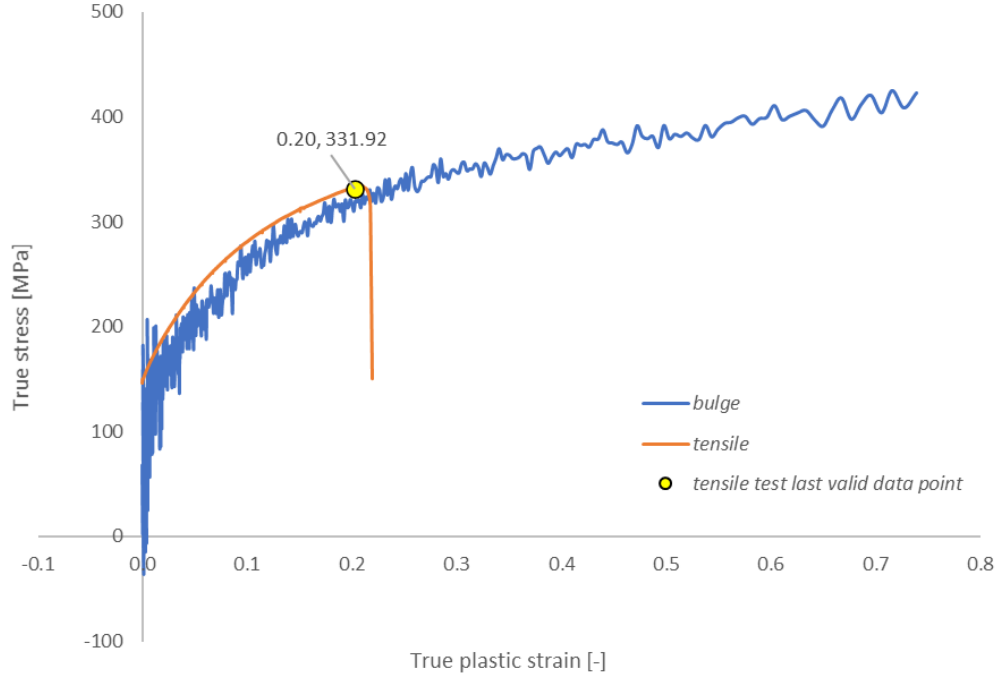


Figure 93 true stress – strain curves for tensile and bulge tests aluminium 6000 Novelis

Up to the end of the uniform elongation, significant fluctuations in bulge test results is evident; besides, tensile test gives larger flow stress values than bulge test in this range. Thus, as discussed before, for smaller value of plastic strain around uniform elongation, tensile test data seems to be more reliable, while for large strains we can extrapolate tensile test based on bulge test results.

4.7.1.1 Tensile test extrapolation in the post-uniform strain range

First step: evaluation of the true plastic strain at uniform elongation (ε_{1-UE}) in the rolling direction is chosen as a *reference value for the equivalent strain* (ε_{E-ref}),

$$\varepsilon_{1-UE} = \varepsilon_{E-ref} \quad .$$

According to the data provided by the supplier,

$$\varepsilon_{1-UE} = \ln \left[1 + \left(A_{gt}/100 - R_m/E \right) \right] = 0.2021 = \varepsilon_{E-ref} \quad .$$

Second step: the stress at the uniform strain of the tensile tests is used as the *reference flow stress* (σ_{f-ref}) i.e. the ultimate tensile strength transformed to a true stress. However, since the exact data point corresponding with the uniform elongation (i.e. A_{gt} , R_m pair) does not exist in the data set, the stress value related to the uniform elongation will be read and used instead of given R_m ,

$$\sigma_{f-ref} = 331.92 \text{ MPa} .$$

Third step: finding the point (m) in the bulge test data satisfying the following condition,

$$\begin{cases} \sigma_{B,m} \cdot |\varepsilon_{3,m}| \leq \sigma_{f-ref} \cdot \varepsilon_{E-ref} \\ \text{and} \\ \sigma_{B,m+1} \cdot |\varepsilon_{3,m+1}| \geq \sigma_{f-ref} \cdot \varepsilon_{E-ref} \end{cases} .$$

Where, is derived as, $\sigma_{f-ref} \cdot \varepsilon_{E-ref} = 67.089 \text{ MPa}$. Now, having this in mind, we should go through the bulge test data and look for the biaxial stress-thickness strain pair giving the same value. So that, the requested reference stress of the bulge test can now be computed by *simple linear interpolation*,

$$\sigma_{B-ref} = \sigma_{B,m} + \frac{\sigma_{B,m+1} - \sigma_{B,m}}{\sigma_{B,m+1} \cdot |\varepsilon_{3,m+1}| - \sigma_{B,m} \cdot |\varepsilon_{3,m}|} \cdot (\sigma_{f-ref} \cdot \varepsilon_{E-ref} - \sigma_{B,m} \cdot |\varepsilon_{3,m}|) .$$

Here, according to the bulge test data, $\sigma_{B-ref} = 322.77 \text{ MPa}$.

Fourth step: biaxial stress ratio (f_{bi}) calculation, obtained by,

$$f_{bi} = \frac{\sigma_{B-ref}}{\sigma_{f-ref}} = \frac{322.77}{331.92} = 0.972$$

As described before, extrapolation is done by adding the bulge tests data at equivalent strains larger than the uniform strain of the tensile test to the uniaxial stress strain curve.

According to the above-mentioned procedure, the following result for tensile test extrapolation is obtained,

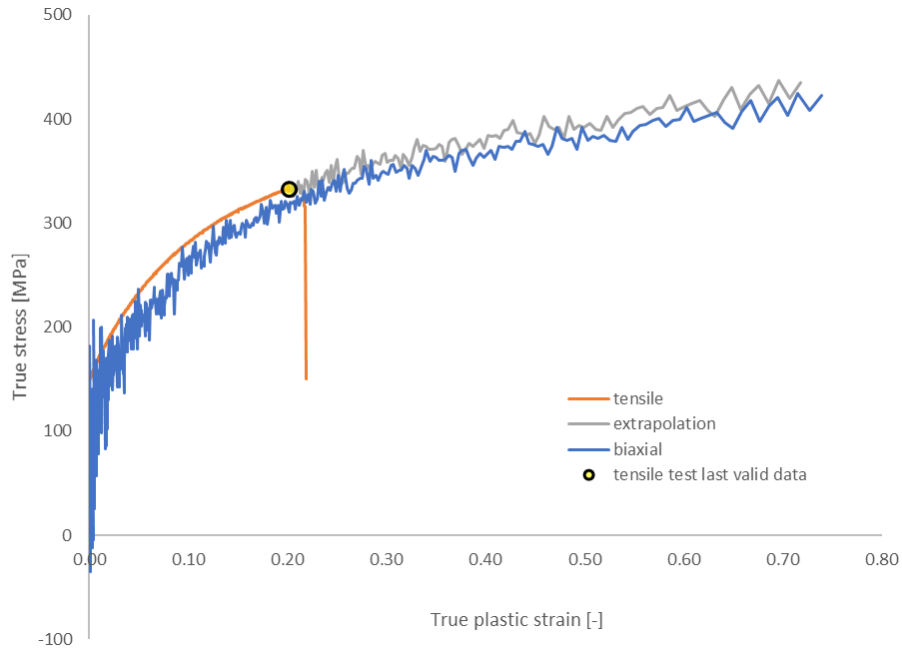


Figure 94 flow stress curve from tensile test data extrapolation with bulge test-aluminium 6000 Novelis

- **Swift/Hockett-Sherby hardening law**

In this section, Swift/Hockett-Sherby hardening law is applied to tensile test results, where also the result will be compared with the extrapolation using bulge test.

Firstly, we consider the extrapolation of tensile test data only through applying SHS hardening law, where merely the error coming from the strain range below uniform elongation is considered. The observed RMSE of fitting SHS 0.75 is calculated to be 0.73.

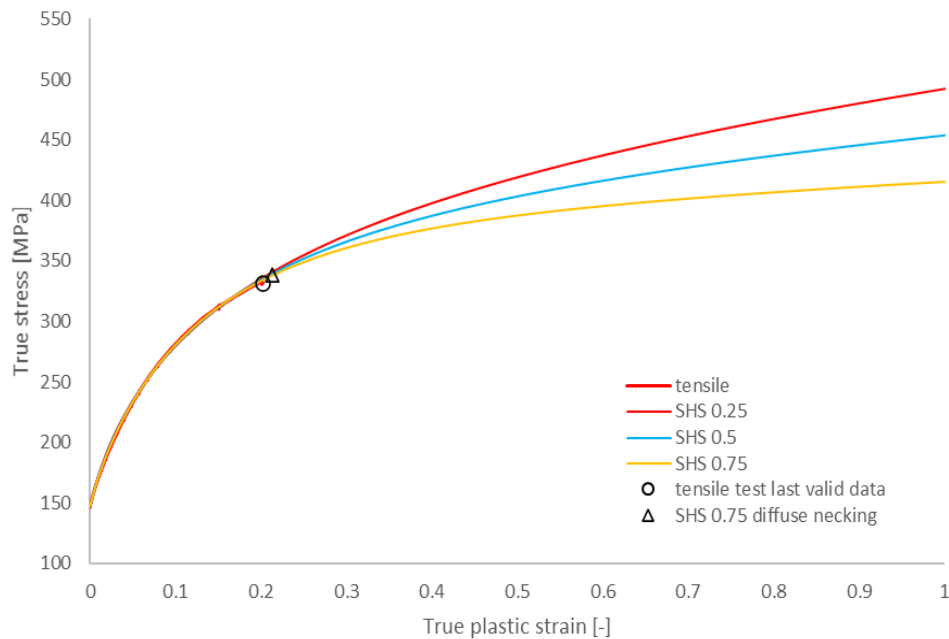


Figure 95 tensile test extrapolation using SHS hardening law-aluminium 6000

With regard to the tensile test data extrapolation using bulge test data, as the number of data points resulted from tensile test is much larger than that of bulge test, in order to reduce the error and have a better hardening law fitting, we need to have a *uniform distribution of data points along the strain range*. To see the effect of data refinement, a comparison is made to show the quality of curve fitting in figures below,

So without data refinement,

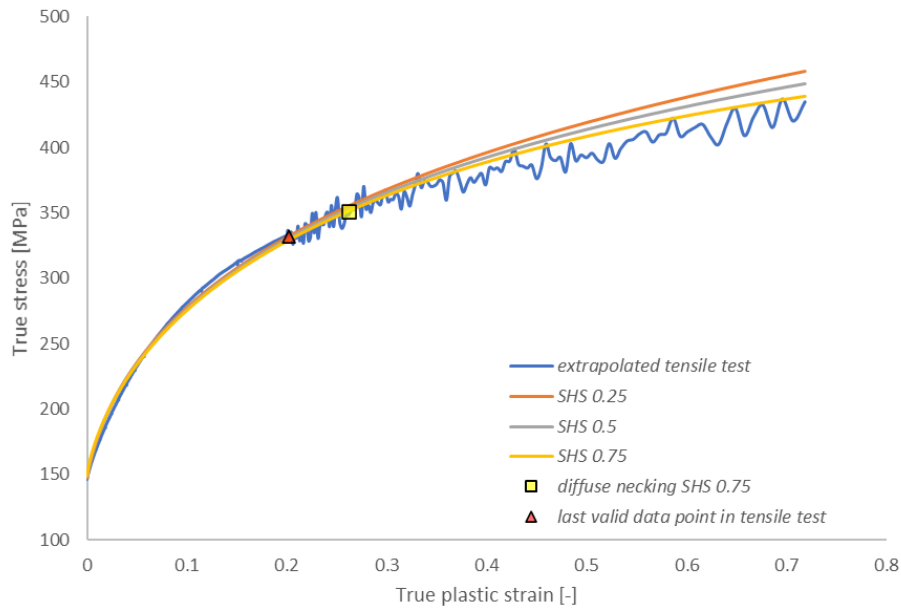


Figure 96 tensile test data extrapolation using bulge test data fitted by SHS hardening law-without data refinement

With data refinement,

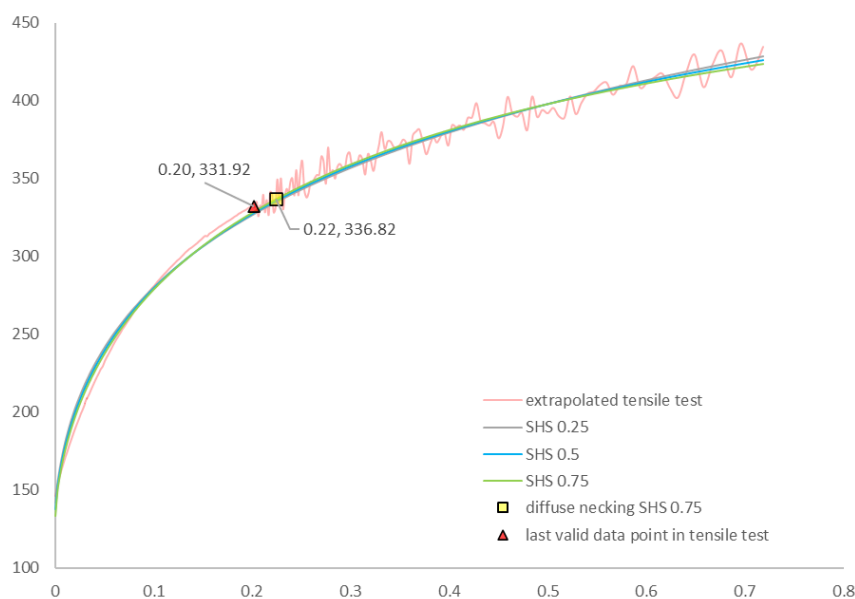


Figure 97 tensile test data extrapolation using bulge test data fitted by SHS hardening law-with data refinement

It can be concluded from the above figures that, data refinement will lead to better fitting for strains larger than uniform elongation, while it leads to negligible error for small strains.

In case we need to import the result into AutoForm software, we need 50 data points coming from SHS 0.75 hardening law curve fitting as shown in the next figure,

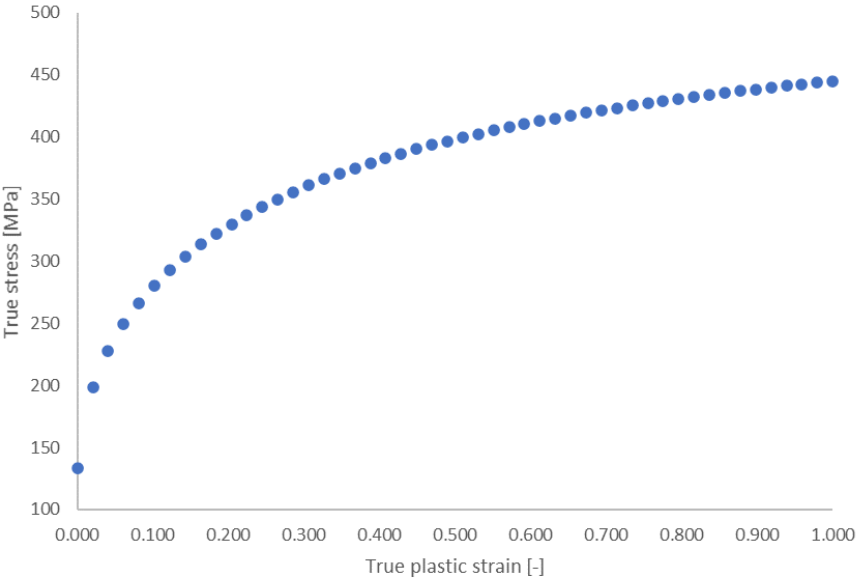


Figure 98 50 data points required to import into FEA SW-aluminium 6000

Furthermore, we can also observe the effect of tensile test data extrapolating with bulge test data, by comparing it with the case in which solely SHS 0.75 hardening law curve is fitted to the tensile test data *before yielding*,

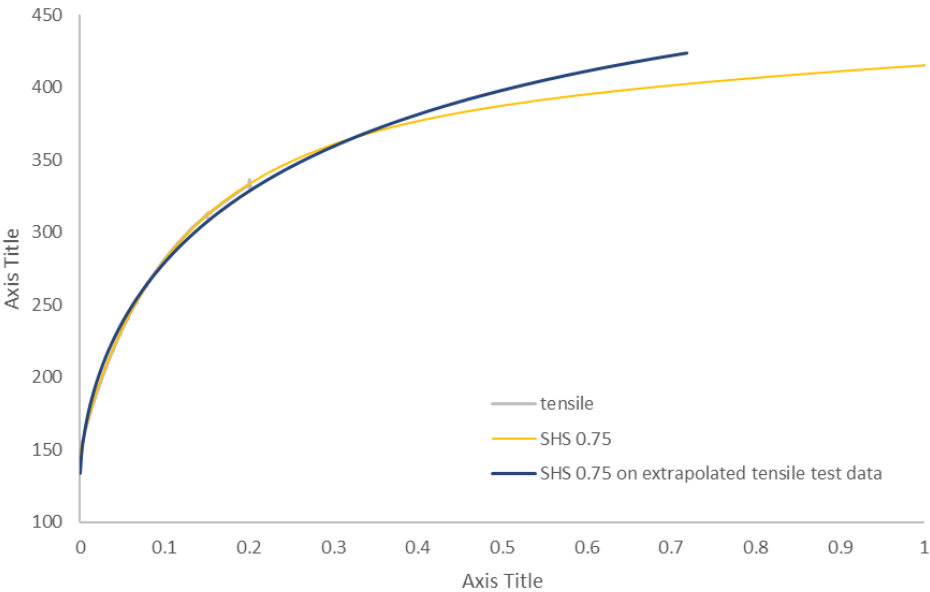


Figure 99 tensile test extrapolations comparison using bulge test data and SHS hardening law-aluminium 6000

- ***κ -exponent function***

The capability of κ -exponent function as a fitting function for aluminium 6000 is observed here and a comparison is also made with HS hardening law.

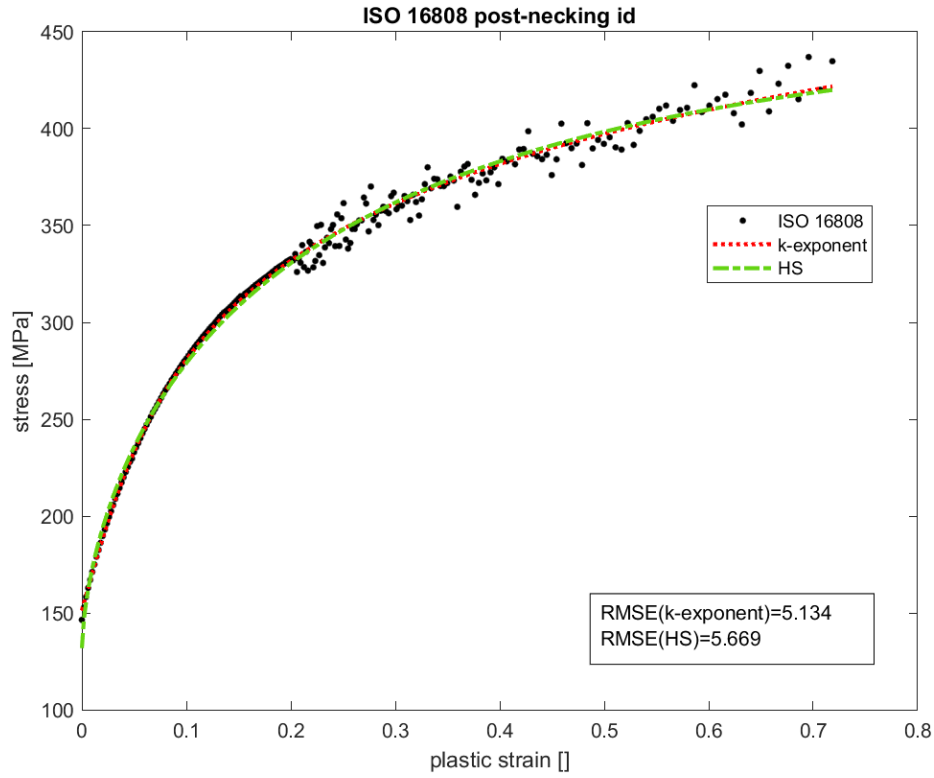


Figure 100 Al6000 flow stress curve fitting, κ -exponent function and HS hardening law using ISO16808

κ -exponent function resulted in the lowest RMSE value among other hardening laws, with a very good behaviour in low values of strain.

4.7.2 DP600 1.2mm Arcelor

The specimen's geometrical and mechanical characteristics derived from uniaxial tensile test are given in the table below,

R_m (N/mm²)	583.51	Tensile strength Stress corresponding to the maximum force (F_m)
$R_{p0.2}$ (N/mm²)	350.31	Proof strength , non-proportional extension, Stress at which a non-proportional extension is equal to a specified percentage of the extensometer gauge length (L_e), normally 0.2% .
A (%)	26.29	Percentage of elongation after fracture , permanent elongation of the gauge length after fracture ($L_u - L_o$), where: final gauge length (L_u) : gauge length after rupture of the test piece, original gauge length (L_o) : gauge length before application of force.
A_{gt} (%)	19.88	Percentage of total elongation at maximum force (F_m)
E (N/mm²)	79298.27	
r_m @ 4%-16.00%	0.90	
n @4.00-6.00% (%)	0.25	
n @10.00-20.00% (%)	0.21	
Thickness (a) (mm)	1.21	
Width (b) (mm)	19.69	
Parallel length	110.00	Parallel portion of the reduced section of the test piece (L_c)
Original length	80.00	Gage length before application of force (L_o)
Original extensometer length	80.00	Original extensometer gage length

4.7.2.1 Tensile test extrapolation in the post-uniform strain range

Working on the data sheet given by the supplier, the corresponding flow curves for tensile and bulge tests can be shown as below,

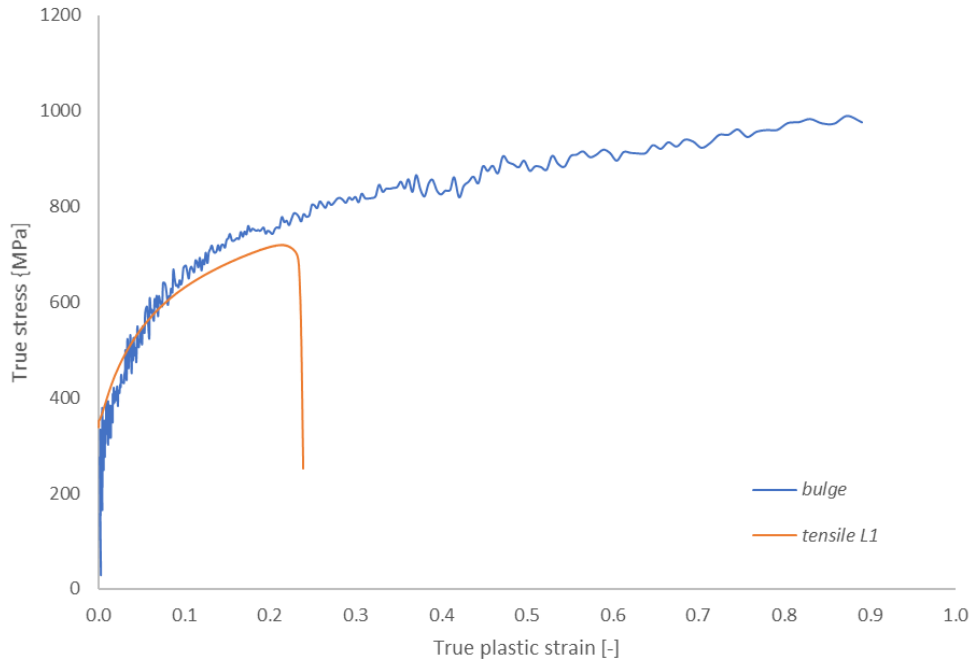


Figure 101 True stress – strain curve DP600

To extrapolate tensile test data beyond uniform elongation, again we follow the following steps,

First step: the reference value for the equivalent strain (ϵ_{E-ref}) is considered to be the true plastic strain at uniform elongation (ϵ_{1-UE}),

$$\epsilon_{1-UE} = \epsilon_{E-ref} .$$

According to the data given by the supplier, (N.B. since the given ultimate tensile strength data point, corresponding to the uniform elongation, cannot be found exactly in the data sheet, the stress value at uniform elongation will be used instead of R_m in the next relations).

$$\epsilon_{1-UE} = \ln \left[1 + \left(A_{gt}/100 - R_m/E \right) \right] = 0.1752 = \epsilon_{E-ref} .$$

Second step: the stress at the uniform strain of the tensile tests is used as the reference flow stress (σ_{f-ref}) i.e. the ultimate tensile strength transformed to a true stress. However, as discussed before, this value will be substituted by the stress value given in the data sheet in front of the uniform elongation,

$$\sigma_{f-ref} = 700.37 \text{ MPa} .$$

Third step: The reference stress in the bulge test should be through this simple linear interpolation,

$$\sigma_{B-ref} = \sigma_{B,m} + \frac{\sigma_{B,m+1} - \sigma_{B,m}}{\sigma_{B,m+1} \cdot |\varepsilon_{3,m+1}| - \sigma_{B,m} \cdot |\varepsilon_{3,m}|} \cdot (\sigma_{f-ref} \cdot \varepsilon_{E-ref} - \sigma_{B,m} \cdot |\varepsilon_{3,m}|) .$$

While $\sigma_{f-ref} \cdot \varepsilon_{E-ref} = 122.67 \text{ MPa}$.

Here, according to the bulge test data sheet, $\sigma_{B-ref} = 743.66 \text{ MPa}$.

Fourth step: biaxial stress ratio (f_{bi}) calculation, obtained by,

$$f_{bi} = \frac{\sigma_{B-ref}}{\sigma_{f-ref}} = \frac{743.66}{700.37} = 1.054 .$$

The following figure shows the result of the above procedure in order to extrapolate tensile test beyond uniform elongation. As discussed before, bulge test cannot present properly the behaviour of the material for strains below the uniform elongation, while on the other hand, data derived from tensile test above uniform elongation is not valid. Hence, to have a good observation, both tests are required to be conducted.

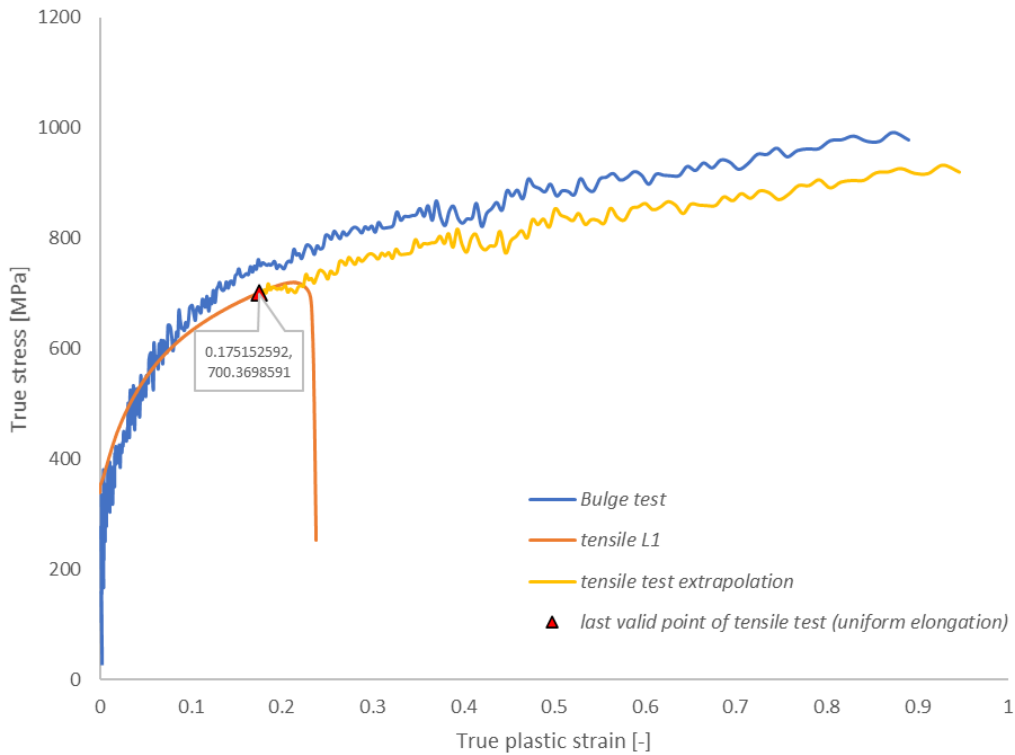


Figure 102 flow stress curve from tensile test data extrapolation with bulge test-DP600

- **Swift/Hockett-Sherby hardening law**

We can also apply Swift/Hockett-Sherby hardening law and observe the fitting error. Moreover, the result will be compared with the extrapolation using bulge test.

Firstly, we consider the extrapolation of tensile test data only through applying SHS hardening law, where merely the error coming from the strain range below uniform elongation is considered.

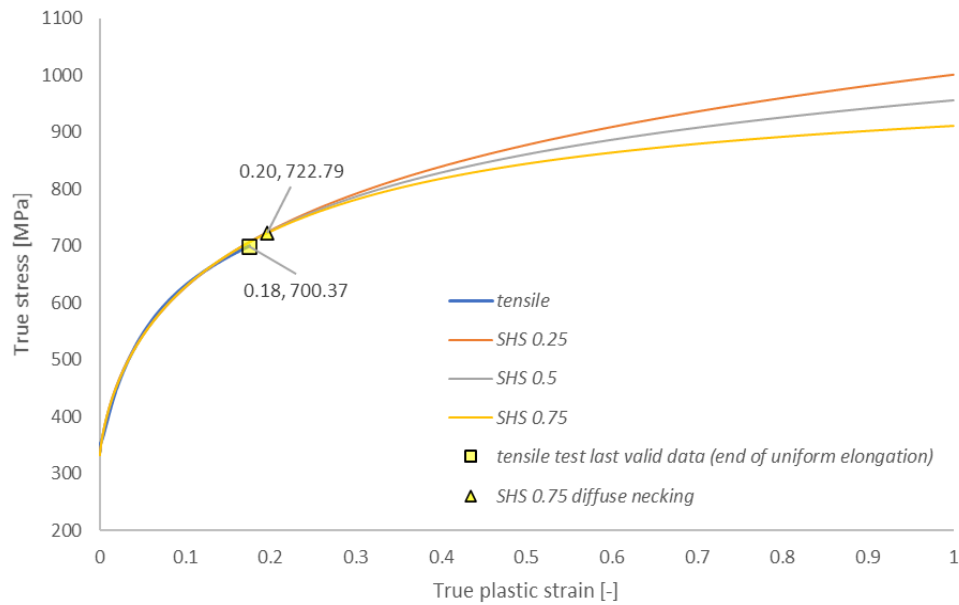


Figure 103 tensile test extrapolation using SHS hardening law-DP600

Data refinement to obtain quality hardening law fitting is also applied here. A comparison is made to show the quality of curve fitting in figures below,

Without data refinement,

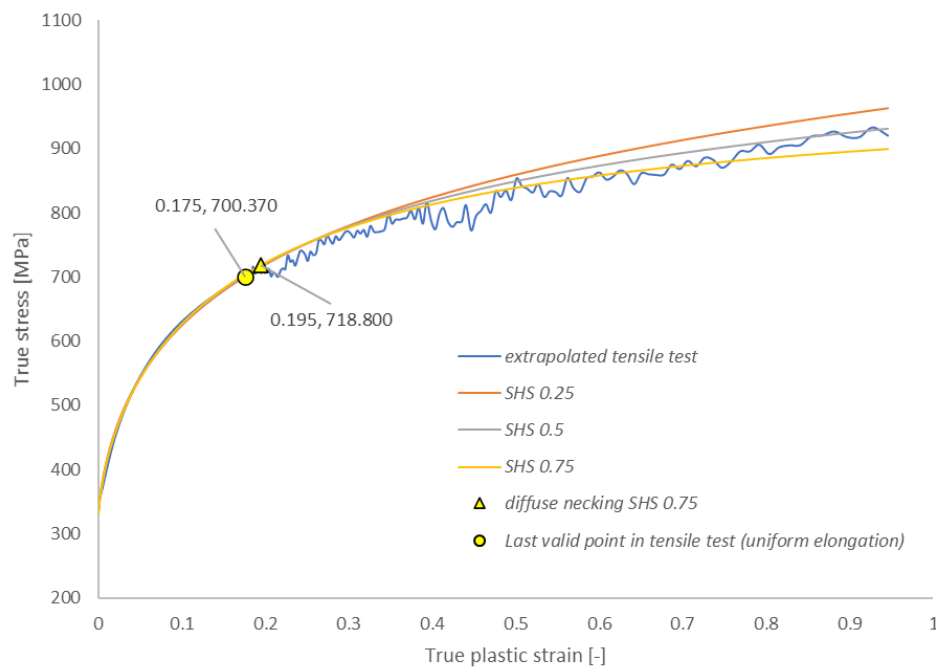


Figure 104 tensile test data extrapolation using bulge test data fitted by SHS hardening law-without data refinement

With data refinement,

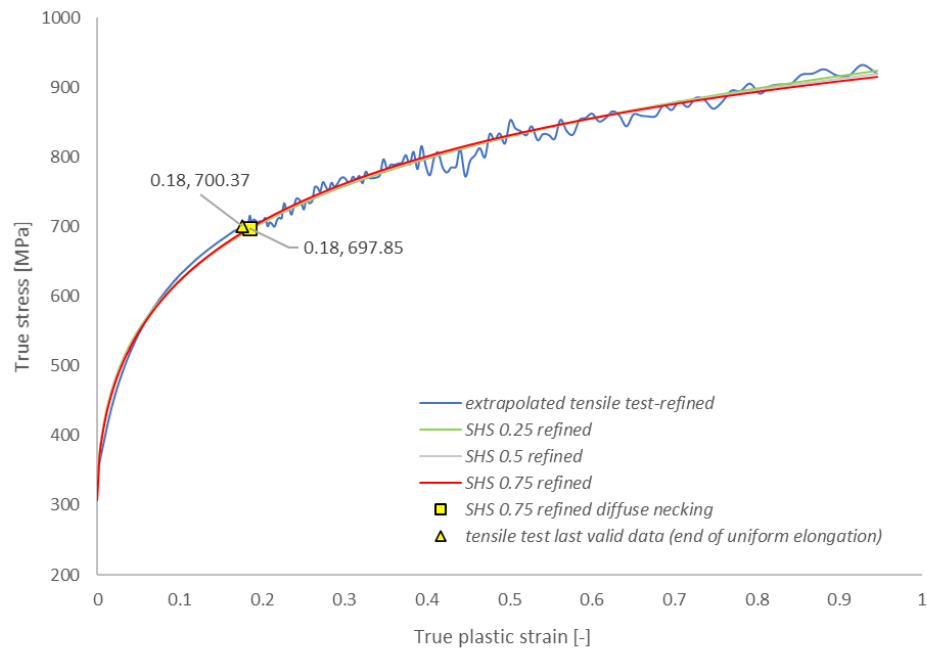


Figure 105 tensile test data extrapolation using bulge test data fitted by SHS hardening law-with data refinement

By employing SHS 0.75 the lowest RMSE of 11.33 is attainable.

To make data usable as an input for AutoForm, the 50 data point are reported in the following figure,

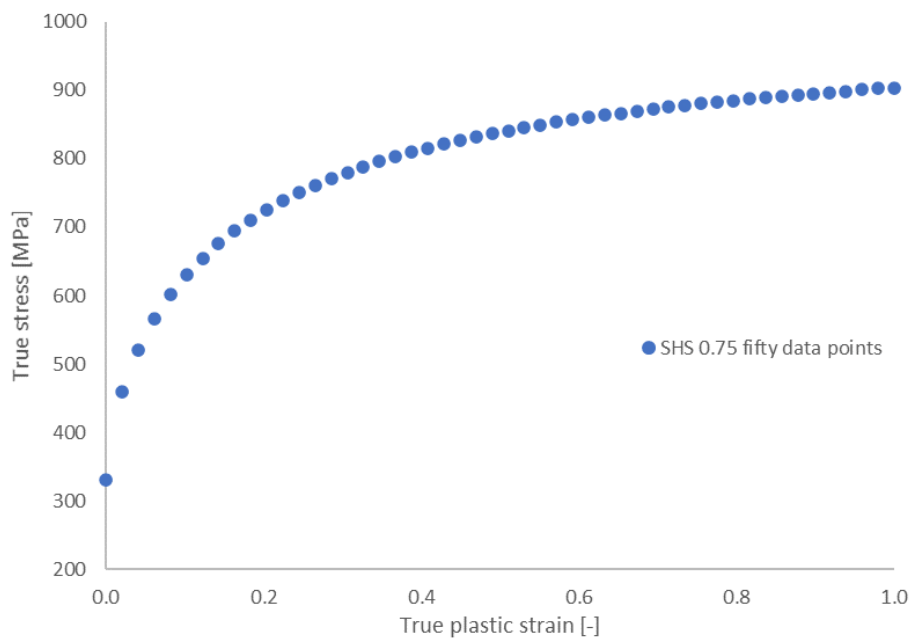


Figure 106 50 data points required to import into FEA SW-DP600

In order to see the effect of using bulge test data in extrapolating tensile test, we can compare the above result with a case in which the extrapolation is done only by minimising the sum of the residuals up to yield point,

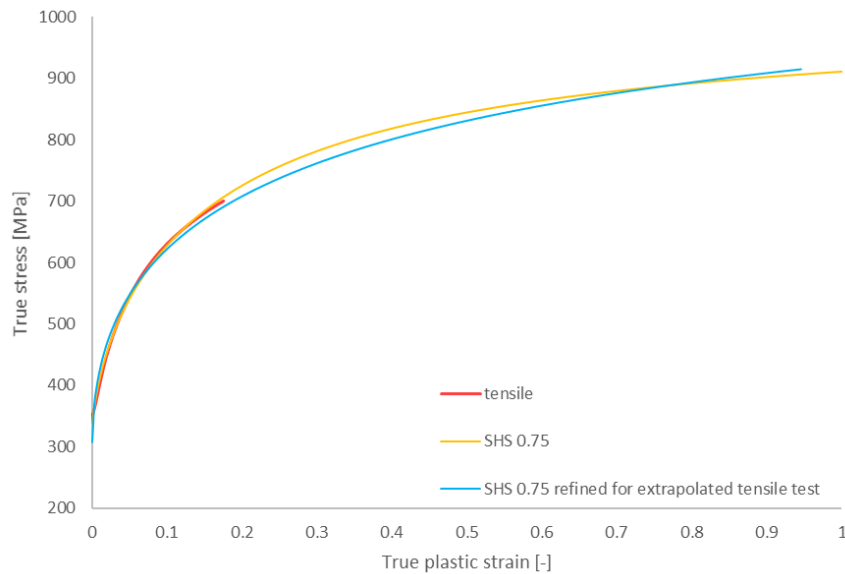


Figure 107 tensile test extrapolations comparison using bulge test data and SHS hardening law-DP600

- ***k*-exponent function**

κ -exponent function is employed in order to compare its fitting ability with that of Hockett-Sherby hardening law.

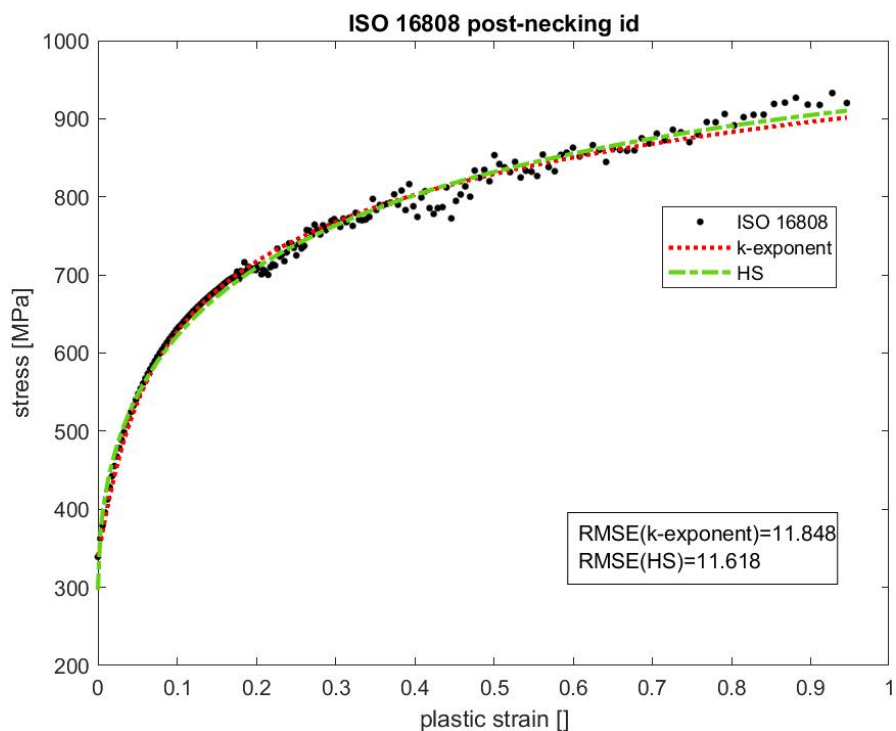


Figure 108 comparison between the flow stress curve fitting of DP600 using ISO 16808

As it can be seen from the above figure, κ -exponent provides a very good fit for small values of strain than HS; however, HS performs better in large deformation. It can be concluded that a linear combination of κ -exponent function and a non-saturated hardening law can attain a very acceptable outcome.

**CHAPTER FIVE: POST-NECKING TENSILE STRESS—
STRAIN BEHAVIOUR IDENTIFICATION OF AHSSs
USING DIGITAL IMAGE CORRELATION TECHNIQUE**

5.1 INTRODUCTION

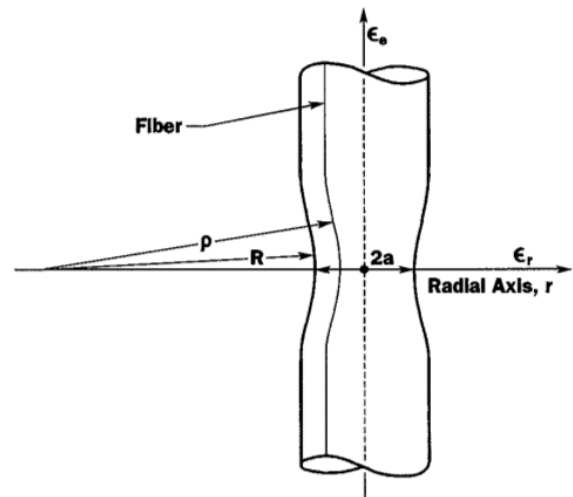
It is well known that in tensile testing, the uniform extension will be limited when the tensile load reaches a maximum value of the material. At this point the test sample starts to neck; so that, the state of stress changes progressively from the *simple uniaxial tension* to a *complicated condition of triaxial stress* in case of a round bar or to a *biaxial stress state* for a thin strip. Because the onset of necking hinders the assumption of uniaxial state of stress, it is impossible to determine a uniaxial true stress-strain relation by the standard tensile test once necking starts to progress. Thus, for applications in which strain exceeds its value at the onset of necking, merely the standard tensile test cannot provide adequate information for material modelling. It will considerably limit the use of FEM for large deformation applications, such as contact forming. Hence, some methods have to be found to identify the post-necking behaviour (74).

It is already demonstrated in chapter two that the hardening behaviour beyond necking can be estimated by extrapolation of the hardening behaviour before the point of maximum uniform elongation. Unfortunately, EM may yield to different results, depending on the hardening law which is fitted to the available experimental data.

5.2 BRIDGMAN METHOD: YES, BUT NOT FOR A FLAT SPECIMEN

Bridgman method (75) has already been discussed in chapter three. Herein, based on a number of assumptions, it will be seen why this method cannot be used in the case of flat samples!

He had three main assumptions, in developing a method aimed at finding the true stress-strain relation beyond necking for a *round bar* (74),



(A) The strain distribution in the minimum section is uniform,

$$\varepsilon_r = \varepsilon_t = -\frac{\varepsilon_a}{2}$$

ε_r radial strain
 ε_r hoop strain
 ε_a axial strain

Aronofsky (76) has shown that they can be assumed uniform across the minimum section. Therefore assumption (A) can be considered reliable (74).

(B) A longitudinal grid line is deformed into a curve at the neck so that its curvature $1/\rho$ is,

$$\frac{1}{\rho} = \frac{r}{aR}$$

ρ radius of curvature of the grid line
 r radius of actual cross section
 a radius of the smallest cross section
 R radius of curvature of the neck

This hypothesis (B) was verified experimentally by Davidenkov and Spiridonova (77).

(C) the ratios of the principal stresses remain constant during loading.

Assumption (C) is not fully verified although it can be assumed as a first approximation (76). Besides, FEA (78) has demonstrated that the stress distribution at the minimum cross section can be approximately defined by Bridgman's equations (74).

Consequently, it is acceptable that if (a) and (R) are precisely observed, Bridgman's correction method can calculate the true stress-strain relation beyond necking as a first approximation in a **rod** (74).

However, Bridgman's correction method is not a handy method in practice; *a set of experiments with various loading conditions is needed to determine the radius of curvature R and the minimum radius a* , which are quite problematic (74). Bridgman also extended his correction method to *flat bars*; however, it is proved that necking for flat samples is far more complicated compared with rods with their circular cross section (74).

Generally, for thin strips two types of instability (flow instability) can be considered;

- *Diffuse Necking (longitudinal necking)*

Its span is much larger than the sample thickness, and is similar to necking in rods. It may end in fracture but is normally followed by another instability process, called localised necking.

- *Localised Necking of thin strips*

Here the neck is a narrow band inclined at an angle to the specimen axis (oblique line), as shown in figure below (74).

The difference between localized and diffused neck during necking of a thin strip is clear in the figure.

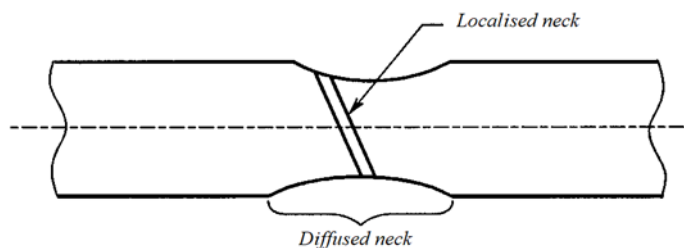


Figure 109 the difference between localized and diffused neck during necking of a thin strip (74)

As soon as localized necking takes place, the width of the sample contracts, but the thickness along the necking band shrinks more, and fracture can happen after a while. *Bridgman's correction method for flat samples does not take into account localized necking*, and so based on the studies of Ling (74), it cannot be applied successfully to flat specimens as all three assumptions were found not to be applicable for flat strips case,

- As it is shown in the following sections, the *strain distribution at the minimum cross-section becomes considerably non-uniform when localized necking begins*. Furthermore, the average axial strain is evaluated significantly smaller than the maximum axial strain at the minimum cross section (76). Hence, even though the instantaneous dimension of the minimum section is already obtained (to compute average axial strain), the equivalent strain is still required to be obtained. As it is implemented here, more complicated techniques such as DIC technique have to be employed to assess strain fields across the minimum cross section (74).
- To obtain the equivalent uniaxial stress, the stress distributions (σ_x and σ_y) in the minimum section must be obtained, where based on Bridgman's method, it requires to *calculate the curvatures of the longitudinal grid lines during necking*. However, in order to measure the curvature, the outer profile and many other longitudinal grid lines across the minimum section should be observed; based on this, Aronofsky's experimental work suggested that, *Bridgman's curvature assumption cannot be applied to flat samples*, as this procedure would make the testing difficult and time consuming (74).
- *stress ratios do not remain constant during loading*, where the *incremental theory of plasticity* should be implemented; this adds more complexity to the analytical solution for the stress distribution at the minimum section (74). This fact not only can be seen in the stress distribution pattern (from uniaxial to biaxial) in the necked zone of the specimen, but as it is discussed later, it also provides us with a better prediction of plastic instability.

5.3 BEHIND THE SCENE: THEORY

In order to describe the plastic behaviour of a material in a general stress state, three elements are required to be employed (48),

- a **Yield Criterion**: a relationship between the stress components at the moment when plastic ‘yielding’ occurs,
- an **Associated Flow Rule**: a relationship between the components of the plastic strain rate and stress,
- a **Hardening Rule**: the evolution of the initial yield stress during the forming process.

Yield function is a relationship among the principal stresses specifying the conditions under which *plastic flow occurs* (48), and normally is defined in the form of an implicit function, like,

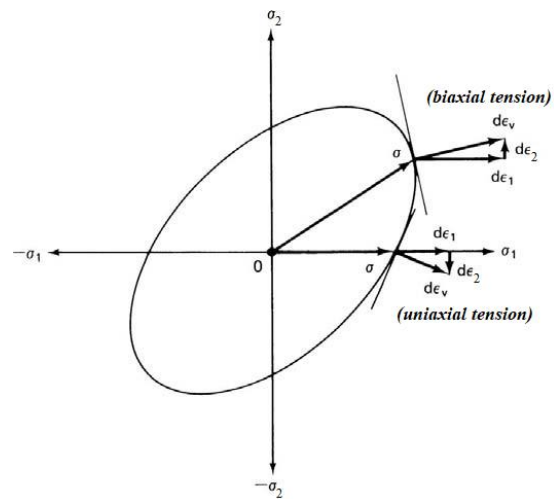
$$f(\sigma_1, \sigma_2, \sigma_3, Y) = 0 \quad .$$

Where $\sigma_1, \sigma_2, \sigma_3$ are the *principal stresses* and Y is the *yield stress* obtained from a simple test (tension, compression or shearing).

Within the range of *elastic deformation*, the strains are defined by *Hooke’s law*. Likewise, for *plastic deformation*, the relation is called the **flow rules** (2). In the most general form the flow rule can be written,

$$d\epsilon_{ij} = d\lambda \left(\frac{\partial f}{\partial \sigma_{ij}} \right) .$$

Regarding to the flow rule, one can interpret it as the *vector sum of the plastic strains which is normal to the yield surface*, this is also called **Normality Principle** (2). In two-dimensions, it can be illustrated as in the figure. So that, if a material is loaded uniaxially beyond its yielding point, the resulting plastic strain is represented by a vector, $d\epsilon_v$ normal to the yield surface, which is the vector sum of $d\epsilon_1, d\epsilon_2$.



5.3.1 Hill's 1948 Yield Criterion: A short review

Theoretical background is described here in considerable details. One can implement even more suitable models to define instability in sheet metal forming. However, obviously, employing more advanced methods needs more parameters to be considered and defined. This fact emphasizes the compelling urge to exploit numerical simulation and mathematical relations in parallel with benefiting from 2D/3D DIC technique.

In 1948, R. Hill proposed an *anisotropic yield criterion* as a generalization of the Huber-Mises-Hencky criterion (79). The material is supposed to have an anisotropy with three orthogonal symmetry planes, and the corresponding yield criterion is defined by a *quadratic yield function* as the following,

$$2f(\sigma_{ij}) \equiv F(\sigma_{22} - \sigma_{33})^2 + G(\sigma_{33} - \sigma_{11})^2 + H(\sigma_{11} - \sigma_{22})^2 + 2L\sigma_{23}^2 + 2M\sigma_{31}^2 + 2N\sigma_{12}^2 = 1$$

Here f is the *yield function*; F, G, H, L, M and N are *constants* specific to the *anisotropy state* of the material, and x, y, z are the principal anisotropic axes. In the case of *sheet metals*, axis 1 is normally *parallel to the rolling direction*, axis 2 is in *the transverse direction* and 3 is *collinear with the normal direction*; so that, the yield criterion may be interpreted as a surface in a six-dimensional space of the stress components. The points located inside the surface represent the elastic states of material deformation, while points on the surface correspond to the plastic state (48).

For the case of **plane stress** ($\sigma_{33} = \sigma_{31} = \sigma_{23} = 0$; $\sigma_{11} \neq 0$; $\sigma_{22} \neq 0$; $\sigma_{12} \neq 0$), the yield criterion becomes,

$$2f(\sigma_{ij}) \equiv (G + H)\sigma_{11}^2 - 2H\sigma_{11}\sigma_{22} + (H + F)\sigma_{22}^2 + 2N\sigma_{12}^2 = 1$$

In case the principal directions of the stress tensor are coincident with the anisotropic axes, (i.e. $\sigma_{11} = \sigma_1$, $\sigma_{22} = \sigma_2$, $\sigma_{12} = 0$), and simplifying constants, F, G, H and N in terms of anisotropy coefficients r_0 and r_{90} , the following equation can be obtained,

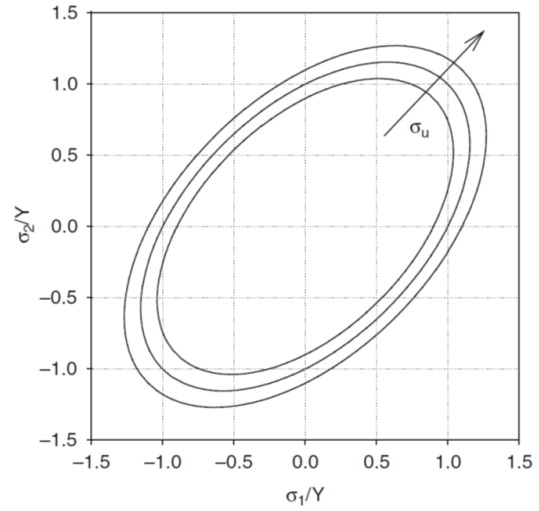
$$\sigma_1^2 - \frac{2r_0}{1+r_0}\sigma_1\sigma_2 + \frac{r_0(1+r_{90})}{r_{90}(1+r_0)}\sigma_2^2 = \frac{r_0(1+r_{90})}{r_{90}(1+r_0)}\sigma_{90}^2$$

This follows that in order to *define the yield under plane stress condition*, three *mechanical parameters*, namely the coefficients r_0 and r_{90} and one of the uniaxial yield stresses σ_0 (or σ_{90}) are needed.

Assuming a material exhibiting only normal anisotropy ($r_0 = r_{90} = r$) and $\sigma_0 = \sigma_{90}$, so that the previous equation can take the following form,

$$\sigma_1^2 - \frac{2r}{1+r}\sigma_1\sigma_2 + \sigma_2^2 = \sigma_u^2$$

Where σ_u is the *initial uniaxial yield stress*. With regard to *isotropic hardening*, if the uniaxial yield stress increases (i.e. loading the material beyond initial yield stress), the yield surface expands uniformly (48).



In this special case of Hill's general anisotropic yield criterion, the *equivalent stress* (σ_{eq}) is a function of the principal stresses (σ_1 and σ_2) and the normal anisotropy coefficient (r). In case x and y directions are aligned with principal directions, the Hill's 48 yield criterion can be rewritten as (48) (80),

$$\sigma_x^2 - \frac{2r}{1+r}\sigma_x\sigma_y + \sigma_y^2 = \sigma_{eq}^2$$

Herein, in order to correct the local stress and strain states at the neck and to obtain a relation between the stress and corresponding plastic strain during deformation process, Hill's normal anisotropic yield criterion and strain fields (measured by DIC technique) must be employed in parallel.

By defining **stress ratio α** , as the ratio of minor stress and major stress, the yield criterion can be rewritten as,

$$\alpha = \frac{\sigma_y}{\sigma_x} \quad \sigma_{eq}^2 = \sigma_x^2 \left(1 - \frac{2r}{1+r}\alpha + \alpha^2 \right)$$

Similar to the idea of Bridgman's correction factor (the ratio of equivalent stress (σ_{eq}) and axial or major stress, σ_x), this approach provides an *instantaneous* true stress correction factor for the 'stress evaluated at necked zone' (80). True local average stress along loading direction at the necked region (major stress, σ_x) can be determined from,

$$\sigma_x = \sigma_{eng,x} e^{\epsilon_x}.$$

Since the equivalent stress and strain will be determined by introducing correction of local stress and strain state at the necked region, using DIC technique, local average strain at neck must be inserted in the above formula for ε_x .

The normal anisotropy coefficient (r) is defined as the ratio of width strain increment ($d\varepsilon_x$) and thickness strain increment ($d\varepsilon_y$),

$$r = \frac{d\varepsilon_y}{d\varepsilon_z} .$$

$d\varepsilon_y$ and $d\varepsilon_z$ can be easily measured directly from *3D DIC experiment*. However, since *2D DIC technique* is used in the lab, $d\varepsilon_z$ can be calculated from *volume consistency condition*. Considering volume remains constant during the *plastic deformation*, one can obtain,

$$d\varepsilon_z = -(d\varepsilon_x + d\varepsilon_y) .$$

Where $d\varepsilon_y$, $d\varepsilon_x$ and $d\varepsilon_z$ are the *increment in true strain* in the *width*, *axial* and *thickness* directions, respectively. In this way, normal anisotropy can be rewritten as,

$$r = \frac{d\varepsilon_y}{-(d\varepsilon_x + d\varepsilon_y)} .$$

Introducing **strain rate ratio (β)**, as the ratio of minor strain rate and major strain rate, one can take the advantage of '*critical (limit) strains*', by taking into account a *proper hardening law* (the same procedure to obtain critical strains is also described for MMFC method). Herein, Ramberg-Osgood strain-hardening law is implemented in Hill's 48 yield criterion, where swift's model is considered for the domain of unstable plastic straining.

As it is discussed in chapter two, the *beginning of necking corresponds to the maximum of the traction force (Considère criterion)*. From the mathematical point of view, this condition can be written as, $dF = 0$. Following simple mathematical manipulations, the *condition of plastic instability* is obtained,

$$\frac{d\sigma}{d\varepsilon} = \sigma .$$

Assuming RO strain-hardening law,

$$\sigma = k \varepsilon_p^n .$$

Then, the condition of plastic instability becomes,

$$\varepsilon_p = n .$$

In other words, according to *Considère* criterion, a material obeying the RO hardening law starts to neck when the plastic strain is equal to the hardening coefficient.

Swift (42) used the *Considère* criterion in order to determine the limit strains in biaxial tension. He analysed a sheet element loaded along two perpendicular directions and applied the *Considère* criterion for each direction. Assuming RO strain hardening law, he obtained the following expressions for the limit strains (48).

f is the *yield function*. $\sigma_1 = f(\alpha)\bar{\sigma}$, considering the simplified equation for Hill's 48.

$$\varepsilon_1^* = \frac{\sigma_1 \left(\frac{\partial f}{\partial \sigma_1}\right)^2 + \sigma_2 \left(\frac{\partial f}{\partial \sigma_2}\right) \left(\frac{\partial f}{\partial \sigma_1}\right)}{\sigma_1 \left(\frac{\partial f}{\partial \sigma_1}\right)^2 + \sigma_2 \left(\frac{\partial f}{\partial \sigma_2}\right)^2} n$$

$$\varepsilon_2^* = \frac{\sigma_2 \left(\frac{\partial f}{\partial \sigma_1}\right)^2 + \sigma_1 \left(\frac{\partial f}{\partial \sigma_1}\right) \left(\frac{\partial f}{\partial \sigma_2}\right)}{\sigma_1 \left(\frac{\partial f}{\partial \sigma_1}\right)^2 + \sigma_2 \left(\frac{\partial f}{\partial \sigma_2}\right)^2} n$$

Thus, the limit strains are derived as functions of the loading ratio α and the mathematical parameters of the material (hardening coefficient n , anisotropy coefficient r , strain-rate sensitivity m , etc), as long as a certain yield function is available.

In the present work, by employing Hill's 48 yield criterion, the limit strains are obtained as,

$$\varepsilon_1^* = \frac{[1 + r(1 - \alpha)] \left(1 - \frac{2r}{1+r} \alpha + \alpha^2\right)}{(1 + r)(1 + \alpha) \left(1 - \frac{1 + 4r + 2r^2}{(1 + r)^2} \alpha + \alpha^2\right)} n \quad \varepsilon_2^* = \frac{[(1 + r)\alpha - r] \left(1 - \frac{2r}{1+r} \alpha + \alpha^2\right)}{(1 + r)(1 + \alpha) \left(1 - \frac{1 + 4r + 2r^2}{(1 + r)^2} \alpha + \alpha^2\right)} n$$

Going back to the strain rate ratio, now one can obtain the ratio in terms of r and α using the above relations,

$$\beta = \frac{(1 + r) \alpha - r}{1 + r - r\alpha} .$$

However, since finding strain rate ratio and normal anisotropy are not a difficult task through image processing, the inverse relation is much more beneficial here,

$$\alpha = \frac{\sigma_y}{\sigma_x} = \frac{(1 + r) \beta + r}{1 + r + r\beta} .$$

Employing incremental work per volume definition ($dw = \sigma_1 d\varepsilon_1 + \sigma_2 d\varepsilon_2 + \sigma_3 d\varepsilon_3 = \sigma_{eq} d\varepsilon_{eq}$) and considering biaxial state of stress ($\sigma_3 = 0$), 'equivalent plastic strain' can be found by,

$$\sigma_{eq} d\varepsilon_{eq} = \sigma_1 d\varepsilon_1 + \sigma_2 d\varepsilon_2 = \sigma_1 d\varepsilon_1 (1 + \alpha\beta) \quad \longrightarrow \quad d\varepsilon_{eq} = d\varepsilon_1 \frac{\sigma_1}{\sigma_{eq}} (1 + \alpha\beta)$$

From the flow rules, strain increment ratio was written previously in terms of normal anisotropy and stress ratio. Thus, now, equivalent strain increment can be deduced in terms of strain increment ratio and normal anisotropy,

$$d\varepsilon_{eq} = d\varepsilon_1 \frac{\sigma_1}{\sigma_{eq}} \left(1 + \frac{(1+r)\beta + r}{1+r+r\beta} \beta \right).$$

Rewriting σ_1/σ_{eq} in terms of r and β , the final relation for *equivalent plastic strain increment* can be found as follows,

$$d\varepsilon_{eq} = d\varepsilon_1 \frac{1+r}{\sqrt{1+2r}} \sqrt{1 + \beta^2 + \frac{2r}{1+r} \beta}$$

All in all, this method is aimed at evaluating *equivalent stress and equivalent plastic strain* by taking into account a *specific strain hardening law*, a *yield criterion* and *DIC technique results*. The resulted equivalent stresses and strains can be interpreted as the corrected true stresses and strains at necked region during deformation, respectively.

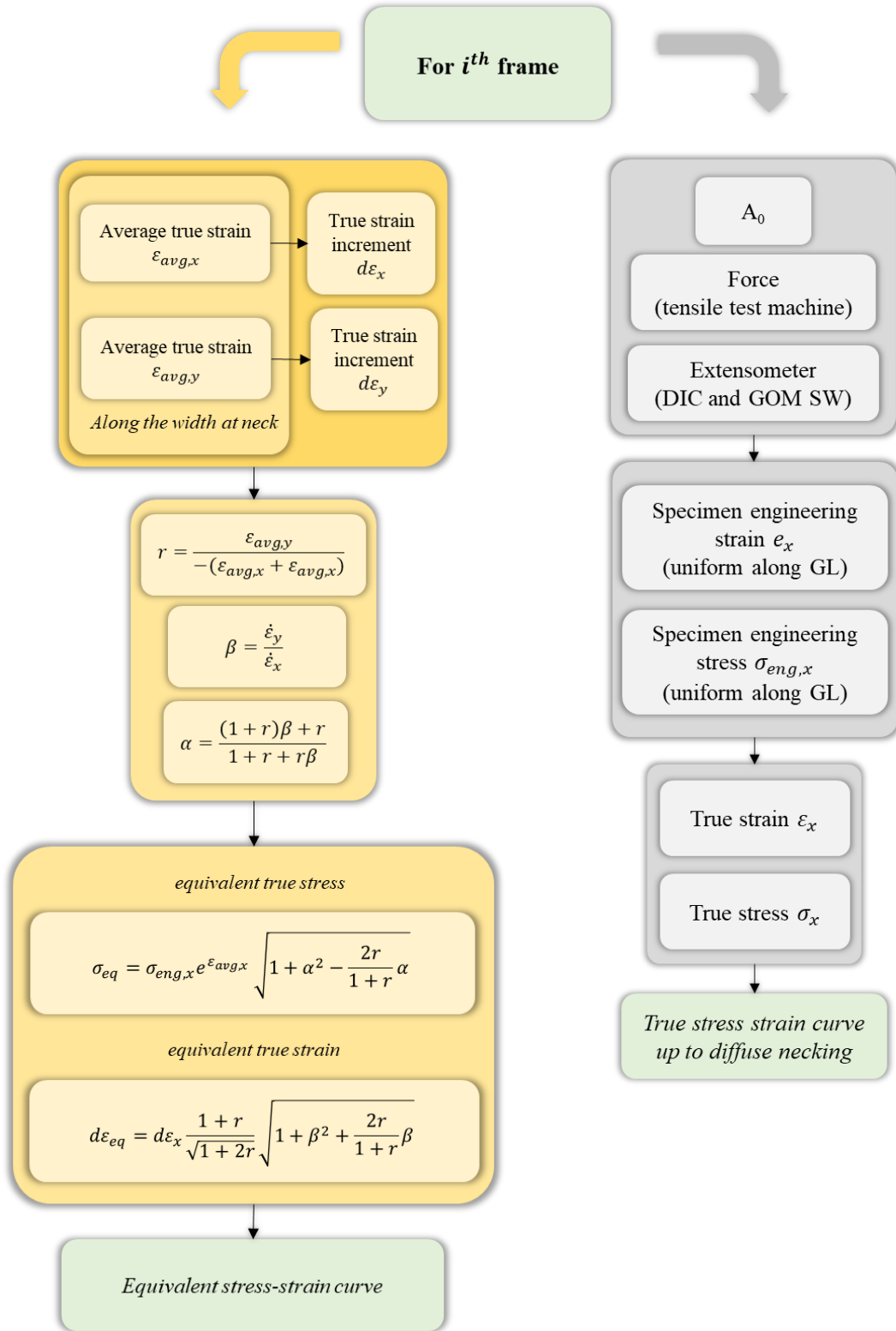


Figure 110 equivalent stress and equivalent plastic strain flowchart

5.4 NECKING: CRITERIA AND MECHANISM

Generally, two types of behaviour can be seen in metallic materials subjected to plastic deformations:

- **Hardening**, caused by the accumulation of plastic deformation,
- **Softening**, caused by the section reduction and the imperfections as well due to the deformations inside the material.

As long as the hardening effect is the dominant one, the localized necking can be ceased; looking more closely, the adjacent material will deform further if the localized deformation produces larger force than the force induced by the adjacent material. Localized necking will take place when the material's maximum force is reached, and the deformation cannot be passed to the adjacent material (81).

5.4.1 Criteria and prediction

In contrast with the *Considère criterion*, in which *only the strain hardening effect was included*, there are some other factors affecting the hardening behaviour, and so must be considered in the study of necking; the strain state by necking plays an important role, beside the *strain rate* and the *temperature* (81).

During the localized necking, the material deforms under **plane strain condition**. Within the uniform deformation period of a simple tensile test, the stress component in width direction (σ_2) is zero, but its value starts to increase during the diffuse necking. Consequently, the increment in the *tensile stress* (σ_1) comes from two factors; firstly because of the hardening effect, and secondly due to the change of the stress state. The material remains quasi-stable without the risk of rupture before the occurrence of plane strain condition. However, gradually the material loses its capability to carry more force, and eventually fails where further deformation will be localized, leading to rupture in the sheet material (81).

As we will see in the following, the engineering strain-stress diagram obtained from tensile test reveals that as the deformation continues, material failure does not take place immediately when force reaches its peak value; interestingly though, *the reaction force inside the specimen remains almost constant until the onset of localized necking*. While the *reduction in the loading force shows the imminence of rupture in the specimen* (81).

Hence, the maximum force criterion cannot be a comprehensive approach to precisely anticipate the fracture. Based on the point of view, the Modified Maximum Force Criterion (MMFC) was proposed (81).

Herein, the introduction of the MMFC model is merely aimed at presenting a more recent (which is still extending) and at the same time a more exact method to predict necking rather than the *Considère* criterion. The study of this model is presented at Appendix B, and can be considered in future observations.

5.5 TENSILE TEST RESULTS OF CP 1400HD SUBSIZE SPECIMEN USING DIC TECHNIQUE AND GOM CORRELATE SW

For detailed analysis on necking and obtaining average values of local strain components (ϵ_x and ϵ_y) at various overall tensile strain levels, a *transversal section, at the necked region* is chosen as shown in the figure,

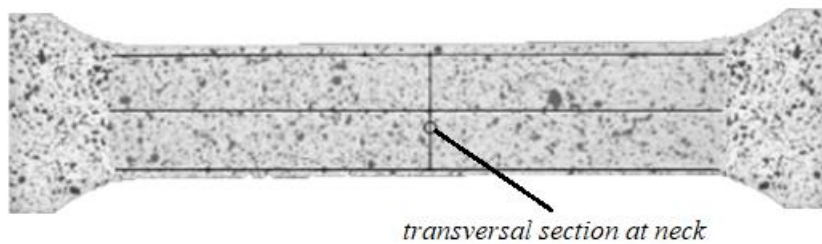


Figure 111 the position of the transversal section at neck-GOM SW

In this section, a transition from uniform strain distribution to a non-uniform one can be anticipated when the strain level inside the specimen rises. Up to the point of maximum load (diffuse necking), the deformation is almost uniform along the specimen GL. From diffuse necking until the formation of localised bands, where the deformation is no longer uniform and uniaxial, the evaluation of the equivalent stress and equivalent plastic strain in the necked region is the main goal of the following discussion.

Localised necking is always accompanied with void formation; since the volume constancy law is only valid up to the small amount of void formation in the necked section, this method can be safely used up to the deformation localisation in the specimen (82) (80).

5.5.1 Position of the neck

The uniform elongation of material ends gradually with the concentration of deformation at a local region, where the location must be known in order to study the local strain distribution which in turn is crucial here to obtain the equivalent stress and strain values during the test.

In this section, firstly, benefiting from the three longitudinal sections constructed along the GL in GOM, the position of the neck will be evaluated. Then, transversal section at necked region is also built to monitor the strain distributions both parallel (ε_x) and perpendicular (ε_y) to the tensile direction.

Although the local strain distribution along the GL will be observed in more detail in the next section, the distribution for larger values of overall strain is presented here in order to evaluate the position of the neck. Below, local distribution of ε_{xx} is shown up to 8.31% engineering strain level,

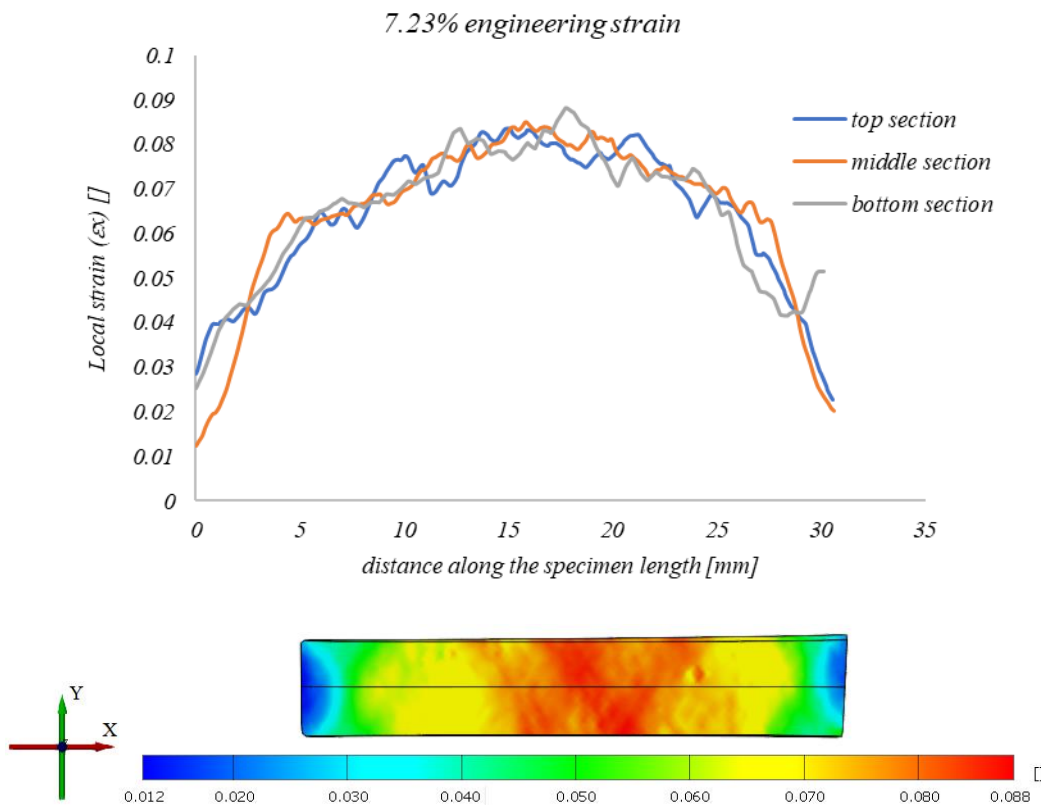


Figure 112 local long. strain distribution along the GL at 7.23% engineering strain level

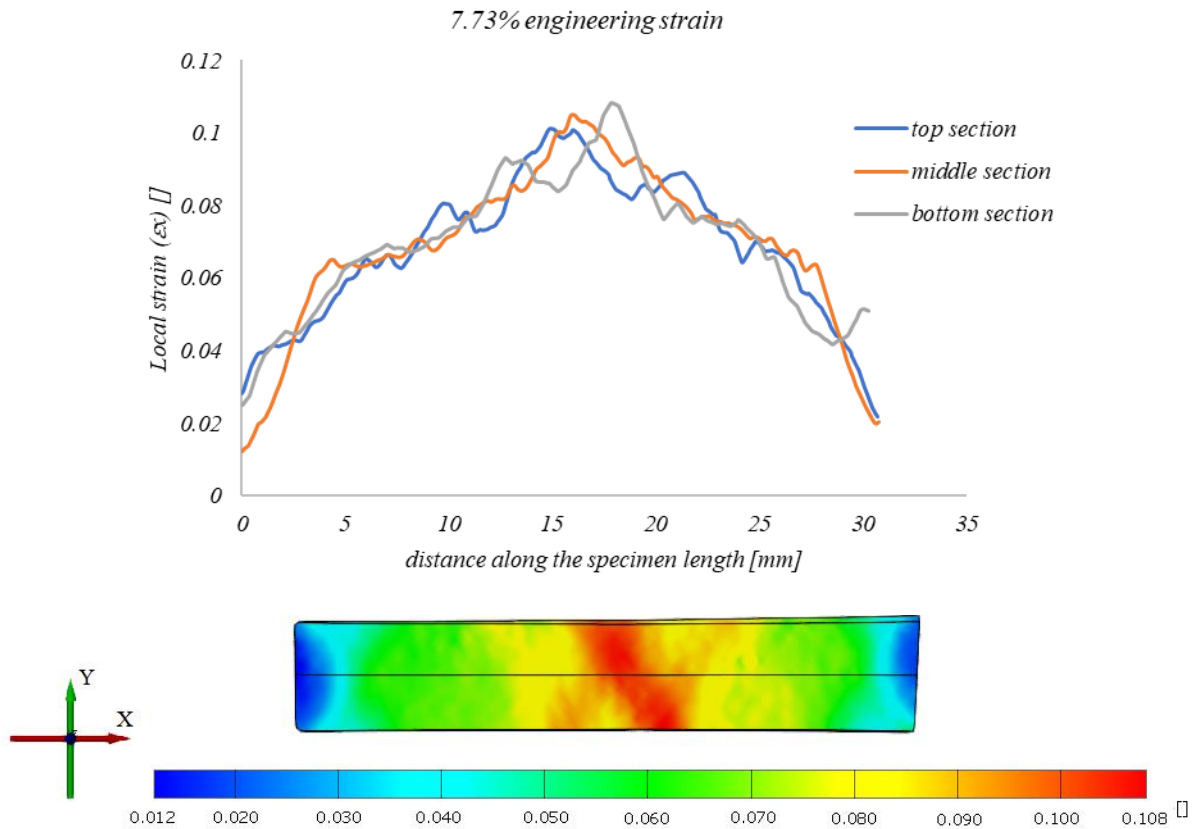


Figure 113 local long. strain distribution along the GL at 7.73% engineering strain level

By comparing the trends of longitudinal strains in three sections (top, middle and bottom), it can be concluded that prior to localised necking longitudinal local strain in all the sections along the GL have the same variations. However, as deformation goes on, different trends can be seen in the three sections. As an example, at 8.31% overall specimen engineering strain, we can see peaks form at different locations along the GL, in figure below,

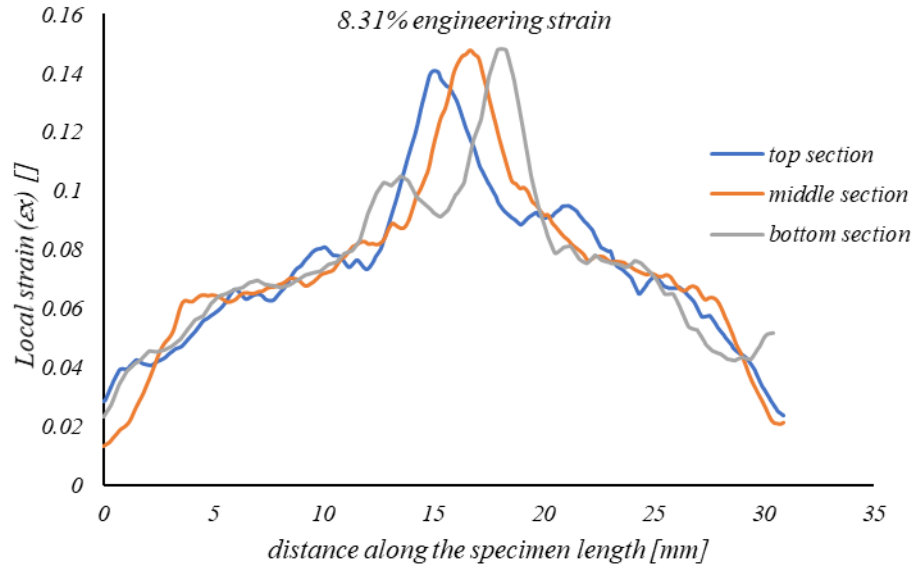


Figure 114 local long. strain distribution along the GL at 8.31% engineering strain level

As discussed before, deformation localisation starts somewhere between 7.47% and 7.92% of total engineering strain. Thus, by observing the corresponding longitudinal local strain variation in the middle section, we can find *the range in which the highest amount of deformation takes place, before entering the localised necking*.

The variation of local strain *parallel to the loading direction* (ϵ_x), along the GL for gradual increase of total engineering strain in the middle section is shown in the next figure.

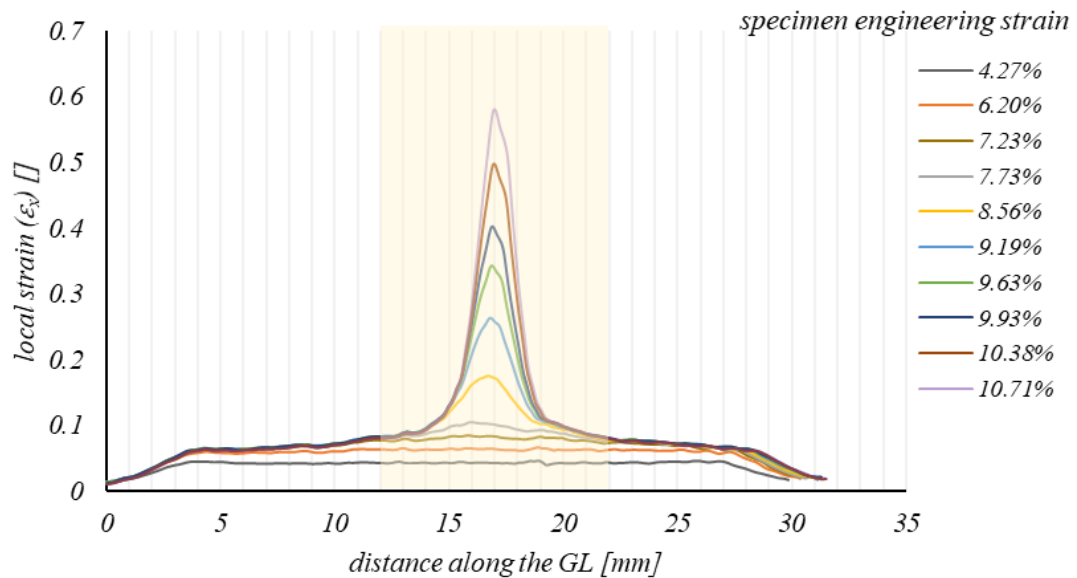


Figure 115 local long. strain distribution along the GL at various engineering strain level-CP 1400HD

It can also be seen that the distribution of the longitudinal local strain is almost uniform along the GL up to 7.73% of overall specimen strain.

Perpendicular to the loading direction (ϵ_y), local strain values along the middle section have negative sign as small facets along the section are contracting. However, the value is almost half of the corresponding value for local strain in parallel direction to loading (ϵ_x). Here also the occurrence of localised necking is evident although localised necking leads to a more severe contraction in thickness direction than in width direction.

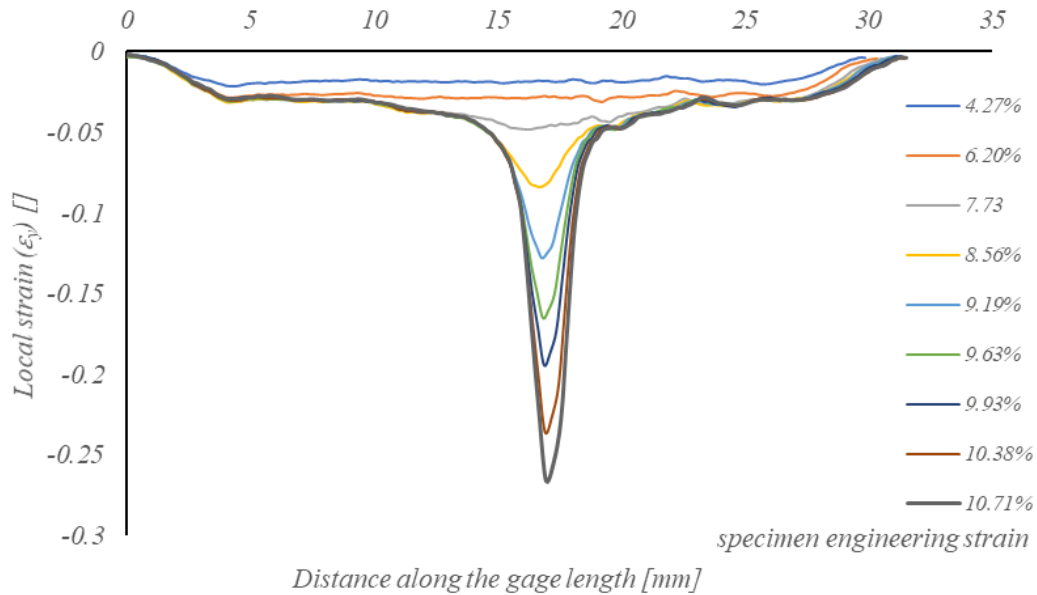


Figure 116 local width strain distribution along the GL at various engineering strain level-CP 1400HD

Strain in thickness direction can be evaluated using GOM, by inspecting ‘thickness reduction’ menu, where it assumes the *volume constancy*¹⁶ and finds the thickness reduction regarding this law¹⁷,

$$d\epsilon_{zz} = -(d\epsilon_{xx} + d\epsilon_{yy})$$

However, more precise results can be attained using 3D DIC technique. It is clear to observe the uniform thickness reduction up to 6.20% engineering strain level in specimen,

¹⁶ Volume constancy law is only applicable till localised necking, due to significant void formation in many materials.

¹⁷ Although the volume change associated with plastic deformation is zero, as long as the void percolation is negligible, the elastic deformation associated with uniaxial tension leads to a non-zero volume change, which needs to be considered in the calculation of the true stress. Therefore, the more accurate theoretical equation of the true stress in uniaxial tension, when the void formation is negligible, should be obtained (98).

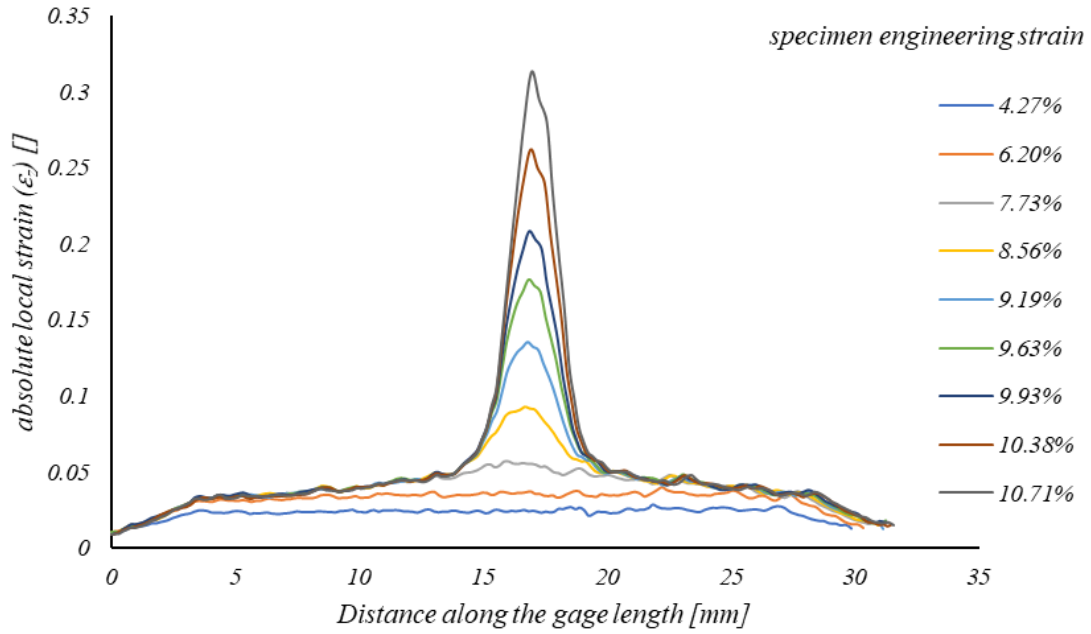


Figure 117 local thickness strain distribution along the GL at various engineering strain level-CP 1400HD

5.5.2 Equivalent stress and equivalent plastic strain evaluation

The procedure to obtain the equivalent stress and corresponding equivalent strain starts with the average values of ε_x and ε_y in the necked section which are collected through DIC technique. Then, benefiting from GOM¹⁸ SW strain field can be observed and analysed.

The true stress-strain curve coming from tensile test is only valid up to necking. Within this stage ($\frac{\partial \sigma_1}{\partial \varepsilon_1} > \sigma_1$), the deformation is uniform along the GL, stress is in uniaxial state where the other stress components are zero, and so the equivalent stress is equal to the stress in loading direction. Thus, one can conclude that, in this range the *equivalent stress-strain curve* lies on top of the *true stress-true plastic strain curve* resulted from test machine.

Quite close to the end of uniform deformation, strain field is not uniform and the stress state is no longer uniaxial along the GL; values of strain in width and thickness directions become considerable, and as a result stress state shifts from uniaxial state towards biaxial one. Thus, equivalent strain and equivalent stress are no longer equal to true strain and true stress values, respectively, and so true strain and true stress values must be corrected to take

¹⁸ Gesellschaft für optische Messtechnik mbH

into account the real behaviour of material. That is why the tensile test data beyond uniform deformation is neglected, as the trend is not representing the real scenario.

As soon as the stress falls behind the hardening rate, strain increment ratio starts to fight against this reduction and tries to keep the equilibrium state stable.

True stress-strain curve is derived from tensile test with the assumption of uniform strain and stress along the gage length in all the sections perpendicular to loading direction. Starting from Force-Elongation diagram of the test machine, the engineering strain is obtained simply by dividing the elongation over initial GL, assuming that all the material along the GL is deforming uniformly (which is only true up to necking, as from necking on, deformation will be concentrated gradually in the middle part of the specimen). On the other hand, engineering stress is attained from force over initial section area, so that it describes a uniform stress distribution in all the sections along the GL (and since no consideration is taken into account for the variation of section area, also this relation is valid withing uniform deformation).

This is all to say that data points coming from tensile test beyond necking must be corrected, while this correction must take into account both the effects of *hardening* and *strain ratio*, as discussed before (81).

Engineering stress values are evaluated by reading the force and knowing the original cross section area of the specimen, while engineering strain is measured through DIC technique, by implementing a virtual extensometer in GOM software, along the GL of the specimen, as shown in figure below,

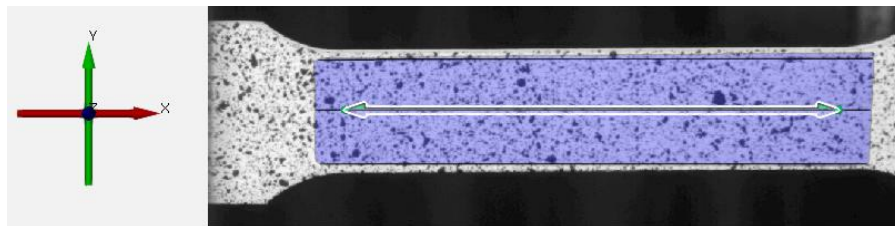


Figure 118 virtual extensometer in GOM software along the GL

The choice of the extensometer gauge length is based on ISO 6892-1:2019 standard; L_e should span as much of the parallel length of the test piece as possible. Ideally, as a minimum, L_e should be greater than $0.50L_o$ (L_o , original gauge length) but less than approximately $0.9L_c$.

Standard geometrical specification of the subsize specimen, which is introduced in ASTM E8/E8M, is shown in the following figure, although the specimen used in this study has slightly different dimensions,

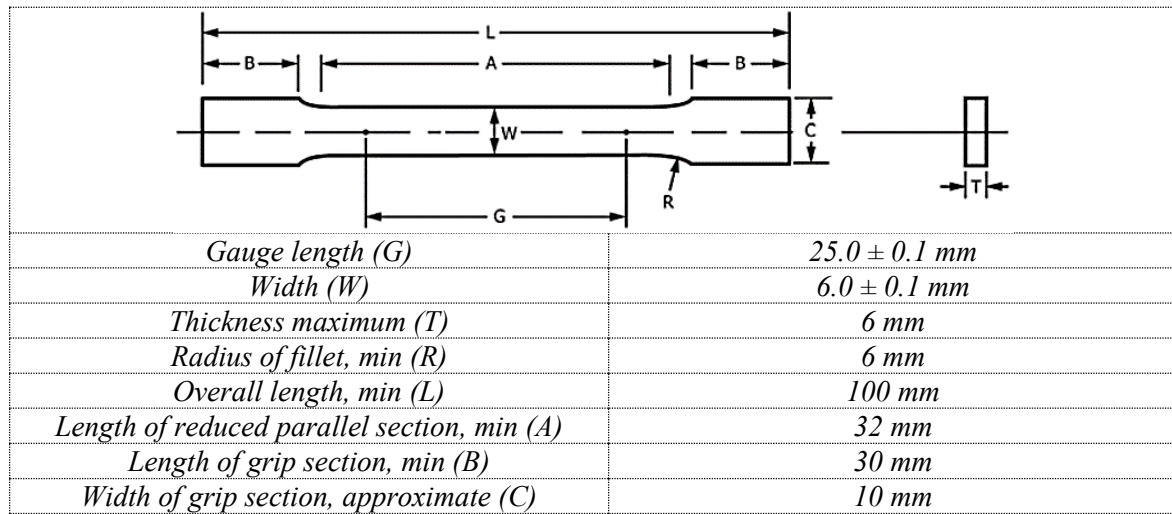


Figure 119 Standard geometrical specification of the subsize specimen ASTM E8/E8M

5.5.2.1 Tensile test results of CP 1400HD subsize specimen

Resulting from tensile test machine's force-elongation diagram, engineering stress-strain curve of CP 1400HD subsize specimen and the corresponding diffuse necking point are illustrated in the figure,

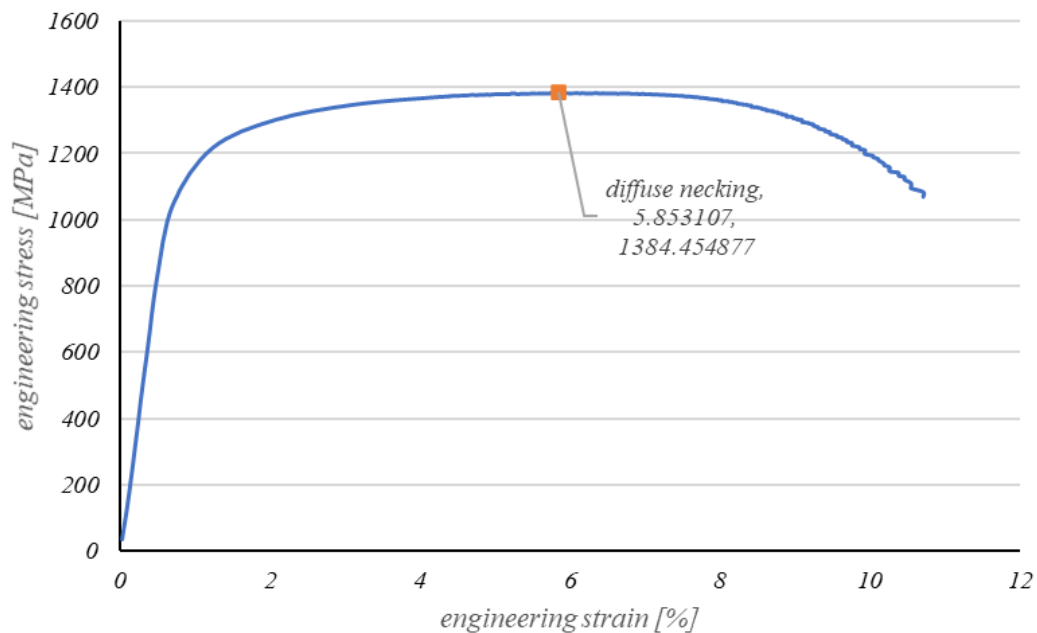
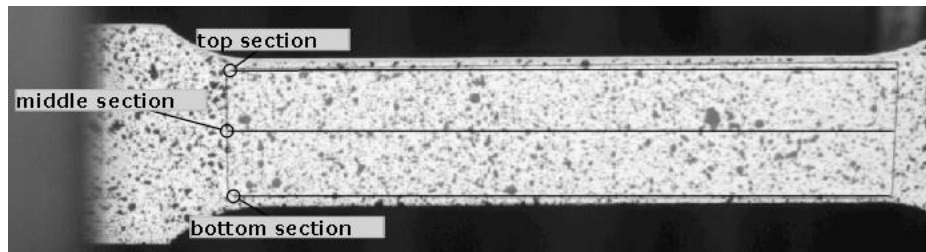


Figure 120 engineering stress-strain curve of CP 1400HD subsize specimen and the corresponding diffuse necking point

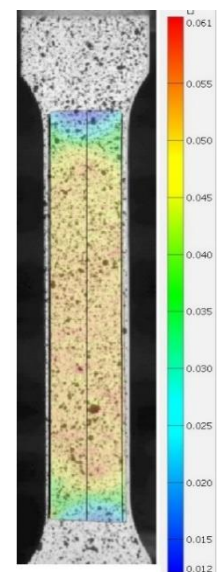
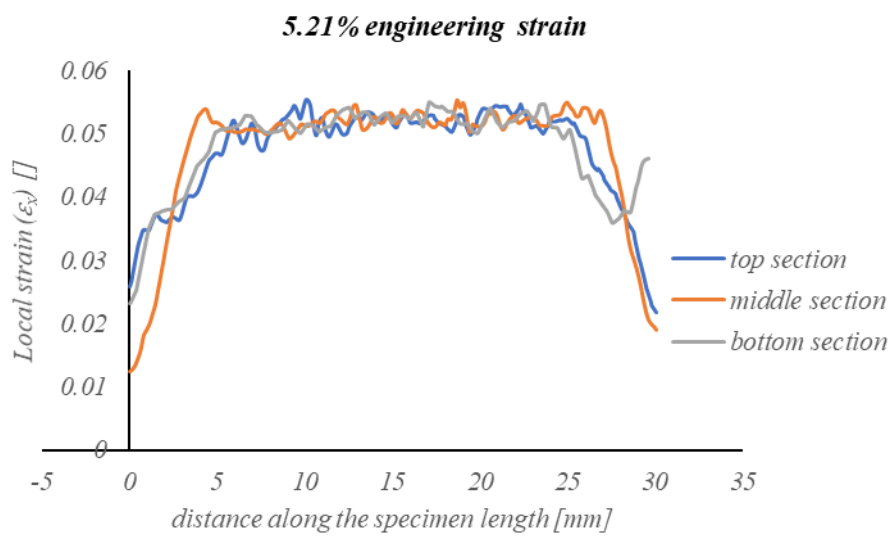
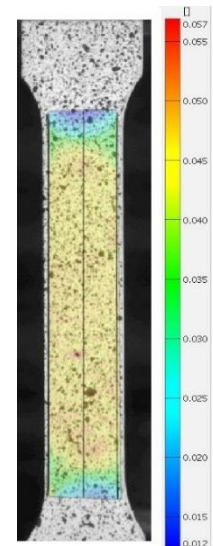
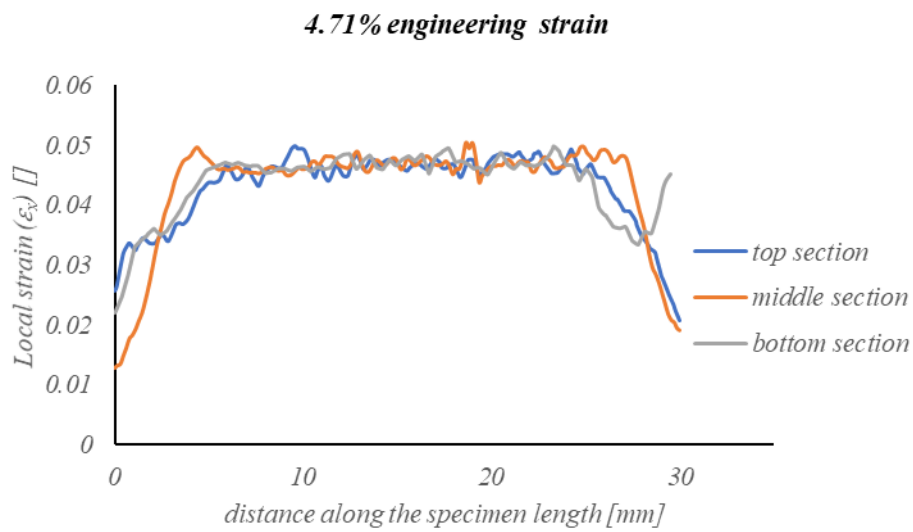
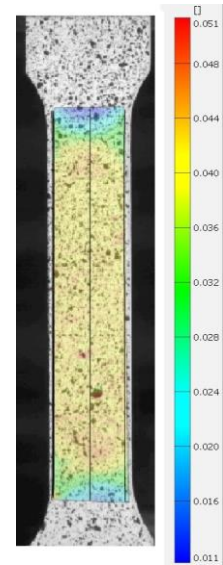
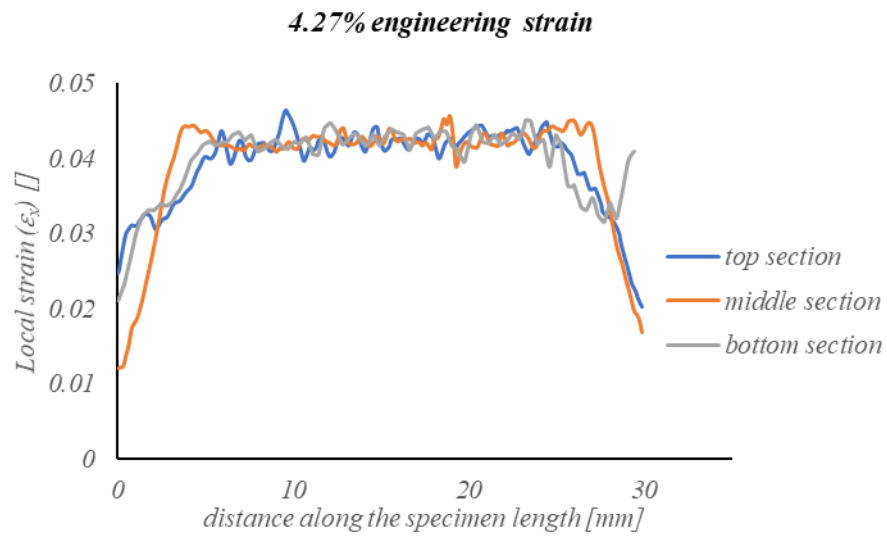
Necking occurs in metals under uniaxial tension when the rate of work hardening becomes lower than the flow stress. This corresponds to the *Considère* criterion, in which diffuse necking initiates at the point of highest load in the load-displacement curve, well before any cracks and failure have appeared in the material¹⁹. Herein, necking is found to be seen at engineering strain value of 5.85%. However, as it is mentioned previously, this criterion only considers work hardening of material, without taking into account the effect of stress state transformation.

The *longitudinal local strain field* via DIC technique can also be worth looking. The longitudinal local strain distribution along the GL in three longitudinal sections (at the top, at the middle and at the bottom of the specimen width) can be used to see how the strain field is changing along the GL, and from which value of the global strain, local strain distribution starts to concentrate in the middle area of the GL.



Contours of local strain component, parallel to the loading direction (ϵ_x) at various overall engineering strain levels during tensile test are also shown below,

¹⁹ Both the strain hardening of the material and the reduction in cross-sectional area of the specimen control the shape of the force-elongation curve. Eventually at a certain point, rate of reduction of load-carrying capacity caused by reduction of area equals the rate of strain hardening. Up to this point the deformation along the gauge section is uniform. However, the deformation will localize after the load reaches its peak value and a neck will form finally. Gradually, almost all the deformation will be concentrated in the necked region (2).



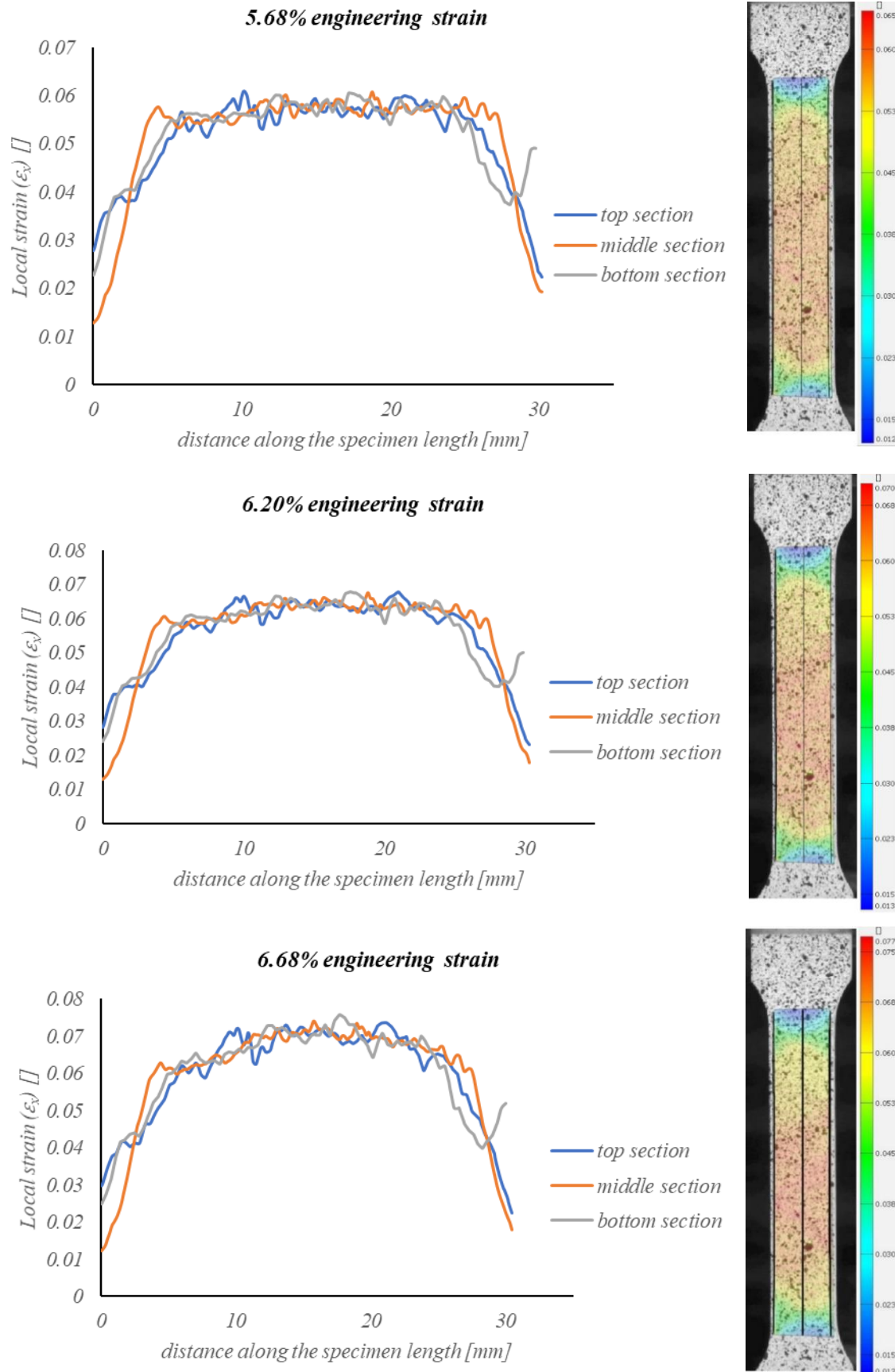


Figure 121 Contours of local strain component (ϵ_x) at various overall engineering strain levels along GL

As can be observed, for engineering strain of 6.20%, the distribution of local strain field is still uniform along a wide range of GL, showing that necking started not exactly at maximum load. Evolution of local strain components (ϵ_x and ϵ_y) at necked zone in various overall strain levels in width direction are shown in the following figures.

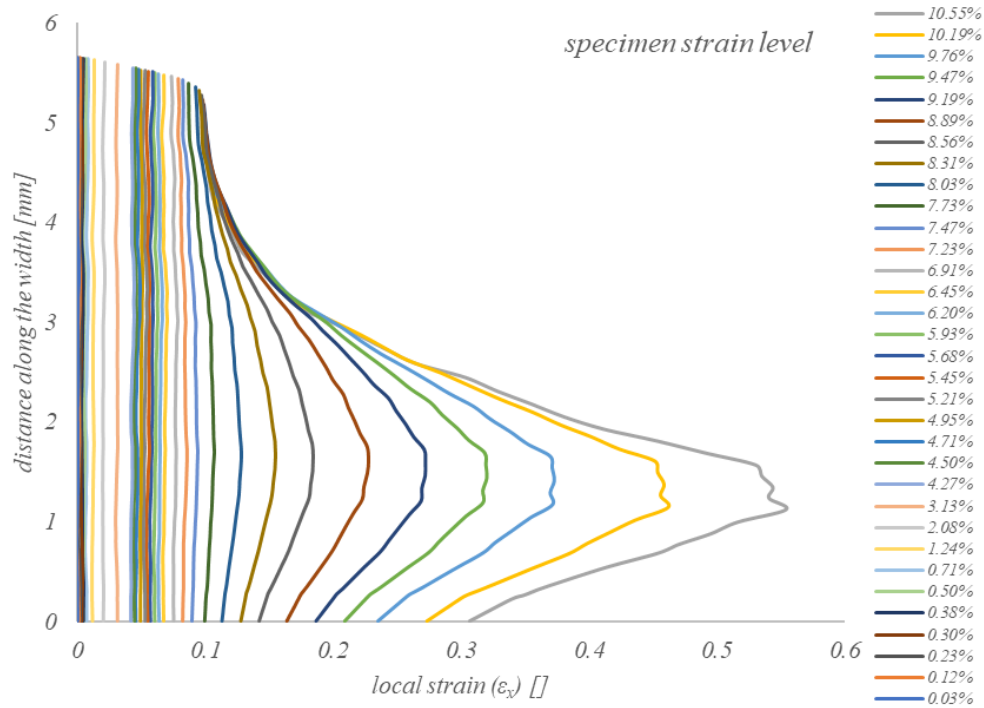


Figure 122 Evolution of local strain component (ϵ_x) at neck in various overall strain levels in width direction

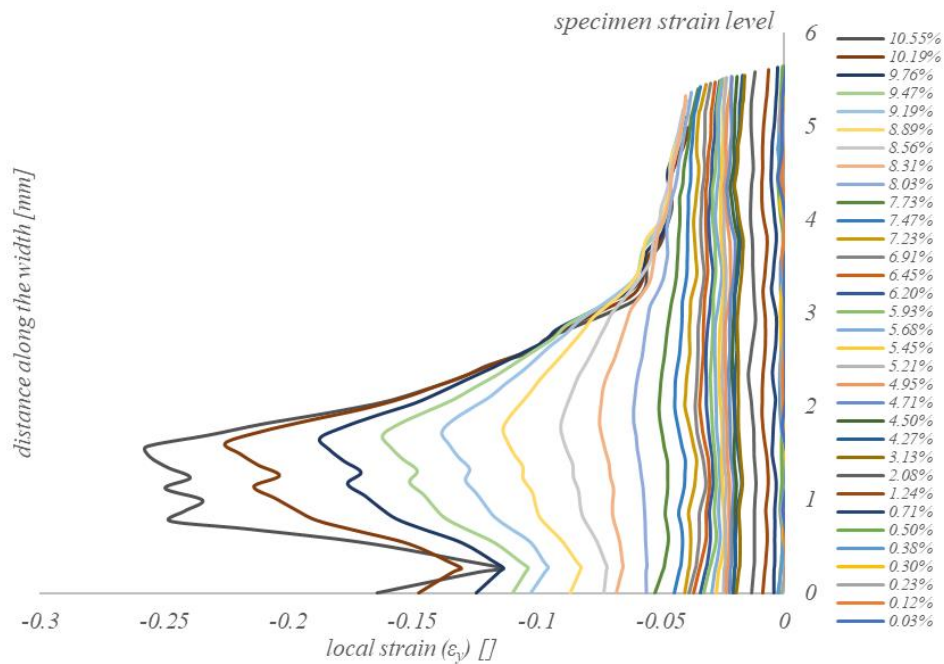


Figure 123 Evolution of local strain component (ϵ_y) at neck in various overall strain levels in width direction

The above distributions can be assumed to be uniform along the section up to 8.03% of engineering strain level in the specimen. Thus, in the proceeding discussion, we can consider an **average** value for the local strain components (ϵ_x and ϵ_y) at necked zone for engineering strain levels below 8.03%.

In order to analyse the evolution of the local average strain components, in the following figure the increments $d\epsilon_x$, $d\epsilon_y$ and $d\epsilon_z$ was evaluated and compared with each other in the necked zone for various overall engineering strain levels; besides, this observation was limited by the fact that the volume consistency law is not applicable in localised necking range.

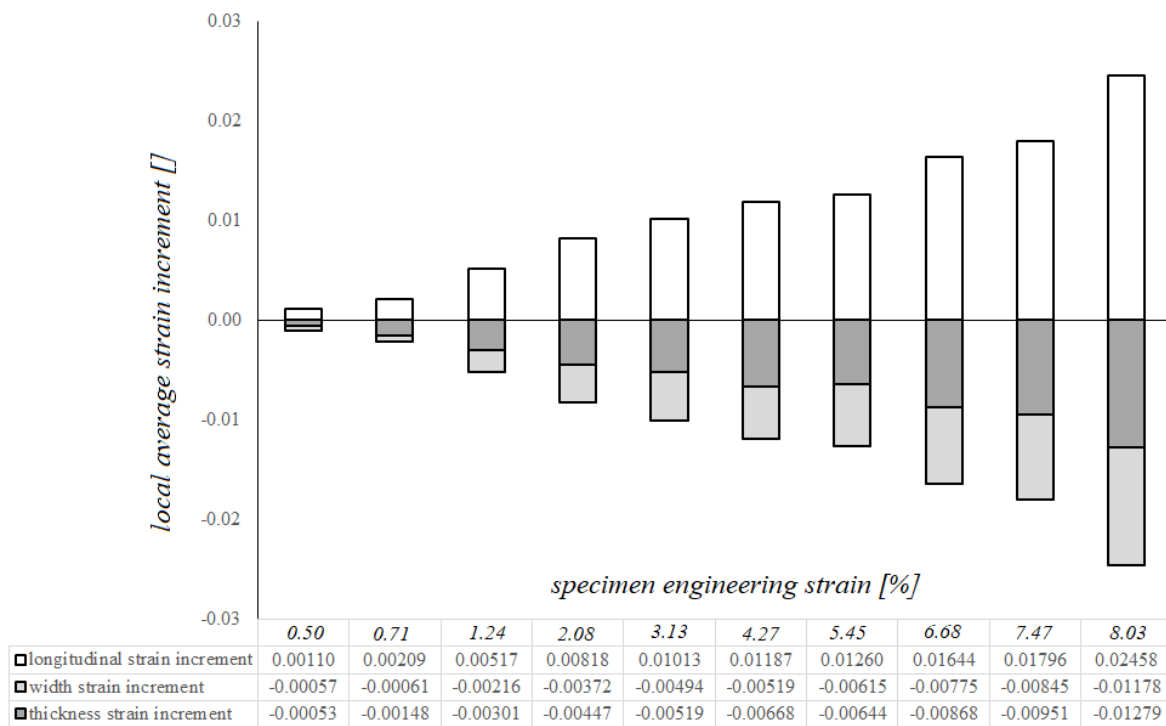


Figure 124 evolution of the local average strain components for various overall engineering strain levels

It is vividly demonstrated that the thinning rate was larger than width reduction rate; in other words, specimen thickness tends to contract more than its width in every engineering strain level of specimen. Moreover, both the tendency to thinning and tendency to width reduction increase as the strain level in specimen gets larger. It is also worth mentioning that either thickness strain or width strain is almost half of the longitudinal strain, while thinning is more dominant.

Furthermore, since thinning is more evident than width reduction, the specimen can tolerate only small magnitude of longitudinal deformation after necking before fracture happens.

5.5.2.2 Normal anisotropy coefficient and strain rate ratio

After computing the averages of local strain components at neck for each frame, (r) and strain rate ratio (β) can be calculated. Then, having stress ratio (α), which was already written in terms of r and β , equivalent stress can be attained.

There are some considerations regarding normal anisotropy coefficient; firstly, r is normally considered to be constant, although it is not always a valid assumption without observing it closely. Secondly, r is normally computed as the total strain ratio, although plastic strain ratio should be used. Furthermore, r value is very sensitive to *the accuracy of the measurements*; so that, even negligible errors in the measured strains leads to a considerable error in the calculated r value (83).

With regard to the above considerations, *strain decomposition* must be applied to the strains field coming from GOM SW, as it was needed to implement plastic parts of the strain in the following discussion, ranging from normal anisotropy to yield criterion, so that in the end we can obtain equivalent strain-equivalent plastic train curve.

$$\begin{cases} \epsilon_{avg,x}^{pl} = \epsilon_{avg,x}^{tot} - \epsilon_{avg,x}^{el} = \epsilon_{avg,x}^{tot} - \frac{\sigma_{true,x}}{E} \\ \epsilon_{avg,y}^{pl} = \epsilon_{avg,y}^{tot} - \epsilon_{avg,y}^{el} = \epsilon_{avg,y}^{tot} - \frac{\nu \sigma_{true,x}}{E} \end{cases}$$

As it was mentioned before, stress ratio can be determined by,

$$\alpha = \frac{(1+r)\beta + r}{1+r+r\beta}.$$

Considering the above points, one can obtain the variations of r and β like the following figures,

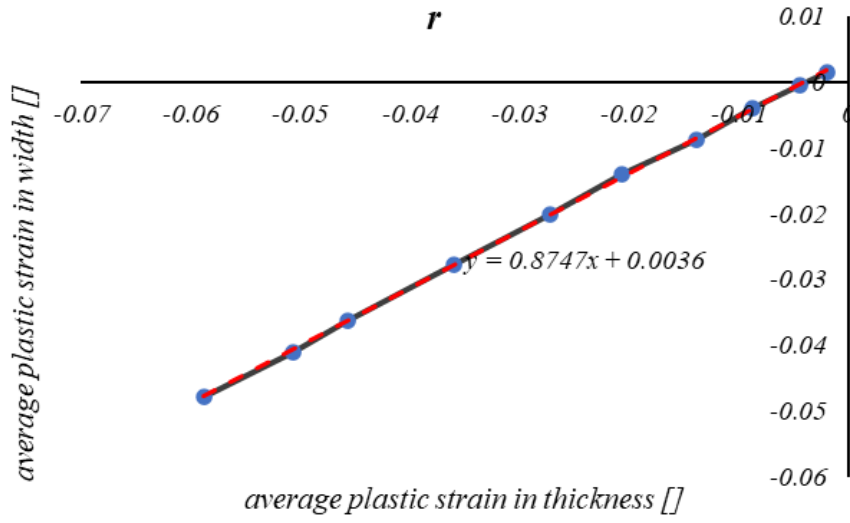


Figure 125 variation of normal anisotropy-CP 1400HD

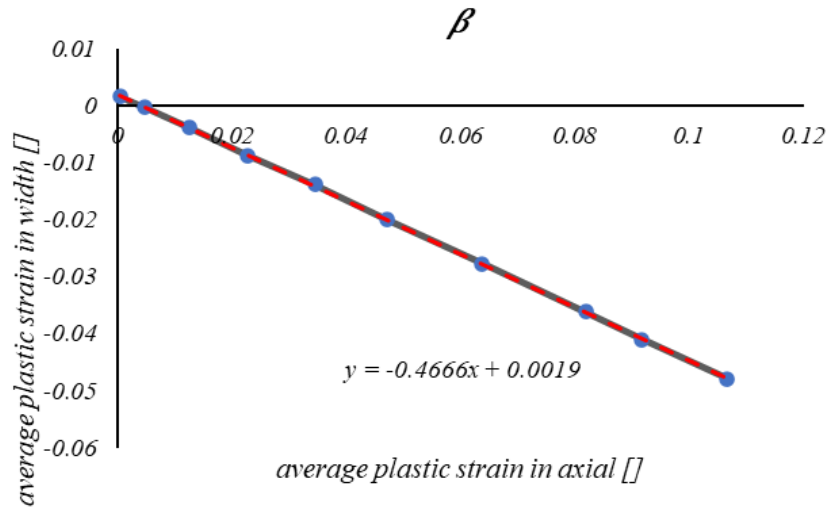


Figure 126 variation of strain rate ratio-CP 1400HD

Finally, equivalent stress and the corresponding equivalent plastic strain can be obtained by following relations,

$$\sigma_{eq}^2 = \sigma_x^2 \left(1 - \frac{2r}{1+r} \alpha + \alpha^2 \right) \quad d\varepsilon_{eq} = d\varepsilon_1 \frac{1+r}{\sqrt{1+2r}} \sqrt{1 + \beta^2 + \frac{2r}{1+r} \beta}$$

Comparing the previously obtained flow stress curve from tensile test (which was only valid up to necking) with the equivalent stress-equivalent plastic strain, it is clearly observed that the method proposed here can represent the behaviour of the material during plastic deformation up to 10.67% of plastic strain; almost two times of the plastic strain corresponding to the uniform elongation.

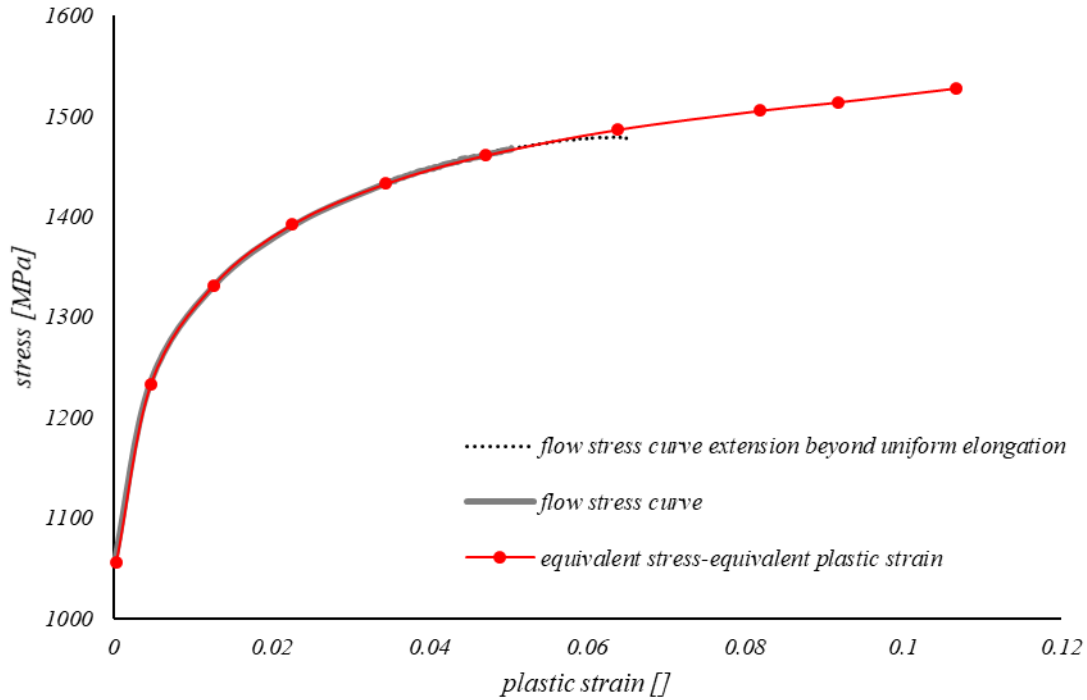


Figure 127 equivalent stress-equivalent plastic strain for CP 1400HD including post-necking behaviour

5.5.3 Necking mechanism in CP 1400HD subsize specimen using DIC technique

For this thin rectangular specimen, at a high local strain level, inclined bands of localized deformation (intense shear deformations (84)) start to appear inside the neck (85). However, inside the diffuse necking zone, there is a gradual evolution in the strain state condition: from 3-axis to 2-axis strain state (86). According to the studies of Hill (87) and Lian and Zhou (88), severe local section thinning can be identified before fracture by solely *longitudinal* and *thickness* strains, where width strain is almost zero.

Localized necking is based on zero strain along the necking band, so that the onset of localized necking corresponds to a plane strain deformation mode (86) (88).

If we continue to observe the distribution of longitudinal local strain field along the GL, it is possible to find the position of the localisation bands which progressively take place in the last steps of the test prior to failure (89) (86).

Despite the fact that fringe analysis²⁰ is not conducted in this thesis work, the local strain distribution along the gage length can demonstrate the main four stages of strain field evolution (90). These stages can be symbolised by the following pattern shape,

- Parallel shape '|||'
- Hourglass shape ')('
- X shape 'X'
- Slash shape '/'

Genuinely, the plastic deformations come from the movements of the dislocations inside the metal materials. Therefore, the deformations can be named uniform only in macroscopic scale. Constant and homogenous strain field appears in the first stage is evident (parallel shape). In other words, in the elastic and homogenous plastic deformation stages, no variation in the local strain distribution appearance can be observed (90).

Gradually the plastic deformation within the gage length becomes inhomogeneous; strain field starts to concentrate in the centre of the specimen with a shape mostly like an hourglass shape ')('. The shape can be assumed as two crossing localisation bands (90), as it is shown in figure below,

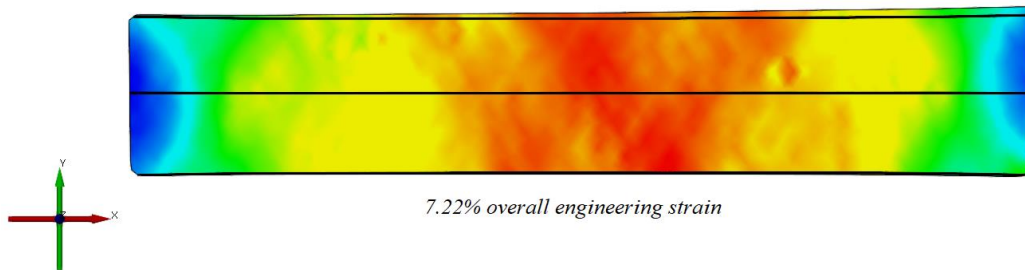


Figure 128 two crossing localisation bands immediately after the onset of inhomogeneous deformation

As plastic deformation goes on, this hourglass shape narrows progressively and take a shape like letter 'X', in such a way that the local strain intensity is higher in the middle of the specimen in comparison with the two edges of the specimen (90). As shown in figure below, in the areas next to the 'X', where the strain level is considerably lower, the deformation is no longer plastic and the material undergoes elastic unloading when the force decreases.

²⁰ Electronic speckle pattern interferometry (ESPI) is a technique in which laser light together with image processing of a surface are employed in order to demonstrate static/dynamic displacements. The visualisation is in the form of fringes on the images.

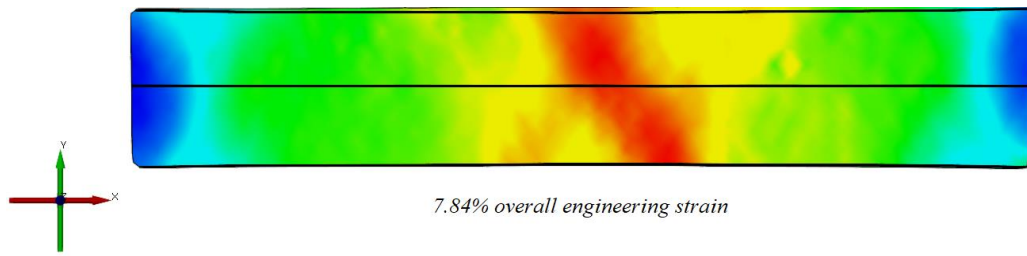


Figure 129 'X' shape bands during plastic deformation

At the onset of the localisation, the hourglass has almost a symmetric shape; however, when the shape turns into 'X', the symmetry is no longer seen. Then the deformation starts to concentrate in one of the bands (or one of the branches of 'X') called the *dominant band*. The other band fades gradually, so that a slash shape '/' will appear in the neck. In the end, the specimen breaks along the dominant band (90).

A closer look at the strain field along the GL during the tensile test of CP 1400HD subsize specimen (figure below) reveals that, shortly after the start of diffuse necking (at strain value around 7.73%), two asymmetric crossing localization bands (X-shape) start to form with an angle with respect to the tensile direction. The two bands, then, continue to evolve but at different rates, and finally, one of the bands stabilizes, so that its inclination leading to fracture remains quite stable (slash-shape) and the other band fades away. However, the width of the remaining band falls rapidly before fracture occurs (90).

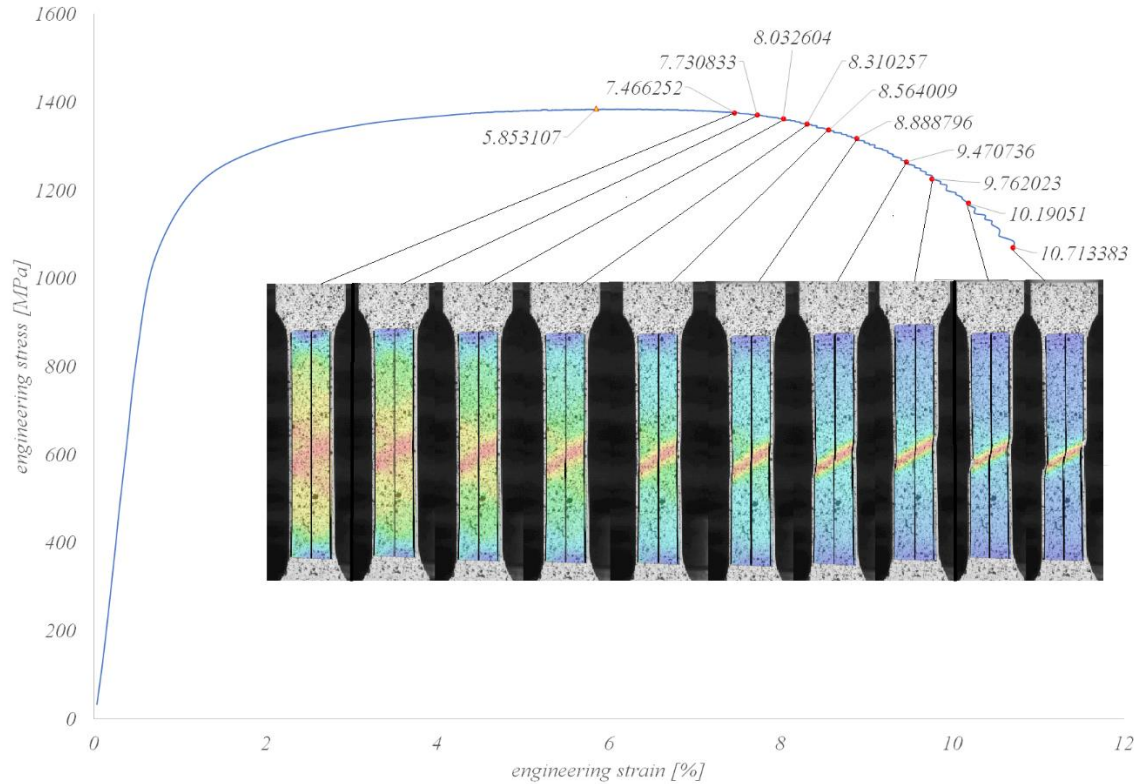


Figure 130 evolution of the strain field during post-necking deformation

The delay beyond the load maximum before the onset of localized necking is mainly proportion with the length to width ratio of the specimen (for the same material); the smaller the ratio, the more imminent will be the localized oblique neck. On the other hand, the material softening caused by the nucleation and growth of voids, makes the localization more impending (91).

In this study, the transition from the symmetric hourglass to the asymmetric 'X' is interpreted as a criterion for the onset of localised necking²¹ (90). The localised necking stage can be assumed to have two sub-stages; as can be seen in the following figure, one in which the disappearing band is present (around 7.92% engineering strain), and second stage in which it almost fades (around 8.03% engineering strain).

Thus, observing the strain field from GOM, localised necking can be assumed to form somewhere between 7.47% and 7.92% of engineering strain.

²¹ Another possible solution is also offered by the ISO 12004-2-2009 standard, which is called 'time-independent' evaluation. However, there are 'time-dependent' solutions as well (86), for example Hora et al (96) and Merklein et al (97). In time-dependent methods strain distributions as the function of time are used for evaluation, where time derivatives of longitudinal or thickness strains are exploited to identify the onset of local necking.

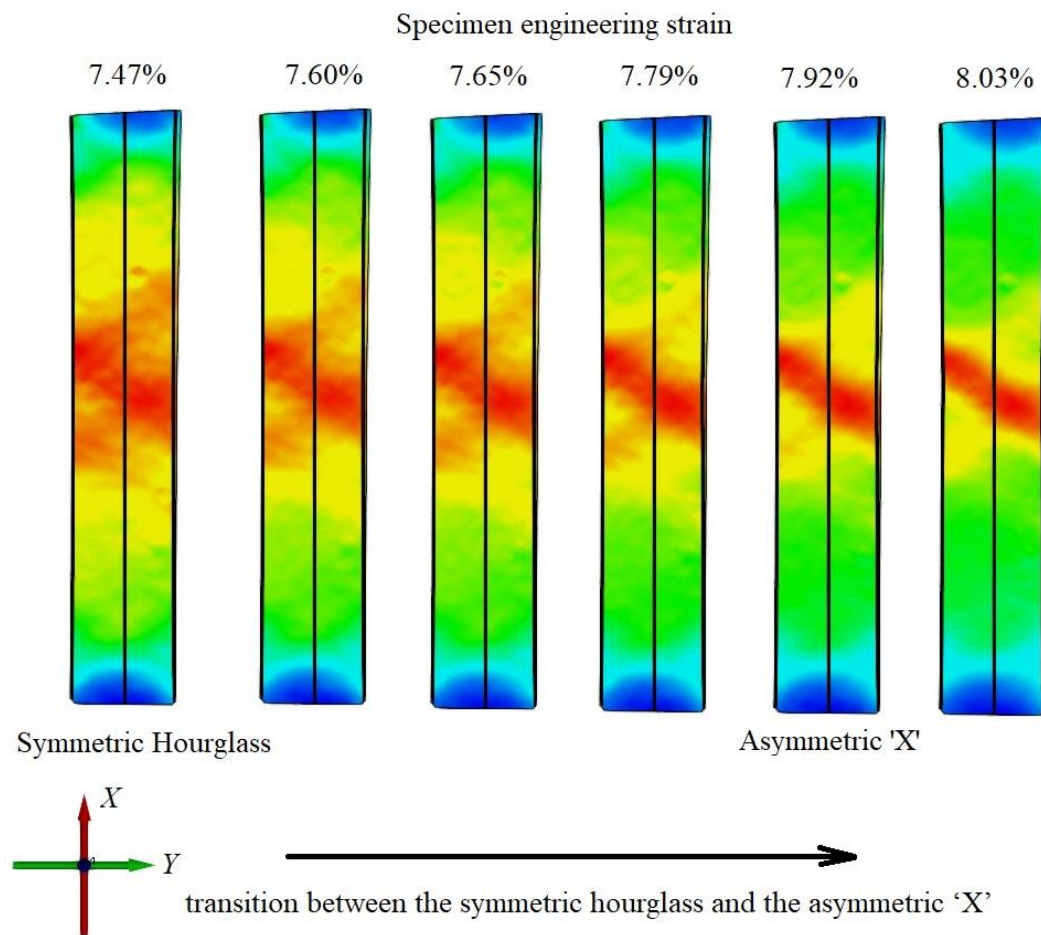


Figure 131 transition between the symmetric hourglass and asymmetric 'X' CP1400HD

5.6 TENSILE TEST RESULTS OF QP 1180-SUBSIZE SPECIMEN USING DIC TECHNIQUE AND GOM CORRELATE SW

Engineering stress-strain curve for QP 1180-subsize specimen is illustrated here, where the diffuse necking is obtain based on the Considère criterion,

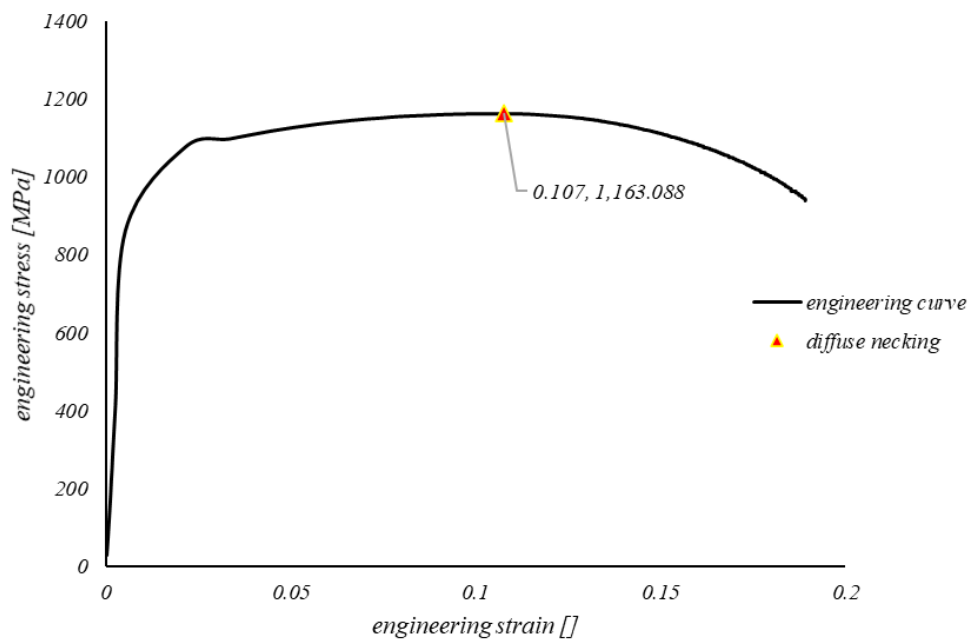


Figure 132 Engineering stress-strain curve for QP 1180-subsize specimen

And the corresponding true stress-true strain diagram would be,

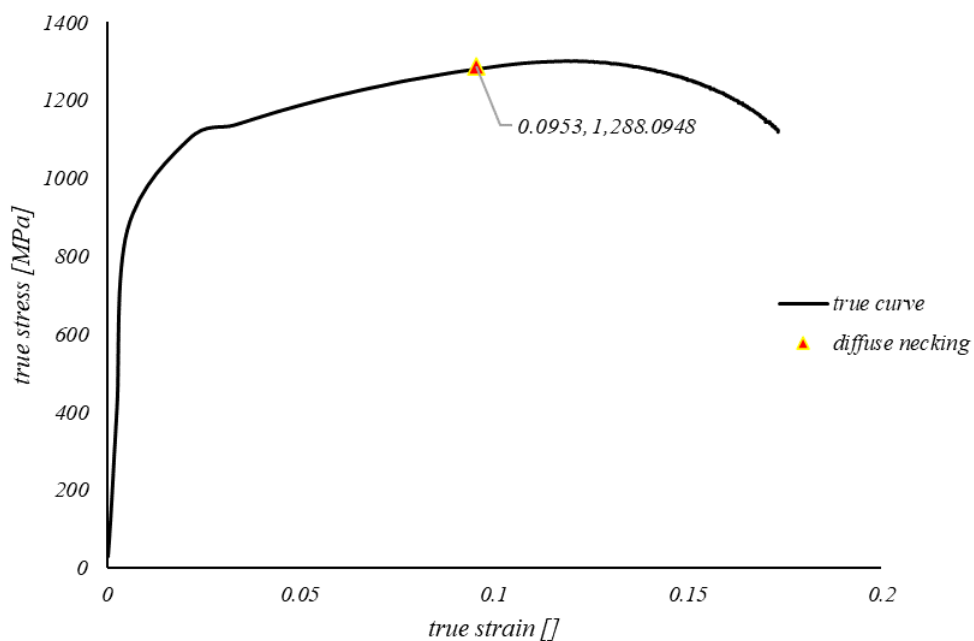


Figure 133 true stress-strain curve for QP 1180-subsize specimen

To continue with the proposed method, the strain level from which the localised necking starts is needed to be identified first. This can be obtained by observing the local strain distribution along the GL of the specimen. At the same time, the location of localization can be observed through the DIC technique results.

Figure below shows the distribution of local longitudinal strain (ϵ_x) in various overall engineering strain levels in specimen. As it has mentioned before, according to Considère criterion, necking formed around 10.75% engineering strain. In other words, the flow stress curve derived from tensile test is only valid up to maximum load.

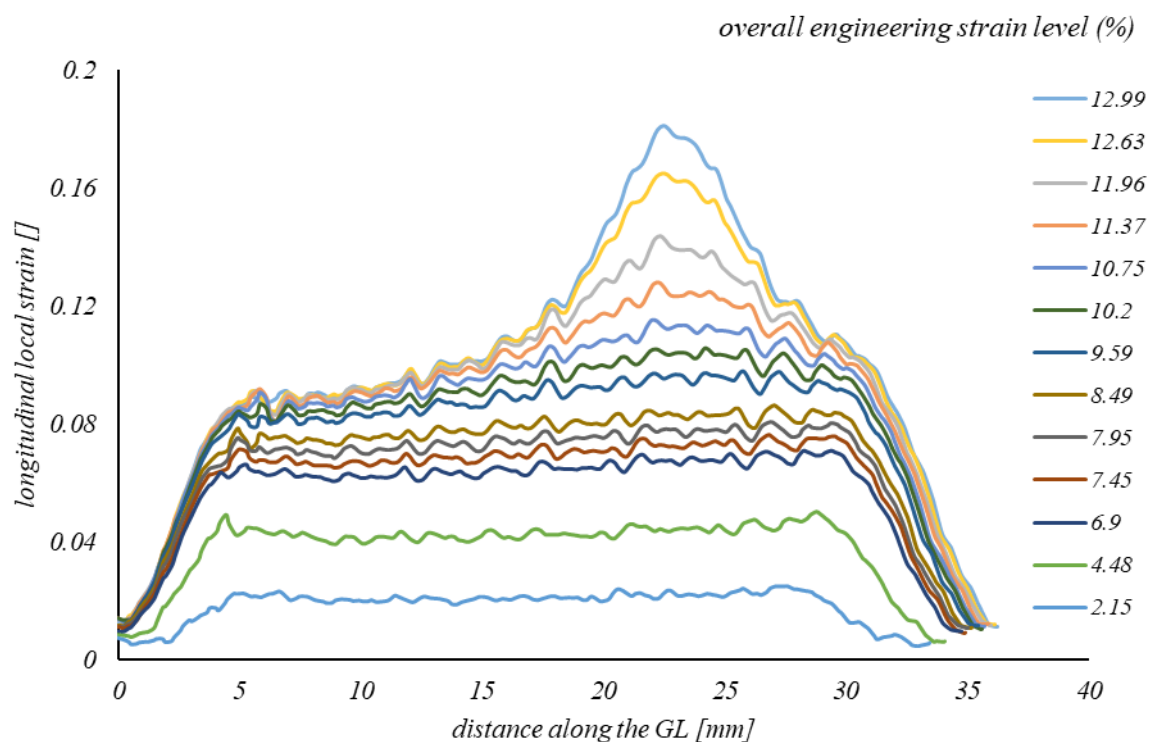


Figure 134 distribution of local longitudinal strain (ϵ_x) in various overall engineering strain levels-QP 1180 subsize specimen

As deformation continues to grow, the longitudinal local strain starts to concentrate gradually on the right half of the specimen,

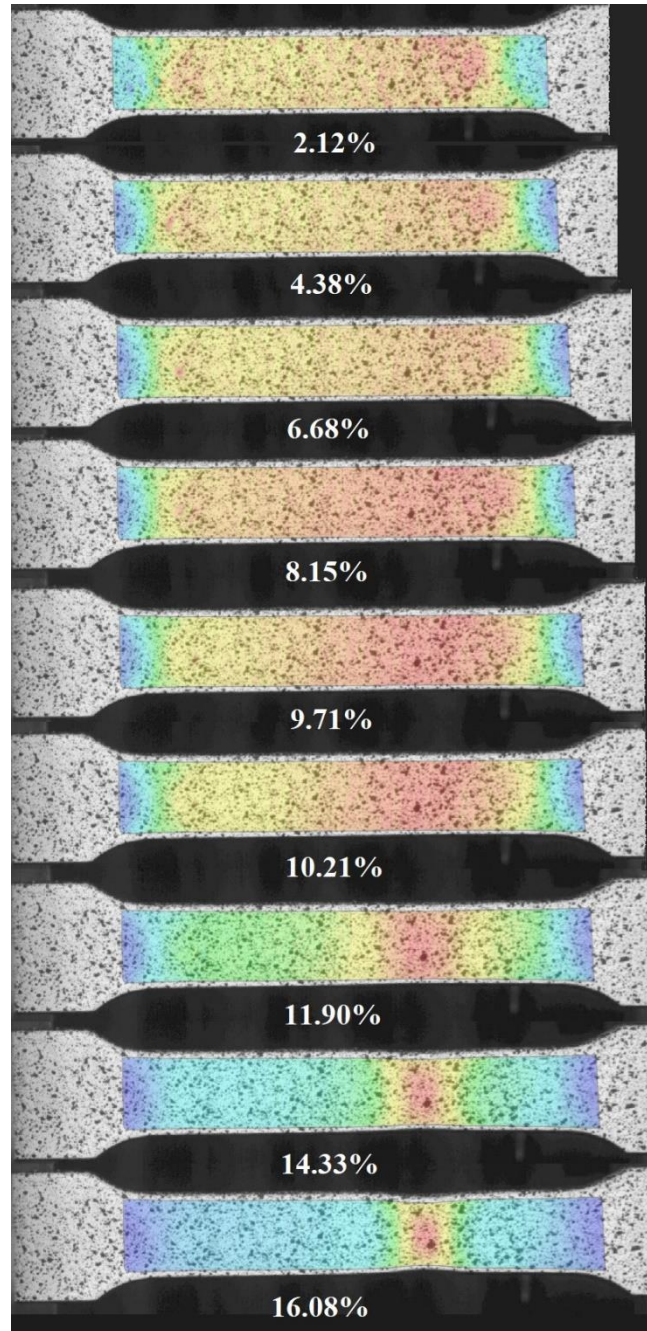


Figure 135 longitudinal local strain distribution in QP 1180 subsize specimen

Now taking into account the necked section, in order to assess the equivalent stress-equivalent plastic strain, the average values of strain, both in x and y directions, should be obtained.

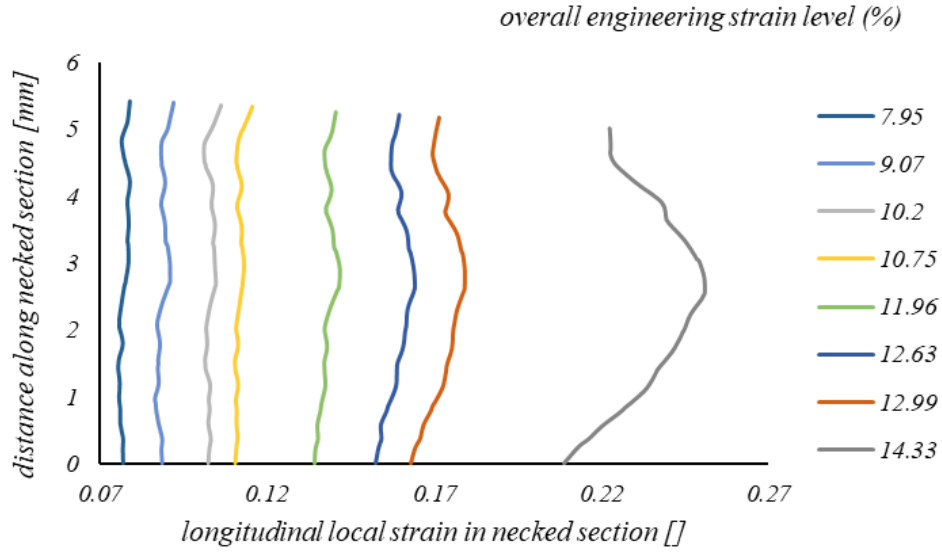


Figure 136 longitudinal local strain (ϵ_x) distribution along the width at neck-QP 1180

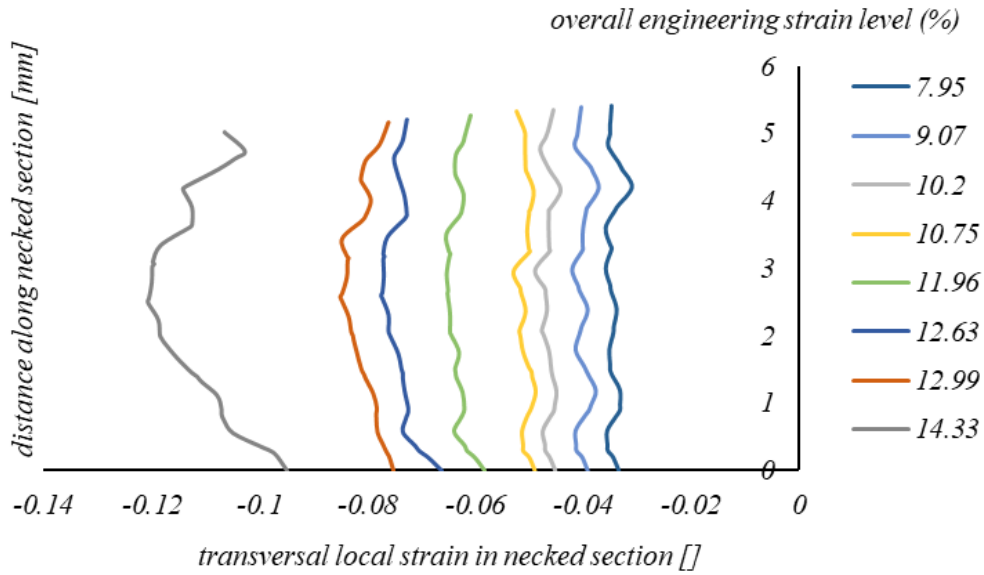


Figure 137 transversal local strain (ϵ_y) distribution along the width at neck-QP 1180

From the figures above, it can be clearly observed that *strains at necked section can be assumed to be uniform till 12.99% of engineering strain level in specimen*. Thus, the following computation regarding equivalent plastic strain and equivalent stress are bounded to this amount of overall strain. It can be said that this method is capable of determining the equivalent stress and equivalent plastic strain in a range starting from diffuse necking until the formation of localised necking.

Normal anisotropy coefficient and strain rate ratio are derived from plastic terms of average strains at the necked section. From the figures in the following, these values can be obtained.

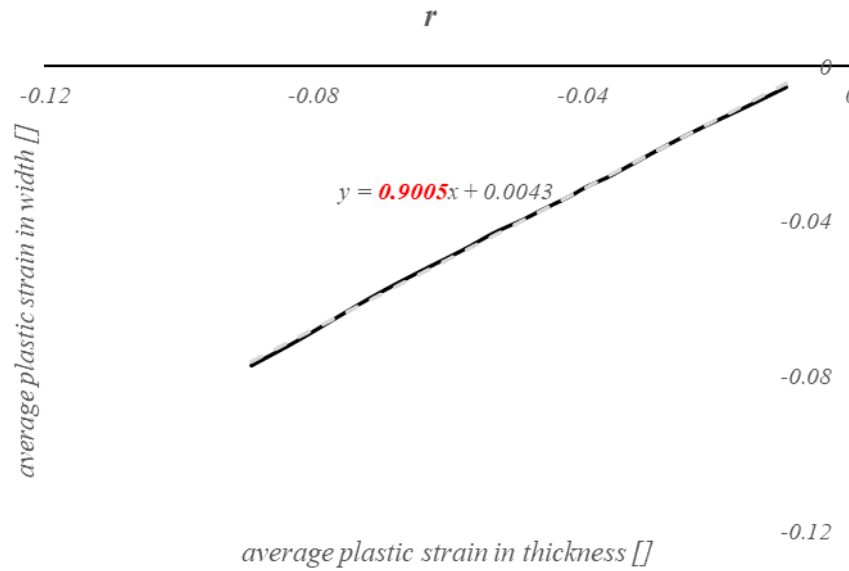


Figure 138 variation of normal anisotropy-QP 1180

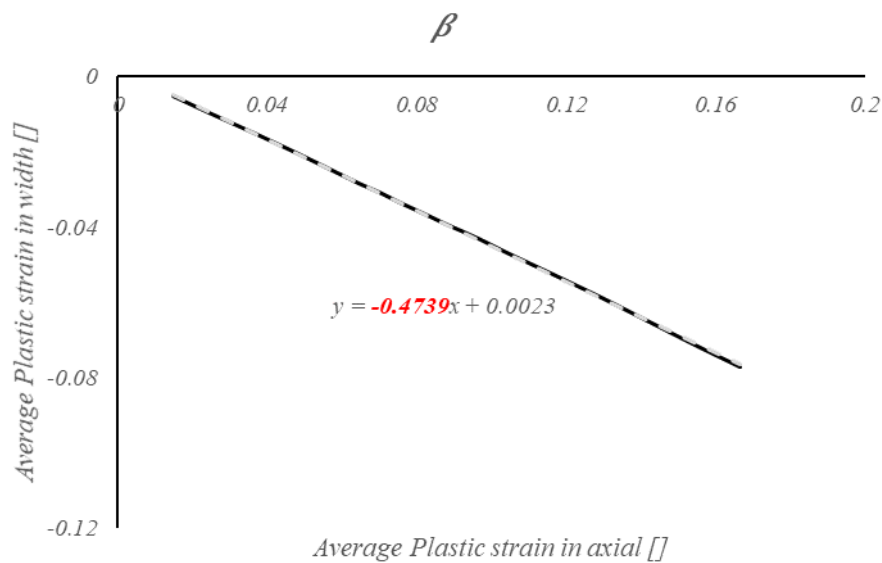


Figure 139 variation of strain ratio-QP 1180

Taking into account the previously-mentioned relations for equivalent stress and equivalent plastic strain, the next diagram illustrates the post-necking behaviour of QP 1180, in which the equivalent curve is also able to represent the pre-necking behaviour.

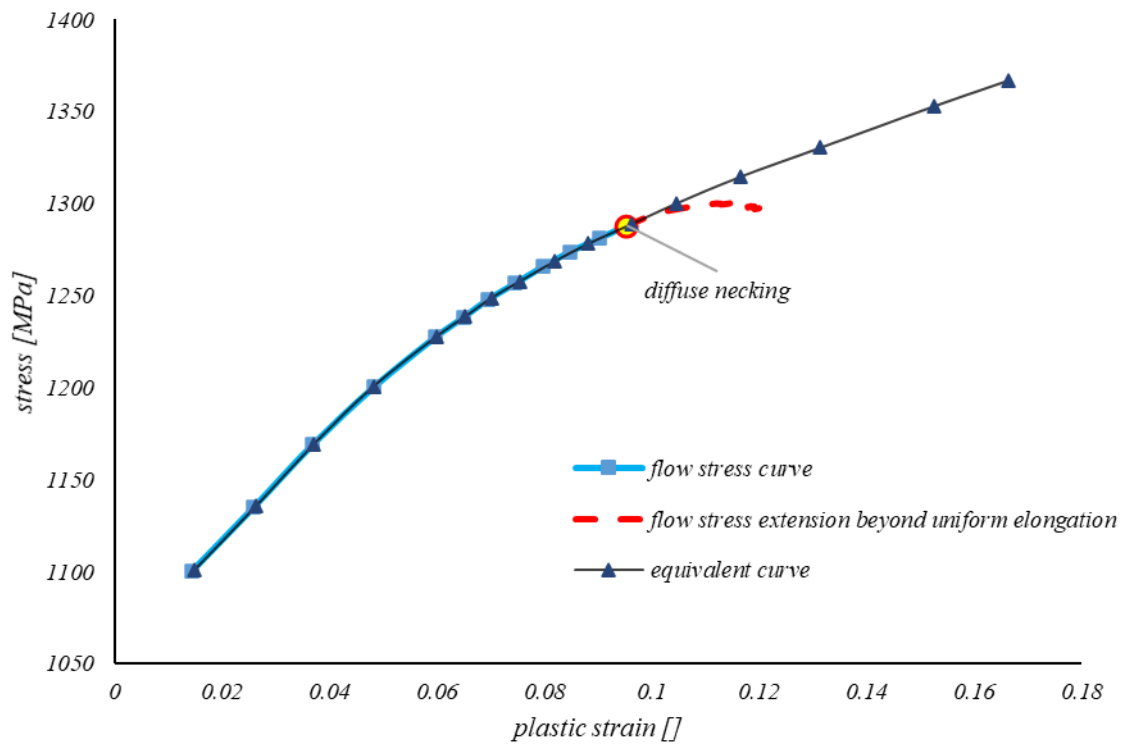


Figure 140 equivalent stress-equivalent plastic strain for QP 1180 including post-necking behaviour

Although a point on the flow stress curve was named as ‘diffuse necking’ point, this phenomenon does not take place at a certain point and time during deformation. Instead, as it is demonstrated in the following figure, deformation is no longer homogenous in GL, even for lower levels of deformation than 10.75%. Theoretically, as it was discussed before, the *Considère criterion* illustrates the onset of necking as the position of *maximum load in force elongation diagram*. However, a closer look at the strain field along the GL would promote the idea that, necking starts before the point of maximum load, and so the assumption of uniform elongation was discarded way before diffuse necking point shown on engineering curve. This condition will make a difference in the evaluation of the strain; while a uniform deformation assumption must be taken into account for evaluating the flow stress curve, as soon as the strain field starts to concentrate inside a range in the GL, the flow stress curve obtained directly from tensile test result is not reliable anymore.

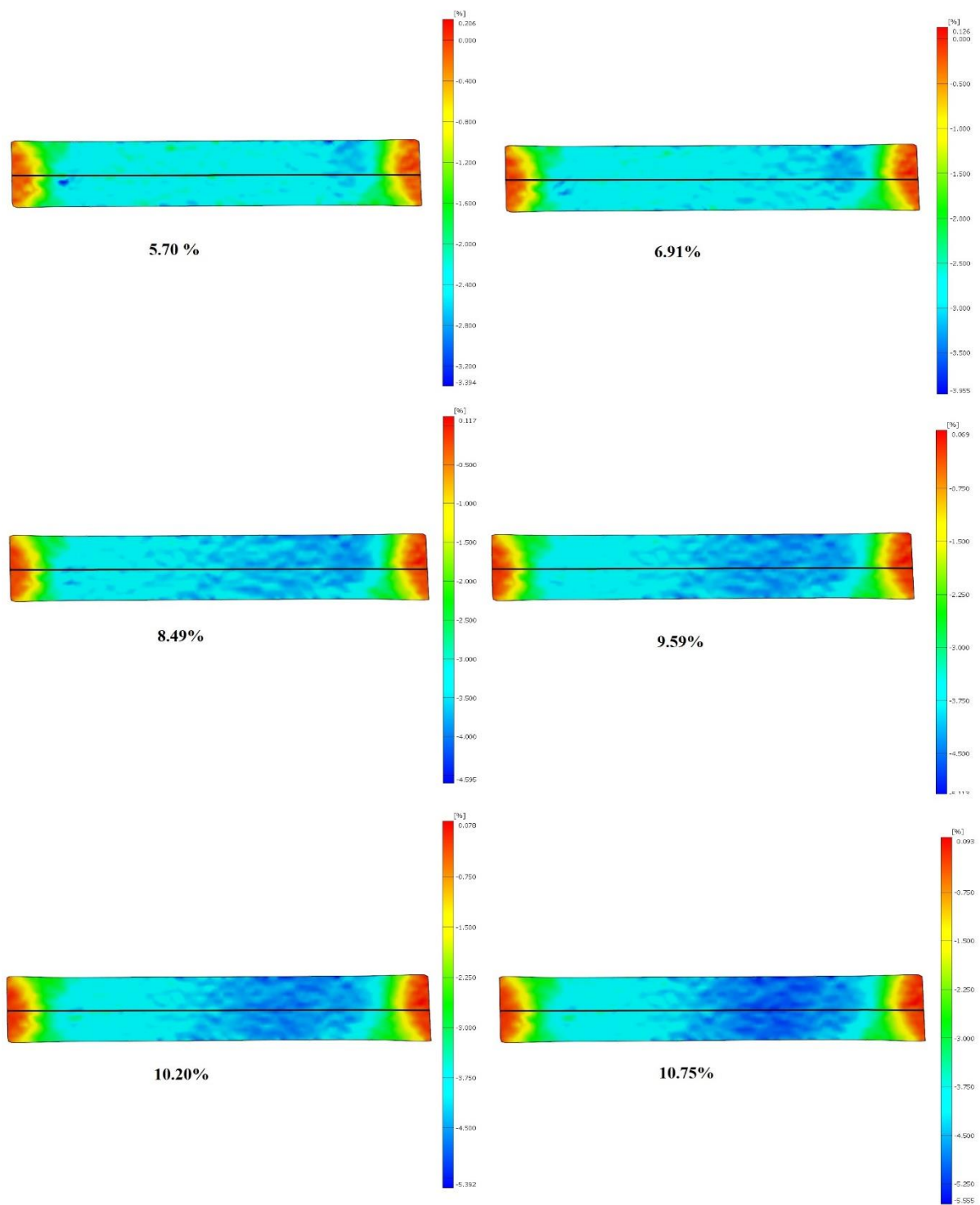


Figure 141 evolution of the longitudinal strain distribution along the GL of a QP 1180 subsize specimen

5.7 A REVIEW ON THE PROPOSED METHOD

The method proposed in this chapter was used to study the post-necking behaviour of CP 1400HD and CP 1180 steels. In this method, the only available data comes from a tensile test machine equipped with a camera to capture the spackled surface of the specimen during the test. Besides, benefiting from Hill's 48 yield criterion and choosing RO strain hardening law, equivalent stress-equivalent plastic strain curve of the material under uniaxial tension test can be obtained for strain levels between the uniform elongation and localized necking.

The method still needs further investigation both from numerical simulation and reliability points of view. Hence, it is a good practice to compare the result with post-necking behaviour of the material obtained through biaxial test.

Some important factors should be studied deeper, such as the effect of voids formation on the onset of localized necking; where it was a limiting factor to this method that constrains the volume constancy assumption. On the other hand, according to the strain distribution at the necked region, the normal anisotropy and strain rate ratio are considered constant during deformation, although their variation must be taken into account, as the state of stress and strain are changing during the deformation.

CHAPTER SIX: VALIDATION OF THE EQUIVALENT FLOW STRESS CURVE USING FEA

6.1 INTRODUCTION

In order to verify the reliability of the equivalent stress-equivalent plastic strain curve, obtained through the combination of DIC technique and Hill's 48 yield criterion, the curve is implemented in the numerical simulation of the same experimental test. Both the validity and the effectiveness of the previously-obtained flow stress curve can be evaluated via two observations,

- The same experimental applied force-displacement curve, and
- The same experimental strain gradient (DIC results),

should be obtained in our FEA of the same specimen.

Furthermore, employing Hill's 48 yield criterion in this FEA, strain field in width and thickness direction at necked region were compared in the two models.

Since the equivalent flow curve has merely exploited tensile test data up to diffuse necking, the present validation can only be done in this range. However, the writer believes that the equivalent curve should work in other sheet forming processes with the same material up to larger values of strain, but its effectiveness and precision depends on the quality of the yield criterion.

The tensile test was simulated numerically using an isotropic hardening elastic-plastic FE model, and developed in the nonlinear code ABAQUS standard, student edition 2020.

6.2 FINITE ELEMENT MODELLING AND ANALYSIS

6.2.1 Pre-processing

At the beginning, the same geometry of the subsize test specimen used in tensile test was modelled via *Part Module* of the SW. The dimensions (according to ASTM E8/E8M) are shown here again, where a large radius (e.g. 6.35 mm for CP 1400 test specimen) is built into the sides to avoid stress concentration,

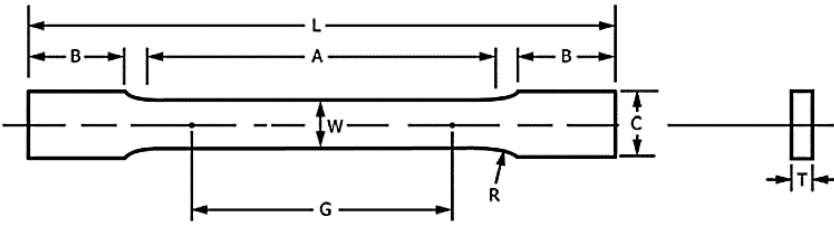
	
<i>Gauge length (G)</i>	$25.0 \pm 0.1 \text{ mm}$
<i>Width (W)</i>	$6.0 \pm 0.1 \text{ mm}$
<i>Thickness maximum (T)</i>	6 mm
<i>Radius of fillet, min (R)</i>	6 mm
<i>Overall length, min (L)</i>	100 mm
<i>Length of reduced parallel section, min (A)</i>	32 mm
<i>Length of grip section, min (B)</i>	30 mm
<i>Width of grip section, approximate (C)</i>	10 mm

Table 31 geometrical specifications of subsize specimen ASTM E8/E8M

The specimen used in this study had slightly different dimensions; for CP 1400HD specimen, 6.39 mm width and 1.2 mm thickness were selected, while for QP, a width of 6.52 mm and a thickness of 2.1 mm were tested.

Due to the symmetry of the problem about the mid-span, mid-width and mid-thickness, it was possible to model only 1/4 (or even 1/8) of the specimen, and apply boundary conditions accordingly. However, although there was a limitation for the maximum number of nodes in student version of ABAQUS, a model with original dimensions was built within the part module for a better understanding of the general problem.

On the other hand, node number limitation also led to apply an adjustment in the length of the sample head; thus, its interaction with the boundary conditions was closely observed through trial and error, and eventually its length was reduced to half of the original one (17 mm instead of 34 mm).

A three dimensional solid element with 8-node (linear brick element), combined with reduced integration and hourglass control (C3D8R) was used for the model discretisation. Each of the nodes had three degrees of freedom in translation, so that even large strains and visco-plasticity could be studied properly.

With regard to the material properties, the elastic deformation region could be defined by Young's modulus of the material and Poisson's ratio. On the other hand, concerning plastic deformation, the equivalent stress-plastic strain curve was implemented, while, as it was mentioned previously, the chosen plasticity model was *isotropic hardening* with Hill's 48 anisotropic quadratic yield criterion.

ABAQUS introduces an anisotropic yield and creep model for materials that demonstrate different yield or creep behaviour in different directions (92). Anisotropic yield behaviour was modelled by employing *yield stress ratios* R_{ij} , that were applied in Hill's potential function. In the case of anisotropic yield, the yield stress ratios are defined with regard to a reference yield stress σ^0 , (given for the metal plasticity definition); in a way that if σ_{ij} is applied as the only nonzero stress, the corresponding yield stress is $R_{ij}\sigma^0$. Hence, a *local orientation* must also be defined in ABAQUS to introduce the direction of anisotropy (92).

Herein, as normal anisotropy coefficient (*r-value*) (rather than *yield stress ratio*) was evaluated through DIC technique, a very brief review of Hill's anisotropic yield function is presented here in order to define the relationship between yield stress ratios R_{ij} and strain ratios (*Lankford's r-values*) r_{ij} . The following theoretical method was extracted from Abaqus Documentation, 2020.

Hill's potential function is a simple extension of the von Mises function, which can be expressed in terms of rectangular Cartesian stress components as,

$$f(\sigma) = \sqrt{F(\sigma_{22} - \sigma_{33})^2 + G(\sigma_{33} - \sigma_{11})^2 + H(\sigma_{11} - \sigma_{22})^2 + 2L\sigma_{23}^2 + 2M\sigma_{31}^2 + 2N\sigma_{12}^2}$$

where F, G, H, L, M and N are constants obtained by tests of the material in different orientations, and they are defined as,

$F = \frac{(\sigma^0)^2}{2} \left(\frac{1}{\bar{\sigma}_{22}^2} + \frac{1}{\bar{\sigma}_{33}^2} - \frac{1}{\bar{\sigma}_{11}^2} \right)$ $= \frac{1}{2} \left(\frac{1}{R_{22}^2} + \frac{1}{R_{33}^2} - \frac{1}{R_{11}^2} \right)$ $G = \frac{(\sigma^0)^2}{2} \left(\frac{1}{\bar{\sigma}_{33}^2} + \frac{1}{\bar{\sigma}_{11}^2} - \frac{1}{\bar{\sigma}_{22}^2} \right)$ $= \frac{1}{2} \left(\frac{1}{R_{33}^2} + \frac{1}{R_{11}^2} - \frac{1}{R_{22}^2} \right)$ $H = \frac{(\sigma^0)^2}{2} \left(\frac{1}{\bar{\sigma}_{11}^2} + \frac{1}{\bar{\sigma}_{22}^2} - \frac{1}{\bar{\sigma}_{33}^2} \right)$ $= \frac{1}{2} \left(\frac{1}{R_{11}^2} + \frac{1}{R_{22}^2} - \frac{1}{R_{33}^2} \right)$ $L = \frac{3}{2} \left(\frac{\tau^0}{\bar{\sigma}_{23}} \right)^2 = \frac{3}{2R_{23}^2}$ $M = \frac{3}{2} \left(\frac{\tau^0}{\bar{\sigma}_{13}} \right)^2 = \frac{3}{2R_{13}^2}$ $N = \frac{3}{2} \left(\frac{\tau^0}{\bar{\sigma}_{12}} \right)^2 = \frac{3}{2R_{12}^2}$	<p>$\bar{\sigma}_{ij}$ is the measured yield stress value when σ_{ij} is applied as the only nonzero stress component.</p> <p>σ^0 is the user-defined reference yield stress specified for the metal plasticity definition.</p> <p>R_{ij} are anisotropic yield stress ratios,</p> $R_{11} = \frac{\bar{\sigma}_{11}}{\sigma^0} \quad R_{12} = \frac{\bar{\sigma}_{12}}{\tau^0}$ $R_{22} = \frac{\bar{\sigma}_{22}}{\sigma^0} \quad R_{13} = \frac{\bar{\sigma}_{13}}{\tau^0}$ $R_{33} = \frac{\bar{\sigma}_{33}}{\sigma^0} \quad R_{23} = \frac{\bar{\sigma}_{23}}{\tau^0}$ <p>Because of the form of the yield function, all of these ratios must be positive.</p> $\tau^0 = \sigma^0 / \sqrt{3}$
---	--

Since the anisotropic material data are already obtained in terms of *ratios of width strain to thickness strain*, mathematical relationships are then necessary to convert the strain ratios to stress ratios that can be input into ABAQUS (92).

As far as sheet metal forming applications are concerned, *plane stress condition* can be quite a reliable assumption; x, y as the “rolling” and “cross” directions in the plane of the sheet, and z in the thickness direction. From a *design viewpoint*, ‘desired anisotropy’ is normally considered as the type in which the sheet is *isotropic in the plane* and has an *increased strength in the thickness direction*, which is normally referred to as *transverse anisotropy*. *Planar anisotropy*, on the other hand, is a type of anisotropy, characterized by different strengths in different directions in the plane of the sheet (92).

Considering a *transversely anisotropic material* ($r_x = r_y$) for tensile test simulation (as it is assumed for evaluation of equivalent stress and strain), and defining σ^0 in the metal plasticity model to be equal to $\bar{\sigma}_{11}$, one can derive R_{ij} using flow rule, as

$$R_{11} = R_{11} = 1$$

$$R_{33} = \sqrt{\frac{r_x + 1}{2}}$$

Here, r_x was previously obtained from experimental tensile test; 0.8748 and 0.9005 for CP 1400HD and QP 1180, respectively. R_{11} , R_{22} and R_{33} now can be used in FEA SW in order to define the corresponding Hill'48 yield criterion parameters, in combination with initial yield strength (σ^0 or σ^{90}).

Concerning the meshing of the model, a couple of simulations with different numbers of element (with focus on the middle region) are done to observe the numerical convergence of the problem. Eventually, it is found that above 564 linear hexahedral elements of type C3D8R, the resulted load-elongation curves are almost identical. Thus, the following mesh configuration with 564 elements is selected.

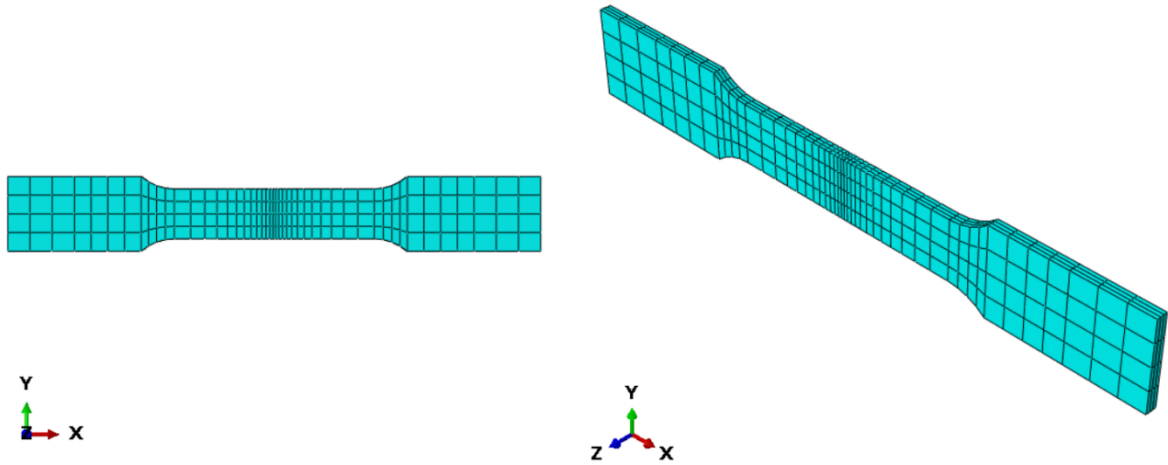


Figure 142 subsize specimen meshing in Abaqus

According to Choung and Cho's work (93), there would be merely a marginal difference between the results of full integration element²² (C3D8) and reduced integration element (C3D8R) in simulating a tensile test. Moreover, eight-node-plane-stress element with

²² For complicated finite element problems, using high order elements, it becomes necessary to use numerical integration to calculate the stiffness matrix, which then leads to evaluate displacement matrix. Reduced integration uses a lesser number of Gaussian co-ordinates when solving the integral. Clearly, the more Gaussian co-ordinates you have for each element, the more accurate your answer will be, but this has to be compared with the cost of computation time. Displacement-based FE formulations always over-estimate the stiffness matrix and the use of fewer integration points should produce a less stiff element. Hence, especially in non-linear problems, it is advisable to use reduced integration instead of full integration. The slight loss of accuracy is counteracted by a better approximation to real problem (ref. www.researchgate.com, available 2021).

reduced integration (74) (CPS8R) is shown to provide acceptable results, as far as tensile test simulation is concerned.

To *trigger diffuse necking*, it is only needed to apply a finer mesh around the centre of the specimen (where large strain gradient can take place), without imposing any geometric imperfections in the width of the model (93). Furthermore, by observing the stress distribution in the necked zone, no sign of large stress concentration was seen in the high-density mesh region.

For each step in the analysis, using *Step Manager*, one can decide whether Abaqus accounts for *nonlinear effects from large displacements and deformations*; such that, if the displacements in a model due to loading are relatively small during a step, the effects may be small enough to be ignored. However, in situations where the loads on a model result in large displacements, imposing nonlinear geometric effects can become crucial. The ‘*Nlgeom*’ setting for a step determines whether ABAQUS will account for geometric nonlinearity in that step. Herein, since the focus was on the deformation up to diffuse necking, no significant changes in evaluated deformation were observed in this range, even when *Nlgeom* option was turned off. However, in larger values of strain, this option showed a considerable outcome on the strain field.

Based on the *Dirichlet type BCs* (imposed displacements), the nodes on the upper and lower surfaces of one of the specimen’s head are fixed, while on the other side, based on the provided tensile tests’ data sheet, a total displacement of 5.97 mm along the tensile axis is applied by 0.008 mm step for CP1400HD, for instance.

6.2.2 Post-processing: analysis of the numerical results

6.2.2.1 Load-displacement curves comparison

Based on the previously obtained results from image processing, equivalent stress-equivalent plastic strain curve was achieved in chapter five, for both CP1400HD and QP1100. As an important result, the material plastic behaviour for far larger strain levels than what can be attained through common uniaxial tensile test is already available. The above-mentioned curves then can be extended benefiting from a proper strain hardening law (here, Ramberg-Osgood law is used). The results are shown in the following figures,

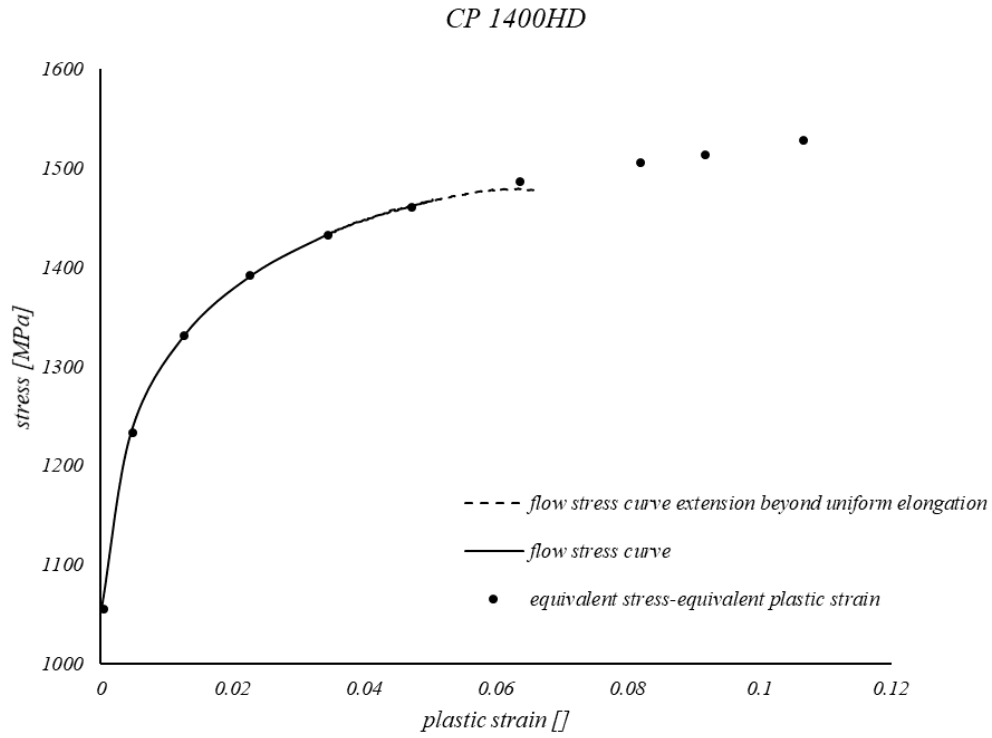


Figure 143 equivalent flow stress curve for CP 1400HD

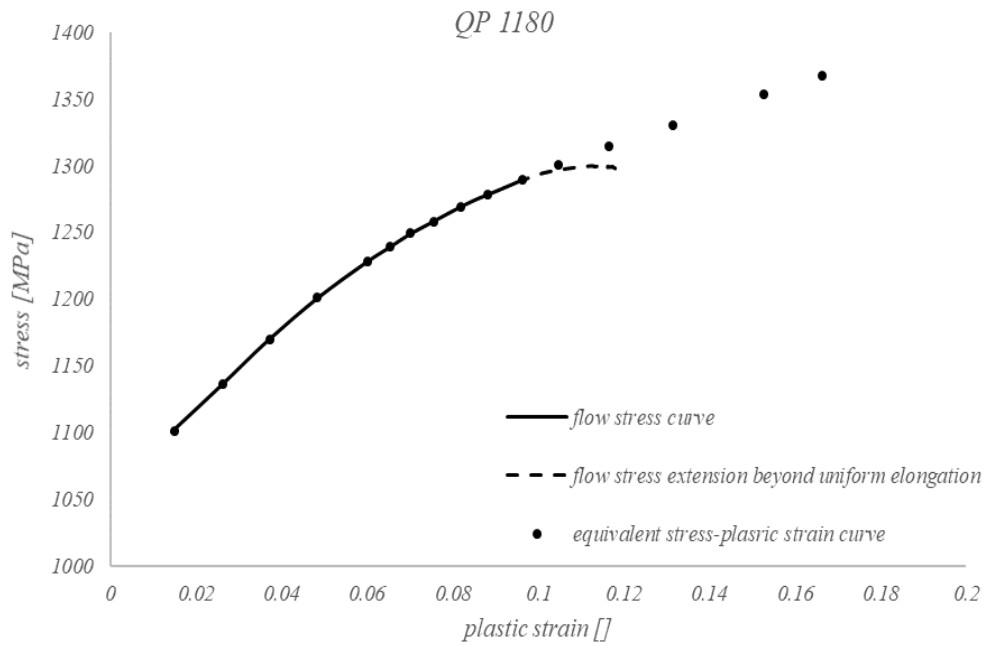


Figure 144 equivalent flow stress curve for QP 1180

As it was stated, by extrapolating the equivalent curve using RO hardening law, the following results were obtained, which then can be implemented in FEA as material model inputs,

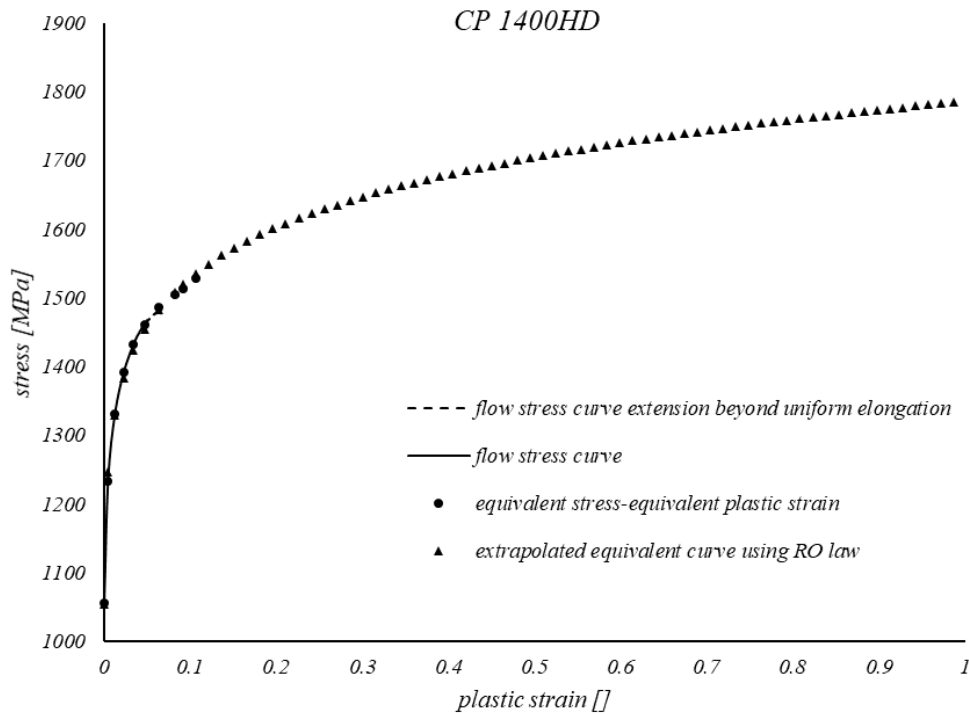


Figure 145 fitting and extrapolation of the equivalent flow curve with RO hardening law-CP 1400HD

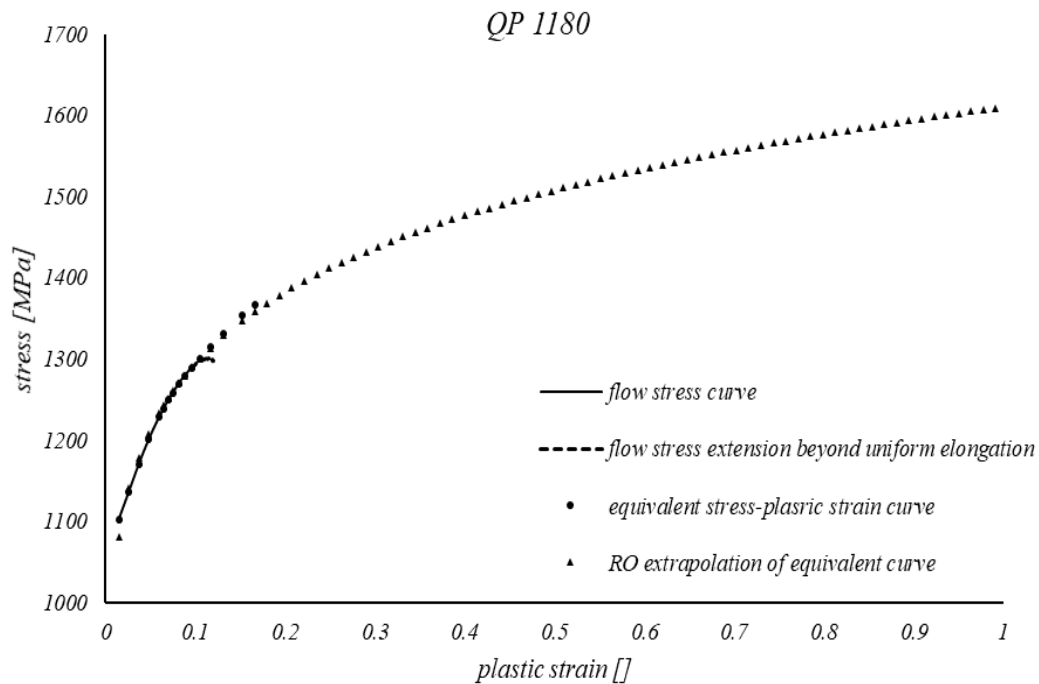


Figure 146 fitting and extrapolation of the equivalent flow curve with RO hardening law-QP 1180

The resulted flow stress curve is then imported into the material module of the FE SW, so as to define the plastic response of the material during forming operation. Finally, by comparing the force-elongation diagrams as well as the strain fields of FEA with that of

experiment, (while keeping all the other conditions the same as in the experimental tensile test of the material) the reliability of the flow stress curve can be assessed.

Experimental load-displacement curve can be obtained through tensile test machine output. A comparison was made between the 'load vs elongation' curve of the tensile test and that of the numerical simulation, in which the same two points of extensometer were also chosen on the FE model in order to evaluate the elongation during deformation.

The reaction force in FEA was obtained at the centre of the specimen, as shown in the following figure,

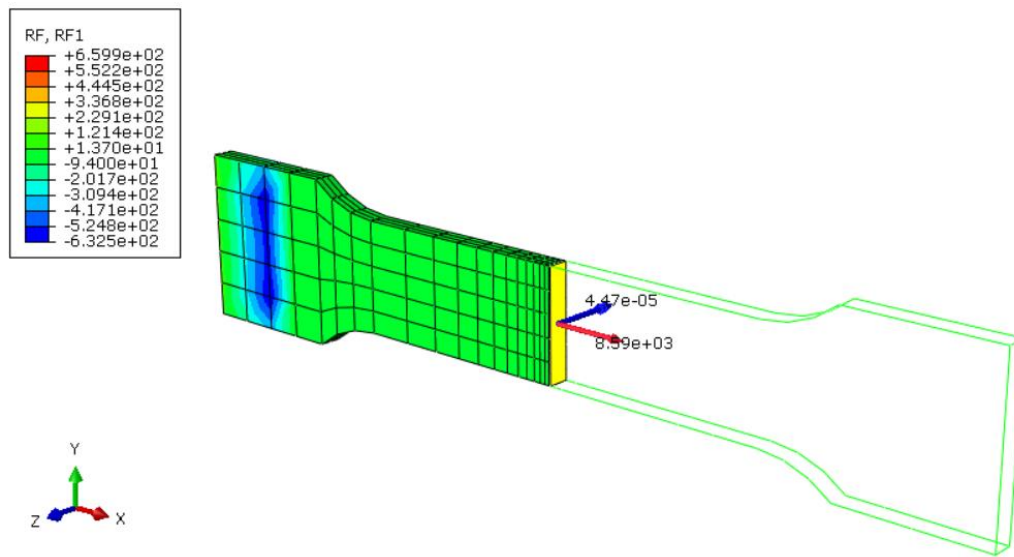


Figure 147 reaction force in FEA obtained at the centre of the model

On the other hand, the relative displacement between two sections (corresponding to the zone actually measured with the extensometer in tensile test) leads to obtain the elongation in FEA,

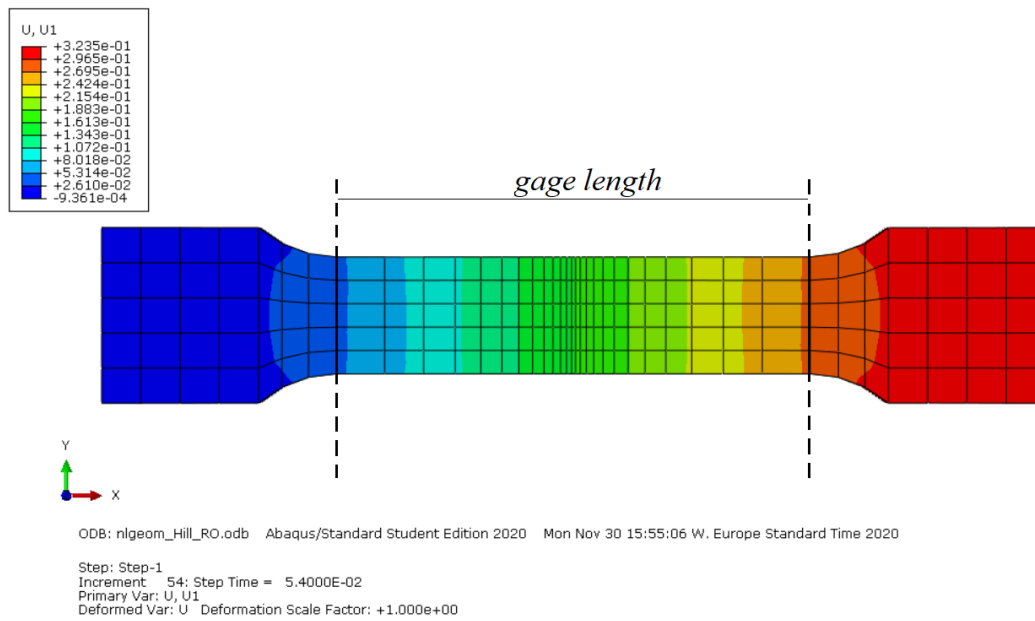


Figure 148 relative displacement between two sections to obtain the elongation in FEA

Figures below compare the ‘force-elongation’ results coming from FEA and experiment, for both CP 1400HD and QP 1180,

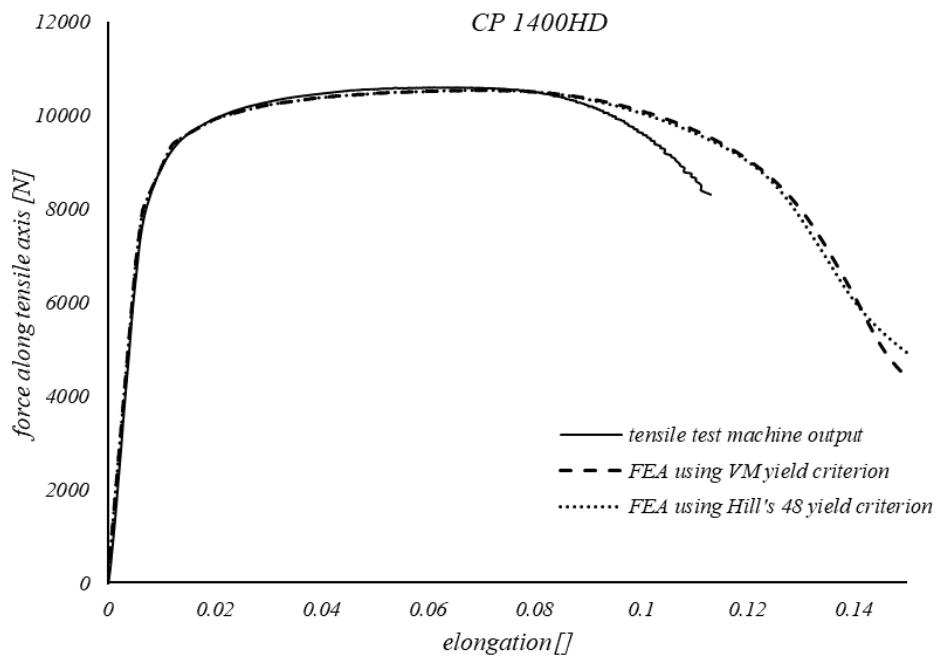


Figure 149 load vs elongation curve of the tensile test and that of the numerical simulation-CP 1400HD

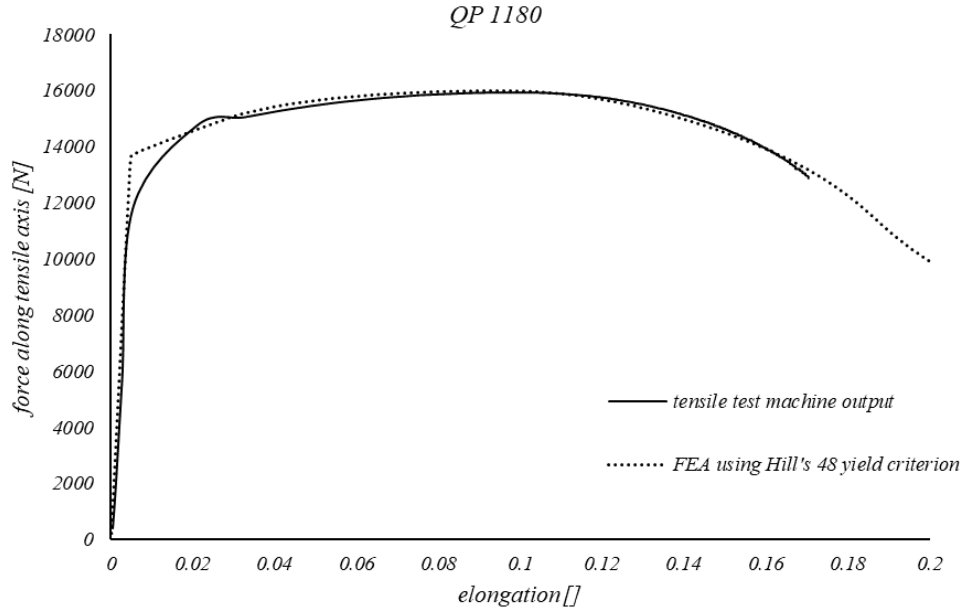


Figure 150 load vs elongation curve of the tensile test and that of the numerical simulation-QP 1180

This comparison shows that the numerically-simulated tensile test is able to reproduce the experimental test until the onset of longitudinal necking; while above this point, the two curves do not lie on top of each other due to different flow stress curves. The small difference between the results in QP 1180, on the one hand, may come from the fact that not enough data points were available from the tensile test machine in that range; on the other hand, the initial yield point in equivalent flow stress curve still needed to be adjusted based on the missing information.

Moreover, theoretically, the necking appears when the slope of the force-elongation curve reaches zero value, as according to Considère criterion, $\frac{d\sigma}{d\varepsilon} = \sigma$. As soon as longitudinal necking takes place, mechanical extensometer measurements are erroneous due to the presence of *strain heterogeneity*. This phenomenon also occurs in the *finite element simulation*.

6.2.2.2 Strain fields comparison

Strain fields corresponding to both FEA and tensile experiment (DIC technique) are compared in this section.

At the same elongation (6%, which is almost equal to the elongation at diffuse necking for CP 1400HD), the longitudinal strain distribution along the gage length was obtained for the elements shown in the figure below,

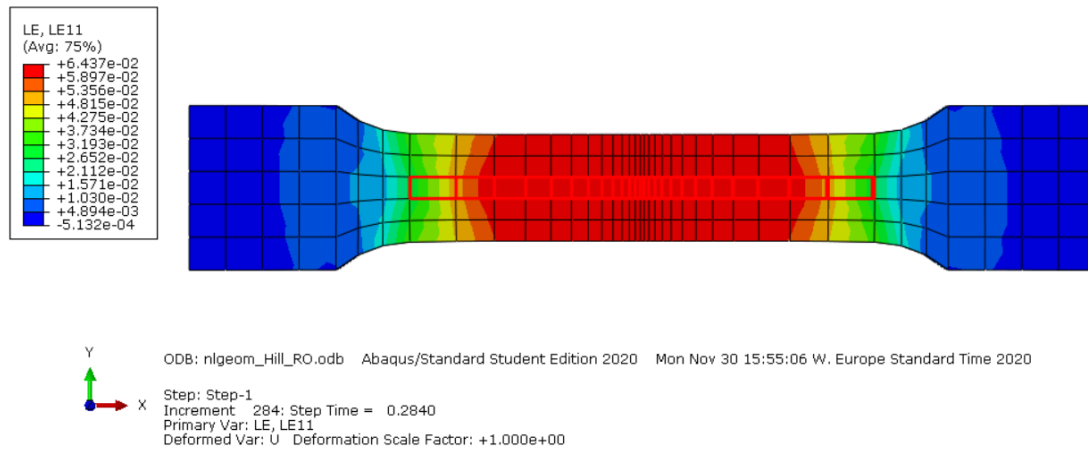


Figure 151 elements used to obtain the longitudinal strain distribution along the gage length

The longitudinal strain (ϵ_{xx}) distribution along the gage length is reported in the following figure, showing an average between 6% and 7%, as it was expected in the uniform elongation,

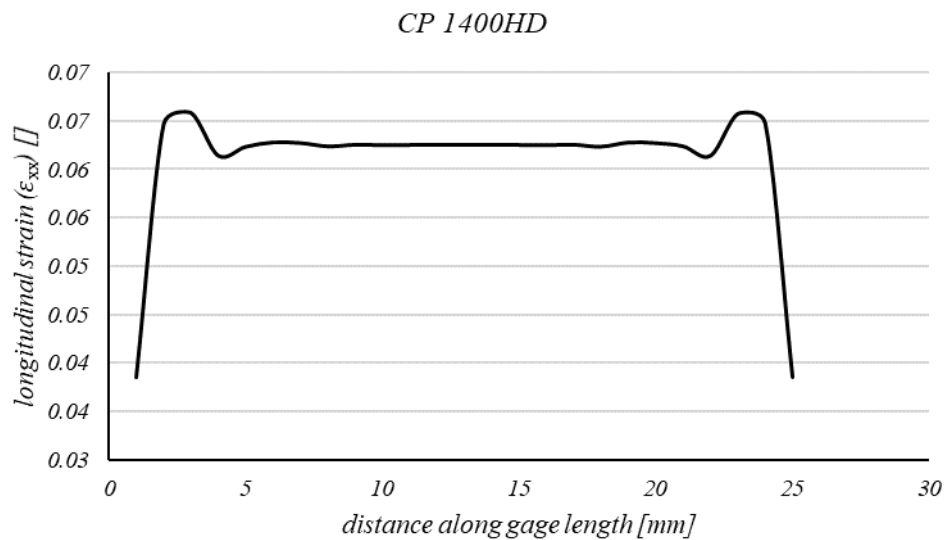


Figure 152 longitudinal strain (ϵ_{xx}) distribution along the gage length from FEA-CP 1400HD

On the other hand, from DIC results, the longitudinal strain along the specimen gage length was already obtained and illustrated in the following figure,

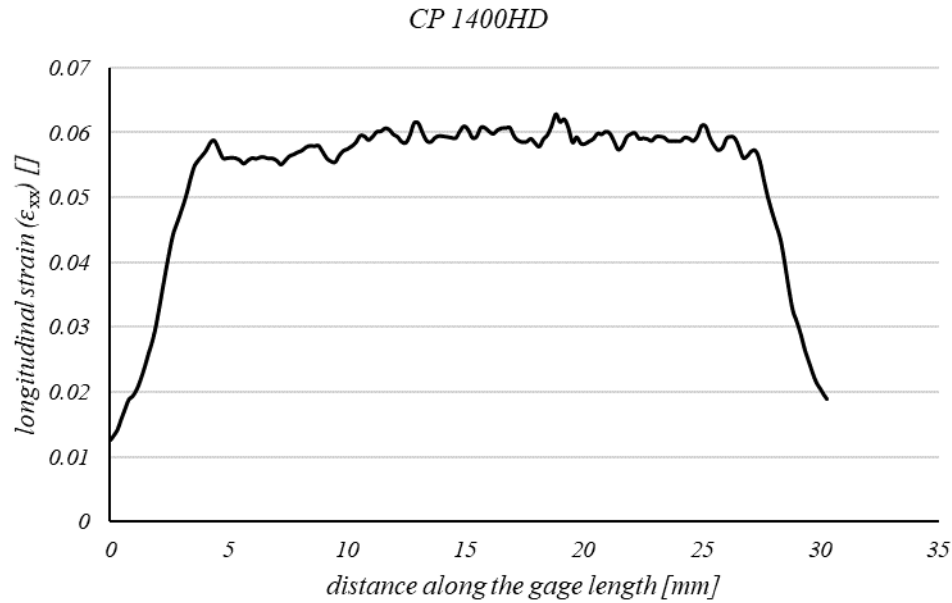


Figure 153 longitudinal strain (ϵ_{xx}) distribution along the gage length from tensile test-CP 1400HD

Looking at the above figures, one can observe only a marginal difference between the longitudinal strain gradients obtained from DIC and FEA; an average value of 6.29% was obtained for longitudinal strain in FE simulation, while slightly lower value of average longitudinal strain along GL, around 5.87%, was observed in image processing method.

The writer believes that, regardless of the effect of the element size and convergence of strain values, firstly, it should be noted that in real tensile test of CP 1400HD, larger strains can be seen on the *right end of the specimen in comparison with its left end* (as can be seen in the last figure), showing that the neck is going to start not in the centre, but closer to the right side of the specimen (as opposed to what occurred in FEA). Perhaps, by applying a geometrical imperfection (e.g. a slight width reduction) in the centre of the specimen, the two results could be even more similar to each other. Secondly, as the plastic behaviour imported in FEA includes also post-necking behaviour of the material, necking occurs in considerably larger values of strain in comparison with the tensile test itself. This may lead to larger capacity of the material to accumulate strain before entering necking, leading to larger value of longitudinal strain.

Furthermore, significantly lower values of strain on both ends are resulted from the grips effect, where the stress magnitude is lower.

A comparison was also made between the numerical simulation result and the image processing of test specimen for QP 1180 at specimen total strain value of 10% (at diffuse

necking point). The total longitudinal strain along the specimen GL obtained from FEA is shown in the following figure,

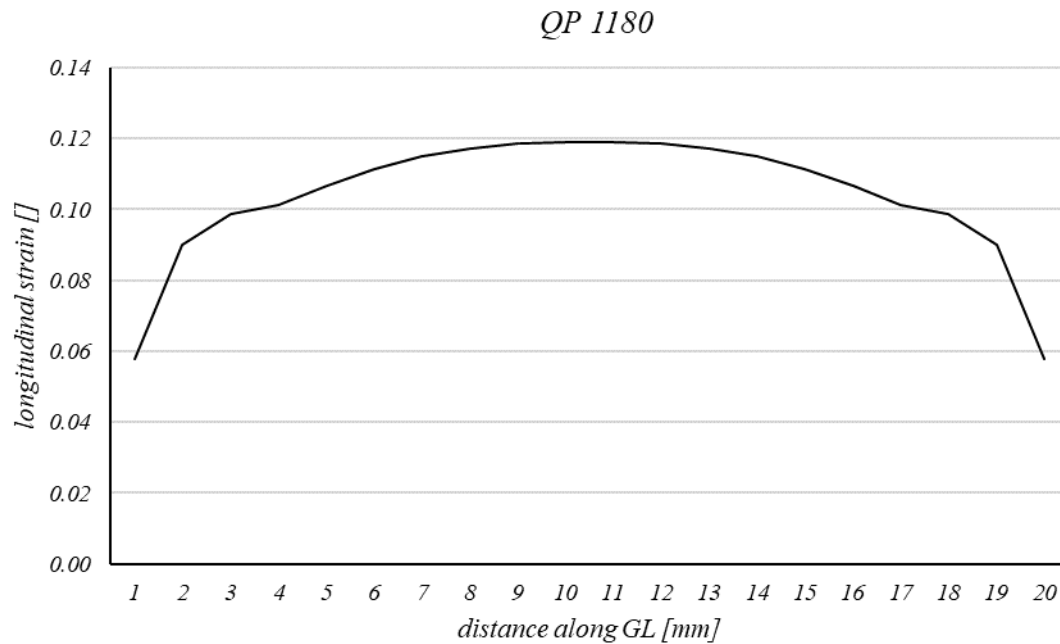


Figure 154 longitudinal strain (ϵ_{xx}) distribution along the gage length from FEA-QP 1180

On the other hand, DIC technique resulted in the following longitudinal strain distribution along the specimen gage,

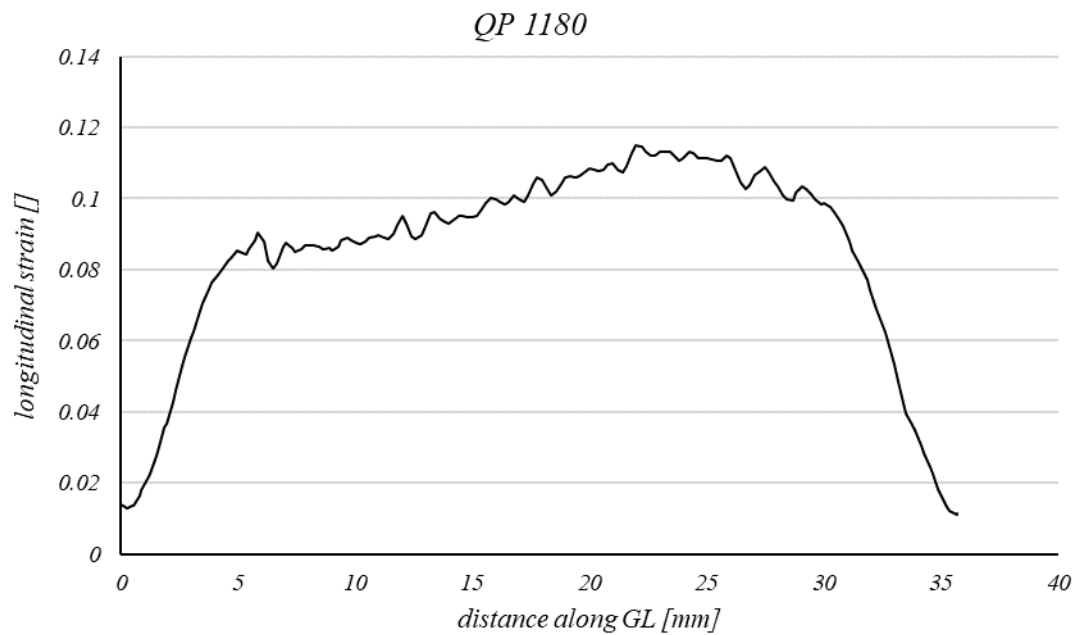


Figure 155 longitudinal strain (ϵ_{xx}) distribution along the gage length from tensile test-QP 1180

Even from the QP 1180 results, it is clear to observe the effect of ‘off-centre necking’ on the distribution of longitudinal strain along the GL.

Thus, from the load-displacement curve and strain field comparison, it can be deduced that the equivalent stress-equivalent plastic strain relationship is correctly determined up to the specimen’s total strain value of 6% for CP 1400HD and 10% for QP 1180.

6.2.3 Further investigation on FE results

Strain fields in longitudinal, width and thickness directions at *necked region* were also investigated. From DIC technique longitudinal and width strain at neck were directly obtained through 2D image processing SW, GOM, while thickness strain was derived from volume consistency principle. Concerning FEA, these values at specimen total strain value of 6% for CP 1400HD and 10% for QP 1180 (corresponding with diffuse necking) are presented in this section and compared with the strain field at neck in real tensile test.

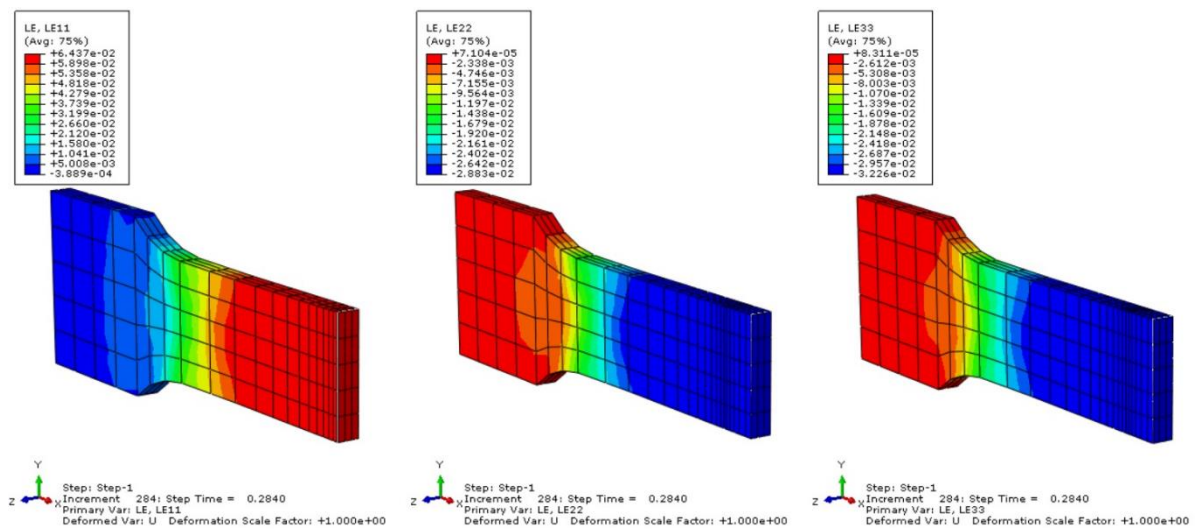


Figure 156 Strain field in longitudinal, width and thickness directions

6.2.3.1 Strain in longitudinal direction (ϵ_{xx}) at neck: CP 1400HD and QP 1180

Looking at the distribution of the longitudinal strain (ϵ_{xx}) at neck resulting from FEA of CP 1400HD, the average value is found to be around 6.25%, with a maximum taking place at the centre of the section,

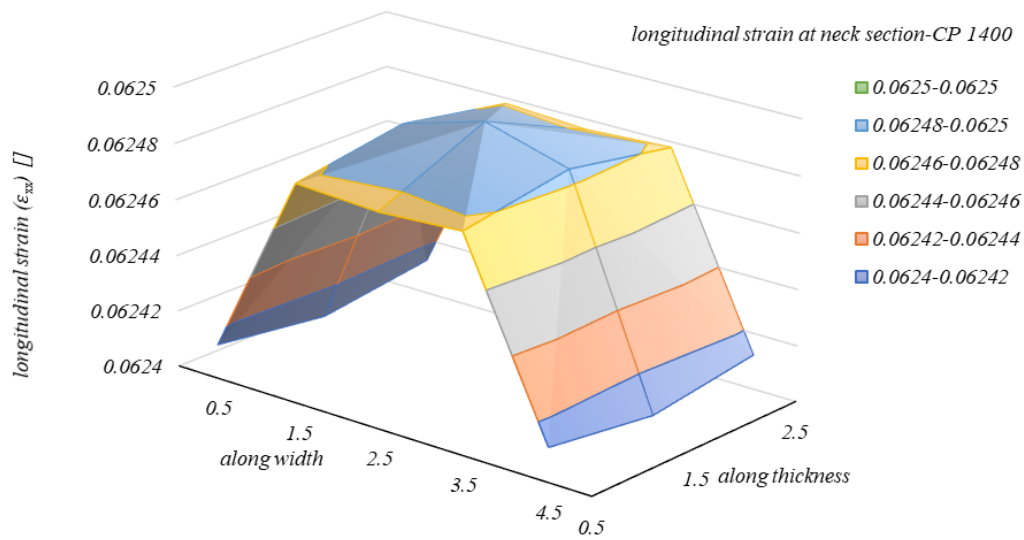


Figure 157 Strain in longitudinal direction (ϵ_{xx}) at neck from FEA-CP 1400HD

On the other hand, longitudinal strain at necked section obtained from DIC technique shows both the same trend and values as can be seen in the following figure,

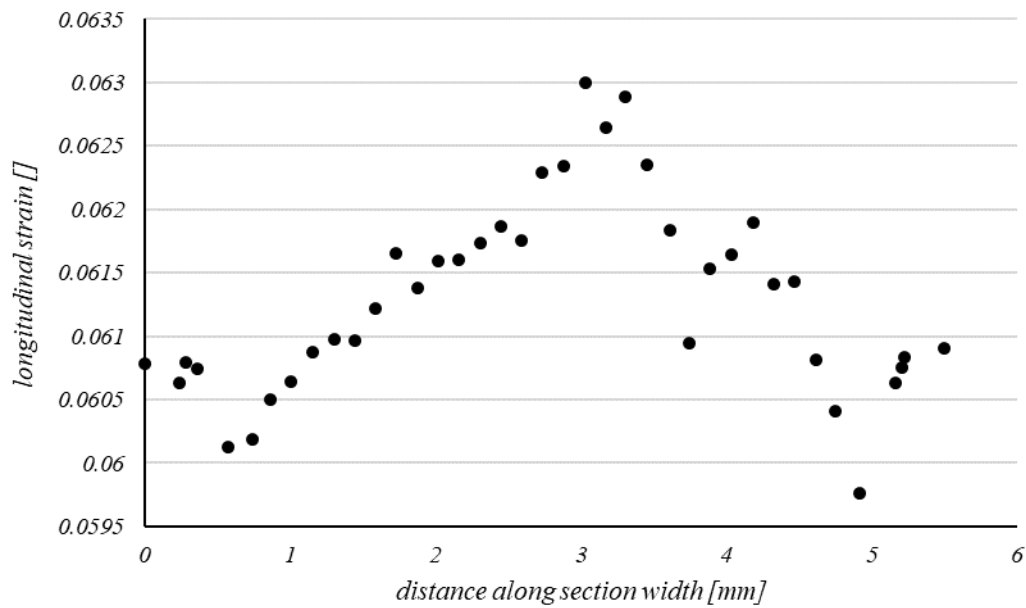


Figure 158 Strain in longitudinal direction (ϵ_{xx}) at neck from tensile test-CP 1400HD

For QP 1180, the longitudinal strain distribution at neck results in the following diagram, where the variation is in a range between 11.6% and 12%,

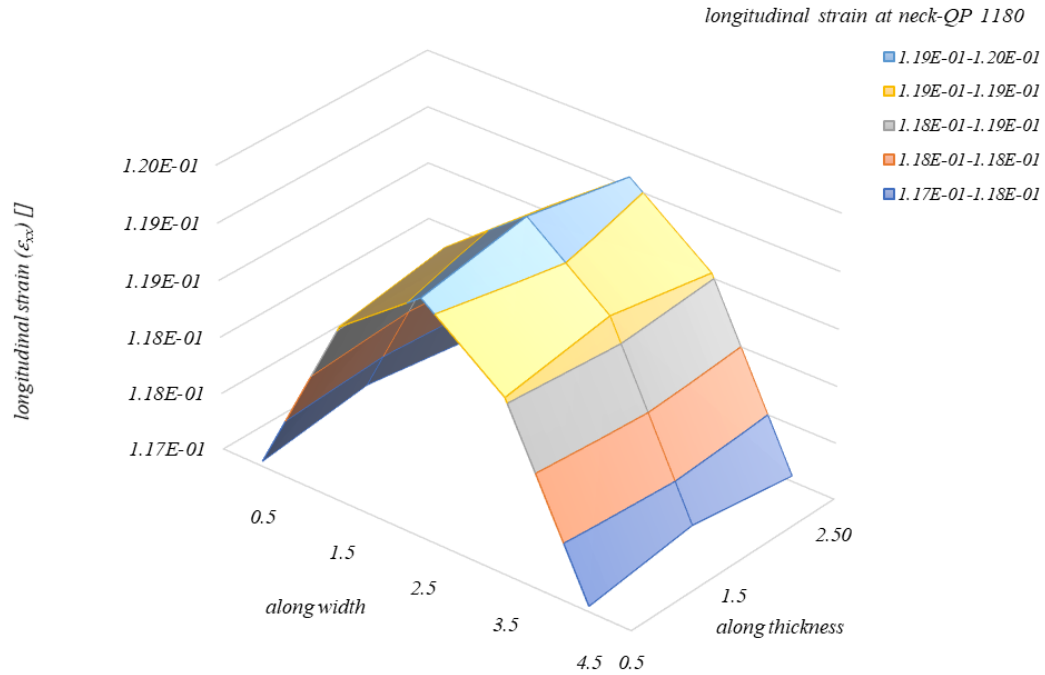


Figure 159 Strain in longitudinal direction (ϵ_{xx}) at neck from FEA-QP 1180

Similarly, DIC technique yields to a longitudinal strain (ϵ_{xx}) distribution over the neck with a variation between 11% and 11.3%, as it is shown in the following figure,

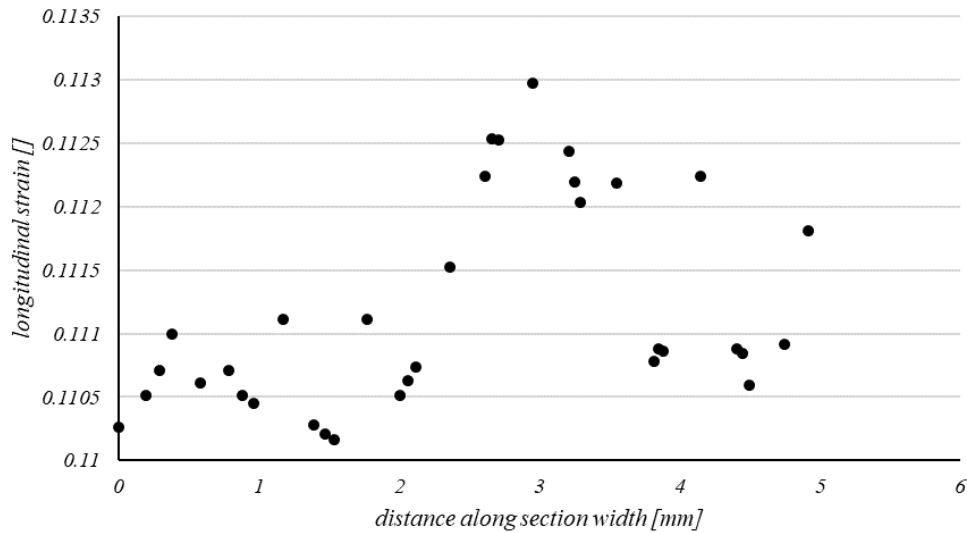


Figure 160 Strain in longitudinal direction (ϵ_{xx}) at neck from tensile test-QP 1180

6.2.3.2 Strain in width direction (ϵ_{yy}) at neck: CP 1400HD and QP 1180

Strain distribution in the width direction (ϵ_{yy}) of the section can also be assessed through the post-processing of the conducted FEA. Figure below shows the variation of the width strain at neck,

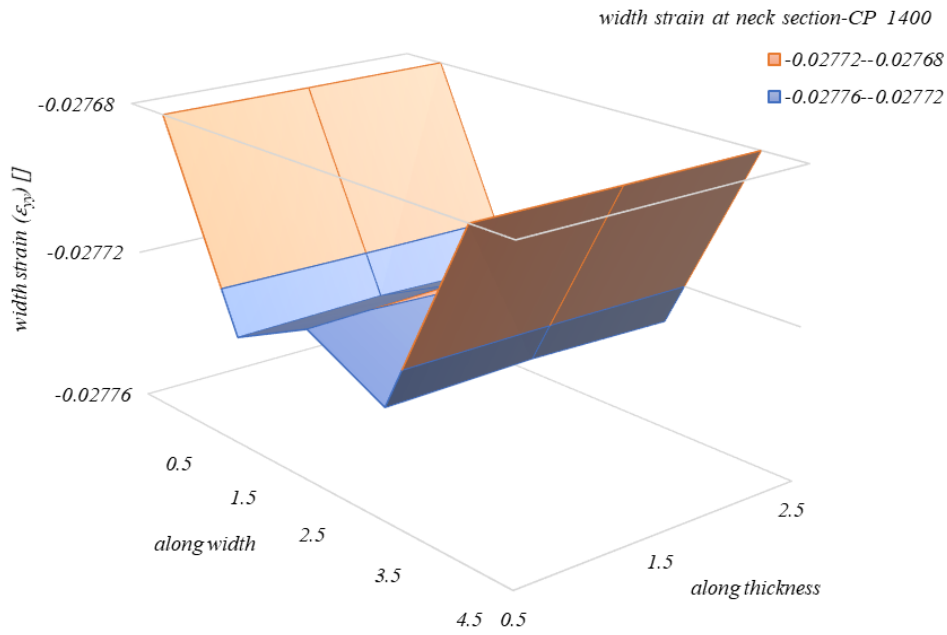


Figure 161 Strain in longitudinal direction (ϵ_{yy}) at neck from FEA-CP 1400HD

For the sake of a comparison with image processing results, one can observe that in both cases, the width strain have a negligible variation over the section, and the values are varying almost in the same range. From GOM SW, the following result is obtained for width strain (ϵ_{yy}) along the neck,

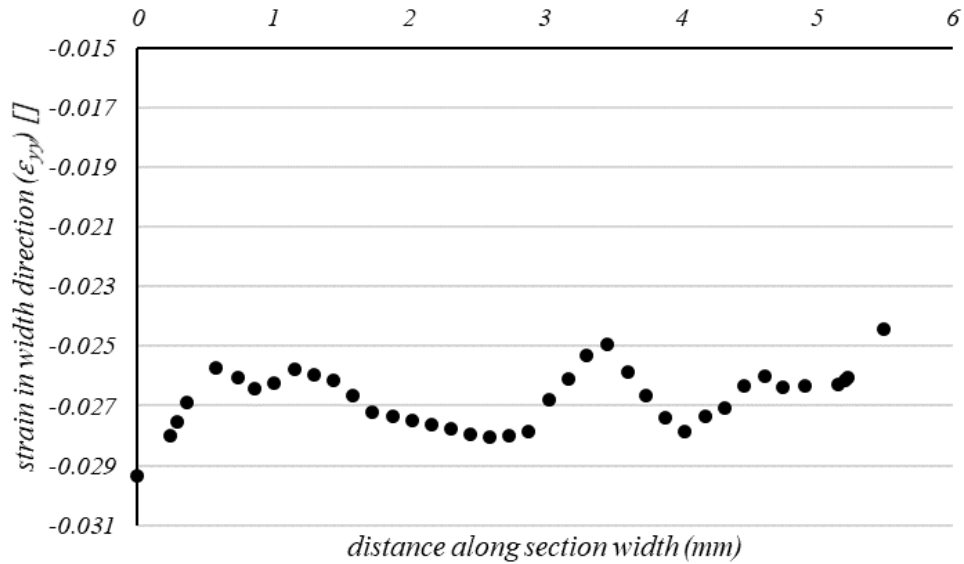


Figure 162 Strain in longitudinal direction (ϵ_{yy}) at neck from tensile test-CP 1400HD

Same analysis is also done for QP 1180; as shown in the following figure obtained from FEA, the variation is more evident along the width, while along thickness only small change in width strain can be observed,

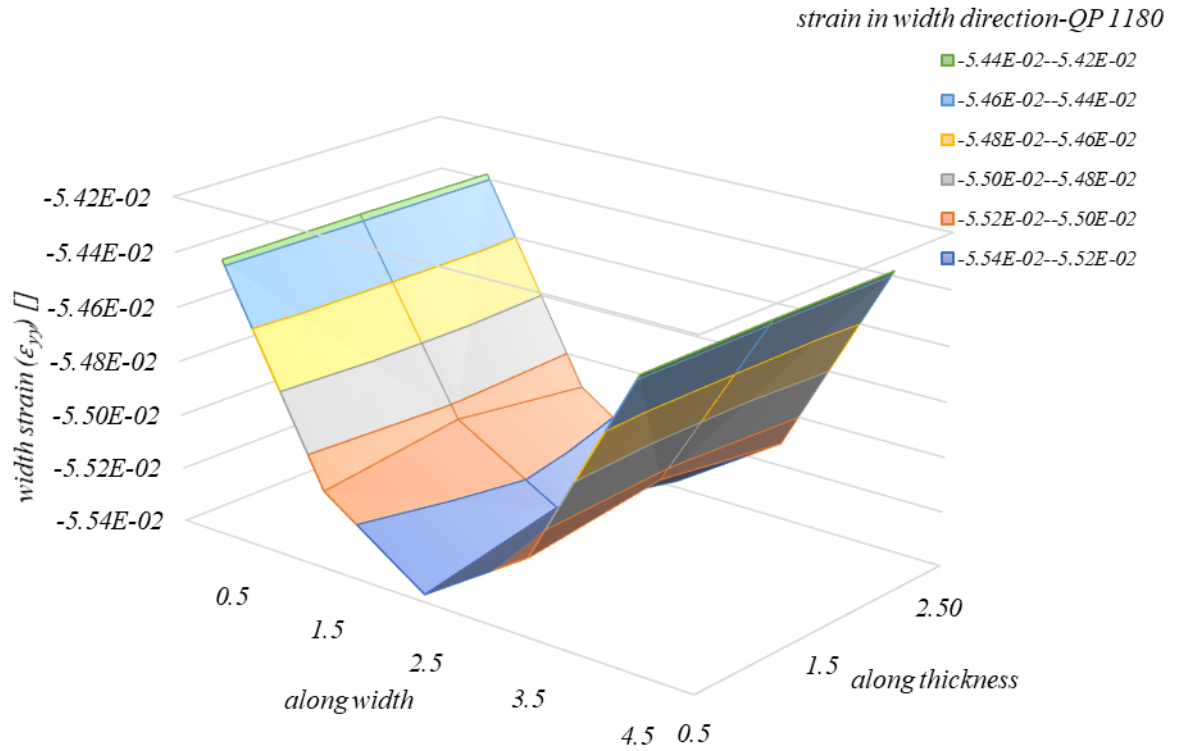


Figure 163 Strain in longitudinal direction (ϵ_{yy}) at neck from FEA-QP 1180

The range of width strain variation is observed to be between -5.44% and -5.54%, with a maximum in the centre of the specimen's width. On the other hand, image analysis of QP 1180 tensile test led to the following variation of width strain at neck section,

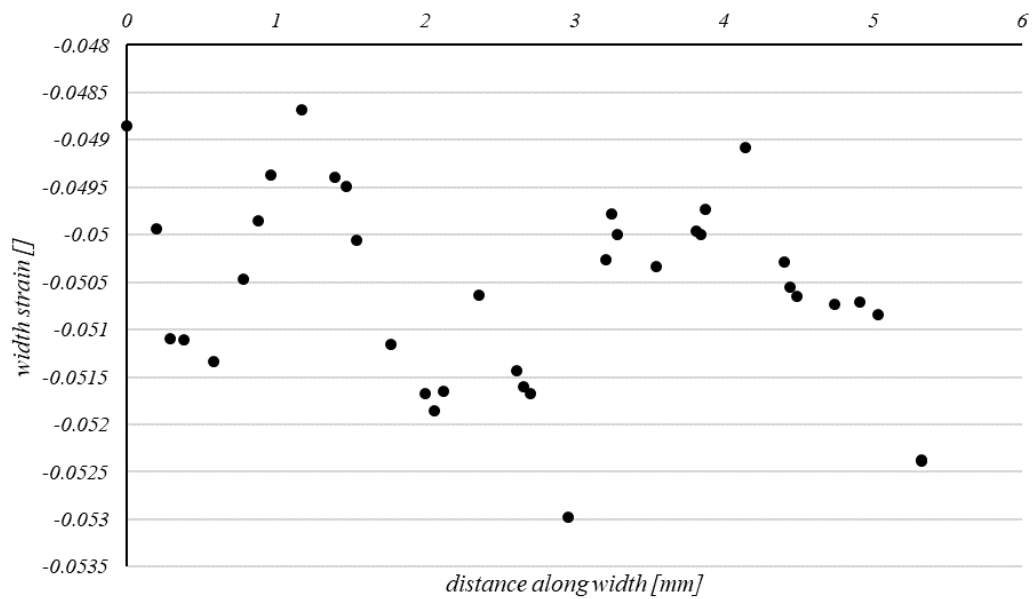


Figure 164 Strain in longitudinal direction (ϵ_{yy}) at neck from tensile test-QP 1180

The scatter of the data is in a range between -4.85% and -5.30%, with a maximum in the centre of the specimen width, which is very close to the FEA results.

6.2.3.3 Strain in thickness direction (ϵ_{zz}) at neck: CP 1400HD and QP 1180

With regard to the thickness strain (ϵ_{zz}), FEA gives the distribution as it is shown in the following figure,

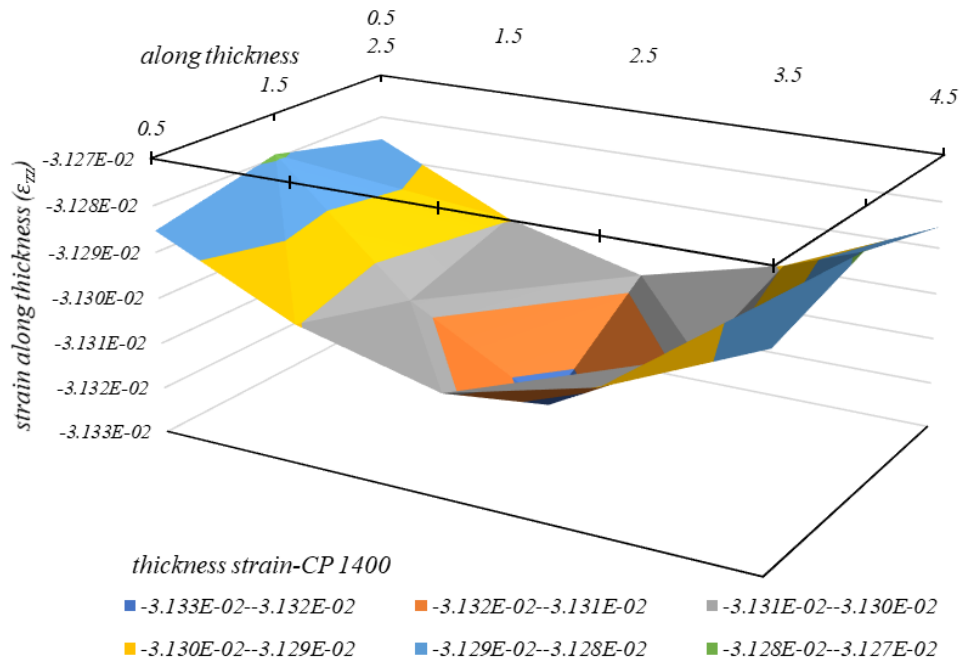


Figure 165 Strain in longitudinal direction (ϵ_{zz}) at neck from FEA-CP 1400HD

While using 2D image processing, the strain in thickness direction can be found via volume consistency equation. As it can be observed, the maximum happens at the centre of the section (3.8%), but the value is not exactly the same as it is obtained from FEA (3.13%).

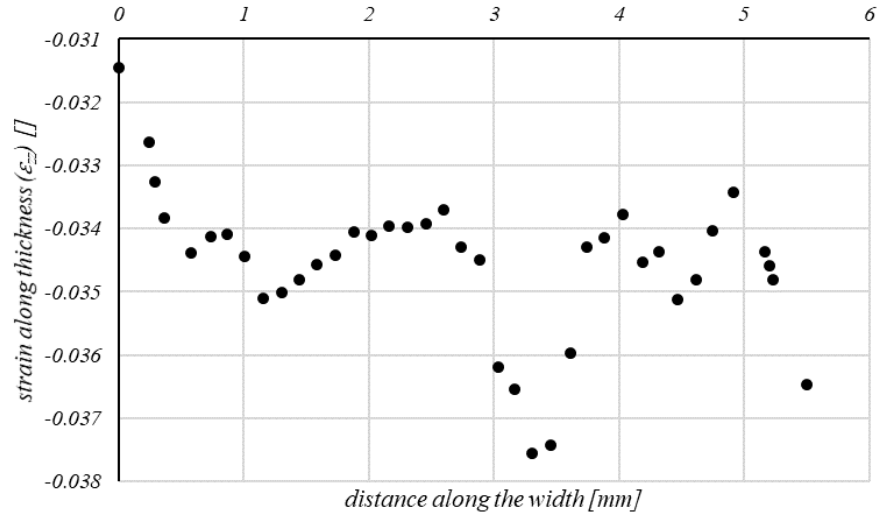


Figure 166 Strain in longitudinal direction (ϵ_{zz}) at neck from tensile test-CP 1400HD

Looking at the strain in thickness direction at neck, numerical simulation and image processing lead to the following observations,

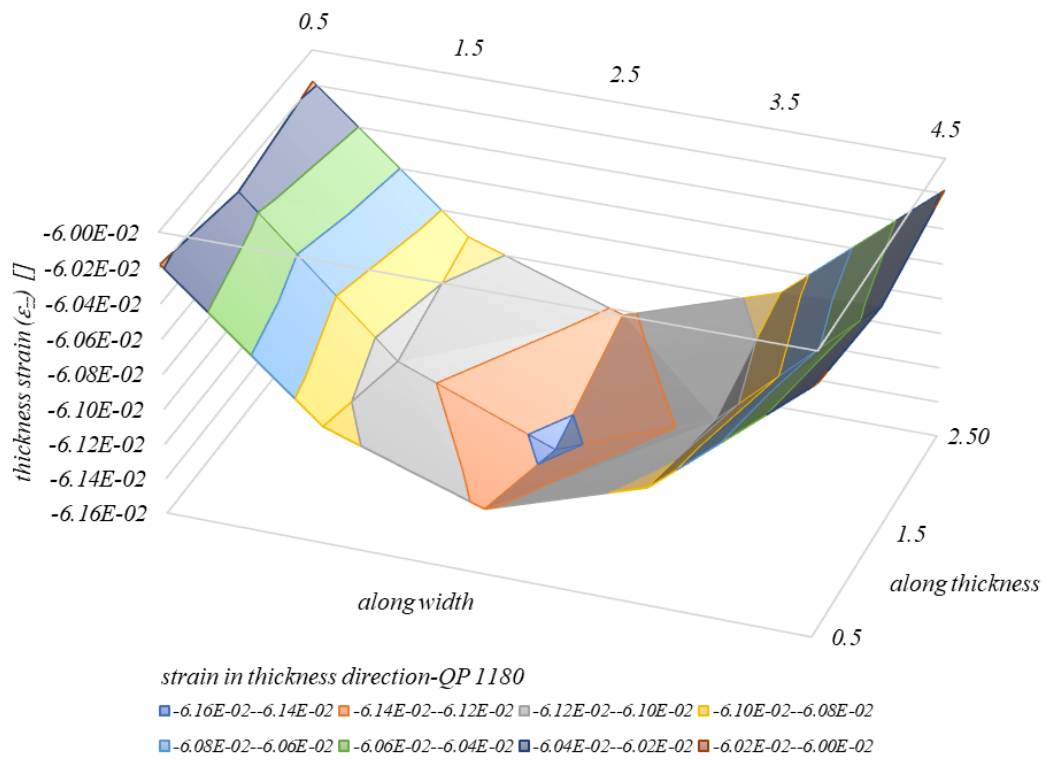


Figure 167 Strain in longitudinal direction (ϵ_{zz}) at neck from FEA-QP 1180

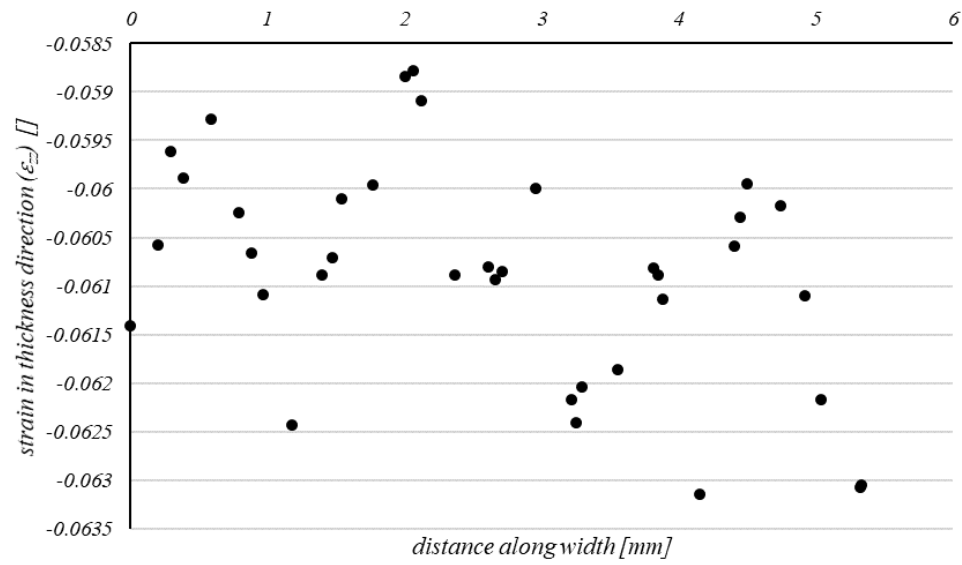


Figure 168 Strain in longitudinal direction (ϵ_{zz}) at neck from tensile test-QP 1180

Where both the findings show the thickness strain at neck to be somewhere between -5.85% and -6.30%.

6.3 A REVIEW ON THE FEA OF THE TENSILE TEST

The previously-obtained equivalent stress–equivalent plastic strain curve was introduced into a finite element code to simulate numerically the same tensile test. On the one hand, the good reproduction of the load–displacement curve with the finite element code validates the quality of the stress–strain curve. While on the other hand, this numerical simulation validates the image analysis measurements since the strain levels simulated are almost identical to the experimental ones, both within the gage length and in necked zone, until the onset of transversal necking. From this study, determining a precise flow stress curve was shown to have a role of paramount importance when a deep drawing simulation is to be conducted.

CHAPTER SEVEN: CONCLUSION AND POSSIBLE FUTURE WORKS

General approaches corresponding to the post-necking behaviour identification of metallic materials were discussed in this thesis work by exploiting a number of uniaxial and biaxial tests in combination with DIC technique. It was also highlighted that a material model is a crucial input of any forming simulation which needs a certain yield criterion, an associated flow rule as well as a hardening rule to define its plastic deformation. While with regard to its failure, forming limit curves are necessary to be observed. Although extrapolation method gives only an overlook of the behaviour beyond diffuse necking, both experiment and simulation must be employed in our approach preferably inside an optimization process so as to reach a good approximation of the post-necking material behaviour.

κ -exponent function was employed for the first time in order to find a fitting function by means of a nonlinear regression analysis of pre-necking data points. The results demonstrated that κ -exponent provided a very good fit for small values of strain than HS; however, HS performs better in large deformation. Thus, a linear combination of κ -exponent function and a non-saturated hardening law can lead to a very good fit to extrapolated flow stress data points.

With a tensile test machine equipped with a camera to capture the spackled surface of the specimen, Hill's 48 yield criterion, accompanied with a proper strain hardening law, was used to draw the equivalent stress-equivalent plastic strain curve to strain levels beyond the uniform elongation. Although this method still needs further investigation both from numerical simulation and reliability points of view, it seems a good practice to compare the result with post-necking behaviour of the material obtained through biaxial test. On the other hand, some important factors can be studied deeper in future observations; the effect of voids formation on the onset of localised necking, for instance, where they are both inevitable and considerable for most materials entering necking. As the present work was influenced by the lack of micromechanical knowledge on void formations, this phenomenon constrained the volume constancy assumption. Hence, it would be quite noteworthy to conduct an observation in microscopic scale to assess the significance of void formation in large deformation, and the amount of error may arise in the forming simulation if this simplifying assumption is taken into consideration. On the other hand, although based on the strain distribution at the necked region, the normal anisotropy and strain rate ratio were considered constant during deformation, their variation must be taken into account, as the state of stress and strain are changing during the deformation.

As far as necking is concerned, Considère criterion was employed in chapter five to approximate the engineering strain level in which diffuse necking starts to form during tensile test. However, image processing demonstrated that longitudinal necking takes place in lower levels of strain than the point of maximum force. The results provokes the idea of implementing a more precise criterion for diffuse necking approximation. While, concerning localized necking, time-dependent and time-independent approaches are available in literatures as an alternative to DIC technique direct observations.

The good reproduction of the load–displacement curve in FEA proved the quality of the stress–strain curve. Moreover, this numerical simulation was able to validate the image analysis measurement, as the strain levels obtained from FEA were comparable to the experimental ones, until the onset of longitudinal necking. However, the position of the neck and the inclination of shear bands in a specimen under uniaxial tensile test is totally different from the result of FEA, meticulous care should go into modifying the geometries of both the specimen and the corresponding FE model. This adjustment seems to be a *must* when one is dealing with a FE-based inverse method in order to optimise the parameters of the material model.

With regard to the validation of the equivalent stress-strain curve, it would also be interesting to observe the application of the equivalent flow stress curve in the numerical simulation of the biaxial test and to compare the stress and strain distribution at the apex with the real test of the same material.

Further and even more importantly though, the equivalent stress-strain curve, obtained in chapter five, was principally derived from average value of strain field in each level of total strain within gage length. This fact implies that, as the strain field starts to localise, finding the average value of strains (in longitudinal and transverse directions) is no longer meaningful and acceptable, which in turn, significantly restricted this method. Unfortunately, the writer could not find a way to overcome this limitation; however, an efficient alternative might be to study principal effective strains, as it was described in 5.4.2, (FLC evaluation using MMFC).

Regardless of the method chosen for post-necking behaviour identification, future assessments should be initiated with a detailed study on the determination of the most suitable yield criterion/surface for the material under investigation, which is only achievable by doing a series of uniaxial and biaxial tests, and then observing which criterion is able to

fit these experimental data effectively, as well as what are the resulted yield criterion's parameters. In the next step, the selected general approach plays its role mostly by minimising a cost function, wherein, benefiting from DIC technique, the strain field within the gage length should be observed a priori. It has already found that, although '*complete solutions*' to identify the strain hardening behaviour beyond longitudinal necking seems to be suitable and effective, solutions solely based on FE-based inverse approach are not only time consuming, but also the coupling between the experimentally investigated quantities, such as strain fields, and the numerically evaluated quantities can be a stumbling block within the procedure. While, according to the literatures, complete solutions like, VFM (discussed in chapter two) showed a very good agreement with experiments and is deserved to be studied in a whole new work. Other test methods, such as 'multiaxial stress test using tubular specimen' and 'shear test', rather than 'uniaxial tensile test' can also be taken into account in order to obtain large deformation without plastic instability.

BIBLIOGRAPHY

1. *Material Characterisation for Metal Forming Simulation. NAFEMS. [Online]*
<https://www.nafems.org/downloads>.
2. Hosford, W. F. and Caddell, R. M. *Metal Forming: Mechanics and Metallurgy. 4th edition. s.l. : Cambridge University Press, 2011.*
3. Kessler, Lutz , et al. *Challenges in material model selection for industrial forming simulation. s.l. : ThyssenKrupp Steel Europe, 2012.*
4. Dutton, T. *Why do Manufacturing Simulation. NAFEMS. [Online] 2017.*
5. *Material characterization for numerical simulation of manufacturing of automotive part made of magnesium alloy. Pietrzyk, Maciej , et al. 6, 2020, Archives of Civil and Mechanical Engineering, Vol. 20.*
6. Visrolia, A. *Material Testing for Manufacturing Process Simulation. nafems. [Online] www.nafems.org.*
7. Donald R. Askeland, Wendelin J. Wright. *The Science and engineering of materials. s.l. : Global Engineering, 2014.*
8. *the aluminium effect. European Aluminium. [Online] <https://european-aluminium.eu/about-aluminium/the-aluminium-effect/>.*
9. Djukanovic, G. *Aluminium Alloys in the Automotive Industry: a Handy Guide. Aluminium insider. [Online] 2019. <https://aluminiuminsider.com/aluminium-alloys-automotive-industry-handy-guide/>.*
10. *5000 series aluminum sheet. aluminum supplier. [Online] <https://www.aluminumsupplier.com/5000-series-aluminum-sheet/>.*
11. *6000 series aluminum sheet. aluminum supplier. [Online] <https://www.aluminumsupplier.com/6000-series-aluminum-sheet/>.*
12. *Complex Phase (CP) Steels. world auto steel. [Online] <https://www.worldautosteel.org/steel-basics/steel-types/complex-phase-cp-steels/>.*
13. *Data sheet Complex-phase steels. voestalpine. [Online] <https://www.voestalpine.com/ultralights/content/download/4522/file/Complex-phase-Steels-voestalpine-EN-12062019.pdf?inLanguage=eng-GB>.*

14. *Advanced High-Strength Steel (AHSS) Definitions*. world auto steel. [Online] <https://www.worldautosteel.org/steel-basics/automotive-advanced-high-strength-steel-ahss-definitions/>.
15. Raabe, h. Dierk. *Quench and partitioning (Q&P) steels*. [Online] <http://www.dierk-raabe.com/martensite-alloys-and-transformations/quench-partitioning-steels/>.
16. *Evolutionary strategies for identification and validation of material model parameters for forming simulations*. Bäck, T, Heinle, I and Kessler, L. Dublin : Proc. Genetic and Evolutionary Computation Conference, 2011.
17. *Identification and validation of yield locus parameters with respect to industrial forming simulation needs*. Beier, T, et al. Aachen : in Proceedings of ICTP , 2011.
18. *Advances in Post-necking Flow Curve Identification of Sheet Metal through Standard Tensile Testing*. Coppieters, S, et al. s.l. : AIP Conference Proceedings, 2013. Vol. 1567, p. 632.
19. Bridgman, P.W. *Studies in Large Plastic Flow and Fracture*. NY : McGraw-Hill, 1952.
20. Siebel, E and Schwaigerer, S. *Archiv für das Eisenhüttenwesen*. 1948, Vol. 19.
21. Ghosh, A.K. . s.l. : *Metallurgical transactions A*, 1977, Vol. 8A , pp. 1221-1232.
22. Ayres, R.A. . s.l. : *Metallurgical transactions A*, 1983, Vol. 14A, pp. 2269-2275.
23. *Determining material true stress–strain curve from tensile specimens with rectangular cross-section*. Zhang, Z.L., et al. 36, s.l. : *Int. J. Solids Struct.*, 1999, pp. 3497-3516.
24. *A study on determining true stress–strain curve for anisotropic materials with rectangular tensile bars*. Zhang, Z.L., et al. s.l. : *Int. J. Solids Struct.*, 2001, Vol. 38, pp. 4489-4505.
25. Tarantola, A. *Inverse Problem Theory, Methods for Data Fitting and Model Parameter Estimation*. New York, USA : Elsevier Publisher B.V., 1987.
26. Koc, P. and Štok, B. s.l. : *Computational Materials Science*, 2004, Vol. 31, pp. 155-168.
27. Kajberg, J. and Lindkvist, G. s.l. : *International Journal of Solids and Structures*, 2004, Vol. 41, pp. 3439-3459.

28. Identification of material parameters directly from metal forming processes. Ghouati, O. and Gelin, J. s.l. : *J. Mater. Process. Technol.*, 1998, pp. 560-564. , Gelin, J.-C., 1998. ..
29. A finite element-based identification method for complex metallic material behaviors. Ghouati, O. and Gelin, J. s.l. : *Comput. Mater. Sci.*, 2001, Vol. 21, pp. 57-68.
30. Pierron, F. and Grédiac, M. . *The Virtual Fields Method. Extracting Constitutive behaviour from full-field deformation measurements.* London : Springer, 2012.
31. Identification of the post-necking hardening behaviour of sheet metal by comparison of the internal and external work in the necking zone. Coppieters, S, et al. 3, s.l. : *Journal of Materials Processing Technology*, 2011, Vol. 211, pp. 545-552.
32. Identification of Elasto-Plastic Constitutive Parameters from Statically Undetermined Tests Using the Virtual Fields Method. Pannier, Y, et al. 46, s.l. : *Experimental Mechanics*, 2006, pp. 735-755.
33. Identification of plastic constitutive parameters at large deformations from three dimensional displacement fields. Rossi, M. and Pierron, F. 59, s.l. : *Computational Mechanics*, 2012, pp. 53-71.
34. Coppieters, S., et al. 211, s.l. : *Journal of Materials Processing Technology*, 2011, pp. 545-552.
35. Determination of True Stress-Strain-Curves and Normal Anisotropy in Tensile Tests with Optical Strain Measurement. H. Hoffmann, C. Vogl. 1, s.l. : *CIRP Annals*, 2003, *CIRP Annals*, Vol. 52, pp. 217-220.
36. Variation of Normal Anisotropy Ratio " r " during Plastic Forming. Aleksandrovic, S., et al. 6, s.l. : *Journal of Mechanical Engineering*, 2009, Vol. 55, pp. 392-399.
37. Banabic, D., et al. *Formability of Metallic Materials: Plastic Anisotropy, Formability Testing, Forming Limits, Engineering Materials.* s.l. : Springer-Verlag Berlin Heidelberg, 2000.
38. Identification of Post-Necking Hardening Phenomena in Ductile Sheet Metal. S. Coppieters, T. Kuwabara. 54, s.l. : *Experimental Mechanics*, 2014.
39. The relationship between stress and strain for homogeneous deformation. Voce, E. s.l. : *Int Inst Met* , 1948.

40. *Large strain deformation of polycrystalline metals at low homologous temperatures.* J. E. Hockett, O. D. Sherby. 23, s.l. : *J Mech Phys Solids* , 1975, Vol. 2.
41. *The influence of strain hardening and strain-rate sensitivity on sheet metal forming.* K., Ghosh A. 99, s.l. : *J Eng Mat Tech*, 1977, Vol. 3.
42. *Plastic instability under plane stress.* H.W., Swift. 1952 : *Journal of the Mechanics and Physics of Solids*, 1:1–18.
43. *Evaluating the flow stress of aerospace alloys for tube hydroforming process by free expansion testing.* M. Saboori, et al. s.l. : *Int. J. Adv. Manuf. Technol.*, 2013.
44. Wierzbicki, Tomasz. *Structural Mechanics*. [Online] 2013.
<https://ocw.mit.edu/courses/mechanical-engineering/2-080j-structural-mechanics-fall-2013/index.htm>.
45. *Physics and phenomenology of strain hardening: the FCC case.* UF. Kocks, H. Mecking. s.l. : *Prog Mater Sci*, 2003, Vol. 48.
46. *Determination of strain hardening parameters of tailor hardened boron steel up to high strains using inverse FEM optimization and strain field matching.* Ellera, T.K. et al.,. s.l. : *Journal of Materials Processing Technology*, 2016. .
47. *The κ -statistics approach to epidemiology.* Kaniadakis G, Baldi MM, Deisboeck TS, Grisolia G, Hristopulos DT, Scarfone AM, Sparavigna A, Wada T, Lucia U. 1, s.l. : *Sci Rep*, 2020, Vol. 10.
48. Banabic, Dorel. *Sheet Metal Forming, Constitutive Modelling and Numerical*. s.l. : Springer, 2010.
49. Altan, Taylan and Tekkaya, Erman. *Sheet metal forming fundamental*. s.l. : ASM International, 2012.
50. *Metallic materials — Sheet and strip — Determination of biaxial stress-strain curve by means of bulge test with optical measuring systems.* ISO Standards. [Online] 2014. ISO 16808:2014.
51. Altan, Taylan. *the fabricator*. [Online] November 2007.
<https://www.thefabricator.com/stampingjournal/article/bending/dissecting-defects---part-ii>.

52. *An automated hydraulic bulge tester.* Young, R.F., Bird, J.E. and Duncan, J.L. s.l. : *J. Applied Metalworking*, 1981, Vol. 2.
53. *On the Determination of Flow Stress Using Bulge Test and Mechanical Measurement.* Abel D. Santos, Pedro Teixeira, A. Barata da Rocha, and F. Barlat. s.l. : *AIP Conference Proceedings*, 2010.
54. *Determination of sheet material properties using biaxial bulge tests.* Taylan Altan, et al. Chemnitz, Germany : *Proceedings of the 2nd Int. Conference on Accuracy in Forming Technology*, Nov. 13-15, 2006, .
55. Fallahiarezoodar, Ali and Altan, Taylan. *Determining flow stress data by combining uniaxial tensile and biaxial bulge tests.* Centre for precision forming, The Ohio State University. [Online] October 2015.
https://ercnsm.osu.edu/sites/ercnsm.osu.edu/files/uploads/676-5_0.pdf.
56. *Factors affecting the accuracy of flow stress determined by the bulge test.* Billur, E., Demiralp, Y., Groseclose, A. R., Wadman, B., & Altari, T. s.l. : *10th International Conference on Technology of Plasticity, ICTP 2011*, 2011.
57. *Hydraulic bulge test for stress-strain curve determination and damage calibration for Ito-Goya model.* Campos, Hugo, et al. s.l. : *6th European Conference on Computational Fluid Dynamics (ECFD VI)*, 2014.
58. *Determination of Flow Stress by the Hydraulic Bulge Test.* J. Slota, E. Spišák. 47, (2008), 13-17. : *Metallurgia* , 2008, Vol. 47.
59. *Biaxial stress-strain relationship of sheet metal from hydraulic bulging test.* Stachowicz, F. Vancouver B.C., Canada : *5th International multidisciplinary conference*, 2003.
60. *Analytical and Experimental Evaluation of the Stress-Strain Curves of Sheet Metals by Hydraulic Bulge Tests.* L. Lazarescu, D.S. Comsa, D. Banabic. 473, s.l. : *Key Engineering Materials*, 2011.
61. *Plastic deformation of a circular diaphragm under pressure.* Gleyzal, A. 70, s.l. : *appl. Mech., Trans. Am. SOC. mech. Engrs*, 1948, Vol. 3.
62. *A theory of the plastic bulging of a metal diaphragm by lateral pressure.* Hill, R. s.l. : *Phil. Mag*, 1950, Vol. 7.

63. *Der hydraulische Tiefungsversuch und die Ermittlung von Fließkurven (The hydraulic bulge test and the determination of the flow stress curves)*. Panknin, W. Germany : Institute for Metal Forming Technology, University of Stuttgart, 1959.
64. *Hydrostatic bulging of circular diaphragms*. Chakrabarty, J., & Alexander, J. M. 3, s.l. : *Journal of Strain Analysis*, 1970, Vol. 5.
65. *Analytical methodology for the determination of the flow curves of aluminum and steel alloys using the hydraulic bulge tests*. H. Alharthi, S. Hazra, D. Banabic, R. Dashwood. s.l. : *AIP Conference Proceedings*, 2016.
66. *Accurate characterization of biaxial stress-strain response of sheet metal from bulge testing*. J. Min, T. B. Stoughton, J. E. Carsley, B. E. Carlson, J. Lin, X. Gao. s.l. : *International Journal of Plasticity*, 2017, Vol. 94.
67. *A model study of the effect of the size of the die shoulder in hydroforming*. H.M. Shang, V.P.W. Shim. s.l. : *J. Mech. Work. Technol.*, 1984, Vol. 10.
68. *Accurate determination of biaxial stress-strains relationships from hydraulic bulging tests of sheet metals*. Atkinson, M. s.l. : *Int. J. Mech. Sci.*, 1997, Vol. 39.
69. *Superplastic forming of a spherical shell out a welded envelope*. A.A. Kruglov, F.U. Enikeev, R.Ya. Lutfullin. A323, s.l. : *Materials Science and Engineering* , 2002.
70. *Accurate determination of flow curves using the bulge test with optical measuring systems*. Mulder, J., Vegter, H., Aretz, H., Keller, S., van den Boogaard, A.H. s.l. : *Journal of Materials Processing Technology*, 2015.
71. *An experimental study on the comparative assessment of hydraulic bulge test analysis methods*. M. Koç, E. Billur and Ö.N. Cora. s.l. : *Mat. Design*, 2011, Vol. 32.
72. *Yield curve determination using the bulge test combined with optical measurement*. Keller S., Hotz W., Friebe H. s.l. : *IDDRG 2009 congress*, 2009.
73. *Determination of the flow stress of five AHSS sheet materials (DP 600, DP 780, DP 780-CR, DP 780-HY and TRIP 780) using the uniaxial tensile and the biaxial Viscous Pressure Bulge (VPB) tests*. A. Nasser, A. Yadav, P. Pathak, T. Altan,. s.l. : *Journal of Materials*, 2010.
74. *Uniaxial True Stress-Strain after Necking*. Ling, Y. s.l. : *AMP Journal of Technology*, June, 1996, Vol. 5.

75. Bridgman, P.W. *Studies in Large Plastic Flow and Fracture*. New York : McGraw-Hill, 1952.
76. *Evaluation of Stress Distribution in the Symmetrical Neck of Flat Tensile Bars*. Aronofsky, J. s.l. : *J. App. Mech.*, March 1951.
77. *Analysis of the State of Stress in the Neck of a Tensile Test Specimen*. Spiridonova, N.N. Davidenkov and N.I. s.l. : *Proc. ASTM*, 46, 1147-1158, 1946.
78. *Numerical Analysis of the Stress-Strain Curve and Fracture Initiation for Ductile Material*. Li, K.S. Zhang and Z.H. s.l. : *Engrng. Fracture Mech.*, 1994, Vol. 49.
79. *A theory of the yielding and plastic flow of anisotropic metals*. R., Hill. London : *Proceedings of the Royal Society London A*, 193:281–297, 1948.
80. *Identification of Post-necking tensile stress–strain behavior of steel sheet: an experimental investigation using digital image correlation technique*. Surajit Kumar Paul, Satish Roy, S. Sivaprasad, H.N. Bar, and S. Tarafder. s.l. : *JMEPEG*, 27:5736–5743, (2018).
81. *Modified maximum force criterion, a model for the theoretical prediction of forming limit curves*. P. Hora, L. Tong and B. Berisha. s.l. : *Int J Mater Form* 6:267–279, 2013.
82. *Identification of the Continuum Damage Parameter: An Experimental Challenge in Modeling Damage Evolution*. C.C. Tasan, J.P.M. Hoefnagels, and M.G.D. Geers. s.l. : *Acta Mater.*, 2012, Vol. 60.
83. *Variation of Normal Anisotropy Ratio "r" during Plastic Forming*. S. Aleksandrovi, M. Stefanovi, D. Adamovi, V. Lazi. 6, s.l. : *Journal of Mechanical Engineering* , 2009, Vol. 55.
84. *Flow localization in the plane strain tensile test*. V. Tvergaard, A. Needleman and K. K. Lo. 2, s.l. : *J. Mech. Phys. Solids*, 1981, Vol. 29.
85. *Determination of anisotropy and material hardening for aluminum sheet metal*. N. Tardif, S. Kyriakides. s.l. : *International Journal of Solids and Structures*, 2012, Vol. 49.
86. *Characterisation of Diffuse and Local Necking of Aluminium Alloy Sheets Using DIC Technique*. Sz. Szalai, D. Harangozó, I. Czinege. 3, 2019, Vol. 12.
87. *On discontinuous plastic states, with special reference to localized necking in thin sheets*. Hill, R. s.l. : *Jou nal of the Mechanics and Physics of Solids*, 1952, Vol. 1.

88. *Diffuse necking and localized necking under plane stress*. Lian, J., Zhou, D. s.l. : *Materials Science and Engineering A*, 1989.
89. *Mechanical Properties Identification of Sheet Metals by 2D-Digital Image Correlation Method*. V. Nguyen, S. Kwon, O. Kwon and Y. Kim. s.l. : *Advances in Material & Processing Technologies Conference*, 2017.
90. *A Closer Look at the Diffuse and Localised Necking of A Metallic Thin Sheet: Evolution of the Two Bands Pattern*. Bao, C., Francois, M., and Le Joncour, L. s.l. : *Strain*, 2016, Vol. 52.
91. *Necking in tensile bars with rectangular cross-section*. Tvergaard, V. s.l. : *Computer Methods in Applied Mechanics and Engineering*, 1993, Vol. 103.
92. *Abaqus Documentation, student edition 2020*. [Online]
93. *Study on true stress correction from tensile tests*. Choung, J.M., Cho, S.R. s.l. : *J Mech Sci Technol*, 2008, Vols. 22, 1039-1051.
94. Coruk, E and Karadogan, C. *Steel Research International, Special Edition*. 2011.
95. *A criterion for local necking*. Ramaekers, J.A.H. 1, s.l. : *Journal of Materials Processing Technology*, 2000, Vol. 103 .
96. *A generalized approach for the prediction of necking and rupture phenomena in the sheet metal forming*. P. Hora, B. Berisha, M. Gorji, N. Manopulo. Mumbai, India. : *IDDRG Conference*, 2012.
97. *Time dependent determination of forming limit diagrams*. M. Merklein, A. Kuppert, M. Geiger. 1, s.l. : *CIRP Annals - Manufacturing Technology*, 2010, Vol. 59 .
98. *A method of the direct measurement of the true stress–strain curve over a large strain range using multi-camera digital image correlation*. J. Li, G. Yang, T. Siebert, M.F. Shi, L. Yang. s.l. : *Optics and Lasers in Engineering*, 2018, Vol. 107.

APPENDIX A

VFM application in metal plasticity

Pannier and his co-workers²³ published the first application of *virtual field method* in metal plasticity, where actual experimental data was used for this study. The goal of this observation was to obtain the material constants of Voce hardening law with the VFM. The research was intended to experimentally validate the application of the virtual fields method in order to identify the elastoplastic behaviour from full-field optical measurements method.

Taking into account Voce's nonlinear hardening model, the six parameters will be identified: Young's modulus E , Poisson's ratio ν , and the plastic parameters σ_0 , R_0 , R_{inf} and b , where the use of an inverse procedure is therefore necessary to identify the constitutive parameters,

$$\sigma_{voce} = \sigma_0 + R_0 \varepsilon_p + R_{inf} (1 - \exp(-b \varepsilon_p))$$

σ_0 : the initial yield stress,
 R_0 : linear asymptotic hardening modulus,
 R_{inf} and b the parameters that describe the non-linear part of the response in the initial yielding zone.

²³ Y. Pannier, S. Avril, R. Rotinat, F. Pierron, *Identification of Elasto-Plastic Constitutive Parameters from Statically Undetermined Tests Using the Virtual Fields Method*, *Experimental Mechanics*, 46 735-755 (2006).

In this first attempt of using VFM, a uniaxial stress configuration was considered, where a flat dogbone specimen has been chosen so that the longitudinal stress only varies in longitudinal direction, while the other stress components remain comparatively small.

Displacement fields have been evaluated through the image processing at each load step on each side of the specimen. The calculation of the *partial derivatives of the displacement field to obtain the strain field* should be done with high accuracy as this process can amplify the effect of noise and so filtering seems to be quite important.

After obtaining the actual displacement and strain fields, the procedure to identify the elasto-plastic model can be initiated. Having in mind the *basic equation for quasi-static non-linear VFM*, the constitutive equations with the general form of $\bar{\sigma} = g(\bar{\epsilon})$ (where g is a given function of the actual strain components but also of the constitutive parameters) can be applied,

$$-\int_V g(\bar{\epsilon}) : \bar{\epsilon}^* dV + \int_S \bar{T} \cdot \bar{u}^* dS = 0 \quad (a)$$

If the actual strain field is heterogeneous, for any new virtual field implemented in equation (a), a new relation involving the constitutive parameters will be derived, which is the main property of the VFM. With a given set of virtual fields, equation (a) is used to collect the unknown constitutive parameters. The key factor in VFM is the *choice of the virtual fields*. The number and the type of the virtual fields depend on the nature of function $g(\bar{\epsilon})$.

Two different cases are encountered,

- Identification of the Elastic Parameters

In this step, a linear dependency exists between the constitutive equations and the constitutive parameters (as in linear elasticity). In this case, writing equation (a) with as many virtual fields as unknowns results in a linear system of equations by which the parameters can be obtained directly after inversion, provided that the actual strain field is heterogeneous and the virtual fields are independent.

- Identification of Plastic Parameters

In this step, there is no linear dependency between the constitutive equations and the constitutive parameters (as in Elasto-plasticity). The identification strategy is on the basis of the minimization of a residual with regard to equation (a).

Herein, the procedure to obtain elastic parameters is demonstrated as an example.

Identification of the Elastic Parameters

Before the onset of plastic deformation, the response of the specimen is linear elastic. Assuming a plane stress state in the specimen, for an isotropic material the following well-known hook's law can be written,

$$\begin{pmatrix} \sigma_{xx} \\ \sigma_{yy} \\ \sigma_{xy} \end{pmatrix} = \begin{bmatrix} \frac{E}{1-\nu^2} & \frac{\nu E}{1-\nu^2} & 0 \\ \frac{\nu E}{1-\nu^2} & \frac{E}{1-\nu^2} & 0 \\ 0 & 0 & \frac{E}{1+\nu} \end{bmatrix} \begin{pmatrix} \varepsilon_{xx} \\ \varepsilon_{yy} \\ \varepsilon_{xy} \end{pmatrix} \quad (b)$$

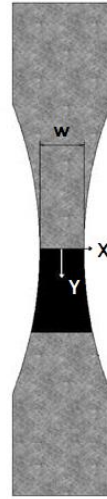
E: Young's modulus
 ν : Poisson's ratio.

Inserting equation (b) into equation (a),

$$\begin{aligned} \frac{E}{1-\nu^2} \int_S (\varepsilon_{yy} \varepsilon_{yy}^* + \varepsilon_{xx} \varepsilon_{xx}^*) dS \\ + \frac{\nu E}{1-\nu^2} \int_S (\varepsilon_{xx} \varepsilon_{yy}^* + \varepsilon_{yy} \varepsilon_{xx}^*) dS \\ + \frac{E}{1+\nu} \int_S \varepsilon_{xy} \varepsilon_{xy}^* dS = \frac{1}{t} \int_{S_f} \bar{T} \cdot \bar{u}^* dS \end{aligned} \quad (c)$$

t : the thickness of the specimen

S : the area of the zone of interest, (the black-coloured area)



Two virtual displacement fields as \bar{v}^{*1} and \bar{v}^{*2} have been defined, in order to find the two material constants for the elastic part,

$$\bar{v}^{*1} \quad \begin{cases} v_x^{*1}(x, y) = v_y^{*1}(x, y) = 0 & \text{for } y < 0 \\ \begin{cases} v_x^{*1}(x, y) = 0 \\ v_y^{*1}(x, y) = -y \end{cases} & \text{for } 0 < y < L \\ \begin{cases} v_x^{*1}(x, y) = 0 \\ v_y^{*1}(x, y) = -L \end{cases} & \text{for } y > L \end{cases}$$

$$\bar{v}^{*2} \quad \begin{cases} v_x^{*2}(x, y) = v_y^{*2}(x, y) = 0 & \text{for } y < 0 \\ \begin{cases} v_x^{*2}(x, y) = xy(y-L) \\ v_y^{*2}(x, y) = 0 \end{cases} & \text{for } 0 < y < L \\ \begin{cases} v_x^{*2}(x, y) = 0 \\ v_y^{*2}(x, y) = 0 \end{cases} & \text{for } y > L \end{cases}$$

Where L is the length of the area of interest.

Feeding the above virtual displacement fields into equation (c), and solving for Young's modulus E , Poisson's ratio ν , one will obtain,

$$\left\{ \begin{array}{l} \nu = -\frac{\int_S y(y-L) \varepsilon_{xx} dS + \int_S x(2y-L) \varepsilon_{xy} dS}{\int_S y(y-L) \varepsilon_{yy} dS - \int_S x(2y-L) \varepsilon_{xy} dS} \\ E = \frac{(1-\nu^2)PL}{t(\int_S \varepsilon_{yy} dS + \nu \int_S \varepsilon_{xx} dS)} \end{array} \right. \quad (d)$$

In the next step, the strain fields measured for all the load steps were inserted into equation (d). However, among all the load steps a certain first few numbers of them will result in acceptable values of E and ν .

APPENDIX B

MMFC: an introduction

Unlike Some kinds of failures such as wrinkling and spring back that can be obtained directly, the study of *rupture needs a great endeavour as the localized necking is concentrated in a very narrow band*. From the numerical simulation point of view, as the position of rupture is not easily predicted, in order to model the necking or very high deformation gradient, a vast number of fine elements must be employed for assessing the rupture. An alternative method is to conduct the study by benefiting from some *failure prediction models*. The concept of Forming Limit Curves (FLC) is currently the most acceptable approach for necking prediction in the numerical simulation of sheet forming processes (81).

Based on the MMFC model, *additional tensile stress is induced as diffuse necking happens*, postponing the occurrence of localized necking. MMFC model takes into account more factors to define the material behaviour in this range, and so far better approximation can be attained. The *classic criterion of maximum force solely considers the influence of hardening behaviours*, while *the effect of yield loci is totally neglected*. In fact, the yield loci, either isotropic or anisotropic, play a very important role in the failure process, so that, without considering the effect of yield loci, the resulted FLC would not be able to demonstrate the real material behaviour (81).

Following the *original maximum force criterion*, (here, P is used as force symbol, to avoid confusion with yield criterion symbol, F)

$$dP = d(\sigma_1 A) = d\sigma_1 A + \sigma_1 dA > 0 \quad (a)$$

➤ Provided that only *strain hardening* effect is taken into account, it can be defined as,

$$d\sigma_1 = \frac{d\sigma_1}{d\varepsilon_1} d\varepsilon_1 .$$

As metallic materials normally follow volume consistency law during plastic forming,

$$\frac{dA}{A} = -d\varepsilon_1 .$$

Inserting the last two relations into equation (a), and considering the fact that in tensile test, $\sigma_1 = \bar{\sigma}$ and $\varepsilon_1 = \bar{\varepsilon}$, we reach the Swift formulation (81),

$$\frac{d\bar{\sigma}}{d\bar{\varepsilon}} > \bar{\sigma} .$$

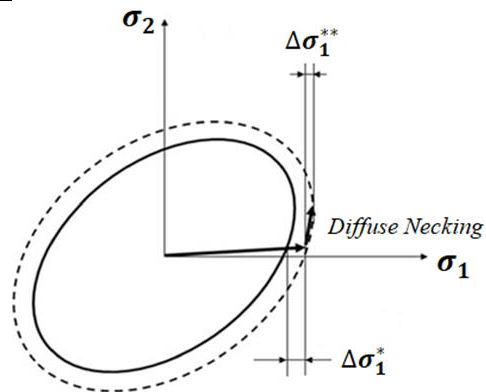
➤ **However**, as it was mentioned before, the stress σ_1 is not only a function of strain hardening but also the *strain ratio* $\beta = d\varepsilon_2/d\varepsilon_1$. Thus, the stress increment $d\sigma_1$ can be modified as,

$$d\sigma_1 = \frac{\partial \sigma_1}{\partial \varepsilon_1} d\varepsilon_1 + \frac{\partial \sigma_1}{\partial \beta} d\beta \quad (b)$$

$\Delta \sigma_1^* : \frac{\partial \sigma_1}{\partial \varepsilon_1} d\varepsilon_1$: describes the strain hardening effect,

$\Delta \sigma_1^{**} : \frac{\partial \sigma_1}{\partial \beta} d\beta$: describes additional hardening caused by the *transformation of stress states*.

Thus, two types of hardening during diffuse necking can be seen in the figure (81).



By substituting relation (b) into the original form (a), the modified maximum force criterion can be formulated as,

$$\frac{\partial \sigma_1}{\partial \varepsilon_1} d\varepsilon_1 + \frac{\partial \sigma_1}{\partial \beta} d\beta > \sigma_1 d\varepsilon_1 \quad (c)$$

As long as $\frac{\partial \sigma_1}{\partial \varepsilon_1} > \sigma_1$, $d\beta$ is zero and β keeps constant: *uniform deformation state*.

Gradually, the stress increases due to the work hardening influence, however the hardening rate $\frac{\partial \sigma_1}{\partial \varepsilon_1}$ starts to decrease for most of the metallic materials; so that, as soon as the condition $\frac{\partial \sigma_1}{\partial \varepsilon_1} > \sigma_1$ is violated, β (strain increment ratio: $\Delta \varepsilon_2 / \Delta \varepsilon_1$) will alter correspondently to keep the equilibrium state stable. The variation of the strain increment ratio affects the stress state, and can be demonstrated by the yield locus applicable to the material (81). These effects are looked in more details here.

Having β (the strain increment ratio) and $\alpha = \sigma_2 / \sigma_1$ (the stress ratio) in mind, generally the relations $\sigma_1 = f(\alpha) \bar{\sigma}$ and $\Delta \bar{\varepsilon} = g(\beta) \Delta \varepsilon_1$ can be discussed provided that the yield function $F(\sigma_1, \sigma_2) = 0$ is known.

The terms $\partial \sigma_1 / \partial \varepsilon_1$ and $\partial \sigma_1 / \partial \beta$ can be obtained as (81),

$$\left\{ \begin{array}{l} \frac{\partial \sigma_1}{\partial \varepsilon_1} = \frac{\partial \sigma_1}{\partial \bar{\sigma}} \frac{\partial \bar{\sigma}}{\partial \bar{\varepsilon}} \frac{\partial \bar{\varepsilon}}{\partial \varepsilon_1} = f(\alpha) g(\beta) H' \\ \frac{\partial \sigma_1}{\partial \beta} = \frac{\partial \sigma_1}{\partial \alpha} \frac{\partial \alpha}{\partial \beta} = f'(\alpha) \bar{\sigma} \frac{\partial \alpha}{\partial \beta} = f'(\alpha) H / \left(\frac{\partial \beta}{\partial \alpha} \right) \end{array} \right. \quad \begin{array}{l} H = H(\bar{\varepsilon}) : \text{hardening function} \\ H' : \text{slope of the hardening curve} \end{array}$$

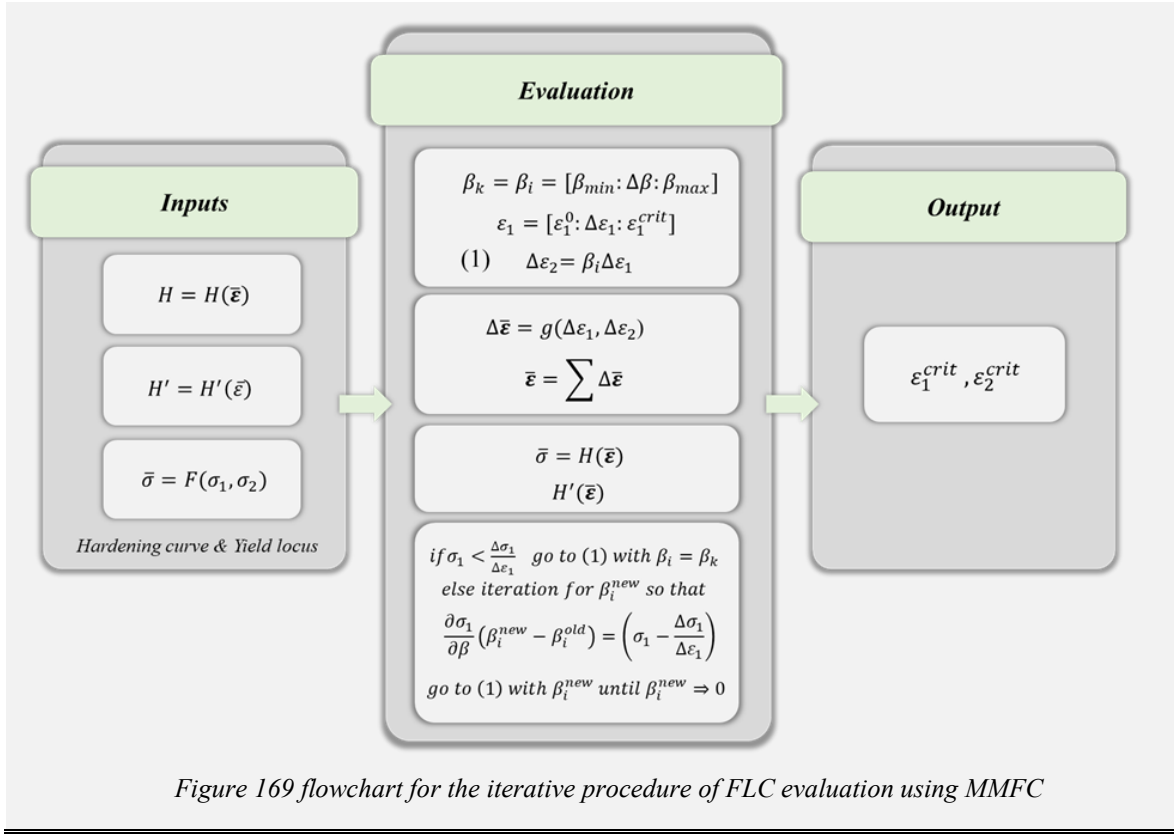
From the definition of β , it is clear that $\beta = \frac{\partial F}{\partial \sigma_{22}} / \frac{\partial F}{\partial \sigma_{11}}$ can be evaluated through employing a proper yield locus, so that one can readily derive the derivation $\frac{\partial \beta}{\partial \alpha}$.

Rewriting (c) as below, the modified formulation of *maximum force criterion* is achieved as,

$$\frac{\partial \sigma_1}{\partial \varepsilon_1} + \frac{\partial \sigma_1}{\partial \beta} \frac{\partial \beta}{\partial \varepsilon_1} > \sigma_1$$

Application of MMFC in FLC evaluation

In order to conduct a theoretical study on the evaluation of FLC, one can follow the above procedure; diffuse necking, however, is a nonlinear process in which significant variations can be observed in all auxiliary functions as well as the stress and strain ratios, α and β . Thus, it is advisable to do the calculation numerically using the following flowchart,



Having critical strains in hand, it is possible to obtain the equivalent strain, which is then can be used to evaluate equivalent stress-equivalent strain curve, as discussed in section 6.3.